

ENHANCED SEPARATIONS STRATEGIES FOR COMPLEX SAMPLE  
CHARACTERIZATION USING ION MOBILITY-MASS SPECTROMETRY

By

J. Rafael Montenegro Burke

Dissertation

Submitted to the Faculty of the  
Graduate School of Vanderbilt University  
in partial fulfillment of the requirements

for the degree of

DOCTOR OF PHILOSOPHY

in

Chemistry

August, 2016

Nashville, Tennessee

Approved:

Date:

Professor John A. McLean \_\_\_\_\_

Professor David E. Cliffler \_\_\_\_\_

Professor David M. Hercules \_\_\_\_\_

Professor Ned A. Porter \_\_\_\_\_

Professor Janet E. Macdonald \_\_\_\_\_

Für die, die immer an mich geglaubt haben,  
und in dieser Reise mich bedingungslos unterstütz haben

## ACKNOWLEDGEMENTS

This work was made by generous support from the National Institutes of Health grants 5UH3TR000491-04 and 3UH3TR000491-04S1, the Defense Threat Reduction Agency grant HDTRA-09-1-0013, the Vanderbilt Institute for Chemical Biology, the Vanderbilt Institute for Integrative Biosystems Research and Education and Vanderbilt University College of Arts and Science.

First of all, I would like to thank my Ph.D. advisor, Professor John A. McLean, for providing me with the freedom to explore my own interests and at the same time, help me navigate through those uncharted territories. In the past 5 years, Prof. McLean has thought me so much, not only science, but teaching and life philosophy as well. For that, and so much more, I thank him.

I would like to thank my dissertation committee members Dr. David E. Cliffel, Dr. Janet E. Macdonald, Dr. Ned A. Porter and Dr. David. M. Hercules, who each have helped in refining my abilities as a scientist, with valuable suggestions and guidance. Additionally, thank you Prof. Hercules for being like a second mentor to me and for the many insightful discussions that went beyond our collaboration and contributions in Chapter 4 of this work.

Beyond my committee, I have been fortunate to work with fantastic people. Without them, the work described in this dissertation would have never been possible. Prof. David M. Aronoff has provided an invaluable collaboration, resulting in important contributions in Chapters 2 of this dissertation. Furthermore, his mentorship from the beginning has been essential and helped me see the broader impacts of my work, and for that I cannot thank him enough. Dr. Libin Xu and Dr. Kristina Adams Waldorf, I learned

many new things through our work together. Dr. Jody May has been a fantastic source of knowledge and I thank him for sharing it throughout our multiple discussions. Connor Lamberson has been both a great friend and a source of invaluable lipidomics knowledge, matched only by his willingness to help.

Many thanks to all the former and current graduate students and postdoctoral researchers in the McLean research laboratory. In particular, I want to thank Dr. Jeffrey Enders, Dr. Cody Goodwin and Dr. Jay Forsythe for their mentorship when I was an early graduate student.

I would like to thank my family. I could not have reached this point without their endless love, support and encouragement throughout my life. I cannot put into words how grateful I am for each and everyone of them. Lastly, I must thank Caitlin Nossett who has been there, listening patiently, motivating me and bringing happiness to my life during the many ups and downs of graduate school.

## TABLE OF CONTENTS

ACKNOWLEDGEMENTS .....	iii
LIST OF TABLES .....	viii
LIST OF FIGURES .....	ix
LIST OF ABBREVIATIONS/NOMENCLATURE/SYMBOLS .....	xi

### Chapter

I. SEPARATIONS IN MASS SPECTROMETRY-BASED CHEMICAL ANALYSIS.....	1
1.1. Introduction.....	1
1.2. Ion Mobility-Mass Spectrometry .....	3
1.2.1. Ion-Mobility Fundamentals .....	4
1.2.2. Travelling Wave Ion Mobility Spectrometry.....	7
1.3. Pre-ionization Separations .....	8
1.3.1. Liquid Chromatography.....	12
1.3.2. Supercritical Fluid Chromatography.....	13
1.3.3. Size Exclusion Chromatography.....	14
1.4. Integration of Pre-ionization Separations with Ion Mobility-Mass Spectrometry.....	17
1.4.1. Analyte Coverage.....	17
1.4.2. Peak Capacity and Peak Capacity Production Rate .....	23
1.4.3. Tandem Ion Mobility Methods and Fragment Ion Correlation .....	26
1.5. Summary and Objectives of Dissertation Research.....	30
1.6. Acknowledgements.....	33
1.7. References.....	34
II. UTILIZATION OF SUPERCRITICAL FLUIDS FOR ENHANCED CHARACTERIZATION IN LIPIDOMICS .....	43
2.1. Introduction.....	43
2.2. Experimental .....	49

2.3.	Results and Discussion .....	53
2.3.1.	Optimization of SFC Separation Using Lipid Standards .....	53
2.3.2.	Analysis of Lipid Extracts from Mouse Brain .....	54
2.3.3.	Deconvolution of Co-eluting Lipid Classes by IM Separation.....	59
2.3.4.	Fatty Acid Composition of Individual Lipid Classes Obtained by Post-mobility Fragmentation in Negative Mode .....	62
2.3.5.	Gene Expression Confirms <i>in vitro</i> Polarization of MDMs .....	66
2.3.6.	Membrane Phospholipid Composition of MDMs.....	68
2.3.7.	Fatty Acid Composition of Different Lipid Classes in Polarized MDMs .....	73
2.4.	Conclusions.....	81
2.5.	Acknowledgements.....	83
2.6.	References.....	84

### III. METHODS FOR METABOLOME COVERAGE EXPANSION FOR UNTARGETED BIOMOLECULAR INTERROGATION .....94

3.1.	Introduction.....	94
3.2.	Experimental.....	96
3.3.	Results and Discussion .....	103
3.3.1.	Metabolic Perturbations .....	104
3.3.2.	Self-organized Maps .....	105
3.3.3.	Temporal Metabolic Signatures in APAP Toxicity .....	111
3.4.	Conclusions.....	117
3.5.	Acknowledgements.....	118
3.6.	References.....	119

### IV. ANALYSIS ADVANCES FOR CHARACTERIZATION OF WIDE MASS RANGE MOLECULAR COMPOSITION.....122

4.1.	Introduction.....	122
4.2.	Experimental.....	124
4.3.	Results and Discussion .....	127
4.3.1.	Exploration of SEC Stationary Phases with Polyesters and Polyurethanes .....	127
4.3.2.	Application of Novel Chromatographic Behavior for the Separation and Characterization of Polyethylene Glycol Compounds.....	135

4.4.	Conclusions.....	141
4.5.	Acknowledgements.....	142
4.6.	References.....	143

V.	PERSPECTIVES AND PROPOSED IMPROVEMENTS ON THE APPLICATION OF SEPARATIONS WORKFLOWS FOR HIGH TEMPORAL RESOLUTION MEASUREMENTS .....	145
----	--	-----

Appendix

A.	References of Adaptation for Chapters.....	152
B.	Supporting Information for Chapter II.....	153
C.	Supporting Information for Chapter III .....	164
D.	Supporting Information for Chapter IV .....	218
E.	Curriculum Vitae .....	224

## LIST OF TABLES

Table 1.1	Peak capacity comparison of different pre-ionization separation techniques .....	27
Table 2.1	Fatty acid percentage composition of individual lipid classes obtained from MS <sup>E</sup> in negative mode.....	65
Table 3.1	Drug exposures to different liver bioreactors .....	100
Table 3.2	Metabolites from ROIs in single chemical stimulus indicated in Figure 3.4.....	112
Table 4.1	Structural assignments for PE 225, PUR 262 oligomers and PEG compounds .....	126
Table 4.2	Calculation of ionization efficiencies for cyclic (crown-ethers) and dimethylated PEG oligomers .....	140



## LIST OF FIGURES

Figure 1.1	2D-separation plot of mass-to-charge ratio and ion mobility .....	6
Figure 1.2	Conceptual plots of physical properties of different physical states.....	11
Figure 1.3	Conceptual plot of the relation between molecular weight and elution time in chromatography .....	16
Figure 1.4	Three-dimensional separations space of pre-ionization separation coupled to IM-MS .....	18
Figure 1.5	Comparison of analyte coverage of different separation techniques .....	20
Figure 1.6	Differences in the analyte coverage between positive- and negative-ion mode.....	22
Figure 1.7	Peak capacity diagram of IM-MS (100 – 1000 $m/z$ ).....	25
Figure 1.8	Schematic of tandem experiments in IM-MS .....	28
Figure 2.1	Supercritical Fluid Chromatogram of lipid standards.....	55
Figure 2.2	Chromatogram of lipid extracts from mouse brain with and without IM in negative mode.....	56
Figure 2.3	Illustration of post-mobility fragmentation ( $MS^E$ ) of individual peaks in both positive and negative modes.....	58
Figure 2.4	IM-MS deconvolution of sulfatides and plasmalogen or alkyl- ether-linked phosphatidylglycerols .....	60
Figure 2.5	IM deconvolution of sulfatides and diacyl phosphatidylglycerols .....	61
Figure 2.6	IM deconvolution of phosphatidylinositols and phosphatidylethanolamine .....	63
Figure 2.7	IM deconvolution of phosphatidylserines and phosphatidic acids .....	64
Figure 2.8	<i>In vitro</i> polarization of MDMs confirmed using gene expression.....	67
Figure 2.9	Three-dimensional PCA plot of lipid profiles for control, M1, M2a and M2c MDM.....	70

Figure 2.10	Comparison of relative distribution of individual lipid classes in the cytosolic leaflet in controls, M1, M2a and M2c MDM .....	71
Figure 2.11	Comparison of relative distribution of individual lipid classes in the luminal side in controls, M1, M2a and M2c MDM.....	72
Figure 2.12	Changes in arachidonic acid composition for different lipid classes for controls, M1, M2a and M2c macrophages .....	75
Figure 3.1	Configuration of artificial capillaries inside the bioreactor .....	97
Figure 3.2	SOM metabolome timeline of APAP treated LBRs and controls.....	107
Figure 3.3	SOM metabolome timeline of APAP and NAC treated LBRs and Controls .....	109
Figure 3.4	SOM differential metabolic profiles identifying ROIs .....	110
Figure 3.5	Selected metabolites time profiles after drug exposure .....	116
Figure 4.1	Elution plots of the molecular weights of cyclic (circles) and linear (squares) chains versus their elution times in SEC.....	126
Figure 4.2	Temperature dependence of elution profiles for PE 225 .....	130
Figure 4.3	Expanded SEC elution plot of the molecular weights of cyclic chains of PE 225 and Extracted ion chromatograms (EIC) of linear and cyclic PE-225 B chains .....	134
Figure 4.4	Extracted ion chromatograms of linear and cyclic PEG compounds .....	136
Figure 4.5	Elution plot of the molecular weights of the diverse PEG compounds versus their elution times in SEC .....	138
Figure 5.1	Cell culture-microdialysis-MS platform.....	148
Figure 5.2	Comparison of Ubiquitin mass spectra in media before and after microdialysis.....	150

## LIST OF ABBREVIATIONS/NOMENCLATURE/SYMBOLS

$\Phi$	Peak capacity
$\Phi \text{ s}^{-1}$	Peak capacity production rate
2D	Two-dimensional
3D	Three-dimensional
AA	Arachidonic acid
ACN	Acetonitrile
APAP	Acetaminophen
APC	Advance polymer chemistry
CE	Ceramide
CID	Collision induced dissociation
DTIM	Drift tube ion mobility
ESI	Electrospray ionization
FWHM	Full width at half maximum
FA	Formic acid
GC	Gas chromatography
GPC	Gel permeation chromatography
GSH	Glutathione, reduced
GSSG	Oxidized glutathione
HPLC	High-performance liquid chromatography
H <sub>2</sub> O	Water
IM	Ion mobility

IM-MS	Ion mobility-mass spectrometry
IMS	Ion mobility spectrometry
IL-4	Interleukin 4
IL-10	Interleukin 10
IFN $\gamma$	Interferon $\gamma$
LBR	Liver bioreactor
LC	Liquid chromatography
LPS	Lipopolysaccharide
MALDI	Matrix-assisted laser desorption/ionization
MDM	Monocyte-derived macrophage
MeOH	Methanol
MEDI	Metabolite Expression Dynamics Investigator
MGDG	Monogalactosyldiacylglycerol
ms	Millisecond
MS	Mass spectrometry
MS/MS	Tandem mass spectrometry
MS <sup>E</sup>	Untargeted tandem mass spectrum
MVSA	Multivariate statistical analysis
<i>m/z</i>	Mass-to-charge ratio
NAC	N-acetyl cysteine
PA	Phosphatidic acids
PC	Phosphatidylcholine
PCA	Principal component analysis

PE	Phosphatidylethanolamine
PEG	Polyethylene glycol
PG	Phosphatidylglycerol
PI	Phosphatidylinositol
PL	Phospholipid
PLS-DA	Partial least-squares discriminant analysis
ppm	Parts-per-million
PS	Phosphatidylserine
ROI	Region of interest
SM	Sphingomyelin
S/N	Signal-to-noise ratio
TOF	Time-of-flight
TWIM	Traveling wave ion mobility
UPLC	Ultra-performance liquid chromatography
UV	Ultraviolet
Q	Quadrupole

## CHAPTER I

### SEPARATIONS IN MASS SPECTROMETRY-BASED CHEMICAL ANALYSIS

#### *1.1. Introduction*

Life sciences have benefited greatly from numerous advances in mass spectrometry (MS) techniques in the last decades due to its selectivity, sensitivity and broad dynamic range.<sup>1,2</sup> Its robustness and capability to rapidly analyze samples makes it an ideal technique for large-scale studies that require high-throughput. While MS has been largely utilized to answer biological questions, synthetic scientist, and in particular, polymer chemists have taken advantage of the quantitative relationship between intensity and concentration to characterize a wide range of oligomers and polymers as well.

A challenge prevalent in the single dimension MS analysis of complex samples is that isobaric interferences produced by molecules with the same mass tend to occur, leading to difficulties in data interpretation. Considering the low diversity of elements found in biomolecules and synthetic polymers (H, C, N, O, P and S) as well as the long chains built by C-C bonds, the possibilities of multiple analytes possessing the same molecular formulas but different structures or atom arrangement are considerably high. This limitation necessitates a secondary analytical technique orthogonal to molecular mass, which combined create a multidimensional analysis. Traditionally, chromatographic separations are coupled on-line with mass spectrometers and mass spectra are acquired over the length of the chromatogram. This results in a two-

dimensional analysis with chromatographic retention time and mass-to-charge ratio ( $m/z$ ) represented on each axis.

The various types of separations coupled to MS can be divided into two groups depending on whether the separation occurs pre- or post-ionization. Ion-mobility (IM), as the name suggests, is a post-ionization separation technique. In IM, ions are separated based upon their gas-phase packing efficiency, which provides information about structure and conformation on the order of milliseconds (ms).<sup>3, 4</sup> However, the need for analyte ionization prior to mobility separation is a major limitation. This plays an important role in the analysis of complex biological samples where ion suppression effects decrease the analyte coverage, reproducibility and accuracy of measurements. On the other hand, ion suppression effects can be addressed by combining pre-ionization separations with MS. This pairing is widely used with mobile phases in different physical states such as gas, liquid and supercritical fluid. The coupling of gas chromatography (GC) is mostly applied to the analysis of volatile compounds,<sup>5, 6</sup> while liquid chromatography (LC) or more commonly known, high performance liquid chromatography (HPLC) can be applied for a wider range of molecules.<sup>7-10</sup> The use of supercritical fluids for chromatographic purposes has not been widely adopted. Early in the development of this technology, technical limitations in pressure controllers and injection systems diminished the confidence in its potential. Nonetheless, supercritical fluid chromatography (SFC) provides access to faster separations and polarities not easily accessible to other mobile phases due to the special physical properties of supercritical fluids.<sup>11</sup> For the characterization of synthetic polymers, size exclusion chromatography (SEC) is most commonly used, both on and off-line.<sup>12</sup> In SEC, the separation is based on

molecular weight or chain length, allowing for shorter and longer chains to be ionized and detected with less interferences and biases.

The aim of this introductory chapter is to provide an overview of the different separation techniques coupled to IM-MS and review the advantages and benefits realized from three-dimensional separation, which include IM between pre-ionization and mass analysis for the profiling and identification of metabolomic studies, as well as the characterization of complex synthetic polymer mixtures.

## ***1.2. Ion Mobility-Mass Spectrometry***

Mass spectrometry and ion mobility techniques could be broadly described as gas-phase separations of charged particles.<sup>13</sup> MS operates under vacuum ( $10^{-5} - 10^{-9}$  Torr) in order to avoid collision with neutral particles and provides molecular weight information. On the other hand, IM pressure regions are in the order of 1-10 Torr, where collisions with neutral gas are necessary for the basic principles of the separation, providing molecular size information. The coupling of IM-MS is possible due to the differences in their separations speed. Mass spectra in TOF instruments are collected on the order of  $\mu\text{s}$ , while IM separations is on the order of ms. This translates to several MS spectra being acquired for each IM spectrum. As both techniques utilize charged particles for their analysis, ion sources considerations need to be recognized.

The most common soft ionization sources in the analysis of biomolecules and synthetic polymers are electrospray ionization (ESI) and matrix assisted laser desorption/ionization (MALDI) and they offer complementary capabilities.<sup>14-16</sup> The three main differences between these ionization techniques are important when considering the



type of experiment to perform. First, charge state of the analytes varies between both ionization techniques. MALDI generally generates singly charged ions in the form of  $[M+H]^+$ ,  $[M+Na]^+$ , etc., where M is the intact analyte. On the other hand, ESI generates both singly and multiply charged ions primarily as multiprotonated species, e.g.  $[M+H_n]^{n+}$ . Typically in ESI, larger molecules such as proteins, peptides and polymers tend to be multiply charged, while small molecules such as metabolites and short chain oligomers tend to be singly charged. In addition to the inherent complexity of biological samples, partitioning the signal of each analyte into several charge states further convolutes the interpretation of the sample composition. Secondly, the high tolerance of non-volatile salts present in the sample in MALDI reduces the number of steps in sample preparation. However, an empirical knowledge of appropriate matrices is necessary. Third, and probably most significant in the selection during experimental design is the pulsed and continuous ion generation modes of MALDI and ESI, respectively. This has pragmatic implications regarding the technical integration of these ionization techniques to other instrumental components.

As mentioned previously, isobaric molecules cannot be separated by MS alone. However, other separation techniques coupled to MS can resolve these interferences. In the next sections IM will be discussed in more detail.

### ***1.2.1. Ion Mobility Fundamentals***

The concepts of gas-phase IM separations and the coupling to MS have existed for over a century and since the 1960s, respectively.<sup>17-19</sup> But the adoption in the analysis of biomolecules was delayed until the implementation of the two primary soft ionization

techniques, ESI and MALDI.<sup>20-26</sup> Despite its great potential and the expansion into the biological fields, IM-MS was initially only available to a few laboratories who could build the instruments in-house. However the introduction of a commercially available IM-MS instrument a decade ago transformed IM into a widely utilized technique, similar to the integration of liquid chromatography and mass spectrometry (LC-MS).<sup>27-30</sup>

Generally, IM can be defined as the velocity (kinetic energy) of ions in a neutral gas. Differences in ions velocities, travelling through a neutral gas is primarily dependent on their structure (size and shape) and not their mass (molecular formula). Smaller ions experience fewer collision with the neutral gas, and thus drift faster than larger ions. This takes place in a mobility separation drift tube (DT) or cell composed of stacked ring electrodes that apply an electric field across a defined region (DTIM). This DT is filled with an inert gas, usually helium or nitrogen at a constant pressure. Other names such as gas-phase electrophoresis and plasma chromatography have also been to describe the IM analytical technique.<sup>31, 32</sup>

In the fields of bioanalysis, IM has the potential of separating complex samples based on the differences in gas-phase packing efficiencies among the different classes of biomolecules.<sup>33-37</sup> For example, lipids are less efficient in their gas-phase packing than peptides with similar molecular weights due to their long fatty acid chains. The trend for the IM-MS separation of biomolecules is illustrated in Figure 1.1.

IM experiments can be divided into temporally and spatially dispersive methods. While temporally dispersive methods separate ions in time but along the same path, spatially dispersive methods separate ions along different trajectories. Temporally dispersive methods can obtain a complete IM spectrum in one cycle. In contrast, spatially

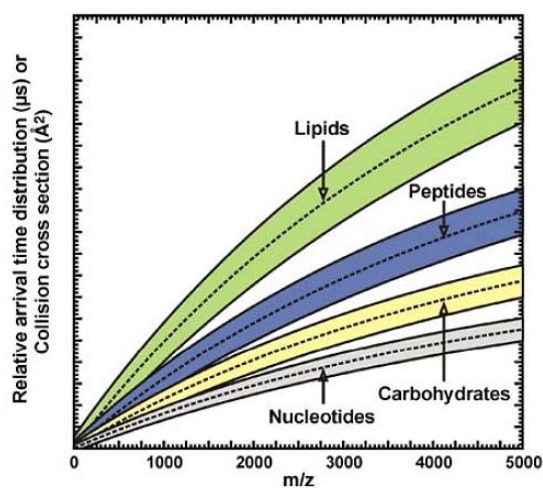


**Figure 1.1.** 2D-separation plot of mass-to-charge ratio (MS) and ion mobility (IM). Different biomolecular classes are separated based upon their gas phase packing efficiency allowing for separation of isobaric molecules. Adapted from L.S. Fenn and J.A. McLean, *Analytical and Bioanalytical Chemistry* **2008**, 391, 905-909, Figure. 2(a), with permission from Springer Science+Business Media.

dispersive methods are conventionally configured to transmit ions within a narrow range of mobilities at a time. This work focuses on temporal ion dispersion through the use of travelling wave ion mobility instrumentation.

### ***1.2.2. Travelling Wave Ion Mobility***

Despite travelling wave ion mobility (TWIM) being a relatively new IM technique, it was the first commercially available IM instrument (Syantp HDMS, Waters Corporation).<sup>38</sup> The basic components of the travelling wave IM are similar to those in DTIM, where ions travel through the drift region under the influence of an electric field filled with a low static pressure (1-5 Torr) of nitrogen gas. In TWIM the ring electrodes confine ions to the center of the device to reduce ion loss by applying a radio-frequency potential.<sup>39</sup> A key difference between TWIM and DTIM is the manner in which ions are propelled through the drift region. In TWIM, a pulsed voltage is applied on neighboring ring electrodes and is rapidly switched in the direction of the mass spectrometer (TOF). This generates a travelling wave with the capacity of separating ions by their mobility. Smaller ions are capable of traveling with or “surf” the wave and have higher velocities. On the other hand, larger ions due to the higher number of collisions have a slower velocity and cannot travel efficiently with the wave. These slower ions roll over the top of the wave and wait for the next wave cycle to carry them forward. The number of times an ion rolls over a wave is directly related to its mobility. In this manner, only ions that roll over a wave will be separated and ions with different sizes travelling in the same wave will arrive at the same time with no useful mobility separation. Therefore, tuning of factors such as traveling wave height and velocity and the neutral drift gas pressure is

necessary in order to obtain high quality mobility separation and avoid activation via high-energy ion-neutral collision-induced dissociation (CID).<sup>39</sup>

### ***1.3 Pre-ionization Separations***

Pre-ionization separations techniques are commonly coupled to both MS and IM-MS in order to circumvent analyte signal interferences. Despite the potential of IM to separate isobaric interferences, a third dimensional separation is commonly needed due to two limitations: i) IM has a limited resolving power of *ca.* 40 (author's laboratory), resulting in limited mobility separation for analytes of interest contained within complex samples and ii) ion suppression effects have long been known to hinder the ionization process particularly in ESI sources. Thus, if an insufficient number of ions are generated in the ion source, low signal-to-noise ratios (S/N) will be observed in the mass spectrum. This ultimately limits the limit of detection and dynamic range of the analysis. The underlying reason for these suppression effects is due to the fundamentals of electrospray, including droplet formation and fission. Previous work suggests that reduced evaporation efficiency is the most likely suppression mechanism.<sup>40-44</sup> The main reasons for this reduced evaporation are hypothesized to be several-fold.

- i) Non-volatile molecules increase the boiling point by altering the colligative properties of the solution.
- ii) Certain non-volatile compounds (*e.g.* detergents) can have a high surface activity and accumulate on the surface blocking analyte and solvent molecules from reaching the outer surface of the droplet. This results in a higher surface tension

and decreases the evaporation of the solvent from the droplet, which are key processes for both the charge residue model and the ion evaporation model.

- iii) Non-volatile salts can crystallize during ESI, causing co-crystallization with analyte molecules preventing the transition from liquid- to gas-phase.
- iv) Large sphere of hydration of strongly solvated ions (*e.g.* Na<sup>+</sup>, K<sup>+</sup>, etc.) restrict the mobility of analyte molecules to the surface of the droplet.
- v) Competition for the charge can occur between different analytes with different affinities to adopt a charge being present in the same droplet, causing ion suppression. This type of ion suppression effects are not easily avoided in the analysis of complex samples, whereas different offline techniques for the removal of detergents and salts are widely utilized to address the often causes of suppression.

The use of pre-ionization separations reduces ion suppression effects by separating the different analytes of complex samples to a different droplet composition and reducing the number of co-eluting molecules at a particular time. Furthermore, the separation of non-volatile salts from analytes of interest increases the ionization efficiency of the ESI source. Several pre-ionization techniques have been utilized with both MS and IM-MS. Gas chromatography, high performance liquid chromatography and capillary electrophoresis (CE) have proved to be amenable for enhancing peak capacity and orthogonality in the analysis of complex samples.<sup>45-48</sup> One shortcoming of coupling condensed-phase separations with IM-MS is the reduction of throughput and analysis speed. While IM-MS spectra can be acquired in ms, condensed-phase chromatography techniques range in the order of minutes to hours. As mentioned previously, the

application of LC separations can be applied to wider range of analytes and it is not restricted to only volatile compounds, as is the case for GC. However, the high viscosity and low diffusivity of water and organic solvents combined with the trend of smaller particle size ( $< 2\mu\text{m}$ ) stationary phases (ultra or ultra-high performance liquid chromatography, UPLC or UHPLC) cause extremely high column backpressure, resulting in lower flow rates. Some of these limitations can be addressed by utilizing supercritical fluid chromatography (SFC). An interesting concept of utilizing the special physical properties of supercritical fluids for chromatography was first described by Klesper and co-workers in 1962 for the separation of organometallic compounds.<sup>49</sup> The supercritical fluid is defined as any substance at a temperature and pressure above its critical point, where distinct liquid and gas phases do not exist. The critical point for  $\text{CO}_2$ , the most common mobile phase used today, lies at  $31.1\text{ }^\circ\text{C}$  and  $72.9\text{ atm}$ . In this region  $\text{CO}_2$  acts as both gas and liquid therefore, has the density and extraction properties of a liquid and diffusivities and viscosity characteristics of a gas (Figure 1.2). These properties allow for higher flow rates compared to LC techniques. Increased flow rates decrease the analysis time, which can be of great benefit in large studies.<sup>50-53</sup>

A subset of LC is size exclusion chromatography (SEC), which applications range from the separation of large proteins in the life sciences to the characterization of synthetic oligomers and polymers in large-scale industry processes. The advantage of SEC is the separation of molecules based only on size and length regardless of their chemical composition and atom arrangement, similarly to IM. Interestingly, both IM and SEC have been utilized in obtaining useful structural information about specialized polymers in their respective conformations in both solution and gas-phase.<sup>54-59</sup>

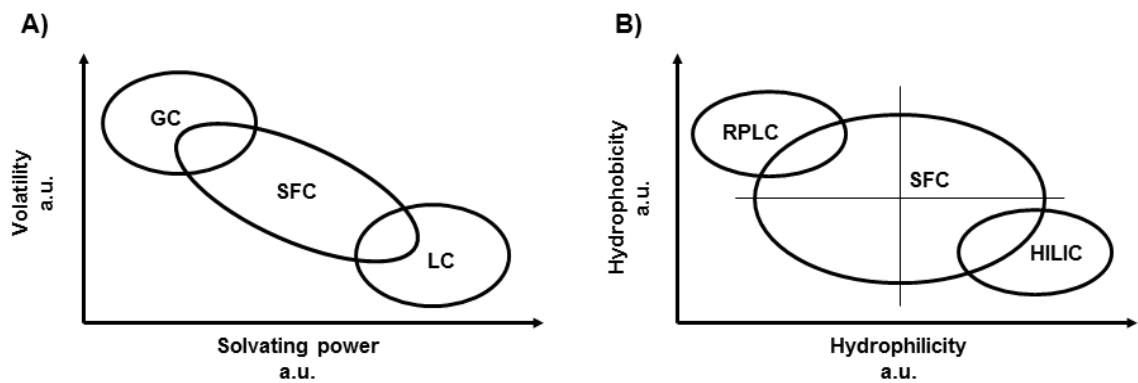


**Figure 1.2.** (A) Schematic of the relationship between solvating power and volatility of analytes in gas chromatography (GC), liquid chromatography (LC) and SFC. (B) Schematic of the wide polarity coverage of analytes in SFC compared to normal phase (HILIC) and reversed phase liquid chromatography (RPLC).



### 1.3.1. *Liquid Chromatography*

Separating very polar high molecular weight biopolymers was at one time thought to be impossible by GC due to concerns of thermal instability. This challenge attracted the interest of many scientists and led to the development of HPLC in the 1960s.<sup>60, 61</sup> The basic principle of LC separations could be described as exploiting differential chemical and physical interactions (*e.g.* adsorption, partition, hydrogen-bonding, etc.) between analytes and both mobile and stationary phases. In current LC column technology, the most predominant stationary phase material used are porous silica particles with different surface chemistries tailored for different applications. For example, reversed phase liquid chromatography (RP-LC) stationary phase consists of silica particles with long aliphatic chains, usually C18, which are design to retain analytes based on their hydrophobic characteristics.<sup>62</sup> On the other hand, HILIC (hydrophilic interaction liquid chromatography) stationary phase consist of a polar particle surface with free hydroxyl-groups or other basic functional groups such as amino or amide moieties. These highly polar functionalized surfaces are designed to retain analytes based on much more complex interactions, such as polarity and electrostatics.<sup>63</sup>

As with the stationary phase, the selection of the mobile phase requires certain considerations. In reversed-phase chromatography, highly aqueous mobile phases are used at the beginning of the chromatogram and gradients increasing the content of organic solvents are applied to systematically release retained molecules from the hydrophobic stationary phase.<sup>64</sup> Conversely, HILIC utilizes high organic solvent composition during the early stages of the separation and gradually increasing the H<sub>2</sub>O content elutes more polar metabolites.

### 1.3.2. *Supercritical Fluid Chromatography*

Historically, supercritical fluid chromatography (SFC) developed an unfavorable reputation of being irreproducible as a result of post-column pressure fluctuations and a low polarity mobile phase (CO<sub>2</sub>), which limited its use to a small number of applications, especially the analysis of nonpolar analytes. Significant technical advancements in the development of pressure regulation instrumentation, and more precise injection systems were subsequently developed to significantly improve analytical reproducibility.<sup>65-68</sup> In order to broaden the applicability of SFC analysis, the community optimized the technique for the analysis of polar analytes by using organic solvents as modifiers (*e.g.* methanol, acetonitrile, etc.) with polar and/or ionic compounds as additives (*e.g.* ammonium acetate, ammonium formate).<sup>69</sup> These improvements allowed both the mobile phase and surface chemistry of the stationary phase to be tailored based on experimental necessity.<sup>70</sup> Recently, these developments have resulted in the application of contemporary SFC to a wide variety of analyte classes (*e.g.* lipids, small molecules and peptides).<sup>71-73</sup> Since the mobile phase is predominately CO<sub>2</sub>, only small amounts of organic solvents are used in contrast to HPLC, which has allowed SFC to be categorized as a “green” analytical tool.<sup>71</sup> Furthermore, numerous parameters can be used independently to optimize separation, such as pressure, temperature, and mobile phase composition, allowing for tunable separations. For example, pressure and temperature affect the density of the mobile phase, which is directly proportional to the solvating power. The mobile phase composition and polarity interacts with both the analytes and stationary phase, which results in polar stationary phases adsorbing modifier molecules (*e.g.* methanol), changing the stationary phase polarity and separation characteristics.<sup>53, 74</sup>

SFC has been coupled to numerous different types of detectors including: ultraviolet-visible (UV-Vis), evaporative light scattering detector (ELSD), Fourier transform infrared (FT-IR) and mass spectrometry (MS) to name a few.<sup>74, 77</sup>

While these advancements have resulted in a highly versatile chromatography technique, one area of SFC separations which requires significant exploration is the selection of both stationary and mobile phases.<sup>53</sup> Conventionally, columns and co-solvents are selected by screening different combinations using representative analyte standards. This approach is costly and time-consuming, but necessary, since predictions of ideal parameters and conditions are not currently available. Screening stationary and mobile phases for retention and separation is straightforward when the analyte composition of the sample is known and standards are available, which is the case in the majority of the studies in the pharmaceutical industry. However, when analyzing unknown biological samples (*e.g.* bacterial extracts, cancer tissue, cell lysate, etc.) in untargeted metabolomic studies, the countless possibilities of different parameter settings is a daunting endeavor. The selection and screening of the optimum mobile phase, stationary phases and other physical parameters (temperature, pressure, etc.) during method development is a formidable challenge, especially when thousands of analytes with different chemistry are present.

### ***1.3.3. Size Exclusion Chromatography***

Size exclusion chromatography, also known as gel permeation or gel filtration chromatography, separates particles on the basis of molecular size.<sup>78</sup> Molecules with different length or size but similar chemical composition will be separated in SEC based

solely on their hydrodynamic volume.<sup>79</sup> The principle lies in that longer chains, with larger hydrodynamic volumes cannot enter the pores of the stationary phase, flowing through the column faster than smaller molecules whose elution path or distance increases when entering the pores. This technique is largely applied to high molecular weight molecules or macromolecular complexes such as proteins and industrial polymers with the purpose of separating different sized particles for further analysis but also for the determination of the molecular weight distribution (MWD).<sup>80, 81</sup>

The characterization of the MWD of synthetic polymers represents a major challenge for polymer chemists in spite of the large economic incentives in detailed formulations of specialized compounds. Some of those challenges are: i) synthetic processes are known to create complex mixtures of products with different physical and chemical properties such as linear, cyclic and dendrimers structures to name a few. This results in different ionization efficiencies for the different species, making quantitation extremely difficult by MS. ii) The separation of such complex mixtures based solely in their chemical composition is achieved only through liquid chromatography at critical conditions (LCCC), where parts of the analyte are made invisible to the stationary phase. However, LCCC requires extensive optimization and the conditions can only be determined empirically.<sup>82, 83</sup> Figure 1.3 illustrates the different chromatographic behaviors of SEC, LCCC and traditional liquid adsorption chromatography (LAC), where only LCCC shows no selectivity for analytes exhibiting different molecular weights.

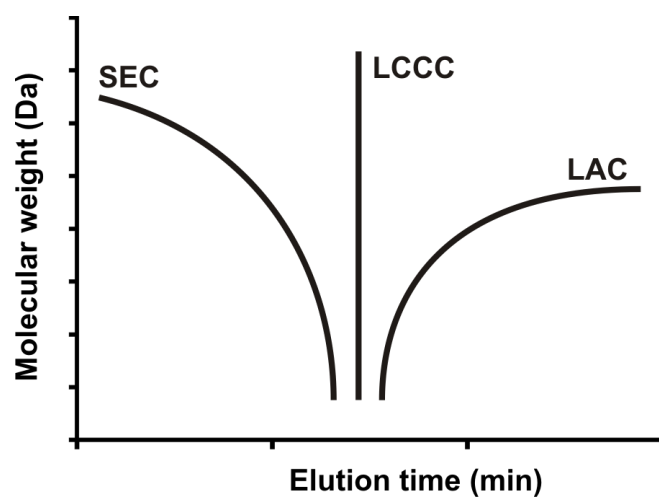


**Figure 1.3.** Conceptual plot of the relation between molecular weight and elution time for size exclusion chromatography (SEC), liquid chromatography at critical conditions (LCCC) and liquid adsorption chromatography (LAC).

#### ***1.4. Integration of Pre-ionization Separations with Ion Mobility-Mass Spectrometry***

The integration of pre-ionization separation to the two-dimensional separation space of ion mobility and mass spectrometry adds a third dimension of separation, which is orthogonal to IM-MS (Figure 1.4). It is worth discussing the fact that that IM and MS are not completely orthogonal to each other due to the correlation of molecular mass and size.<sup>46</sup> This is perceptible when considering that heavier ions will inherently occupy a larger volume or space. This mobility-mass correlation is termed “conformational space”.<sup>84</sup>

##### ***1.4.1. Analyte Coverage***

Comprehensive metabolite coverage, especially for untargeted studies, increases the possibilities of detecting relevant features for biological probing. In an effort to integrate metabolomics into a systems biology-based analysis, all-inclusive analyte coverage incorporating a variety of analytical techniques is desirable. With this in mind, a study was undertaken in which the metabolite coverage between four different separation techniques coupled to IM-MS was evaluated based on the number of features unique to each particular chromatography technique. These consisted of two stationary phases with SFC (silica and ethyl-pyridinium, Si and EP respectively) and two stationary phases with LC (RP and HILIC). The different interactions between stationary and mobile phase inherent amongst these different separation techniques (RP-LC, HILIC, SFC-Si and SFC-EP) suggest very different analyte coverage. For this study, SFC columns were selected based on the “normal phase” characteristics of silica columns and orthogonality of the EP packing material to more common phases, as suggested in previous studies by West and

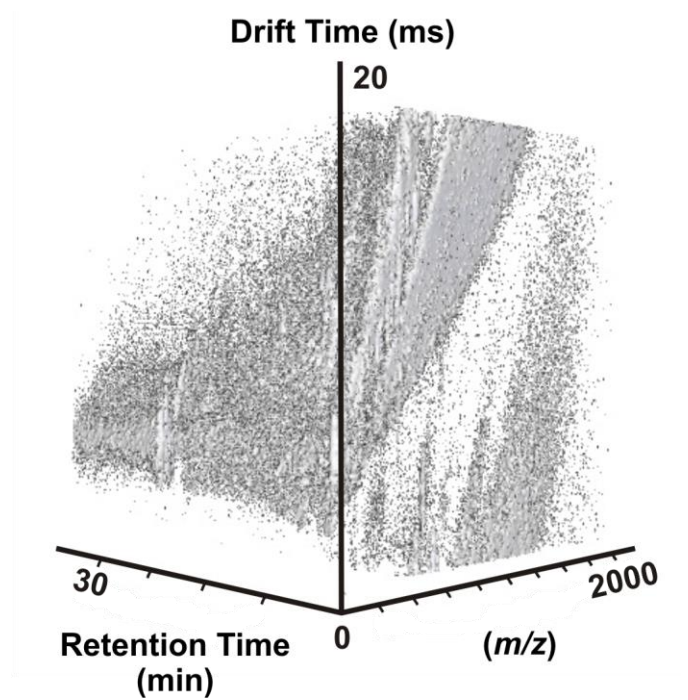


**Figure 1.4.** Three-dimensional separations space of pre-ionization separation (chromatography) coupled to the two-dimensional conformational space of IM-MS.

Lesellier.<sup>85</sup> Previous experiments comparing RP-LC and SFC using a cyano column for separation of pharmaceutical compounds have been conducted,<sup>86</sup> however, to our knowledge, no comprehensive analysis of complex biological samples using RP-LC, HILIC and SFC (Si and EP) have been reported. Siuzdak and coworkers studied differences between HILIC and RP-LC separations of bacterial cell pellets and human cancer cells and determined  $\geq 30\%$  overlap, while in our laboratory results demonstrate an overlap of 2%.<sup>87</sup> These results could be explained by the differences in samples types (bacterial strains, extraction, etc.).

In this work, features detected in positive and negative ion mode were combined and then compared for each separation techniques (Figure 1.5 (A)). The total number of features for each sample results was determined by subtracting the background and eliminating chemical noise using blank samples. The highest number of unique features was detected by RP-LC (1657), while HILIC, SFC-EP and SFC-Si had similar number of detected unique features (966, 979 and 959 respectively). Minimal overlap is observed across all 4 separations (only 8 features). The overlap between HILIC and SFC techniques is much higher (7.6%) than between RPLC and the SFC techniques (2.1%), which suggest that the SFC methods have more “normal-phase” characteristics. When comparing SFC-Si and SFC-EP, the number of overlapping features is only 17.5%. These results indicate very specific types of interactions and specialized chromatography interaction that exist between stationary phase, mobile phase and analytes in supercritical fluid separations, which agree with previous work described by West and Lesellier.<sup>53</sup> Further exploration of different columns with different functional groups (*i.e.* cyano, diol, amino and phenyl) could potentially increase metabolome coverage.



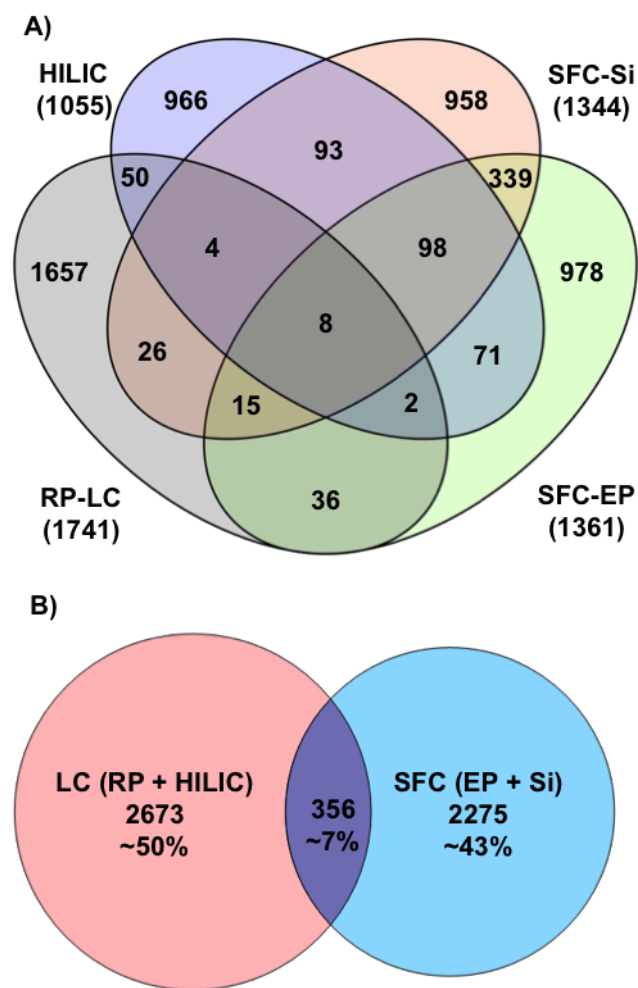


**Figure 1.5.** A) Venn diagram illustrating the number of features observed in the bacterial extract mixture detected by RPLC, HILIC, SFC-Si and SFC-EP and the relations between. B) Venn diagram represents the relation of features detected between LC and SFC separation techniques. The total number of detected species across all separation techniques is 5,304.

A Venn diagram depicting the number of features observed in LC and SFC techniques is contained in Figure 1.5 (B). The LC techniques (RPLC and HILIC) were capable of detecting more than half of the total number of observed features (~57%), however SFC (SI and EP) detected a considerable number of unique features (~43%). These data demonstrate that SFC analyses nearly doubled the number of detected features allowing for a more comprehensive global metabolic profile. In these studies, a total of 5,304 features were observed by combining all techniques (RPLC, HILIC, SFC-Si and SFC-EP).

The ion polarity is another factor to take into consideration due to different analyte affinities to preferentially adopt different ion forms. The different contribution of unique features observed in both positive and negative ion mode for each separation technique investigated is illustrated in Figure 1.6. The data illustrates that the highest number of features detected in RP-LC were in positive mode (~70%, 1265 features). Positive ion mode also contributed slightly more to the number of features in both SFC-Si and SFC-EP techniques (~60% and 56% respectively). On the other hand, ~56% of the features observed in HILIC were also observed in negative ion mode. These results concur with a previous study where, positive and negative ion mode contributed more to RPLC and HILIC respectively.<sup>87</sup>

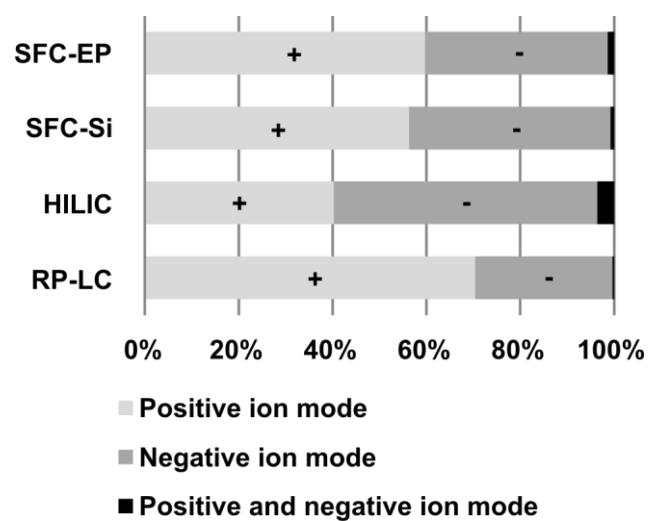


**Figure 1.6.** Metabolome coverage by RP-LC, HILIC, SFC-Si and SFC-EP in both ESI positive and negative ion mode expressed as the percentage of total number of features detected by each separation technique.

#### **1.4.2. Peak Capacity and Peak Capacity Production Rate**

In the evaluation of analytical separation efficiency and throughput, two relevant descriptors are peak capacity ( $\phi$ ) and peak capacity production rate ( $\phi \text{ s}^{-1}$ ). These values represent the number of peaks that theoretically can be observed within the observation range and resolution of a given analysis. Higher peak capacity and peak capacity production rate translate to an increase in the number of samples that can be analyzed during a defined period of time.

Since IM is not completely orthogonal to MS due to the correlation between size and mass,<sup>46</sup> full separations space in IM-MS is not utilized. As a result, the effective area in an IM-MS spectrum must be scaled appropriately by calculating and dividing the average FWHM of several selected peaks in both dimensions (mobility and  $m/z$ ).<sup>88</sup> In order to determine the areas in which analytes emerge, selected peaks with high, medium and low drift times across the entire  $m/z$  range (100 to 1,000) are plotted such that all peaks are enclosed, thereby establishing an empirically derived set of separation boundaries. Peaks detected by several different separation techniques possessing high, medium and low drift times were selected for these calculations. Using these parameters, the effective IM-MS analysis area is calculated. The chromatographic peak capacity ( $\phi$ ) is determined by dividing the total time of the chromatographic run time by the average FWHM of the eluting analytes. Because polarity and hydrogen bonding capability are ostensibly orthogonal to IM-MS measurements, the peak capacity of each platform (SFC with a silica and ethyl-pyridine stationary phase, HILIC and RPLC) was calculated by multiplying by the chromatography dimension. Peak capacity production rates ( $\phi \text{ s}^{-1}$ ) were determined by dividing the total peak capacity by the total analysis time (or

chromatogram length). These calculations are elaborated on later in this section for SFC-EP. What follows is a brief review of experimentally reported peak capacities for these separations techniques, which can be used for theoretical estimations.

Previously, peak capacities have been conservatively measured for SFC and ion mobility to be ~30-50,<sup>89, 90</sup> and ~40,<sup>48</sup> respectively. The peak capacity for high resolution TOF is estimated here as and ~30,000 (routinely, a mass resolution of 15,000 is obtained with the Synapt G2-S in resolution mode with a mass range from 100 to 1000  $m/z$ ) respectively. Theoretically, the combined peak capacity for the LC-IM-MS system described above using conventional LC would be  $\sim 3.6 \times 10^7$  with a peak capacity production rate of  $3.0 \times 10^4 \text{ s}^{-1}$  for a 20 min chromatography run. However, using the above parameters and taking into consideration the speed of SFC, we calculate a peak capacity production rate of  $1.0 \times 10^5 \text{ s}^{-1}$  for a 3 min run, which is comparable to previously reported peak capacity production rates for small molecules (<1000  $m/z$ ) analysis by SFC-MS.<sup>86</sup> In our calculations, we conservatively chose a mass resolution of 15,000 and  $m/z$  between 100 -1000.

Figure 1.7 illustrates the analytical area of IM-MS conformational space plot, with 84 features plotted across all four separation techniques (21 each) and includes selected high and low drift times across the 100-1000  $m/z$  range. Lines were selected to enclose all features and therefore define the effective analysis area of IM-MS (2779.02 ms x Da). Once the analytical area of IM-MS was determined, the peak capacity of the 2-D separation was calculated by dividing by the average FWHM of the selected mobility peaks and  $m/z$  correlated values of peaks extracted from each of the different separation techniques (*e.g.*  $5.49 \times 10^{-3} \text{ ms x Da}$ , IM-MS  $\phi = 5.06 \times 10^5$  for SFC-EP). Subsequently,

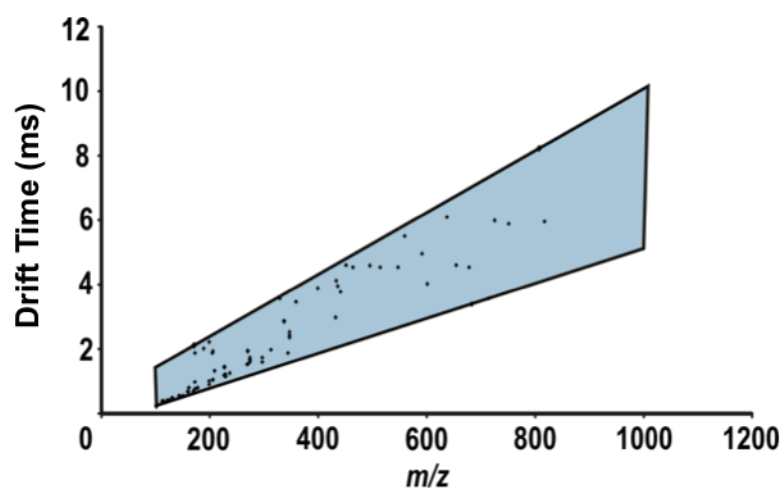


**Figure 1.7.** Peak capacity diagram of IM-MS for the range of 100 – 1000 m/z. The area is calculated by means of integration (2779.02 ms x Da). Lines capable of enclosing all of the selected features in all chromatography types are plotted and used to calculate the effective area of emerging analytes.

total peak capacity of the 3-D separation was calculated by multiplying the peak capacity of each chromatography method (*e.g.* SFC-EP  $\phi = 52$ , 3-D  $\phi = 2.29 \times 10^7$ ). The peak capacity production rate is then calculated by dividing by 720 seconds, which is the full length of the chromatogram ( $\phi \text{ s}^{-1} = 3.18 \times 10^4$ ). Calculations were performed for each experiment type (SFC-Si, SFC-EP, RP-LC and HILIC) (Table 1.1), where similar values were obtained for peak capacities for all separations. However, SFC exhibits higher peak capacity production rates, which underscores the enhanced analytical throughput afforded by SFC.

### ***1.5.3. Tandem Ion Mobility Methods and Fragment Ion Correlation***

Ion mobility-mass spectrometry instrumentation offer substantial flexibility for conduction tandem experiments. Given the necessary transition between pressurized IM and vacuum MS, ion guides, operated at relatively high pressures are used to transfer ions efficiently into and out of the IM region. For TWIMs instruments, this in turn, provides the conditions necessary to perform collision induced dissociation experiments before and after ion mobility separation. In this work, all ion mobility experiments were performed in the Synapt G2 and G2-S platforms, which consist of two ion transfer regions capable of CID experiments in front and after the mobility region in addition to conventional in-source fragmentation. The practical benefit of pre-mobility fragmentation is the possibility to separate the fragmentation product ions in the mobility cell, allowing for mobility information to be obtained for the different products (Figure 1.8.). However, in this configuration, isobaric precursor species will not be separated prior to mobility.

**Table 1.1.** Comparison of peak capacity and peak capacity production rate among RPLC, HILIC, SFC-Si and SFC-EP stationary phases.

Instrument setting	Stationary phase	Peak capacity [ $\phi$ ]	Peak capacity production rate [ $\phi \text{ s}^{-1}$ ]
HPLC-IM-MS	C18	$1.86 \times 10^7$	$1.73 \times 10^4$
	HILIC	$1.84 \times 10^7$	$2.04 \times 10^4$
SFC-IM-MS	EP	$2.29 \times 10^7$	$3.18 \times 10^4$
	Si	$1.97 \times 10^7$	$2.74 \times 10^4$



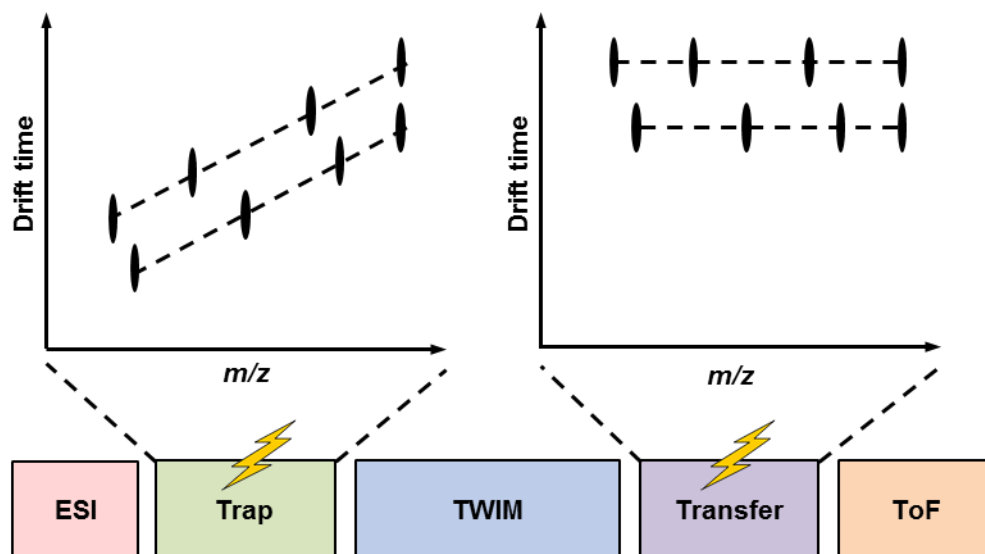


**Figure 1.8.** ESI-TWIM-MS/MS ion fragmentation schematic illustrating the two modes of IM-MS/MS. Fragmentation in the Trap and Transfer region are referred as pre- and post-mobility fragmentation. In pre-mobility fragmentation, ions are fragmented before IM separation (TWIM), resulting in different drift times for the different fragments ions. Alternatively in post-mobility fragmentation, the fragments ions are aligned to their respective precursor ion due to the fact that the mobility measurement is performed on the precursors.

Thus, a convoluted tandem spectrum will be acquired and fragment ions originating from multiple isobaric species will not be resolved.

The alternative tandem mode is to first separate the isobaric interferences by their different mobilities and subsequently fragment the ions in the post-mobility transfer region (Transfer). The result is a correlation of the product ions with the precursor ion in the mobility dimension. In addition to resolving fragment ions originating from isobaric precursors, chemical noise is also attenuated through this fragmentation mode. In this work and other literature this type of tandem experiments is termed “post-mobility”, “parallel ion” or “all ions” fragmentation.<sup>91-93</sup>

In the identification of metabolites, particularly from untargeted workflows, high mass resolution and high mass accuracy are necessary to obtain an accurate measurement of the primary analyte descriptor, molecular mass.<sup>94</sup> High confidence mass information is then used to search databases<sup>95-97</sup> and compare to literature for putative metabolite identifications. Without high mass accuracy, the confidence levels are not high enough for distilling the different possible molecular formulas of the metabolite of interest.

In order to increase the throughput, an approach has been applied to metabolite identification that relies primarily on high mass accuracy to interrogate the entire sample, post separation. This methodology is termed MS<sup>E</sup>, and achieves comprehensive ion fragmentation in to interlaced steps: i) data is acquired over the desired  $m/z$  range in full scan mode.<sup>98</sup> Then ii) collision energy is applied to all ions present in the collision cell (no prior mass selection) in a ramp from low to high energy. This process is repeated over and over again for the duration of the chromatography resulting in two separately accessible data files at each LC time bin, which combines both full scan and

fragmentation data. With the high mass accuracy and post mobility separation of the instrument, product ions can be correlated back to their corresponding precursor ions during offline data analysis. Furthermore, the addition of pre-ionization separation allows for further product-precursor ion correlation by comparing retention times and peak shapes of extracted ion chromatograms.

The limitations inherent to conventional tandem mass spectrometry are also present in tandem experiments incorporating IM, namely the insensitivity to low intensity precursor ions and limited information for structurally similar compounds. For example, fragmentation spectra of compounds differing in one chiral center are indistinguishable from one another and this are insufficient for specific molecular identification. Additionally, constitutional isomers such as leucine and isoleucine yield very similar fragmentation patterns and consequently other techniques such as NMR can provide better information about structural arrangements.

### ***1.5. Summary and Perspectives of Dissertation Research***

Ion mobility techniques rely on the separation of ions in the gas-phase based upon differential velocities under the influence of an electrical field in a neutral gas environment. These differences in the velocity of ions are a result of collisions between the ions and the neutral gas molecules, with larger ions experiencing more collisions than smaller ions due to their larger gas-phase packing efficiency.

The integration of ion mobility separation with mass spectrometry (IM-MS) has been developed for various arrangements all post-ionization as both IM and MS require that the analyte be in ion form. These integrations produce two-dimensional separations

based upon both mobility and mass-to-charge (milliseconds to microseconds, respectively). The differences in separation times allows for hundreds of mass spectra to be obtained for each mobility spectrum. Despite limited orthogonality between these two separations, more information is generated with combined IM-MS and, both peak capacity and signal-to-noise are increased. Furthermore, the correlation between mobility and mass shows dependence upon inherent molecular characteristics such as intramolecular forces, atomic composition and molecular architecture, which allows for preliminary biomolecular and metabolite class designation.

While IM is an important separation technique for differentiating isomers, isobaric molecules with identical molecular formulas can have similar mobilities, which cannot be resolved by IM and thus limits the capabilities of IM-MS for comprehensive analysis. As a result, efforts to expand the coverage of different type of molecules in both complex biological and synthetic samples analysis have turned to coupling IM-MS to pre-ionization separation techniques based on orthogonal properties, mostly through electrospray ionization. The dispersion of analytes to different regions of the chromatogram can increase the analyte coverage by limiting analyte ionization competition in the ion source, while simultaneously reducing concomitant signals in the analysis.

The ability to perform fragmentation experiments between separations in an ion mobility-mass spectrometer increases analyte information, which results in an increased identification confidence. Fragmentation is commonly prefaced with mass-to-charge selection using scanning mass analyzers, commonly a quadrupole (Q), with the goal of isolating a single mass-to-charge band or window. The option of fragmentation both

before and after ion mobility separation results in product ions or isobaric precursor ions separated in the mobility dimension, respectively. Broadband fragmentation ( $MS^E$ ) can be also be obtained by ramping the fragmentation energy applied in the CID process and with ion mobility in post-mobility fragmentation in  $MS^E$  mode product ions can be correlated to their respective precursors.

The large amount of data acquired with a high-resolution mass spectrometer of complex metabolite samples containing thousands of compounds, requires intricate processing and prioritizing steps. Additionally, as described in section *1.4.1. Analyte Coverage*, the selection of pre-ionization technique for untargeted metabolomic studies requires careful consideration, especially in instances where limited sample volumes are available. The focus of the work described herein seeks to utilize different separation techniques with diverse capabilities for improved characterization of complex samples and improve interrogating tools in support of systems biology. Chapter II describes the initial efforts to develop new methodology towards lipidomic studies using the special properties of supercritical fluids. Subsequently, lipidome changes were observed in innate immune cells of distinct phenotypes following polarization. Chapter III focuses on strategies for the analysis of mock-human liver constructs over time following specific toxic and antidote stimuli and comparison of results to *in vivo* metabolism, which resulted in the observation of a number of well-known metabolites. Chapter IV demonstrates the capabilities of state-of-the-art stationary phases and offers an alternative to LCCC for the separation and characterization of telechelic synthetic oligomers. Finally, Chapter V contains perspectives on future directions for both the work described here and, more

broadly, for the development and improvement of analytical tools for temporal interrogation of systems biology.

### ***1.6. Acknowledgements***

This chapter contains the research: Montenegro-Burke, J.R.; Goodwin, C.R.; Bachmann, B.O.; McLean, J.A. Supercritical Fluid Chromatography coupled with Ion Mobility-Mass Spectrometry for analysis of biological samples, In preparation for *Analytical Chemistry*.

We thank Jay Holman for providing us with software to compile different sets of data. This work was funded by the National Institutes of Health (NIH) UH2TR000491, US Defense Threat Reduction Agency (DTRA) HDTRAI-09-1-001 & BMXCL-XL 1-2-0001 (Iyer, LANL), Vanderbilt College of Arts and Sciences, Vanderbilt Institute of Chemical Biology (VICB) and the Vanderbilt Institute for Integrative Biosystems Research & Education (VIIBRE).

## 1.7. References

1. Careri, M.; Mangia, A., Trends Trends in analytical atomic and molecular mass spectrometry in biology and the life sciences. *Anal. Bioanal. Chem.* **2011**, 399, 2585-2595.
2. Griffiths, W. J.; Wang, Y., Mass spectrometry: from proteomics to metabolomics and lipidomics. *Chem. Soc. Rev.* **2009**, 38, 1882-1896
3. Bohrer, B. C.; Merenbloom, S. I.; Koeniger, S. L.; Hildebrand, A. E.; Clemmer, D. E.; Biomolecule Analysis by Ion Mobility Spectrometry. *Annu. Rev. Anal. Chem.* **2008**, 1, 293-327.
4. Clemmer, D. E.; Jarrold, M. F., Ion Mobility Measurements and their Applications to Cluster and Biomolecules, *J Mass. Spectrom.* **1997**, 32, 577-592.
5. Sauer, U., High-throughput phenomics: experimental methods for mapping fluxomes. *Curr. Opin. Biotechnol.* **2004**, 15, 58-63.
6. Tang, Y. J.; Martin, H. G.; Myers, S.; Rodriguez, S.; Baidoo, E. E. K.; Keasling, J. D., Advances in analysis of microbial metabolic fluxes via (13)C isotopic labeling. *Mass Spectrom. Rev.* **2009**, 28, 362-375.
7. Metz, T. O.; Zhang, Q.; Page, J. S.; Shen, Y.; Callister, S. J.; Jacobs, J. M.; Smith, R. D., Future of liquid chromatography-mass spectrometry in metabolic profiling and metabolomic studies for biomarker discovery. *Biomarkers Med.* **2007**, 1, 159-185.
8. Lu, X.; Zhao, X.; Bai, C.; Zhao, C.; Lu, G.; Xu, G., LC-MS-based metabonomics analysis. *J. Chromatogr. B Anal. Technol. Biomed. Life Sci.* **2008**, 866, 64-76.
9. Griffiths, W. J.; Wang, Y., Mass spectrometry: from proteomics to metabolomics and lipidomics. *Chem. Soc. Rev.* **2009**, 38, 1882-1896.
10. Qian, W. J.; Jacobs, J. M.; Liu, T.; Camp, D. G.; Smith, R. D., Advances and challenges in liquid chromatography-mass spectrometry-based proteomics profiling for clinical applications. *Mol. Cell. Proteomics* **2006**, 5, 1727-1744.
11. Taylor, L. T. Supercritical Fluid Chromatography. *Anal. Chem.* **2010**, 82, 4925-4935.
12. Montaudo, G.; Samperi, F.; Montaudo, M. S., Characterization of synthetic polymers by MALDI-MS. *Prog. Polym. Sci.* **2006**, 31, 277-357.
13. Covey, T. R.; Thomson, B. A.; Schneider, B. B., Atmospheric pressure ion sources. *Mass Spectrom Rev.* **2009**, 28, 870-897.

14. Tanaka, K.; Waki, H.; Ido, Y.; Akita, S.; Yoshida, Y.; Yohida, T., Protein and polymer analyses up to  $m/z$  100,000 by laser ionization time-of-flight mass spectrometry. *Rapid Commun. Mass Spectrom.* **1988**, 2, 151-3.
15. Karas, M.; Hillenkamp, F., Laser desorption ionization of proteins with molecular masses exceeding 10,000 daltons. *Anal. Chem.* **1988**, 60, 2299-301.
16. Fenn, J. B.; Mann, M.; Meng, C. K.; Wong, S. F.; Whitehouse, C. M., Electrospray ionization for mass-spectrometry of large biomolecules. *Science* **1989**, 246, 64-71.
17. Barnes, W. S.; Martin, D. W.; McDaniel, E. W., Mass Spectrographic Identification of the Ion Observed in Hydrogen Mobility Experiments. *Phys. Rev. Lett.* **1961**, 6, 110-111.
18. Eiceman, G. A.; Z., Karpas, Introduction to Ion Mobility Spectrometry. in *Ion Mobility Spectrometry, Second Edition*, CRC Press, **2005**.
19. McAfee, K. B. J.; Edelson, D., Identification and Mobility of Ions in a Townsend Discharge by Time-Resolved Mass Spectrometry. *Proc. Phys. Soc. London*, **1963**, 81, 382-384.
20. Gieniec, J.; Mack, L. L.; Nakamae, K.; Gupta, C.; Kumar, V.; Dole, M., Electrospray Mass-Spectroscopy of Macromolecules - Application of an Ion-Drift Spectrometer. *Biomed. Mass Spectrom.* **1984**, 11, 259-268.
21. von Helden, G.; Wytenbach, T.; Bowers, M. T., Inclusion of a Maldi Ion-Source in the Ion Chromatography Technique - Conformational Information on Polymer and Biomolecular Ions. *Int.l J. Mass Spectrom. Ion Processes* **1995**, 146, 349-364.
22. von Helden, G.; Wytenbach, T.; Bowers, M. T., Conformation of Macromolecules in the Gas-Phase - Use of Matrix-Assisted Laser-Desorption Methods in Ion Chromatography. *Science*, **1995**, 267, 1483-1485.
23. Wytenbach, T.; vonHelden, G.; Bowers, M. T., Gas-phase conformation of biological molecules: Bradykinin. *J. Am. Chem. Soc.* **1996**, 118, 8355-8364.
24. Shelimov, K. B., Clemmer, D. E., Hudgins, R. R. & Jarrold, M. F. Protein structure in vacuo: Gas-phase confirmations of BPTI and cytochrome c. *J. Am. Chem. Soc.* **1997**, 119, 2240-2248.
25. Hoaglund, C. S.; Valentine, S. J.; Sporleder, C. R.; Reilly, J. P.; Clemmer, D. E., Three-dimensional ion mobility TOFMS analysis of electrosprayed biomolecules. *Anal. Chem.* **1998**, 70, 2236-2242.



26. Gillig, K. J.; Ruotolo, B.; Stone, E. G.; Russell, D. H.; Fuhrer, K.; Gonin, M.; Schultz, A. J., Coupling high-pressure MALDI with ion mobility/orthogonal time-of flight mass spectrometry. *Anal. Chem.* **2000**, *72*, 3965-3971.
27. Kanu, A. B.; Dwivedi, P.; Tam, M.; Matz, L.; Hill, H. H., Jr., Ion mobility-mass spectrometry. *J. Mass Spectrom.* **2008**, *43*, 1-22.
28. Myung, S.; Lee, Y. J.; Moon, M. H.; Taraszka, J.; Sowell, R.; Koeniger, S.; Hilderbrand, A. E.; Valentine, S. J.; Cherbas, L.; Cherbas, P.; Kaufmann, T. C.; Miller, D. F.; Mechref, Y.; Novotny, M. V.; Ewing, M. A.; Sporleder, C. R.; Clemmer, D. E., Development of high-sensitivity ion trap ion mobility spectrometry time-of-flight techniques: A high-throughput nano-LC-IMS-TOF separation of peptides arising from a *Drosophila* protein extract. *Anal. Chem.* **2003**, *75*, 5137-5145.
29. Taraszka, J. A.; Gao, X. F.; Valentine, S. J.; Sowell, R. A.; Koeniger, S. L.; Miller, D. F.; Kaufman, T. C.; Clemmer, D. E., Proteome profiling for assessing diversity: Analysis of individual heads of *Drosophila melanogaster* using LC-ion mobility-MS. *J. Prot.Res.* **2005**, *4*, 1238-1247.
30. Moon, M. H.; Myung, S.; Plasencia, M.; Hilderbrand, A. E.; Clemmer, D. E., Nanoflow LC/ion mobility/CID/TOF for proteomics: analysis of a human urinary Proteome. *J. Prot.Res.* **2003**, *2*, 589-597.
31. Collins, D. C.; Lee, M. L., Developments in ion mobility spectrometry-mass spectrometry. *Anal. Bioanal. Chem.* **2002**, *3372*, 66-73.
32. Cohen, M. J.; Karasek, F. W., Plasma chromatography TM – a new dimension for gas chromatography and mass spectrometry. *J. Chromatogr. Sci.* **1970**, *8*, 330-337.
33. Fenn, L. S.; McLean, J. A., Biomolecular structural separations by ion mobility-mass spectrometry. *Anal. Bioanal. Chem.* **2008**, *391*, 905-909.
34. Koomen, J. M.; Ruotolo, B. T.; Gillig, K. J.; McLean, J. A.; Russell, D. H.; Kang, M. J.; Dunbar, K. R.; Fuhrer, K.; Gonin, M.; Schultz, J. A., Oligonucleotide analysis with MALDI-ion-mobility-TOFMS. *Anal. Bioanal. Chem.* **2002**, *373*, 612-617.
35. Woods, A. S.; Ugarov, M.; Egan, T.; Koomen, J.; Gillig, K. J.; Fuhrer, K.; Gonin, M.; Schultz, J. A., Lipid/peptide/nucleotide separation with MALDI-ion mobility-TOF MS. *Anal. Chem.* **2004**, *76*, 2187-2195.
36. Fenn, L. S.; Kliman, M.; Mahsut, A.; Zhao, S. R.; McLean, J. A., Characterizing ion mobility-mass spectrometry conformation space for the analysis of complex biological samples. *Anal. Bioanal. Chem.* **2009**, *394*, 235-244.

37. McLean, J. A., The Mass-Mobility Correlation Redux: The Conformational Landscape of Anhydrous Biomolecules. *J. Am. Soc. Mass Spectrom.* **2009**, 20, 1775-1781.
38. Pringle, S. D.; Giles, K.; Wildgoose, J. L.; Williams, J. P.; Slade, S. E.; Thalassins, K.; Bateman, R. H.; Bowers, M. T.; Scrivens, J. H. An investigation of the mobility separation of some peptide and protein ions using a new hybrid quadrupole/travelling wave IMS/oa-ToF instrument. *Int. J. Mass Spectrom.* **2007**, 261, 1-12.
39. Giles, K.; Pringle, S. D.; Worthington, K. R.; Little, D.; Wildgoose, J. L.; Bateman, R. H., Applications of a travelling wave-based radio-frequency only stacked ring ion guide. *Rapid Commun. Mass Spectrom.* **2004**, 18, 2401-2414.
40. Constantopoulos, T. L.; Jackson, G. S.; Enke, C. G., Effects of salt concentration on analyte response using electrospray ionization mass spectrometry. *J. Am. Soc. Mass Spectrom.* **1999**, 10, 625-634.
41. King, R.; Bonfiglio, R.; Fernandez-Metzler, C.; Miller-Stein, C.; Olah, T., Mechanistic investigation of ionization suppression in electrospray ionization. *J. Am. Soc. Mass Spectrom.* **2000**, 11, 942-950.
42. Annesley, T. M., Ion suppression in mass spectrometry. *Clin. Chem.* **2003**, 49, 1041-1044.
43. Mallet, C. R.; Lu, Z. L.; Mazzeo, J. R., A study of ion suppression effects in electrospray ionization from mobile phase additives and solid-phase extracts. *Rapid Commun. Mass Spectrom.* **2004**, 18, 49-58.
44. Jessome, L. L.; Volmer, D. A., Ion suppression: A major concern in mass spectrometry. *LCGC North Am.* **2006**, 24, 498-510.
45. McLean, J. A.; Ruotolo, B. T.; Gillig, K. J.; Russell, D. H., Ion mobility-mass spectrometry: a new paradigm for proteomics. *Int. J. Mass Spectrom.* **2005**, 240, 301-315.
46. Ruotolo, B. T.; Gillig, K. J.; Stone, E. G.; Russell, D. H., Peak capacity of ion mobility mass spectrometry: Separation of peptides in helium buffer gas. *J. Chromatogr. B Anal. Technol. Biomed. Life Sci.* **2002**, 782, 385-392.
47. Ruotolo, B. T.; McLean, J. A.; Gillig, K. J.; Russell, D. H., Peak capacity of ion mobility mass spectrometry: the utility of varying drift gas polarizability for the separation of tryptic peptides. *J. Mass Spectrom.* **2004**, 39, 361-367.
48. Valentine, S. J.; Kulchania, M.; Srebalus Barnes, C. A.; Clemmer, D. E., Multidimensional separations of complex peptide mixtures: a combined high-

- performance liquid chromatography/ion mobility/time-of-flight mass spectrometry approach. *Int. J. Mass. Spectrom.* **2001**, 212, 97-109.
49. Klesper, E. A.; Corwin, A. H.; Turner, D. A., High pressure gas chromatography above critical temperatures. *J. Org. Chem.* **1962**, 27, 700-701.
  50. Lee, M. L.; Markides, K. E., Chromatography with supercritical fluids. *Science*, **1987**, 235, 1342-1347.
  51. Davies, I. L.; Raynor, M. W.; Kithinji, J. P.; Bartle, K. D.; Williams, P. T.; Andrews, G. E., LC/GC, SFC/GC, and SFE/GC. *Anal. Chem.* **1988**, 60, 683A-702A.
  52. Brondz, I. Development of fatty acid analysis by high-performance liquid chromatography, gas chromatography, and related techniques. *Anal. Chim. Acta* **2002**, 465, 1-37.
  53. West, C.; Lesellier, E., A unified classification of stationary phases for packed column supercritical fluid chromatography. *J. Chromatogr. A* **2008**, 1191, 21-39.
  54. Gidden, J.; Kemper, P. R.; Schammel, E.; Fee, D. P.; Anderson, S.; Bowers, M.T., Application of ion mobility to the gas-phase conformational analysis of polyhedral oligomeric silsesquioxanes (POSS). *Int. J. Mass Spectrom.* **2003**, 222, 63-73.
  55. Morsa, D.; Defize, T.; Dehareng, D.; Jérôme, C.; De Pauw, E., Polymer Topology Revealed by Ion Mobility with Mass Spectrometry. *Anal. Chem.* **2014**, 86, 9693-9700.
  56. Jerabek, K.; Characterization of swollen polymer gels using size exclusion chromatography. *Anal. Chem.* **1985**, 57, 1598-1602.
  57. Toy, A. A.; Vana, P.; Davis, T. P.; Barner-Kowollik, C., Reversible Addition Fragmentation Chain Transfer (RAFT) Polymerization of Methyl Acrylate: Detailed Structural Investigation via Coupled Size Exclusion Chromatography–Electrospray Ionization Mass Spectrometry (SEC–ESI-MS). *Macromolecules*, **2004**, 37, 744-751.
  58. Scarff, C. A.; Thalassinos, K.; Hilton, G. R.; Scrivens, J. H., Travelling wave ion mobility mass spectrometry studies of protein structure: biological significance and comparison with X-ray crystallography and nuclear magnetic resonance spectroscopy measurements. *Rapid Commun. Mass Spectrom.* **2008**, 22, 3297-3304.
  59. Kaddis, C. S.; Lomeli, S. H.; Yin, S.; Berhane, B.; Apostol, M. I.; Kickhoefer, V. A.; Rome, L. H.; Loo, J. A., Sizing large proteins and protein complexes by

- electrospray ionization mass spectrometry and ion mobility. *J. Am. Soc. Mass Spectrom.* **2007**, 18, 1206-1216.
60. Karger, B. L., HPLC: Early and Recent Perspectives. *J. Chem. Educ.* **1997**, 74, 45-48.
  61. Henry, R. A. The Early Days of HPLC at Dupont. *LCGC North Am.* **2009**, 27, 146-153.
  62. Horvath, C.; Melander, W., Liquid Chromatography with Hydrocarbons Bonded Phases; Theory and Practice of Reversed Phase Chromatography. *J. Chromatogr. Sci.* **1977**, 15, 393-404.
  63. Buszewski, B.; Noga, S., Hydrophilic interaction liquid chromatography (HILIC)-a powerful separation technique. *Anal. Bioanal. Chem.* **2011**, 402, 231-247.
  64. Theodoridis, G. A.; Gika, H. G.; Want, E. J.; Wilson, I. D. Liquid chromatography-mass spectrometry based global metabolite profiling: A review. *Anal. Chim. Acta*, **2012**, 711, 7-16.
  65. Phinney, K. W., Separating drug enantiomers is ushering in a renaissance of sub- and supercritical fluid chromatography. *Anal. Chem.* **2000**, 72, 204A-211A.
  66. Harris, C. M., Product review: the SFC comeback. *Anal. Chem.* **2002**, 74, 87A-91A.
  67. Smith, R. D.; Wright, B. W.; Yonker, C. R., Supercritical Fluid Chromatography: Current Status and Prognosis. *Anal. Chem.* **1988**, 60, 1323A-1336A.
  68. Taylor, L. T., Supercritical fluid chromatography in perspective. *Chim. Oggi*, **2008**, 26, 14-18.
  69. Lesellier, E., Supercritical fluid chromatography for bioanalysis: practical and theoretical considerations. *Bioanalysis*, **2011**, 3, 125-131.
  70. Taylor, L. T., Supercritical fluid chromatography for the 21st century. *J. Supercrit. Fluids* **2009**, 3, 566-573.
  71. François, I.; Sandra, P., Comprehensive supercritical fluid chromatography × reversed phase liquid chromatography for the analysis of the fatty acids in fish oil, *J. Chromatogr. A*, **2009**, 1216, 4005-4012.
  72. Li, F.; Hsieh, Y., Supercritical fluid chromatography-mass spectrometry for chemical analysis. *J. Sep. Sci.* **2008**, 31, 1231-1237.
  73. Lesellier, E., Retention mechanisms in super/subcritical fluid chromatography on packed columns. *J. Chromatogr. A*. **2009**, 1216, 1881-1890.

74. Yip, H.S.H.; Ashraf-Khorassani, M.; Taylor, L. T., Feasibility of phospholipids separation by packed column SFC with mass spectrometric and light scattering detection. *Chromatographia*, **2007**, 65, 655-665.
75. Zheng, J.; Pinkston, J. D.; Zoutendam, P. H.; Talyor, L. T., Feasibility of Supercritical fluid chromatography/mass spectrometry of polypeptides with up to 40-mers.. *Anal. Chem.* **2006**, 78, 1535-1545.
76. Berger, T. A.; Berger, B. K., Minimizing UV noise in supercritical fluid chromatography. I. Improving back pressure regulator pressure noise. *J. Chromatogr. A*, **2011**, 1218, 2320-2326.
77. Pentoney Jr, S.L.; Shafer, K. H.; Griffiths, P. R.; Fuoco, R., Supercritical fluid chromatography/Fourier transform infrared microscopy. *J. High Resolut. Chromatogr.* **1986**, 9, 168-171.
78. Lathe, G. H.; Ruthven, C. R., The separation of substances and estimation of their relative molecular sizes by the use of columns of starch in water. *Biochem. J.* **1956**, 62, 665-674.
79. Pretorius, N. O.; Willemsse, C. M.; de Villiers, A.; Pasch, H., Combined size exclusion chromatography, supercritical fluid chromatography and electrospray ionization mass spectrometry for the analysis of complex aliphatic polyesters. *J. Chromatogr. A* **2014**, 1330, 74-81.
80. Kostanski, L.; Keller, D. M.; Hamielec, A. E., Size-exclusion chromatography-a review of calibration methodologies. *J. Biochem. Biophys. Methods*, **2003**, 58, 159-186.
81. Hong, P.; Koza, S.; Bouvier, E. S. P., A review size exclusion chromatography for the analysis of protein biotherapeutics and their aggregates. *J. Liq. Chromatogr. Relat. Technol.* **2012**, 35, 2923-2950.
82. Entelis, S. G.; Evreinov, V. V.; Gorshkov, A. V., Functionality and molecular weight distribution of Telechelic polymers. *Adv. Polym. Sci.* **1986**, 76, 129-175.
83. Olesik, S. V., Liquid chromatography at the critical condition. *Anal. Bioanal. Chem.* **2004**, 378, 43-45.
84. Wyttenbach, T.; Bowers, M. T.; Gas-Phase Conformations: The Ion Mobility/Ion Chromatography Method. *Modern Mass Spectrom.* **2003**, 225, 207-232.
85. West, C.; Lesellier, E., Orthogonal screening system of columns for supercritical fluid chromatography. *J. Chromatogr. A* **2008**, 1203, 105-113.

86. Pinkston, J.D.; Wen, D.; Norans, K. L.; Tirey, D. A.; Stanton, D. T., Comparison of LC/MS and SFC/MS for screening of a large and diverse library of pharmaceutically Relevant Compounds. *Anal. Chem.* **2006**, 78, 7467-7472.
87. Ivanisevic, J.; Zhu, Z.; Plate, L.; Tautenhahn, R.; Chen, S.; O'Brien, P. J.; Johnson, C. H.; Marletta, M. A.; Patti, G. J.; Siuzdak, G., Toward 'Omic Scale Metabolite Profiling: A Dual Separation-Mass Spectrometry Approach for Coverage of Lipid and Central Carbon Metabolism.. *Anal. Chem.* **2013**, 85, 6876-6884.
88. Giddings, J. C., Two-dimensional separations: concept and promise. *Anal. Chem.* **1984**, 56, 1258A-1270A.
89. Gao, L.; Zhang, J.; Zhang, W.; Shan, Y.; Liang, Z.; Zhang, L.; Huo, Y.; Zhang, Y., Integration of normal phase liquid chromatography with supercritical fluid chromatography for analysis of fruiting bodies of *Ganoderma lucidum*. *J. Sep. Sci.* **2010**, 33, 3817-3821.
90. Shen, Y.; Lee, M. L., General Equation for Peak Capacity in Column Chromatography. *Anal. Chem.* **1998**, 70, 3853-3856.
91. Riba-Garcia, I.; Giles, K.; Bateman, R. H.; Gaskell, S. J. Evidence for Structural Variants of a- and b-Type Peptide Fragments using combined Ion Mobility/Mass Spectrometry. *J. Am. Soc. Mass Spectrom.* **2008**, 13, 609-613.
92. Thalassinos, K.; Grabenauer, M.; Slade, S. E.; Hilton, G. R.; Bowers, M. T.; Scrivens, J. H., Characterization of Phosphorylated Peptides Using Travelling Wave-Based and Drift Cell Ion Mobility Mass Spectrometry. *Anal. Chem.* **2009**, 81, 248-254.
93. Ruotolo, B, T.; Benesch, J, L. P.; Sandercock, A. M.; Hyung, S.; Robinson, C. V., Ion mobility-mass spectrometry analysis of large protein complexes. *Nat. Protoc.* **2008**, 3, 1139-1152.
94. Patti, G. J., Yanes, O.; Siuzdak, G., Innovation, Metabolomics, the apogee of the omics trilogy. *Nat. Rev. Mol. Cell Biol.* **2012**, 13, 263-269.
95. Smith, C. A.; Maille, G. O.; Want, E. J.; Qin, C.; Trauger, S. A.; Brandon, T. R.; Custodio, D. E.; Abagyan, R.; Siuzdak, G., 2005. METLIN, A Metabolite Mass Spectral Database. *Ther. Drug Monit.* **2005**, 27, 747-751.
96. Sud, M.; Fahy, E.; Cotter, D.; Brown, A.; Dennis, E. A.; Glass, C. K.; Merrill Jr, A. H.; Murphy, R.C.; H. Raetz, C. R.; Russell, D. W., LMSD, LIPID MAPS structure database. *Nucleic. Acids. Res.* **2007**, 35, D527-532.

97. Schmelzer, K.; Fahy, E.; Subramaniam, S.; Dennis, E. A., The lipid maps initiative in lipidomics. *Methods Enzymol.* **2007**, 432,171-183.
98. Bateman, K.; Castro-Perez, J.; Wrona, M.; Shockcor, J. P.; Yu, K.; Oballa, R.; Nicoll-Griffith, D. A.; MS<sup>E</sup> with mass defect filtering for *in vitro* and *in vivo* metabolite identification. *Rapid Commun. Mass Spectrom.* **2007**, 21, 1485-1496.

## CHAPTER II

### UTILIZATION OF SUPERCRITICAL FLUIDS FOR ENHANCED CHARACTERIZATION IN LIPIDOMICS

#### **2.1. Introduction**

Macrophages are tissue resident innate immune cells that defend against infection and help maintain a homeostatic microenvironment.<sup>1, 2</sup> Traditionally, the term “macrophage” described a simple phagocytic leukocyte that existed essentially in two states: a resting/basal state and an activated, proinflammatory state. The latter, classically-activated form of the macrophage was thought to be the major cellular phenotype responsible for antimicrobial activities and the elaboration of inflammatory mediators such as TNF $\alpha$  and interleukins.

This paradigm has been upended by the growing appreciation of cellular plasticity of macrophages to move across many shades of both pro- and anti-inflammatory phenotypes, a process referred to as polarization. Akin to T lymphocyte activation, the emerging model illustrated that macrophages are not only activated towards a classical, proinflammatory (M1) state but can also exist in an alternatively-activated, anti-inflammatory (M2) state.<sup>3-5</sup> Most recently, macrophage polarization has gone far beyond the dichotomous M1/M2 model, to include subsets of alternatively activated cells referred to as M2a, M2c, Mhem, etc.<sup>4-7</sup> Polarization alters the repertoire of secreted cytokines, phagocytic capacity, and surface proteins presented by macrophages, allowing the cell to carry out varying effector functions. A number of diseases and pathogenic conditions are associated with specific polarization states,<sup>8-11</sup> making the understanding of macrophage



polarization in the context of health maintenance and disease pathogenesis critical to improving the capacity to prevent macrophage-mediated diseases.

Peripheral blood monocytes, differentiated with macrophage colony stimulating factor (M-CSF) into macrophage-like cells, serve as a predominant human model cell type for characterizing macrophage polarization known as monocyte-derived macrophages (MDMs).<sup>12-16</sup> Classical, M1 polarization is typically generated by stimulating these cells with IFN- $\gamma$  in combination with bacterial lipopolysaccharide (LPS).<sup>12-15</sup> The M2a and M2c phenotypes are generally modeled by incubating monocyte-derived macrophages with either IL-4 or IL-10, respectively.<sup>12-15</sup>

Conventional approaches to define polarized activation states have been confined to gene expression profiles, the display of certain cell surface proteins, or the expression of characteristic intracellular or secreted proteins. Furthermore, marker overlap between polarized subsets is sometimes observed when using these approaches.<sup>14, 17</sup> This lack of marker specificity supports the notion of a spectrum of activation as opposed to distinct subsets and requires the use of several markers when defining similar phenotypic subtypes.<sup>7, 18</sup> Additionally, post-transcriptional and post-translational modifications do not always allow for direct correlation of protein levels. Metabolomics, on the other hand, has the potential to overcome the limitations of genomics and proteomics given its position at the end of the “omics” cascade.<sup>19</sup> While both unbiased proteomic<sup>20, 21</sup> and transcriptomic<sup>13, 15</sup> approaches have been used to more fully characterize macrophage polarization, there are limited studies that have applied an unbiased metabolomic approach to this evolving paradigm. It is well-recognized that metabolic differences between activated macrophages exist<sup>22-24</sup> however, little research has been done to

develop the association between metabolic differences and macrophage polarization and what the relationship between the two entails.

Metabolites are broadly defined as small molecules involved in cell metabolism. A metabolite profile that includes the total metabolites produced by cells is known as the metabolome. An emerging field of science, metabolomics is deeply advanced by the onset of new technologies allowing for the analysis of large data sets.<sup>25, 26</sup> Regardless of their chemical diversity, the totality of lipid molecules in cells is referred to as the lipidome and forms a subset of the metabolome given the rapid metabolism into biologically active metabolites. Located on many cellular structures, particularly membranes, lipids play critical roles in energy storage, membrane structure, and signaling.<sup>27, 28</sup> Many autocrine and paracrine signaling molecules are lipids, including, for example, the eicosanoids, which have substantial immunoregulatory capabilities.<sup>29, 30</sup> Furthermore, dysregulated lipid biosynthesis and metabolism have been implicated in a number of human diseases, such as atherosclerosis,<sup>31</sup> non-alcoholic fatty liver,<sup>32</sup> diabetes,<sup>33</sup> Alzheimer's disease,<sup>34</sup> and cancer.<sup>35, 36</sup>

Advances in lipidomic techniques and strategies, led by the LIPID MAPS consortium, have greatly enhanced our understanding of the distribution and biological roles of lipids.<sup>37-41</sup> Furthermore, modern mass spectrometry (MS) coupled with electrospray ionization (ESI) have played key roles in qualitative and quantitative lipidomic analysis. Typical MS-based lipidomic strategies are shotgun (i.e., direct infusion) lipidomics<sup>37, 42</sup> and liquid chromatography LC-MS lipidomics.<sup>39, 43, 44</sup> Shotgun lipidomics relies on partial intrasource separation of lipid classes through varying the pH of the lipid solution and identification of lipid species by their characteristic

fragmentation in tandem MS analysis.<sup>37, 45</sup> This approach has the advantage of being high-throughput, but it also has several disadvantages: a) suppression of low-abundant species by major polar lipids such as phosphatidylcholines; b) difficulty in analysis of lipid species that are poorly ionized by ESI; and c) inability to provide structural information on isobaric and isomeric species. The LC-MS-based strategy utilizes targeted analysis of each lipid class under conditions that are optimized for that particular class.<sup>39, 43, 44, 46</sup> This strategy has the advantages of being specific, sensitive, and comprehensive, but it also has limitations such as low throughput and once again, no structural information can be obtained. To increase the throughput of the LC-MS lipidomics while maintaining the specificity and sensitivity, improved chromatographic techniques and additional dimensions of separation that is orthogonal to LC and MS would be desired.

Ion mobility spectrometry (IMS) provides such orthogonal separation.<sup>47-52</sup> IMS separate ions based on the mobility of the ions traveling through a neutral background gas (most commonly helium and nitrogen), which is governed by collision frequency between the ions and the neutral gas, i.e., the ion-neutral collision cross section (CCS;  $\Omega$ ). The CCS is determined by the size and shape of the ions in the gas phase and the specific neutral gas, with larger molecules experiencing more collisions than smaller ones. When ion mobility is coupled with mass spectrometry, a two-dimensional separation is achieved on the basis of the charge-to-collision cross section ( $z/\Omega$ ) and the mass-to-charge ( $m/z$ ), respectively. Several ion mobility (IM)-mass spectrometry (MS) techniques have been applied to lipidomic analysis, including drift time ion mobility (DTIM)-MS,<sup>53-55</sup> traveling wave ion mobility (TWIM)-MS,<sup>56, 57</sup> and differential ion mobility spectrometry (DIMS).<sup>58-60</sup> In DTIM-MS, the ions travel through the neutral gas-filled drift tube under a low and

static electric field, which leads to separation of ions on the scale of micro to milliseconds.<sup>49</sup> DTIM offers high IM resolving power and allows direct measurement of CCS. Using DTIM-MS, the Woods<sup>53</sup> and our laboratories<sup>54, 55</sup> have independently reported some separation of different polar lipid classes based on their headgroups and the acyl chain composition. DMS, or asymmetric-field ion mobility spectrometry (FAIMS), separates ions based on their different mobilities at high and low electric fields as the ions are swept by a flowing gas through an asymmetric voltage waveform comprised of high and low fields. Recently, the groups of Ekroos and Dennis successfully applied DMS to both shotgun and LC-based lipidomics, achieving more specific and sensitive analysis.<sup>59, 60</sup> While DMS offers the highest resolving power, the drawbacks include a) only selective ions with certain mobilities in the two fields can pass through the device and b) the separation in DMS does not correlate with the CCS of the ions, i.e., no structural information can be obtained directly and the behavior of certain ions cannot be predicted by CCS values. Traveling wave ion mobility (TWIM) also separates ions based on their CCSs, similar to DTIM, but it uses a migrating low-voltage wave to push the ions through the inert gas,<sup>61</sup> instead of a steady electric field as in DTIM. TWIM offers higher sensitivity than traditional DTIM, but has lower IM resolution and does not allow direct measurement of CCS values. However, CCS of unknown ions can be indirectly calculated by calibrating against appropriate ions with known CCS values.<sup>57</sup> TWIM has been used to characterize the effect of unsaturation on the mobility of phosphatidylcholines,<sup>56</sup> i.e., double bonds on the acyl chain lead to reduction in drift time, and thus smaller CCS. The commercial TWIM platform, used in

this study, is well integrated with different chromatographic separation techniques and MS analysis.

To achieve fast and efficient lipid separation, we turned to supercritical fluid chromatography (SFC). Supercritical fluids (SF) have the density and extraction ability that is similar to liquids, but viscosity and diffusivity more similar to gases, which makes SF suitable for high-speed separation without causing excess backpressure.<sup>62, 63</sup> SFC utilizes a supercritical fluid as mobile phase, with CO<sub>2</sub> being the most common one used because of its wide availability and easily-reached critical state (73 atm and 304 K). Frequently, a small amount of a modifier solvent, such as methanol and acetonitrile, is used to make SFC applicable to the separation of polar compounds. Previous studies comparing the analyte coverage between traditional LC (such as reverse phase, normal phase, and HILIC) and SFC suggest similar coverage for a large and diverse library of compounds, but offering in certain cases some high degree of orthogonality.<sup>64, 65</sup> A few years ago, Bamba and co-workers pioneered the application of SFC-MS in lipidomics, demonstrating separation of lipid classes using a cyano column and separation of lipid species within the same class by the length of the acyl chains using a C18 column.<sup>66</sup>

In this study, we report a) the development of an SFC chromatographic method that rapidly separates over ten lipid classes with a wide variety of polarity; b) coupling of SFC with TWIM-MS to achieve a three-dimensional separation of lipids; c) application of SFC-IM-MS to profiling the lipidome of the brain from wild type mice; and d) interrogate distinct lipidome alterations in macrophages corresponding to major polarization phenotypes (M1, M2a, M2c). We found that ion mobility selection of lipid signals was particularly powerful in increasing the signal-to-noise ratio of the

chromatographic peaks, deconvoluting overlapping lipid species, and fully characterizing fatty acid composition of the different lipid classes in negative ion mode. These findings introduce new technologies that can be used to deepen our current understanding of the molecular biology of macrophage polarization.

## **2.2. Experimental**

### *Materials*

All solvents were CHROMOSOLV-grade (Sigma-Aldrich, St. Louis, MO). Lipid standards were purchased from Avanti Polar Lipids (Alabaster, AL, USA). Lipid standards include phosphatidylcholines (PC, chicken egg), phosphatidylethanolamines (PE, porcine brain), phosphatidylserines (PS, porcine brain), phosphatidylglycerols (PG, chicken egg), phosphatidylinositols (PI, bovine liver), phosphatidic acids (PA, chicken egg), sphingomyelins (SM, porcine brain), ceramides (CE, porcine brain), monogalactosyldiacylglycerol (MGDG, plant) and sulfatides (porcine brain). Triglycerides (TG) were purchased from Nu-Chek Prep, Inc. (Elysian, MN). The standards were prepared as 10  $\mu$ M solutions in a 1:1 mixture of chloroform and 0.1% (w/v) ammonium formate in methanol. Recombinant Human M-CSF and IFN $\gamma$  (PeproTech, Rocky Hill, NJ). Recombinant Human IL-4 and IL-4 (R&D Systems, Minneapolis, MN). HyClone Charcoal/Dextran Treated FBS (GE Healthcare Life Sciences HyClone Laboratories, Logan, Utah). RPMI 1640 Medium 1X without HEPES supplemented with L-Glutamine and Phenol Red (Gibco by Life Technologies, Carlsbad, CA). Ultra-pure LPS from *Escherichia coli* K12 in endotoxin-free water (Invivogen, San Diego, CA).

### *Mice model*

Wild type C57BL/6J mice were purchased from Jackson Laboratories. The mice were kept and bred in Division of Animal Care facilities at Vanderbilt University to give the desired number of 3-week old mice (N = 3). At the appropriate time, the mice were euthanized, brain tissue dissected, and instantly frozen in pre-cooled 2-methylbutane (on dry ice) and stored at -80°C until lipid extraction. All procedures were performed in accordance with the Guide for the Humane Use and Care of Laboratory Animals. The use of mice in this study was approved by the IACUC of Vanderbilt University.

### *Human subjects*

This study was reviewed and approved by the Vanderbilt University Institutional Review Board (protocol #140699). Subjects included healthy, non-pregnant adults (age 18-60). Exclusion criteria included: fever >101 °F in preceding 48 h, antibiotic therapy currently, or within the prior 2 weeks, current immunosuppressive therapy or short-term steroid therapy within the prior 2 weeks, chronic viral infection, including, but not limited to, HIV infection (per self-report), and/or currently diagnosed with or undergoing treatment for cancer

### *Isolation and cultivation of monocyte-derived macrophages*

Peripheral blood mononuclear cells (PBMCs) were isolated from human peripheral blood by density gradient centrifugation using Ficoll-Paque<sup>TM</sup> as outlined by the manufacturer Miltenyi (Auburn, CA). Following centrifugation, monocytes were isolated from PBMCs via negative selection using the Miltenyi Monocyte Isolation Kit

II<sup>®</sup> as instructed by the manufacturer. Monocytes were cultured in 6 well plates at a concentration of  $1.35 \times 10^6$  monocytes per well for seven days in 100ng/mL M-CSF in RPMI+/- with 20% FBS to differentiate into MDM as previously described.<sup>15</sup> Following differentiation, cells were allowed to rest for 24 hours by replacing M-CSF+ RPMI+/- with M-CSF- RPMI+/- prior to carrying out downstream experiments.

#### *Macrophage polarization*

After monocyte differentiation (7 days), cells were treated for 24 hours in RPMI+/- with 5% FBS with 20 ng/mL of polarizing stimuli, IFN $\gamma$ , IL-4 and IL-10 for M1, M2a and M2c respectively. Additionally, 100 ng/mL LPS were added to M1 cells. Cultures destined for both PCR and Lipidome analysis were treated equally.

#### *Lipid extraction*

Lipid extraction of mouse brains (vertical cut half brain; ~ 200 mg) was performed following previously reported procedures and the dried extracts were re-constituted in 1 mL of methylene chloride.<sup>67</sup> Macrophage lipids were extracted with 500  $\mu$ L of 5% HCl and 750 $\mu$ L of Folch solution (2:1, CHCl<sub>3</sub>:MeOH with 17mg/L butylated hydroxytoluene) were added to cell pellets for lipid extraction. Samples were vortexed and centrifuged briefly at 15,000 rpm. The organic layer was removed and dried under vacuum. Samples were stored at -80°C until analysis.



*Supercritical Fluid Chromatography-Ion Mobility-Mass Spectrometry (SFC-IM-MS)*

All MS analyses were conducted on a Synapt G2-S (Waters Corp., Milford, MA) time-of-flight mass spectrometer (TOF-MS) with an electrospray ionization (ESI) source. An UPC<sup>2</sup> SFC (Waters Corp., Milford, MA) system with Ethylene Bridged Hybrid (BEH) Silica column (1.7 $\mu$ m, 3.0 x 100 mm, Waters Corp., Milford, MA) was used. The temperatures of autosampler and column were maintained at 8 and 60 °C, respectively.

Unless otherwise specified, chromatographic conditions for SFC separation were as follows: injection volume 2  $\mu$ L, mobile-phase flow rate 1 mL/min (measured in the liquid state) and column outlet pressure 2000 psi. The mobile-phase composition gradient was as follows: Initial 10% modifier in CO<sub>2</sub> and after injection, modifier concentration increased to 40% in 7 minutes. Then the concentration was increased to 80% in one minute and held at 80% for 4 minutes. The modifier consisted of 10 mM ammonium formate in methanol.

The positive-mode (+) ESI conditions were as follows: capillary, +2.28 kV; sampling cone, 40 V; source temperature, 100 °C; desolvation temperature, 150 °C; desolvation gas flow, 500 L/h; and cone gas flow, 20 L/h, respectively. The traveling wave velocity and height for IM separation were 652 m/s and 40 V, respectively. Leucine-enkephalin (m/z 556.2771) was used for lock mass correction. The negative-mode (-) ESI conditions were the same as that of the positive-mode except for the capillary voltage, source temperature and desolvation temperature (-2.52 kV, 125 °C, 150 °C). The data acquisition was carried out in MS<sup>E</sup> mode with transfer collision energy ramping from 40 to 50V in both positive- and negative-mode.

## *Data Analysis*

Lockspray mass correction was applied after acquisition using the vendor supplied software, followed by batch conversion to mzXML format. After peak filtering, detecting and aligning with XCMS<sup>68</sup> the features (discrete retention time and  $m/z$  values) were assigned to a phospholipid class by their retention time and accurate mass. For further analysis, features only found in standards or databases such as METLIN<sup>69</sup> and LIPIDMAPS<sup>38, 70</sup> with mass tolerance below 10 ppm were taken into account.

## **2.3. Results and Discussion**

### **2.3.1. Optimization of SFC separation using lipid standards.**

We first attempted to develop a SFC chromatographic condition using glycerol lipid and sphingolipid standards with a wide range of polarity, including triglyceride (TG), phosphatidylcholine (PC), sphingomyelin (SM), phosphatidylethanolamine (PE), phosphatidylinositol (PI), phosphatidylserine (PS), phosphatidylglycerol (PG), and phosphatidic acid (PA). We found that using a similar condition to the one reported by Bamba and co-workers, a gradient of 10% to 40% of the modifier solvent (methanol) at a flow rate of 2 mL/min, most lipid classes were eluted from the Waters UPC<sup>2</sup> ethylene-bridged hybrid (BEH) column except for PS and PA. We reasoned that the retention of PS and PA was due to their large polarity. Thus, we applied a rapid increase (within 1 min) in the percentage of methanol from 40% to 80% (at a slower flow rate of 1 mL/min due to large backpressure) after the initial slow gradient from 10% to 40% (over 7 min), which allowed the elution of PA and PS as one peak. Although there is partial overlapping between a few lipid classes, such as PE and PI, PA and PS, etc., the

additional ion mobility separation allowed deconvolution of individual classes as discussed in the following sections. Under the optimized chromatographic condition, all lipid classes were eluted within 11 min as shown in Figure 2.1.

### ***2.3.2. Analysis of lipid extracts from mouse brain***

Brain is the organ that is most rich in lipids. For example, human gray matter contains 36-40% of lipids (out of dry weight), white matter contains 49-66% of lipids, and myelin has the highest lipid content at 78-81%.<sup>71</sup> In addition to the absolute amount, the lipid species found in the brain are quite diverse.<sup>37</sup> Abnormal brain lipid metabolism has been suggested to be associated with a number of human diseases with defective central nervous system, such as Alzheimer's disease,<sup>34</sup> cholesterol biosynthesis disorders,<sup>72</sup> and Niemann–Pick C disease.<sup>73</sup> Thus, a comprehensive lipidomic analysis of the brain is of high significance.

Here we examined the lipid extracts from brain tissues of three-week old wild-type mice using the newly developed SFC-IM-MS method (Figure 2.2). The chromatogram obtained from total ion current (TIC) is somewhat noisy and only a few peaks were recognizable (Figure 2.2 (B)). However, upon extraction of the lipid signals from the two-dimensional IM-MS spectrum (as drift time and mass-to-charge ratio, respectively) (Figure 2.2 (A)), a chromatogram with more peaks and significantly larger S/N was obtained, highlighting the benefit of this three-pronged approach (Figure 1.2 (C)). Not surprisingly, unknown lipid species not tested during our method development were detected. However, after analyzing the accurate mass of the unknown peaks and subsequently additional lipid standards, all peaks in the chromatogram were identified.

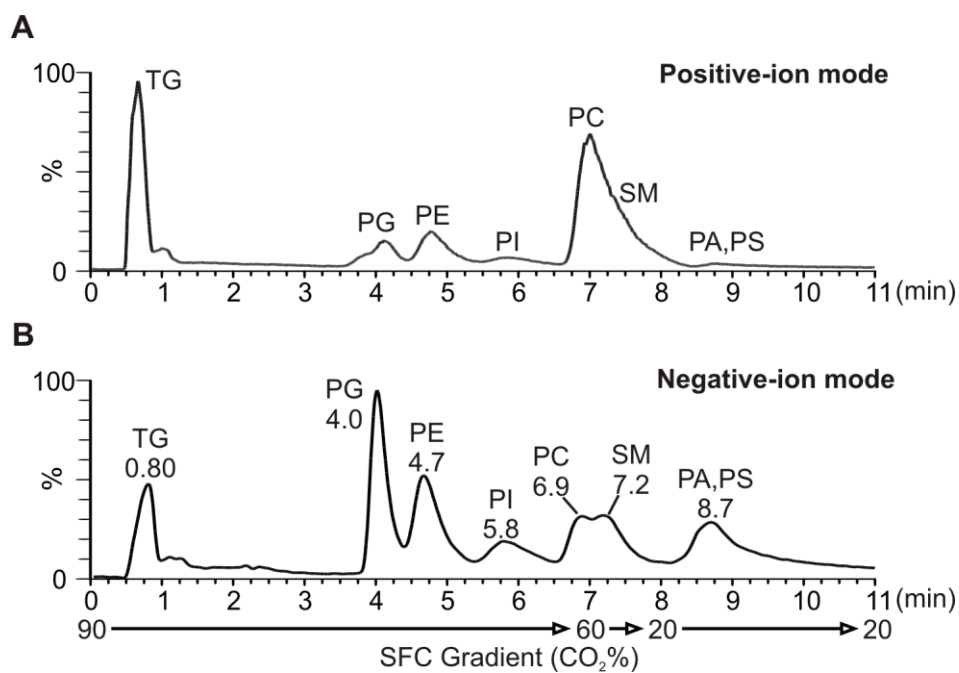


**Figure 2.1.** Chromatogram of lipid standards in A) positive-ion and B) negative-ion mode as described in Experimental. Higher ionization efficiencies are observed for different classes in both positive and negative mode. TG, triglyceride; PG, phosphatidylglycerol; PE, phosphatidylethanolamine; PI, phosphatidylinositol; PC, phosphatidylcholine; SM, sphingomyelin; PA, phosphatidic acid; PS, phosphatidylserine.

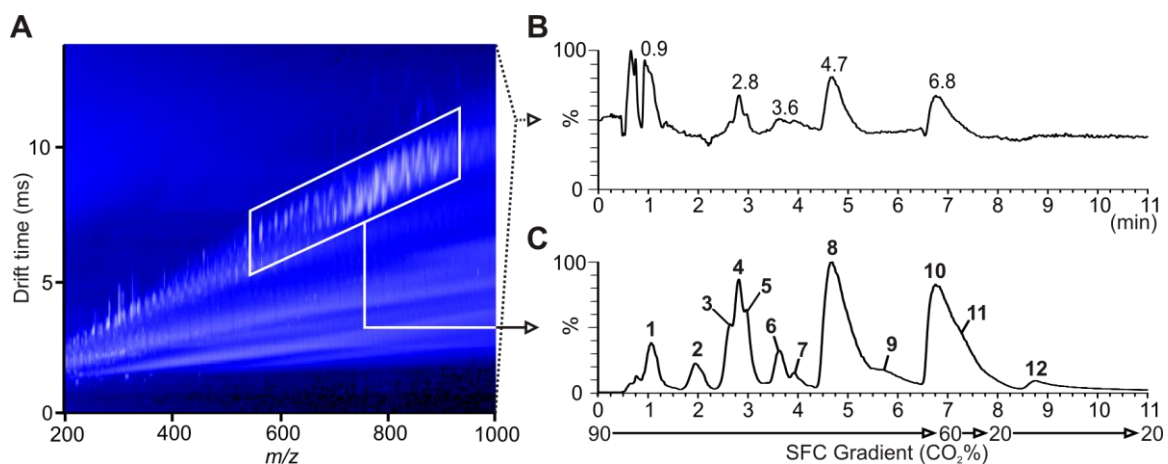


**Figure 2.2.** Chromatogram of lipid extracts from mouse brain with and without IM in negative mode as described in Experimental. A) 2-D lipid region of drift time and mass-to-charge ratio separation space. B) SFC chromatogram without IM extraction. C) SFC chromatogram after IM extraction increases signal-to-noise ratio. **1**, ceramide; **2**, MGDG; **3-5**, cerebroside; **6**, sulfatide + P- or O-phosphatidylglycerol (PG); **7**, sulfatide + diacyl PG; **8**, phosphatidylethanolamine (PE); **9**, phosphatidylinositol (PI); **10**, phosphatidylcholine (PC); **11**, sphingomyelin (SM); **12**, phosphatidic acid (PA)+phosphatidylserine (PS).

The ability of IM separation to remove chemical noises can be reasonably understood based on previous reports.<sup>52, 74</sup> We have shown that at the same  $m/z$  value, lipids occupy the largest gas phase conformation (i.e., CCS), followed by peptides, carbohydrates, and nucleotides, in that order.<sup>52</sup> In other words, lipid ions are the least gas-phase packing efficient among all biological molecules. On the other hand, ions that give rise to chemical noise, such as those formed from other classes of biological molecules (metabolites, peptides, etc.), plasticizer and salt aggregates, generally have high gas-phase packing efficiencies, resulting in smaller CCS. Thus, extraction of the lipid specific two-dimensional IM-MS separation space led to a much cleaner chromatogram as shown in Figure 2.2 (C).

The IM-MS analysis was also carried out with post-mobility collision-induced dissociation (CID) to obtain additional structural information. In  $MS^E$  mode both low- and high-energy spectra for all ions present are collected. Additionally, one unique feature of the post-mobility fragmentation is that all the fragments would align with their corresponding precursors at the same drift time in the IM-MS 2D spectrum, which allows extraction of all MS/MS spectrum for each individual precursor even if the species were eluted at the same time (as long as they are separated in IM). Thus, in the positive ion mode, identification of some lipid classes can be confirmed by their characteristic fragmentation of the headgroups, such as PC, SM, and PE. In the negative ion mode, fatty acid composition (as fatty acid anions) of majority of lipid classes can be obtained. Post-mobility fragmentation of PE in both modes was illustrated in Figure 2.3 as an example, which shows loss of the headgroup and fatty acid anions as the predominant fragments in

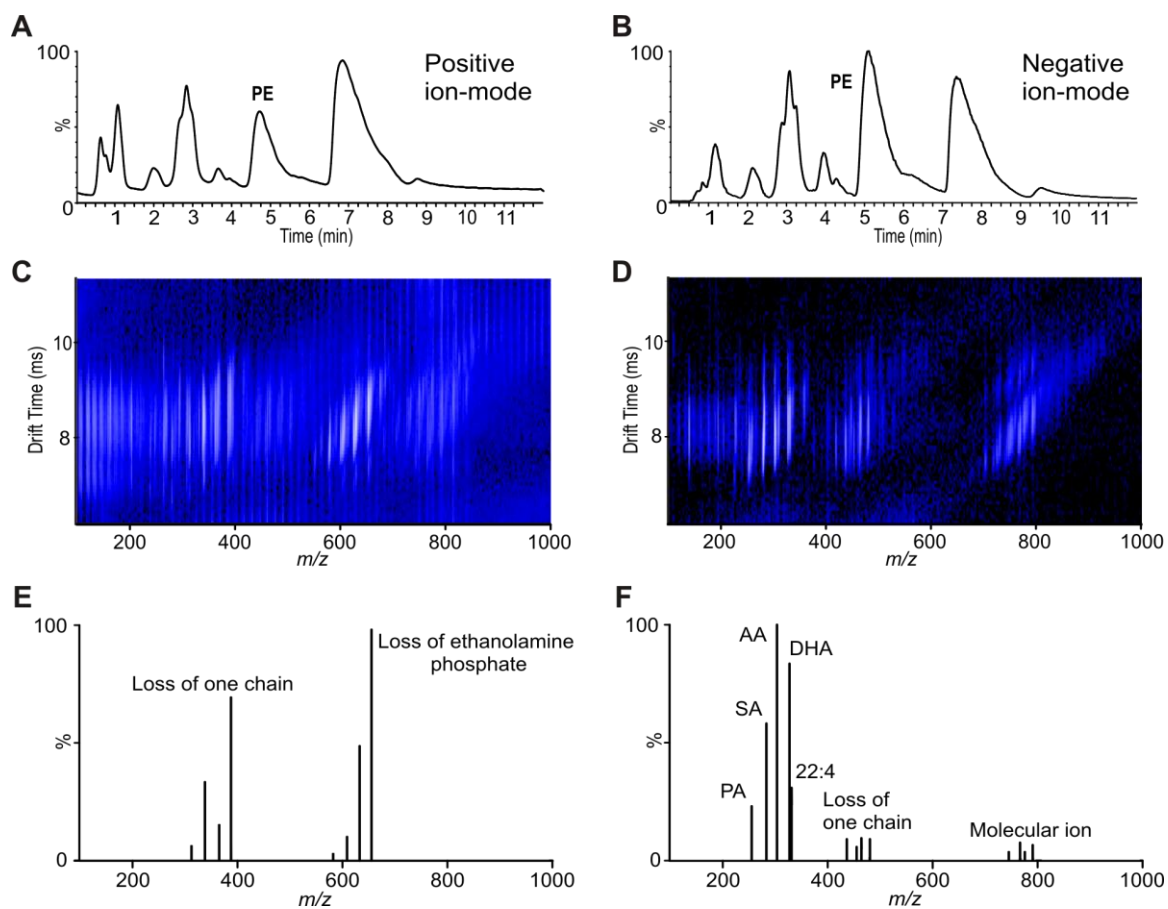


**Figure 2.3.** Illustration of post-mobility fragmentation (MS<sup>E</sup>) of individual peaks in both positive and negative modes. A) and B) show the SFC chromatogram for both positive and negative mode. Panels C) and D) illustrate the 2-D separation space of drift time and mass-to-charge ratio for PE with post mobility fragmentation, where fragments ions (*e.g.* loss of ethanolamine phosphate and arachidonic acid (AA) in E) and F) respectively) have the same drift time as the molecular ion. This advantage of IM facilitates fragment ion to molecular ion assignment in untargeted MS/MS analyses.

positive- and negative-ion mode respectively. Thus, data obtained from the two modes provide complementary information for lipid identification.

### ***2.3.3. Deconvolution of co-eluting lipid classes by IM separation***

Although most lipid classes were separated by SFC, a number of them co-elute or overlap, such as sulfatide and PG, PI and PE, PA and PS, etc. In the event of co-elution, the advantage of the IM separation is evident in deconvolution of individual lipid classes. Because the gas-phase packing efficiencies of different lipid classes are intrinsically different, co-eluting lipid species tend to occupy different space in the IM-MS 2D spectrum further demonstrating the advantages of coupling techniques with separations based on orthogonal physical properties such as IM and SFC (size and polarity, respectively). A few examples are illustrated below (Figures. 2.4-2.7; all in negative ion mode).

As seen in Figure 2.2, sulfatides co-elute with PGs as two peaks at 3.6 and 3.9-min, respectively. By searching through the LIPID MAPS database, we found that PGs eluting at 3.6-min contain mainly ether-linked PGs (plasmalogen or alkyl ether; P- or O-PGs) at sn-1 position (observed as  $[M-H_2O-H]^-$ ) while PGs eluting at 3.9-min are made up of normal diacyl PGs (observed as  $[M-H]^-$ ). This is not surprising considering that brain is rich in plasmalogen lipids, mostly in the form of PE.<sup>75, 76</sup> For each peak, sulfatide and the co-eluting species occupy unique space in the IM-MS 2D spectrum, which allows differentiation of not only the parent ions but also their fragments (Figures. 2.4 and 2.5). Specifically, both types of PGs adopt smaller gas-phase conformations than sulfatides and undergo almost complete fragmentation to give fatty acid anions as the major



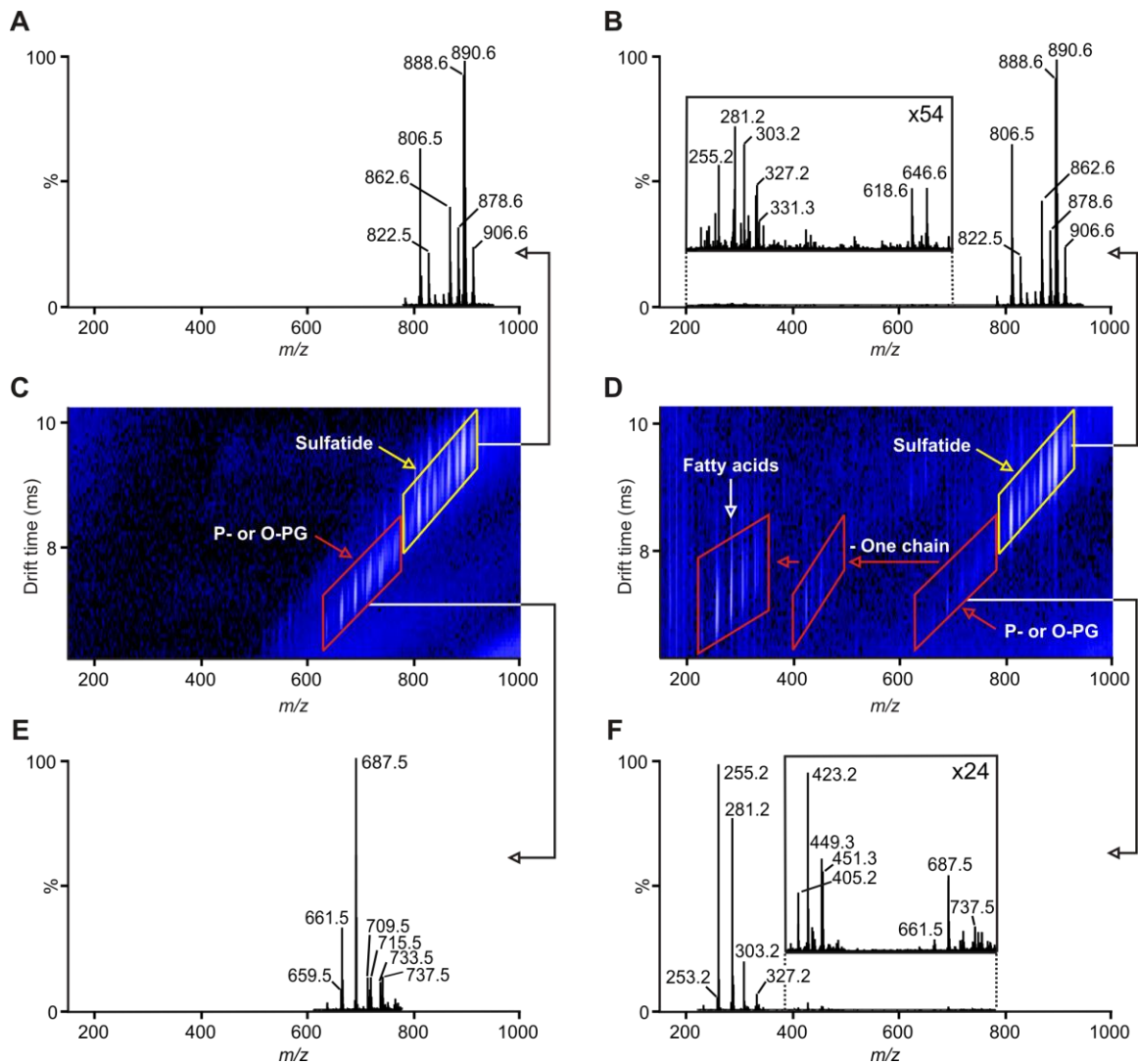


**Figure 2.4.** IM-MS deconvolution of sulfatides (observed as  $[M-H]^-$ ) and plasmalogen or alkyl-ether-linked phosphatidylglycerols (PGs) (observed as  $[M-H_2O-H]^-$ ) on top and bottom panels respectively, co-eluting at 3.6-min.  $MS^E$  in negative mode (right panels) illustrate fragment ions for each particular lipid class. Sulfatides have longer drift times compared to co-eluting PGs but much lower fragmentation yields (panels B and F).

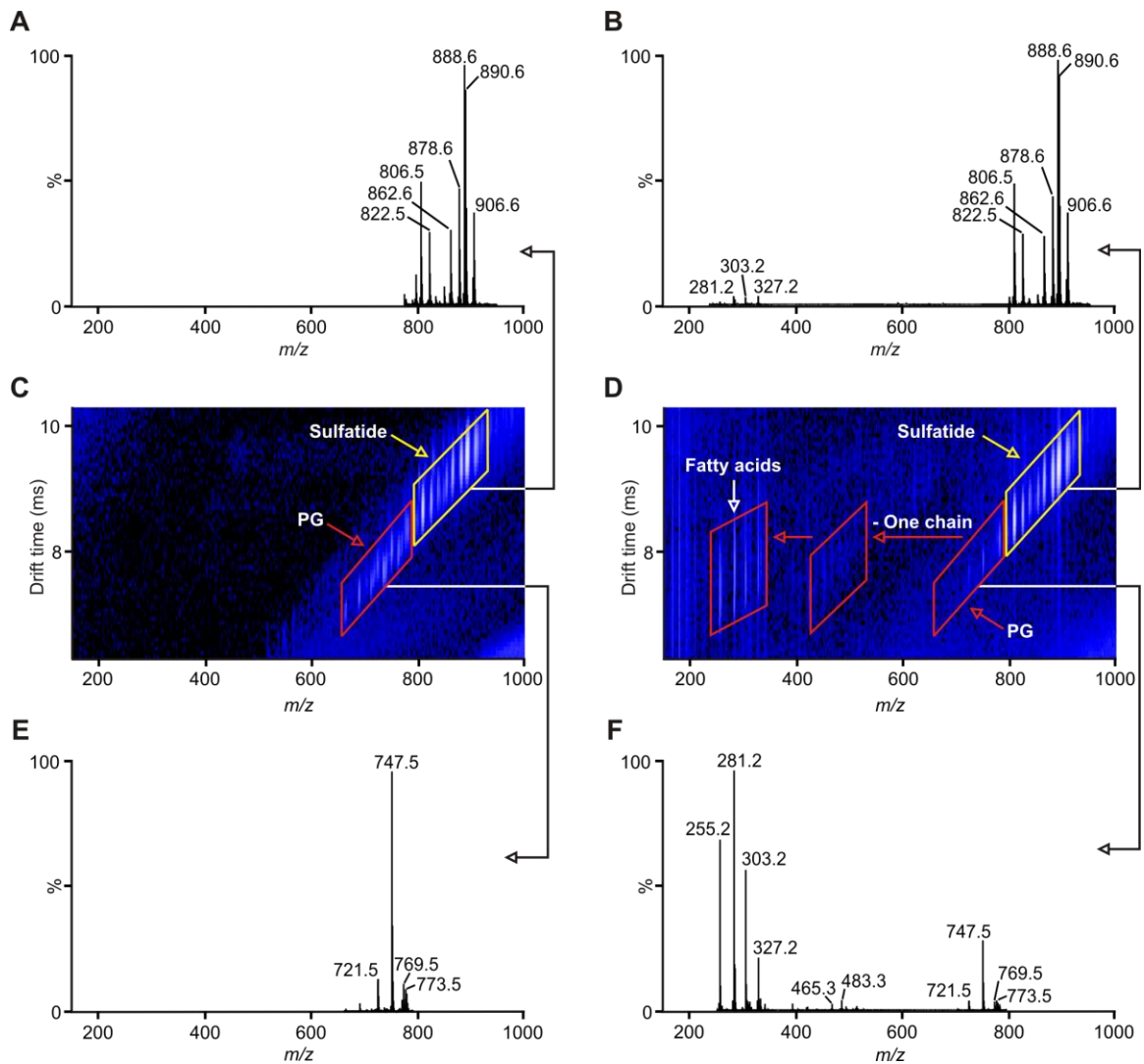


**Figure 2.5.** IM deconvolution of sulfatides (observed as  $[M-H]^-$ ) and diacyl phosphatidylglycerols (PGs) (observed as  $[M-H]^-$ ) on top and bottom panels respectively, co-eluting at 3.9-min using MS<sup>E</sup> in negative mode.

fragments in the negative mode. On the other hand, sulfatides adopt larger conformation and undergo less fragmentation at the same CID conditions. The complete MS and MS/MS spectra of sulfatides can be obtained by the sum of the 3.6 and 3.9-min peaks, followed by extraction of the sulfatide IM-MS 2D spectrum region. A similar approach can be applied to deconvolute the partially overlapping PIs and PEs as well as PAs and PSs as shown in Figures. 2.6 and 2.7.

#### ***2.3.4. Fatty acid composition of individual lipid classes obtained by post-mobility fragmentation in negative mode.***

As discussed above, in the negative ion mode, lipid anions tend to fragment to give fatty acid anions that would reflect the fatty acid composition of each lipid class. In addition, the position of substitution (sn1 and sn2) can in some cases be identified by not fully fragmented ions (loss of one chain) shown in Figure 2.3. By examining the negative-mode MS/MS data of all lipids found in Figure 2.2, three categories of lipid classes can be defined: i) lipid classes that fragment almost completely to fatty acids anions, such as PE, PA, PC, ceramide, MGDG, and PG; ii) lipid classes that give significant, but not predominant, amount of fatty acid anions, such as PI and PS; and iii) those that give minimum amount of fatty acids fragmentation, including sulfatide, cerebroside, and SM. Thus, using the fragmentation information, the fatty acid composition of lipid classes belonging to categories i) and ii) can be qualitatively obtained (Table 2.1). We emphasize that CID fragmentation yields are indirectly proportional to ion mass.<sup>77</sup> Thus, the relative fatty acid composition does not provide

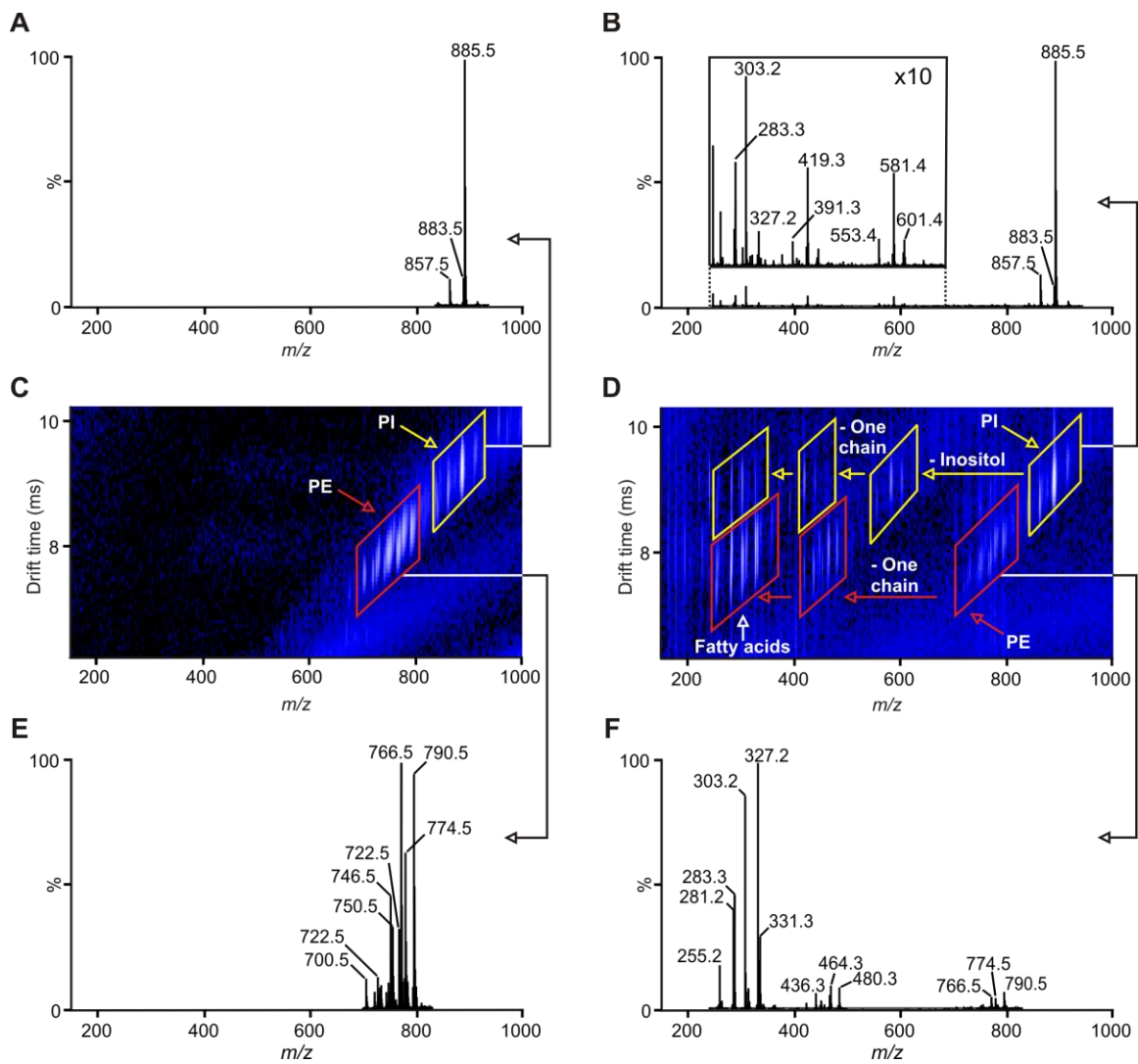


**Figure 2.6.** IM deconvolution of phosphatidylinositols (PIs) and phosphatidylethanolamines (PEs) on top and bottom panels respectively, co-eluting at 5.7-min using MS<sup>E</sup> in negative mode.

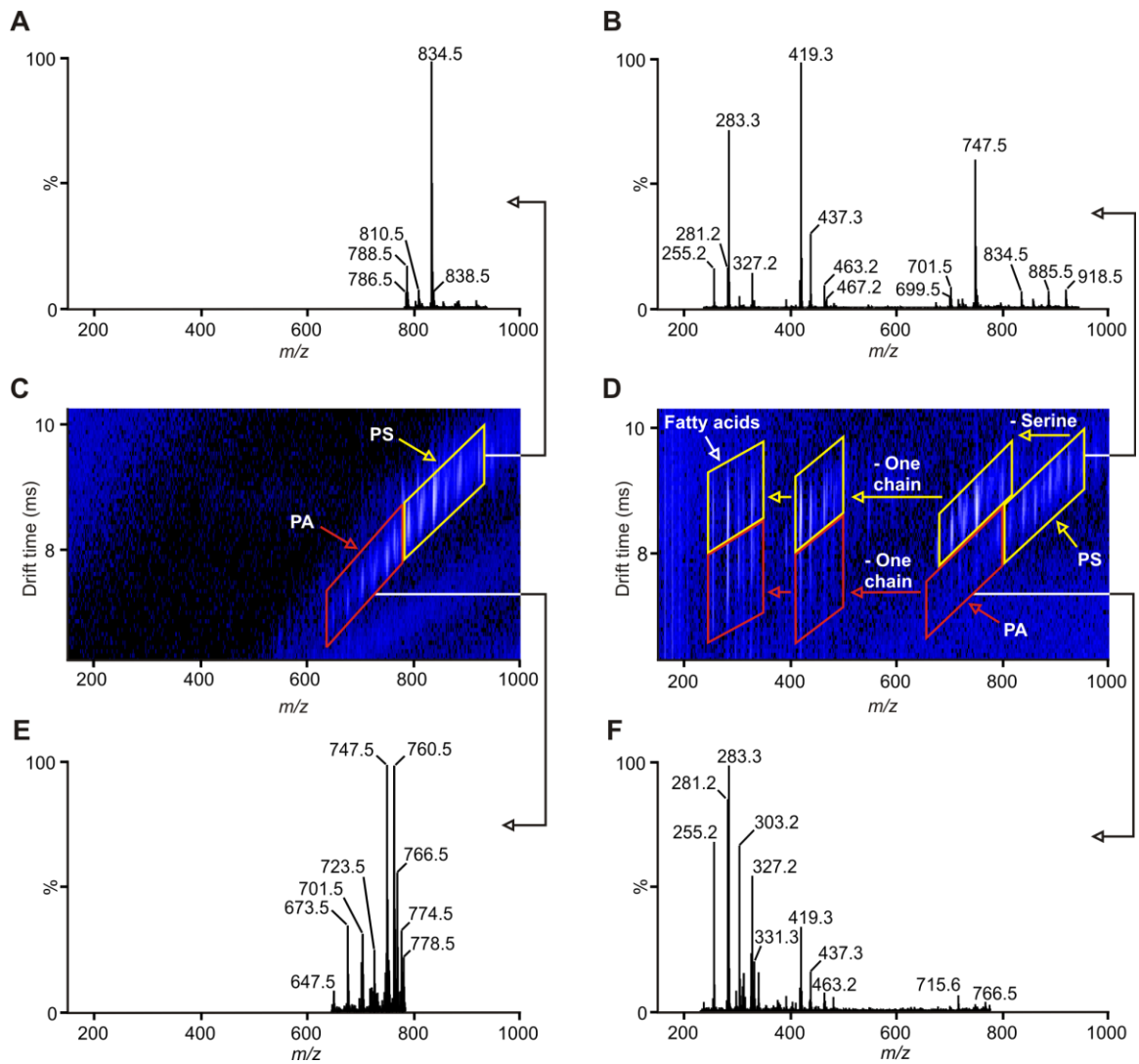


**Figure 2.7.** IM deconvolution of phosphatidylserines (PSs) and phosphatidic acids (PAs) on top and bottom panels respectively, co-eluting at 8.8-min using MS<sup>E</sup> in negative mode.

**Table 2.1.** Fatty acid percentage composition of individual lipid classes obtained from MS<sup>E</sup> in negative mode.

	Lipid Classes									
	Ceramide	MGDG	P- or O-PG	Diacyl PG	PE	PI	PC	PA	PS	
14:0	0	8.8±0.5	1.3±0.2	0.7±0.2	0.3±0.1	0	1.6±0.2	0	0	0
16:0	0.4±0.1	41.4±0.3	39.0±1.5	24.3±1.1	6.3±0.1	11.9±2.6	53.2±7.9	15.7±1.8	10.8±0.5	
18:0	16.2±1.3	15.0±1.0	6.1±2.6	10.1±1.5	17.8±0.8	22.8±0.2	6.2±0.1	25.0±1.9	52.4±0.5	
20:0	0	3.8±0.3	0.2±0.1	0.3±0.1	1.2±0.3	0.3±0.1	0.2±0.1	1.1±0.1	0.5±0.1	
16:1	0	5.2±0.2	3.0±0.1	1.4±0.1	0.8±0.2	0.5±0.2	2.2±0.4	1.1±0.2	0.6±0.1	
18:1	1.5±0.2	18.7±1.7	33.8±2.8	33.9±3.0	17.4±0.7	8.9±0.2	22.6±4.9	20.2±1.0	14.8±0.6	
20:1	78.6±1.5	4.0±0.1	1.0±0.2	1.3±0.4	3.1±0.3	0.8±0.2	0.7±0.1	2.6±0.3	0.9±0.1	
22:1	3.3±0.1	0.8±0.1	0.2±0.1	0	0.6±0.1	0.2±0.1	0.1±0.1	0.5±0.1	0.3±0.1	
18:2	0	0.9±0.9	1.7±0.1	1.4±0.1	0.7±0.1	0.5±0.2	0.9±0.2	1.0±0.1	0.4±0.1	
24:2	0	0	0.1±0.1	0	0.4±0.1	0.2±0.1	0.1±0.1	0.2±0.1	0.2±0.1	
20:4	0	0.8±0.2	9.0±0.5	15.8±0.8	23.2±1.2	43.6±2.9	8.0±1.7	14.4±1.8	3.7±0.3	
22:4	0	0	1.2±0.2	2.1±0.6	8.0±0.3	1.8±0.2	0.7±0.1	4.9±1.5	2.5±0.1	
24:4	0	0	0	0	0.3±0.1	0.2±0.2	0	0.2±0.1	0.1±0.1	
20:5	0	0	0	0	0.1±0.1	0.2±0.1	0	0.1±0.1	0.1±0.1	
22:6	0	0.5±0.2	3.4±0.7	8.7±0.7	20.5±0.6	8.2±0.5	3.5±0.7	13.0±1.3	12.7±0.4	
24:6	0	0	0	0	0.2±0.1	0.1±0.1	0	0.2±0.1	0.1±0.1	
Total PUFA	0	2.1±0.3	15.4±1.4	28.0±1.8	53.2±1.0	54.6±2.9	13.2±2.7	33.8±3.4	19.7±0.7	
Total	100	100	100	100	100	100	100	100	100	100

absolute quantitation data. However, these fatty acid profiles allow for estimations of the composition of the different lipid classes.

Additionally, same lipid class comparisons between different samples can be made. As seen from the table, PE and PI have the highest content (percentage) of polyunsaturated fatty acids (PUFAs). Specifically, PE contains the highest level of docosahexaenoic acid (DHA) while PI is the richest in arachidonic acid (AA). This is consistent with a previous report, which further supports the ability of this lipid profiling technique.<sup>78</sup> Overall, the PUFA content decreases in the order of PI  $\approx$  PE > PA > PG > PS > P- or O-PG > PC > MGDG while ceramides do not contain any PUFA. Note that for ceramides, fatty acyl amide anions were observed instead. Although PCs and SMs strongly co-elute, the fatty acid fragments would mostly originate from PCs due to the smaller fragmentation yields of SMs in comparison to PCs under the CID conditions used in our study (no significant amount of fatty acyl amide anions from SMs were detected).

### ***2.3.5. Gene expression confirms in vitro polarization of MDMs***

Previous studies have identified markers that can be used to characterize polarized macrophages.<sup>14, 15, 79, 80</sup> To confirm that MDMs were successfully polarized into distinct subsets, four representative genes were selected to conduct gene expression profiles of *in vitro* polarized cells in comparison to that of untreated cells (Figure 2.8). CD80 and CCR7 were used as markers of M1 polarization while CD209 and CD163 were used as markers of M2a and M2c polarization, respectively.<sup>14, 15, 79</sup> In response to M1 polarization generated by treating cells with IFN $\gamma$  in combination with LPS, CD80 and CCR7 expression was upregulated compared to untreated controls (Figure 2.8 (A, B) while

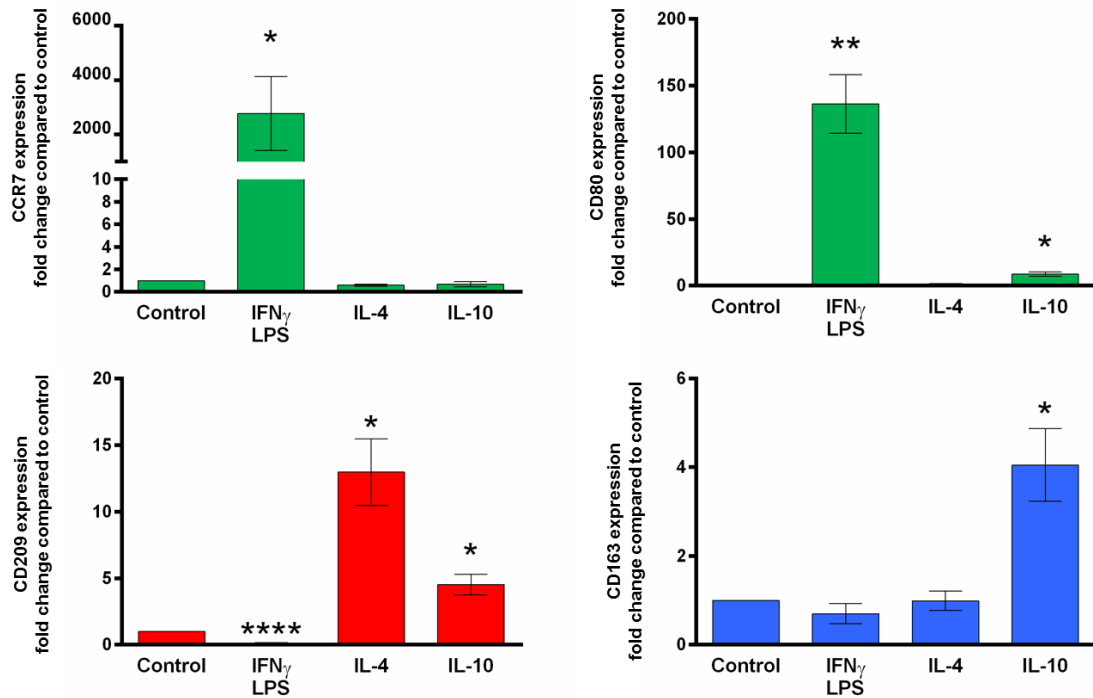


**Figure 2.8.** *In vitro* polarization of MDMs confirmed using gene expression. Following polarization, cells were lysed and evaluated for expression of M1 markers CCR7 (A) CD80 (B), M2a marker CD209 (C) and M2c marker CD163 (D). Values expressed as fold change using  $\Delta\Delta C_t$  method compared to untreated controls. Resting untreated controls were set to 1 and all treatments normalized to GAPDH. (Experiments repeated  $\geq n=4$ ; \* indicates  $p \leq 0.05$ , \*\* indicates  $p \leq 0.01$ , and \*\*\*\* indicates  $p \leq 0.0001$ )



CD209 and CD163 expression were down regulated (Figure 2.8 (C, D)). M2a polarization generated by IL-4 treatment was evidenced by an increase in CD209 expression with no changes seen in M1 or M2c marker expression. In response to IL-10 generated M2c polarization, expression of the M2c marker CD163 was significantly upregulated. IL-10 treatment also induced the expression of CD80 and CD209. Together these data confirm that we can successfully polarize MDMs into M1, M2a, and M2c subsets using well-established *in vitro* stimuli.

### **2.3.6. Membrane phospholipid composition of MDMs**

For the analysis of membrane phospholipid composition, the combination of SFC with IM-MS provides the necessary information for the identification of the lipid classes and their respective fatty acid composition. The separation of phospholipids classes is achieved efficiently based on the polarity of their respective head group, with less polar classes (e.g., phosphatidylglycerols) eluting before more polar classes (e.g. phosphatidylcholines).<sup>66</sup> Subsequently, low- and high-energy spectra collected in MS<sup>E</sup> mode provides accurate mass and fragments for lipid class identification and fatty acid composition in positive and negative ion-mode respectively. Despite the fact that lower intensities are observed for longer chain lengths and higher degrees of unsaturation,<sup>81</sup> the separation of lipid classes prior to ionization minimizes ionization suppression effects and permits direct comparison of the distribution of individual phospholipids species within its class across samples.

Six major membrane phospholipid (PL) classes were identified, phosphatidylcholines (PCs), phosphatidylethanolamines (PE), phosphatidylserines (PS),

phosphatidylglycerols (PG), phosphatidylinositols (PI) and sphingomyelins (SM). Their total mass spectrometry signal (intensity) was calculated and individual species abundancies are reported as the percent (percent contribution or distribution, Tables in Appendix B) of the total signal for each class. This relative quantitation lipidome analysis was able to detect changes in species distribution within each phospholipid class in all 4 activation states. It is evident from the 3D principal component analysis plot in Figure 2.9 that controls and M1 MDMs are the furthest apart in principal component 1. Furthermore, both M2 groups are separated from controls and M1 but group closely in principal components 1 and 2. However, in principal component 3, substantial differences were recognized between M2a and M2c MDM, identifying them as unique “phenotypes” in the three-dimensional macrophage polarization space.

We analyzed the membrane lipid composition of each class independently and compared them across resting, M1, M2a and M2c MDMs. Given the different lipid composition within different organelles and plasma membranes as well as asymmetric lipid distribution, the localization of lipid changes is not surveyed in this lipid profiling study.<sup>28</sup> PL classes mainly located in the cytosolic leaflet or luminal side of plasma membranes are shown in Figures 2.10 and 2.11 respectively. During the polarization of macrophages, distinct phospholipase A<sub>2</sub> enzymes are involved in the arachidonic acid (AA) mobilization for consequent eicosanoid production.<sup>82</sup> Figure 2.10 (A-C) shows the percent composition of selected species (higher composition and higher changes) for PE, PI and PS respectively. Phospholipid species are abbreviated (lipid class, number carbon atoms and double bonds of both acyl chains combined) due to the fact that fragmentation of individual m/z species result in fragments corresponding to various acyl groups,

making the assignment of individual structures not possible. Drops in the composition of species with an unsaturation degree of 4 or higher (possibility of containing AA) were expected for polarized MDMs.<sup>83</sup> However, small overall changes were observed for statistically significant (p-value <0.05) lipids. The highest changes were detected for PE(38:4) and PI(38:4), where the composition decreased after activation by 1.6-2.5 and 2.3-3.8% respectively. Interestingly, the opposite profile was observed for PI(38:5). Given the nature of the percent distribution of all species within a lipid class, the decrease of one species is commensurately compensated by the increase of other species. Thus, lipids with lower degrees of unsaturation show an increase in polarized MDMs such as, PI(36:2), PS(36:2) and PE(34:1). Similarly, on the non-cytosolic (luminal side), changes in the fatty acid distribution of PCs and SMs were observed (Figure 2.11). The increase of PC(30:1), PC(32:0) and PC(34:0) and the decrease of PC(36:4), PC(38:4) and PC(40:5) indicate AA mobilization. However, it is not clear if this mobilization is entirely for lipid mediator synthesis or the release of AA surpasses the eicosanoid production. Another possibility is that the released AA is simply being exchanged with serum proteins as it has been previously reported for RAW 264.7 cells.<sup>84</sup> Figure 2.11 (C) illustrates the changes observed in in PG. These are consistent with the other classes, particularly PE and PC. Higher distribution is determined for species not containing AA (PG(34:1), PG(34:2), PG(36:1) and PG(36:2)) for polarized MDMs compared to resting. Statistically different lipid species, not only between polarized and resting macrophages but also between similar phenotypes such as M2a and M2c are of great interest for the determination of polarization. Six species, PC(32:1), PC(O-32:1), PC(34:3), PI(38:3), PI(38:5) and PS(36:2) are statistically different in the different polarization states. It is

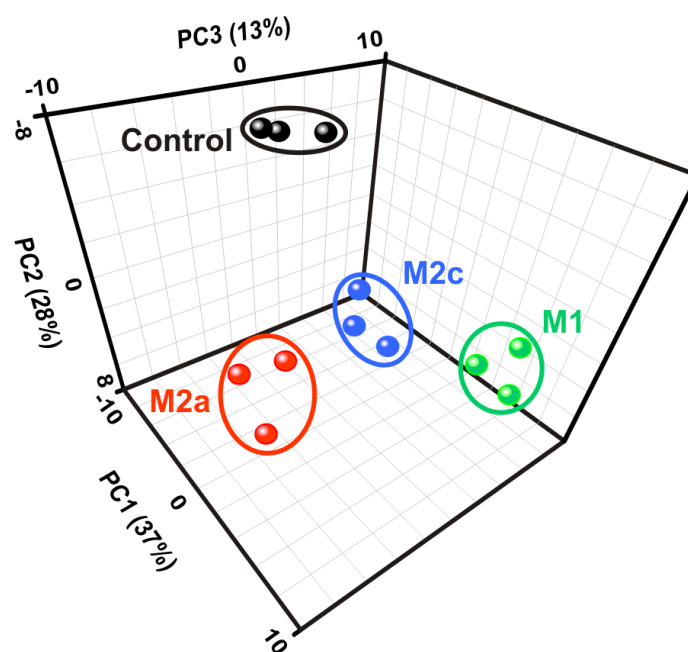


**Figure 2.9.** Three-dimensional PCA plot of lipid profiles for control, M1, M2a and M2c MDM. PC1 separates controls, M1 and both M2 groups (M2a and M2c have similar grouping in PC1). In both PC2 and PC3 M2a and M2c are grouped separately.

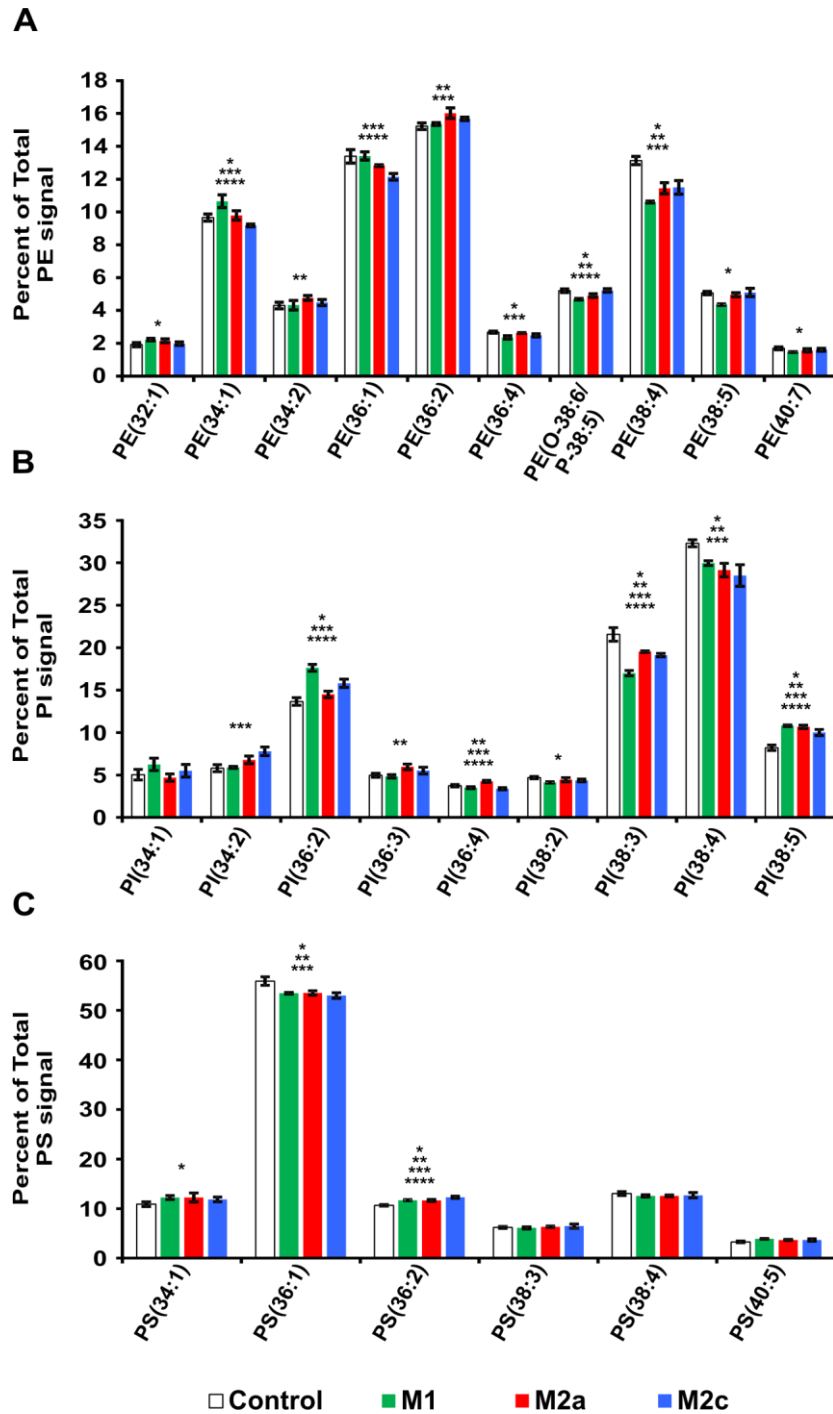


**Figure 2.10.** Comparison of relative distribution of individual lipid classes in the cytosolic leaflet in controls, M1, M2a and M2c MDM. A), B) and C) illustrate the changes for PE, PI and PS respectively. Lipids with highest contribution and changes were plotted. (\* indicates p-value<0.05 for control-M1 comparison, \*\* indicates p-value<0.05 for control-M2a comparison, \*\*\* indicates p-value<0.05 for control-M2c comparison and \*\*\*\* indicates p-value<0.05 for M2a-M2c comparison).

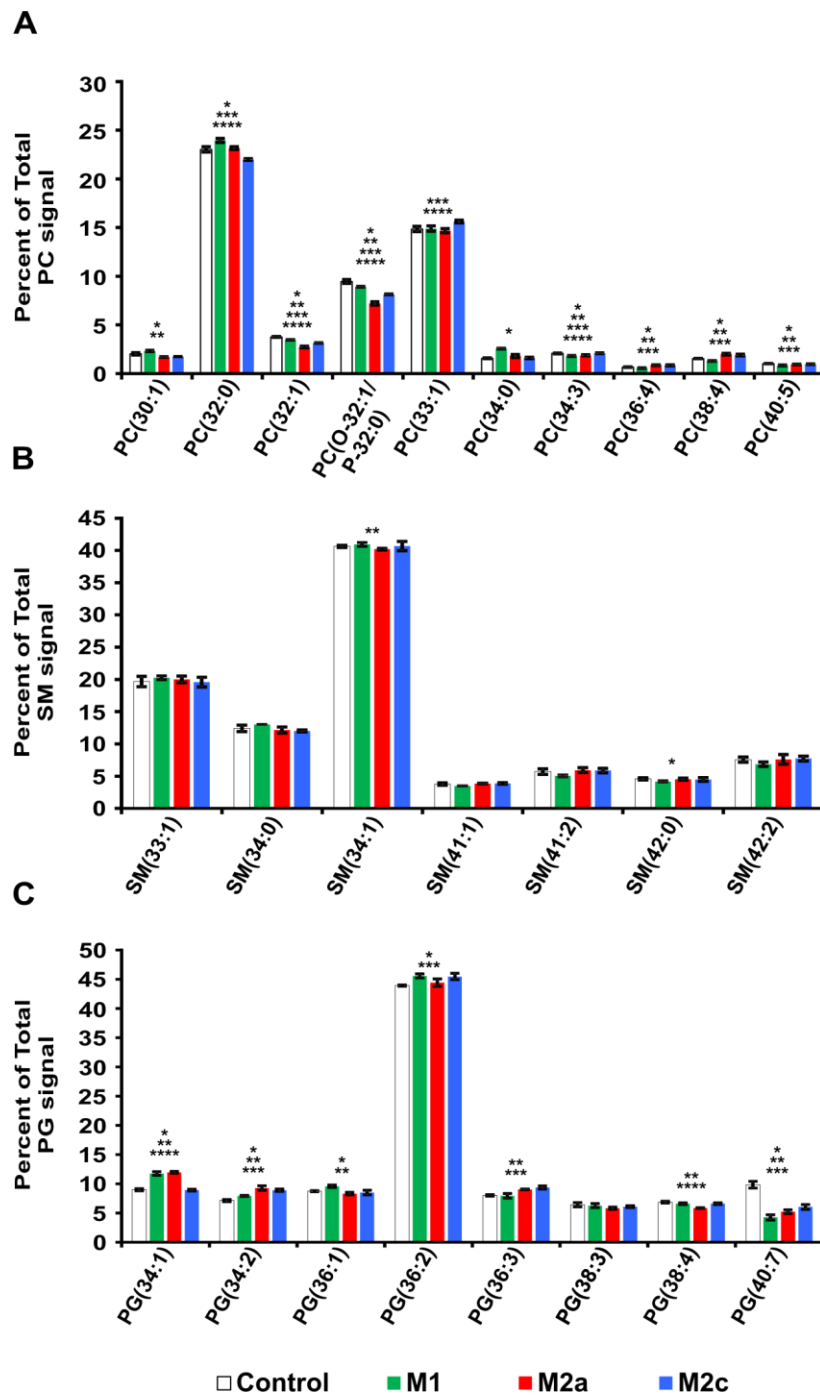


**Figure 2.11.** Comparison of relative distribution of individual lipid classes in the luminal side are illustrated in A) and B) (PC and SM respectively) for controls, M1, M2a and M2c. Panel C) represents the lipid distribution for PG Lipids with highest contribution and changes were plotted. (\* indicates p-value<0.05 for control-M1 comparison, \*\*indicates p-value<0.05 for control-M2a comparison, \*\*\* indicates p-value<0.05 for control-M2c comparison and \*\*\*\* indicates p-value<0.05 for M2a-M2c comparison).

worth noting that only PI(38:5) potentially contains AA. The largest change for species containing AA was observed in PG(40:7). The mechanisms of this particular changes is still unclear however, the fact that macrophages were derived from 3 different donors suggests a higher degree of orchestration in the polarization process.

It should be noted that in spite of little difference in relative distributions, many species showed significantly different profiles across all groups, and the low variabilities (error bars) between biological replicates have an average standard deviation of 3.1% for lipids in all treatments plotted in Figures 2.10 and 2.11. The standard deviations for all species detected and for species with odd-numbered chain fatty acids are 4.2 and 6.7% respectively. The slightly higher deviation for odd-numbered chain fatty acids distribution could be caused by differences in the donor's diet since they are not endogenous.<sup>85</sup>

### ***2.3.7. Fatty acid composition of different lipid classes in polarized monocyte-derived macrophages***

In previous studies, the macrophage fatty acid composition in murine cells has been investigated and absolute quantitative amounts have been reported.<sup>86, 87</sup> In our study, we focused on differences between relative fatty acid compositions for different lipid classes among different groups. It is worth emphasizing that with collision-induced dissociation, fragmentation yields are indirectly proportional to the mass of the ion, so these relative estimations of fatty acid distribution within the same lipid class. Figure 2.12 shows the changes in AA composition of 6 different phospholipid classes for all 4 groups. (These values were selected using Tables B.1-B.4 in Appendix B). AA

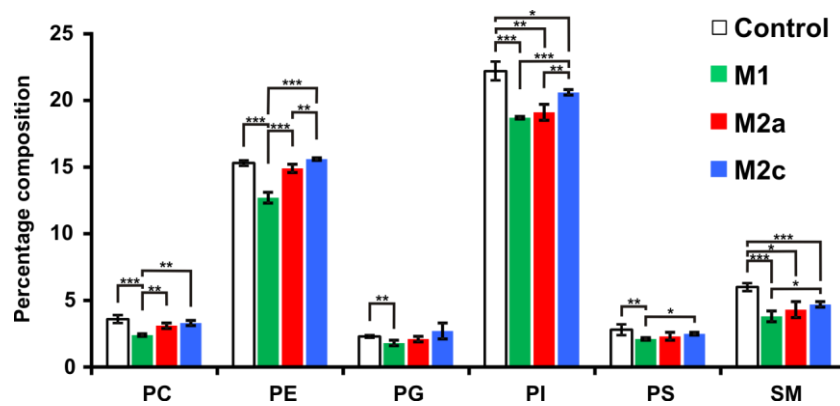


**Figure 2.12.** Changes in arachidonic acid composition for different lipid classes for controls, M1, M2a and M2c macrophages (\* indicates p-value<0.05, \*\* indicates p-value<0.01, \*\*\* indicates p-value<0.005).



composition values decreased after M1 polarization as it would be expected in all lipid classes. The largest changes compared to resting macrophages ( $P < 0.005$ ) are observed in SM, PE and PI with 2.2 and 2.6 and 3.5% decrease respectively. Furthermore, the low AA levels observed in PC and SM could be explained by the low AA and linoleic acid (LA) concentrations in FBS (~7% and 5.5% of fatty acid composition respectively), especially considering the long culture time during derivatization and polarization.<sup>88-92</sup> A previous fatty acid comparison determined that the AA content of total lipids was three times lower in macrophages derived from bone marrow to lipids of peritoneal macrophages.<sup>93</sup> The smallest changes for all 4 groups are observed in PG, which is consistent with a previous study of classically activated murine resident peritoneal macrophages (RPM) cells.<sup>84</sup> Additionally, the AA levels for each lipid class are lower in M1 than in both M2 activation states, supporting the predominant role of cytoplasmic phospholipase A2 (cPLA<sub>2</sub>) in AA mobilization during M1 polarization.<sup>82</sup> Interestingly, AA composition is significantly different ( $p\text{-value} < 0.01$ ) between M2a and M2c MDMs for good substrate lipid classes highly abundant in AA such as PE and PI, with M2c having higher AA levels. Some lipid mediators detected in human MDMs such as resolvins, maresins and protectins are synthesized from docosahexaenoic acid (DHA).<sup>94</sup> Small DHA changes in the fatty acid composition of PG's are observed between resting macrophages, M1 and both M2 subtypes. A decrease from 3.9% composition in resting macrophages to 2.1 and 2.5% was measured after M2a and M2c polarization respectively (Tables B.1-B.4 in Appendix B). However, the biggest change was observed in classical activation with a decrease to 1.6%.

These studies demonstrate that macrophage polarization is associated with changes in the lipidome of MDMs as evidenced by alterations in various classes of membrane phospholipids. Moreover, we have established an innovatively applied methodology for rapid lipid profiling of polarized macrophages. Our untargeted lipid profiling integrated to traditional gene expression analysis allowed for the identification of a wide range of lipid classes for specific macrophage polarization phenotypes. Furthermore, the monitoring of several lipid species has the potential of determining polarization subsets with overlapping phenotypes at the end of the “omics” cascade (Figure 2.9). The methods used in this study advance the field of macrophage polarization research by demonstrating that state-of-the-art lipidomic techniques can be used to further interrogate polarized human macrophages, a class of cells that are still not well characterized.

As previously discussed, our gene expression analysis revealed common caveats that are presented when classifying cells using solely this technique such as marker overlap. This is observed when M2c polarization generated by IL-10 treatment upregulated both CD163 (M2c) and CD209 (M2a) to a similar extent while M2a polarization generated by IL-4 treatment only upregulated CD209 expression. These findings demonstrate the importance of including i) multiple markers for polarization and ii) differently activated macrophages to distinguish between subsets. While we do not provide an exhaustive set of polarization markers, we instead chose 4 markers that display relative specificity between subsets.

After confirming our *in vitro* polarization using gene expression, we sought to explore the extensive lipidome of polarized macrophages and find possible specific

markers. By simultaneously collecting low- and high-energy spectra, both PL and acyl chain composition of the different lipid groups was determined. This methodology was able to depict the global membrane lipidomic picture of macrophage polarization and reveal characteristic lipid species for resting, classic, alternative and deactivated human monocyte derived macrophages.

During the polarization process, different lipid mediators' biosynthetic pathways involving several enzymes are expressed and activated to different extents. Studies have shown that different expression profiles of the major participants in fatty acid mobilization (hydrolysis), cPLA<sub>2</sub> and sPLA<sub>2</sub>, have been observed in human monocyte-derived macrophages treated with LPS + IFN $\gamma$ , IL-4 and IL-10.<sup>95</sup> These phospholipases differ in specificity for fatty acid species and position in the glycerol backbone, affinity to different PL classes and localization within the cell upon activation.<sup>82</sup> Thus, different PL pools are substrates in this highly orchestrated and not fully understood enzymatic process at different times. Furthermore, some crosstalk between both phospholipases has been observed in mouse macrophages (P388D1) and other studies in human neutrophils showed the ability of sPLA<sub>2</sub> to induce leukotriene biosynthesis by activating cPLA<sub>2</sub>.<sup>96, 97</sup> Furthermore, the formation of lysophosphatidylcholine by sPLA<sub>2</sub> in the outer membrane causes an increase of Ca<sup>2+</sup> concentration, which subsequently causes cPLA<sub>2</sub> to be activated and translocated through activating protein kinases needed for the phosphorylation of Ser<sup>505</sup>.<sup>82, 98, 99</sup> On the other hand, in human eosinophils, sPLA<sub>2</sub> induced eicosanoid production at plasma membranes and perinuclear membranes, independently of cPLA<sub>2</sub> activation.<sup>100</sup> These examples show the complexity of interconnectivity in fatty acid release in innate immunity. However, the combination of

the localization and characteristics (specificity and activity) of these phospholipases and the different PL composition of organelle membranes suggest a specific course in which these changes occur in membrane PL composition (Figures 2.10 and 2.11). Generally, lipid species capable of containing AA in either sn-1 or sn-2 positions were of lower abundance in M1 compared to resting macrophages. Alternatively, lipid species with no AA were more abundant in M1 compared to resting macrophages. On the contrary, PI(38:5) is considerably lower in resting macrophages compared to M1 and both M2 phenotypes. Brown and co-workers observed a similar but less drastic trend in murine resident peritoneal macrophages.<sup>84</sup> Anti-inflammatory M2 activation states showed similarities to both resting and classically activated groups. Interestingly, the largest changes between M2a and M2c were detected in lipid classes with high affinity to cPLA<sub>2</sub> (PE, PC and PI) but in AA-free species. The characteristic upregulation of sPLA<sub>2</sub> in M2 macrophages and its lack of sn-2AA specificity suggest that sPLA<sub>2</sub> is most likely the enzyme responsible for the hydrolysis of these species. It should be noted that due to the large size of human macrophages (diameter > 30µm) the amount of PL is significantly high.<sup>95</sup> Therefore, the changes detected in our study between the different treatments are relatively small.

Analysis of fatty acid composition of distinct PL classes allowed us to track global acyl changes and assign them to a region in the polarization spectrum. As mentioned above, the sn-2AA specificity of cPLA<sub>2</sub> is responsible for the majority of the AA release. Across the 6 major PL classes the AA composition was lowest in M1 compared to resting, M2a and M2c macrophages indicating higher AA release in proinflammatory macrophages. This is consistent with previous studies comparing lipid

mediators for M1 and M2a polarized human macrophages after IFN $\gamma$  + LPS and IL-4 treatment respectively, where the biosynthesis of inflammation associated prostaglandins was higher for M1 macrophages compared to M2a. On the contrary, relevant to resolution-associated lipids (resolvins and maresins), we observed a higher release of docosahexaenoic acid (DHA) in M1 compared to M2a (Tables B1-4). However, we measured DHA bound to different PL classes and not the lipid mediators directly. The lipid composition of the cytoplasmic face of Golgi and ER is poorly defined (known cPLA<sub>2</sub> locations);<sup>101</sup> hence, it is not possible to determine the origin and the amount of the AA released for lipid mediator production. Furthermore, the differences in activation and translocation of phospholipases can alter AA mobilization not only by regulating the hydrolysis efficiency but also by inducing translocation to other lipid membranes with different composition. PI and SM had the highest percentage of AA mobilization, with PI showing the largest changes between resting, M1, M2a and M2c macrophages (Figure 1.12). Two interesting observations in the AA metabolism of M2 MDMs are apparent. i) M2c had the lowest AA release in all PL classes and ii) in PE, a substrate to cPLA<sub>2</sub>, no statistical difference was detected between both M2 and resting macrophages, though M2a and M2c are statistically different ( $P < 0.01$ ). Furthermore, PG showed no change in AA composition between resting and both M2 groups. The small composition of AA in SM distributed among different species limited the probabilities of being detected as a SM species during the low-energy spectra collection. Thus, the SM species plotted in Figure 2.11 lack AA.

These experiments were carried out at a single 24 hour time point after treatment. Thus, we are unable to examine the plasticity of polarized profiles at earlier time points

over time and identify lipids that initially contained AA and served as substrate for prostaglandins biosynthesis and were later replenished. Full time course studies with sufficient temporal resolution will be necessary to understand the flux of AA and other fatty acids. Additionally, a global picture of the localization of the AA pools perturbed during macrophage polarization can be determined by fractionation of major organelles /compartments prior to the methodology described herein. Furthermore, it should be noted that various *in vitro* methods are used to differentiate human peripheral blood monocytes into macrophages. Alternative methods of differentiating monocytes into macrophages have been shown to alter downstream activation states.<sup>102-104</sup> Translating *in vitro* polarization studies can also be difficult when factors such as cytokines, cell maturation, cell origin, chemokines, and adhesion that are omitted in the *in vitro* systems play major roles *in vivo*.<sup>105, 106</sup> The nomenclature and methodologies used for modeling macrophage polarization *in vitro* vary greatly within the field and have recently come under fire.<sup>107</sup> We instead chose the most common method of differentiating monocytes, using M-CSF, in an effort to maintain a reproducible experimental standard for the discovery/exploration of phenotypic small molecules changes.

#### **2.4. Conclusions**

Conventionally, to obtain fatty acids composition of glycerol lipids, the individual lipid classes need to be fractionated by chromatographic techniques, followed by base hydrolysis, re-acidification, and re-extraction of each fraction, which is time consuming and labor intensive. The strategy employed in this study provides an efficient way to profile fatty acids composition for the majority of the lipid classes, in addition to

molecular ions, in a single run ( $MS^E$ ). With appropriate standards for each lipids class as described by LIPID MAPS, both the molecular ions and the fatty acids within each class can be quantified.

In summary, a rapid and three-dimensional separation of over ten classes of lipids from mouse brain was achieved by SFC-IM-MS. Combination of full scan and post-mobility fragmentation ( $MS^E$ ) gave a large amount of information from two parallel analyses (positive and negative modes), including individual lipid classes, headgroup information from positive-ion mode, and lipid class fatty acid relative composition from negative-ion mode.

This methodology in combination with the lipid profiling data of both PL and fatty acid composition might be of utility to better understand and quantify the lipidome dynamic changes in the human monocyte derived macrophage polarization spectrum.

## 2.5. Acknowledgements

This chapter contains the research articles: J. Rafael Montenegro-Burke\*, Libin Xu\*, Zeljka Korade, Ned A. Porter and John A. McLean, Expanding Lipidomic Separation Space by Integrating Supercritical Fluid Chromatography with Ion Mobility-Mass Spectrometry. For submission to for *Analytical and Bioanalytical Chemistry* (\*These authors contributed to an equal extent) and J. Rafael Montenegro-Burke\*, Jessica A. Sutton\*, Lisa M. Rogers, John A. McLean and David M. Aronoff, Lipid Profiling of 3-Dimensional Polarization Space of Human Monocyte-derived Macrophages, In preparation for *The Journal of Lipid Research*. (\*These authors contributed to an equal extent).

The authors gratefully acknowledge financial support received from the NIH (K99HD073270 (LX), HD064727 (NP), and UH2TR000491 (JAM), 5UH3TR000491-04 and 3UH3TR000491-04S1(DMA), 5T32HL007737-20 (JAS)), the Defense Threat Reduction Agency (HDTRA1-09-1-00-13 and DTRA100271 A-5196 (JAM)), DMA was supported by the Global Alliance to Prevent Prematurity and Stillbirth (GAPPS) and Burroughs Welcome Fund (BWF).Vanderbilt College of Arts and Science, Vanderbilt Institute of Chemical Biology, Vanderbilt Institute for Integrative Biosystems Research and Education, Vanderbilt Kennedy Center for Research on Human Development. The authors thank Connor Lamberson for helpful discussions.



## 2.6. References

1. Murray, P. J.; Wynn, T.A., Protective and pathogenic functions of macrophage subsets. *Nat. Rev. Immunol.* **2011**, 11, 723-737.
2. Plüddemann, A.; Mukhopadhyay, S.; Gordon, S., 2011. Innate immunity to intracellular pathogens: macrophage receptors and responses to microbial entry. *Immunol. Rev.* **2011**, 240, 11-24.
3. Mills, C. D.; Kincaid, K.; Alt, J. M.; Heilman, M. J.; Hill, A. M.. M-1/M-2 Macrophages and the Th1/Th2 Paradigm. *J. Immunol.* **2000**, 164, 6166-6173.
4. Martinez, F. O.; Helming, L.; Gordon, S., Alternative Activation of Macrophages: An Immunologic Functional Perspective. *Annu. Rev. Immunol.* **2009**, 27: 451-483.
5. Gordon, S.; Martinez, F. O., Alternative Activation of Macrophages, Mechanism and Functions. *Immunity* **2010**, 32, 593-604.
6. Mantovani, A.; Sica, A.; Sozzani, S.; Allavena, P.; Vecchi, A.; Locati, M., The chemokine system in diverse forms of macrophage activation and polarization. *Trends Immunol.* **2004**, 25, 677-686.
7. Mosser, D. M.; Edwards, J. P., Exploring the full spectrum of macrophage activation. *Nat. Rev. Immunol.* **2008**, 8, 958-969.
8. Davis, M. J.; Tsang, T. M.; Qiu, Y.; Dayrit, J. K.; Freij, J. B.; Huffnagle, G. B.; Olszewski, M. A., Macrophage M1/M2 Polarization Dynamically Adapts to Changes in Cytokine Microenvironments in *Cryptococcus neoformans* Infection. *mBio* **4**, **2013**.
9. Lu, J.; Cao, Q.; Zheng, D.; Sun, Y.; Wang, C.; Yu, X.; Wang, Y.; Lee, V. W. S.; Zheng, G.; Tan, T. K.; Wang, X.; Alexander, S. I.; Harris, D. C. H.; Wang, Y., Discrete functions of M2a and M2c macrophage subsets determine their relative efficacy in treating chronic kidney disease. *Kidney Int.* **2013** 84, 745-755.
10. Sisino, G.; Bouckenooghe, T.; Aurientis, S.; Fontaine, P.; Storme, L.; Vambergue, A., Diabetes during pregnancy influences Hofbauer cells, a subtype of placental macrophages, to acquire a pro-inflammatory phenotype. *Biochim. Biophys. Acta – Mol. Basis Disease*, **2013**, 1832, 1959-1968.
11. Mantovani, A., Sozzani, S.; Locati, M.; Allavena, P.; Sica, A., Macrophage polarization, tumor-associated macrophages as a paradigm for polarized M2 mononuclear phagocytes. *Trends Immunol.* **2002**, 23, 549-555.

12. Vogel, D. Y.; Glim, J. E.; Stavenuiter, A. W.; Breur, M.; Heijnen, P.; Amor, S.; Dijkstra, C. D.; Beelen, R. H., Human macrophage polarization *in vitro*, maturation and activation methods compared. *Immunobiology* **2014**, 219, 695-703.
13. Derlindati, E.; Dei Cas, A.; Montanini, B.; Spigoni, V.; Curella, V.; Aldigeri, R.; Ardigo, D.; Zavaroni, I.; Bonadonna, R. C., Transcriptomic analysis of human polarized macrophages, more than one role of alternative activation? *PLoS One*, **2015** 10, e0119751.
14. Ambarus, C. A.; Krausz, S.; van Eijk, M.; Hamann, J.; Radstake, T. R. D. J.; Reedquist, K. A.; Tak, P. P.; Baeten, D. L. P., Systematic validation of specific phenotypic markers for *in vitro* polarized human macrophages. *J. Immunol. Methods*, **2012**, 375, 196-206.
15. Martinez, F. O.; Gordon, S.; Locati, M.; Mantovani, A., Transcriptional profiling of the human monocyte-to-macrophage differentiation and polarization, new molecules and patterns of gene expression. *J. Immunol.* **2006**, 177, 7303-7311.
16. Jaguin, M., Houlbert, N.; Fardel, O.; Lecreur, V., Polarization profiles of human M-CSF-generated macrophages and comparison of M1-markers in classically activated macrophages from GM-CSF and M-CSF origin. *Cell. Immunol.* **2013**, 281, 51-61.
17. Martinez, F. O., Gordon, S., The M1 and M2 paradigm of macrophage activation, time for reassessment. *F1000prime Rep.* **2014** 6, 13.
18. Xue, J., Schmidt, S. V.; Sander, J.; Draffehn, A.; Krebs, W.; Quester, I.; De Nardo, D.; Gohel, T. D.; Emde, M.; Schmidleithner, L.; Ganesan, H.; Nino-Castro, A.; Mallmann, M.R.; Labzin, L.; Theis, H.; Kraut, M.; Beyer, M.; Latz, E.; Freeman, T. C.; Ulas, T.; Schultze, J. L. Transcriptome-based network analysis reveals a spectrum model of human macrophage activation. *Immunity*, **2014**, 40, 274-288.
19. Dettmer, K.; Hammock, B. D., Metabolomics--a new exciting field within the "omics" sciences. *Environ. Health Perspect.* **2004**, 112, A396-397.
20. Reales-Calderon, J. A.; Aguilera-Montilla, N.; Corbi, A. L.; Molero, G.; Gil, C., Proteomic characterization of human proinflammatory M1 and anti-inflammatory M2 macrophages and their response to *Candida albicans*. *Proteomics* **2014**, 14, 1503-1518.
21. Zhang, F., Liu, H.; Jiang, G.; Wang, H.; Wang, X.; Wang, H.; Fang, R.; Cai, S.; Du, J., Changes in the proteomic profile during the differential polarization status of the human monocyte-derived macrophage THP-1 cell line. *Proteomics*, **2015**, 15, 773-786.

22. Kelly, B.; O'Neill, L. A. J., Metabolic reprogramming in macrophages and dendritic cells in innate immunity. *Cell Res.* **2015**, *25*, 771-784.
23. Galvan-Pena, S.; O'Neill, L. A., Metabolic reprogramming in macrophage polarization. *Front. Immunol.* **2014**, *5*, 420.
24. Biswas, S. K.; Mantovani, A.; Orchestration of Metabolism by Macrophages. *Cell Metab.* **2012**, *15*, 432-437.
25. Patti, G. J., Yanes, O.; Siuzdak, G., Innovation, Metabolomics, the apogee of the omics trilogy. *Nat. Rev. Mol. Cell Biol.* **2012**, *13*, 263-269.
26. Sugimoto, M., Kawakami, M.; Robert, M.; Soga, T.; Tomita. M., Bioinformatics Tools for Mass Spectroscopy-Based Metabolomic Data Processing and Analysis. *Curr. Bioinf.* **2012** *7*, 96-108.
27. Wymann, M. P.; Schneider, R., Lipid signalling in disease. Nature reviews. *Mol. Cell. Biol.* **2008**, *9*, 162-176.
28. van Meer, G.; Voelker, D. R.; Feigenson, G. W., 2008. Membrane lipids, where they are and how they behave. *Nat. Rev. Mol. Cell Biol.* **2008**, *9*, 112-124.
29. Mason, K. L.; Rogers, L. M.; Soares, E.M.; Bani-Hashemi, T.; Downward, J. E.; Agnew, D.; Peters-Golden, M.; Weinberg, J. B.; Crofford, L. J.; Aronoff, D. M., Intrauterine Group A Streptococcal Infections Are Exacerbated by Prostaglandin E2. *J. Immunol.* **2013**, *191*, 2457-2465.
30. Soares, E. M.; Mason, K. L.; Rogers, L.M.; Serezani, C. H.; Faccioli, L. H.; Aronoff, D. M., Leukotriene B4 Enhances Innate Immune Defense against the Puerperal Sepsis Agent Streptococcus pyogenes. *J. Immunol.* **2013**, *190*, 1614-1622.
31. Berliner, J. A.; Leitinger, N.; Tsimikas, S., The role of oxidized phospholipids in atherosclerosis. *J. Lipid. Res.* **2009**, *50*, S207-212.
32. Musso, G.; Gambino, R.; Cassader, M.; Recent insights into hepatic lipid metabolism in non-alcoholic fatty liver disease (NAFLD). *Prog. Lipid. Res.* **2009**, *48*, 1-26.
33. Gross, R. W.; Han, X., Lipidomics in diabetes and the metabolic syndrome. *Methods Enzymol.* **2007**, *433*, 73-90.
34. Di Paolo, G.; Kim T. W., Linking lipids to Alzheimer's disease, cholesterol and beyond. *Nat. Rev. Neurosci.* **2011**, *12*, 284-296.

35. Santos, C.R.; Schulze, A., Lipid metabolism in cancer. *The FEBS Journal*, **2012**, 279,2610-2623.
36. Sounni, N. E.; Cimino, J.; Blacher, S.; Primac, I.; Truong, A.; *et.al.*, Blocking lipid synthesis overcomes tumor regrowth and metastasis after antiangiogenic therapy withdrawal. *Cell Metab.* **2014**, 20,280-294.
37. Han, X.; Gross, R. W., Shotgun lipidomics, electrospray ionization mass spectrometric analysis and quantitation of cellular lipidomes directly from crude extracts of biological samples. *Mass Spectrom. Rev.* **2005**, 24,367-412.
38. Schmelzer, K.; Fahy, E.; Subramaniam, S.; Dennis, E. A., The lipid maps initiative in lipidomics. *Methods Enzymol.* **2007**, 432,171-183.
39. Quehenberger, O.; Armando, A. M.; Bown, A. H.; Milne, S. B.; Myers, D. S.; *et.al.*, Lipidomics reveals a remarkable diversity of lipids in human plasma. *J. Lipid. Res.* **2010**, 51,3299-3305.
40. Dennis, E. A.; Deems, R. A.; Harkewicz, R.; Quehenberger, O.; Brown, H. A.; *et.al.* A mouse macrophage lipidome. *J. Biol. Chem.* **2010**, 285,39976-39985.
41. Quehenberger, O.; Dennis, E. A.; The human plasma lipidome. *N. Engl. J. Med.* **2011**, 365,1812-1823.
42. Schwudke, D.; Liebisch, G.; Herzog, R.; Schmitz, G.; Shevchenko, A.; Shotgun lipidomics by tandem mass spectrometry under data-dependent acquisition control. *Methods Enzymol.* **2007**, 433,175-191.
43. Merrill, A. H. Jr.; Sullards, M. C.; Allegood, J.C.; Kelly, S.; Wang, E.; Sphingolipidomics, high-throughput, structure-specific, and quantitative analysis of sphingolipids by liquid chromatography tandem mass spectrometry. *Methods*, **2005**, 36,207-224.
44. Ivanova, P. T.; Milne, S. B.; Byrne, M.O.; Xiang, Y.; Brown, H. A., Glycerophospholipid identification and quantitation by electrospray ionization mass spectrometry. *Methods Enzymol.* **2007**, 432,21-57.
45. Han, X., Neurolipidomics, challenges and developments. *Front. Biosci.* **2007**, 12,2601-2615.
46. Harkewicz, R.; Dennis, E. A., Applications of mass spectrometry to lipids and membranes. *Annu. Rev. Biochem.* **2011**, 80,301-325.
47. Clemmer, D. E.; Hudgins, R. R.; Jarrold, M. F., Naked Protein Conformations, Cytochrome c in the Gas Phase. *J. Am. Chem. Soc.* **1995**, 117,10141-10142.

48. von Helden, G.; Wytenbach, T.; Bowers, M. T., Conformation of macromolecules in the gas phase, use of matrix-assisted laser desorption methods in ion chromatography. *Science*, **1995**, 267,1483-1485.
49. McLean, J. A.; Ruotolo, B.T.; Gillig, K. J.; Russell, D.H., Ion mobility-mass spectrometry, a new paradigm for proteomics. *Int. J. Mass. Spectrom.* **2005** 240,301-315.
50. Kanu, A. B.; Dwivedi, P.; Tam ,M.; Matz, L.; Hill Jr, H. H. Ion mobility-mass spectrometry. *J. Mass. Spectrom.* **2008**, 43,1-22.
51. Fenn, L. S.; McLean, J. A., Biomolecular structural separations by ion mobility-mass spectrometry. *Anal. Bioanal. Chem.* **2008**, 391,905-909.
52. Fenn, L. S.; Kliman, M.; Mahsut, A.; Zhao, S. R.; McLean, J. A., Characterizing ion mobility-mass spectrometry conformation space for the analysis of complex biological samples. *Anal. Bioanal. Chem.* **2009**, 394,235-244.
53. Jackson, S. N.; Ugarov, M.; Post, J. D.; Egan, T.; Langlais, D.; *et.al.* A study of phospholipids by ion mobility TOFMS. *J. Am. Soc. Mass. Spectrom.* **2008**, 19,1655-1662.
54. Kliman, M.; May, J. C.; McLean, J. A., Lipid analysis and lipidomics by structurally selective ion mobility-mass spectrometry. *Biochim Biophys Acta, Mol. Cell. Biol. Lipids* **2011** 1811,935-945.
55. May, J. C.; Goodwin, C. R.; Lareau, N. M.; Leaptrot, K. L.; Morris, C. B.; *et.al.*, Conformational ordering of biomolecules in the gas phase, nitrogen collision cross sections measured on a prototype high resolution drift tube ion mobility-mass spectrometer. *Anal. Chem.* **2014**, 86,2107-2116.
56. Kim, H.I.; Kim, H.; Pang, E. S.; Ryu, E. K.; Beegle, L. W.; *et.al.*, Structural Characterization of Unsaturated Phosphatidylcholines Using Traveling Wave Ion Mobility Spectrometry. *Anal. Chem.* **2009**, 81,8289-8297.
57. Ridenour, W. B.; Kliman, M.; McLean, J. A.; Caprioli, R. M., Structural characterization of phospholipids and peptides directly from tissue sections by MALDI traveling-wave ion mobility-mass spectrometry. *Anal. Chem.* **2010**, 82,1881-1889.
58. Shvartsburg. A.; Isaac, G.; Leveque, N.; Smith, R.; Metz, T., Separation and Classification of Lipids Using Differential Ion Mobility Spectrometry. *J. Am. Soc. Mass. Spectrom.* **2011**, 22,1146-1155.

59. Lintonen, T.P.; Baker, P.R.; Suoniemi, M.; Ubhi, B. K.; Koistinen, K. M.; *et.al.* Differential mobility spectrometry-driven shotgun lipidomics. *Anal. Chem.* **2014**, 86,9662-9669.
60. Baker, P. R.; Armando, A. M.; Campbell, J. L.; Quehenberger, O.; Dennis, E. A., Three-dimensional enhanced lipidomics analysis combining UPLC, differential ion mobility spectrometry, and mass spectrometric separation strategies. *J. Lipid. Res.* **2014**, 55, 2432-2442.
61. Pringle, S. D.; Giles, K.; Wildgoose, J. L.; Williams, J. P.; Slade, S. E.; *et.al.*, An investigation of the mobility separation of some peptide and protein ions using a new hybrid quadrupole/travelling wave IMS/oa-ToF instrument. *Int. J. Mass Spectrom.* **2007**, 261,1-12.
62. Taylor, L. T., Supercritical fluid chromatography. *Anal. Chem.* **2008**, 80,4285-4294.
63. Li, F.; Hsieh, Y., Supercritical fluid chromatography-mass spectrometry for chemical analysis. *J. Sep. Sci.* **2008**, 31,1231-1237.
64. Pinkston, J. D.; Wen, D.; Morand, K. L.; Tirey, D. A.; Stanton, D. T., Comparison of LC/MS and SFC/MS for Screening of a Large and Diverse Library of Pharmaceutically Relevant Compounds. *Anal. Chem.* **2006**, 78,7467-7472.
65. Weller, H. N.; Ebinger, K.; Bullock, W.; Edinger, K. J.; Hermsmeier, M. A.; *et.al.*, Orthogonality of SFC versus HPLC for small molecule library separation. *J. Comb. Chem.* **2010**, 12,877-882.
66. Bamba, T.; Shimonishi, N.; Matsubara, A.; Hirata, K.; Nakazawa, Y; *et.al.*, (2008) High throughput and exhaustive analysis of diverse lipids by using supercritical fluid chromatography-mass spectrometry for metabolomics. *J. Biosci. Bioeng.* **2008**, 105,460-469.
67. Xu. L.; Korade, Z.; Rosado, D. A.; Liu, W.; Lamberson, C. R; *et.al.*, An oxysterol biomarker for 7-dehydrocholesterol oxidation in cell/mouse models for Smith-Lemli-Opitz syndrome. *J. Lipid. Res.* **2011**, 52,1222-1233.
68. Smith, C. A.; Want, E. J.; O'Maille, G.; Abagyan, R.; Siuzdak. G., XCMS, processing mass spectrometry data for metabolite profiling using nonlinear peak alignment, matching, and identification. *Anal. Chem.* **2006**, 78, 779-787.
69. Smith, C. A.; Maille, G. O.; Want, E. J.; Qin, C.; Trauger, S. A.; Brandon, T. R.; Custodio, D. E.; Abagyan, R.; Siuzdak. G., 2005. METLIN, A Metabolite Mass Spectral Database. *Ther. Drug Monit.* **2005**, 27, 747-751.

70. Sud, M.; Fahy, E.; Cotter, D.; Brown, A.; Dennis, E. A.; Glass, C. K.; Merrill Jr, A. H.; Murphy, R.C.; H. Raetz, C. R.; Russell, D. W., LMSD, LIPID MAPS structure database. *Nucleic. Acids. Res.* **2007**, 35, D527-532.
71. O'Brien, J. S.; Sampson, E. L. Lipid composition of the normal human brain, gray matter, white matter and myelin. *J. Lipid Res.* **1965**, 6,537-44.
72. Porter, F. D.; Herman, G. E., Malformation syndromes caused by disorders of cholesterol synthesis. *J. Lipid Res.* **2011**, 52,6-34.
73. Vanier, M. T. Lipid changes in Niemann-Pick disease type C brain, personal experience and review of the literature. *Neurochem. Res.* **1999**, 24,481-489.
74. Tempez, A.; Ugarov, M.; Egan, T.; Schultz, J. A.; Novikov, A.; et.al., Matrix implanted laser desorption ionization (MILDI) combined with ion mobility-mass spectrometry for bio-surface analysis. *J. Proteome Res.* **2005**, 4,540-545.
75. Han, X.; Holtzman, D. M.; McKeel Jr, D. W., Plasmalogen deficiency in early Alzheimer's disease subjects and in animal models, molecular characterization using electrospray ionization mass spectrometry. *J. Neurochem.* **2001**, 77,1168-1180.
76. Braverman, N. E.; Moser, A. B., Functions of plasmalogen lipids in health and disease. *Biochim. Biophys. Acta* **2012**, 1822,1442-1452.
77. Sleno, L.; Volmer, D. A., Ion activation methods for tandem mass spectrometry. *J. Mass Spectrom.* **2004**, 39,1091-1112.
78. Nussbaum, J. L.; Neskovic, N.; Mandel, P., The fatty acid composition of phospholipids and glycolipids in Jimpy mouse brain. *J. Neurochem.* **1971**, 18,1529-1543.
79. Joerink, M.; Rindsjö, E.; van Riel, B.; Alm, J.; Papadogiannakis, N., Placental macrophage (Hofbauer cell) polarization is independent of maternal allergen-sensitization and presence of chorioamnionitis. *Placenta* **2011**, 32, 380-385.
80. Svensson, J.; Jenmalm, M. C.; Matussek, A.; Geffers, R.; Berg, G.; Ernerudh, J., Macrophages at the Fetal–Maternal Interface Express Markers of Alternative Activation and Are Induced by M-CSF and IL-10. *J. Immunol.* **2011**, 187, 3671-3682.
81. Brugger, B.; Erben, G.; Sandhoff, R.; Wieland, F. T.; Lehmann, W. D., Quantitative analysis of biological membrane lipids at the low picomole level by nano-electrospray ionization tandem mass spectrometry. *Proc. Natl. Acad. Sci. U. S. A.* **1997**, 94, 2339-2344.

82. Dennis, E. A.; Cao, J.; Hsu, Y. H.; Magrioti, V.; Kokotos, G., Phospholipase A2 enzymes, physical structure, biological function, disease implication, chemical inhibition, and therapeutic intervention. *Chem. Rev.* **2011**, 111, 6130-6185.
83. Funk, C. D., Prostaglandins and leukotrienes, advances in eicosanoid biology. *Science* **2001**, 294, 1871-1875.
84. Rouzer, C. A.; Ivanova, P. T.; Byrne, M. O.; Milne, S. B.; Marnett, L. J.; Brown, H. A., Lipid profiling reveals arachidonate deficiency in RAW264.7 cells, Structural and functional implications. *Biochemistry* **2006**, 45, 14795-14808.
85. Vlaeminck, B.; Fievez, V.; Cabrita, A. R. J.; Fonseca, A. J. M.; Dewhurst, R. J., Factors affecting odd- and branched-chain fatty acids in milk, A review. *Anim. Feed Sci. Technol.* **2006**, 131, 389-417.
86. Dennis, E. A.; Deems, R. A.; Harkewicz, R.; Quehenberger, O.; Brown, H. A.; *et.al.*, A mouse macrophage lipidome. *J. Biol. Chem.* **2010**, 285, 39976-39985.
87. Quehenberger, O.; Armando, A.; Dumlao, D.; Stephens, D. L.; Dennis, E. A., Lipidomics analysis of essential fatty acids in macrophages. *Prostaglandins Leukot. Essent. Fatty Acids* **2008**, 79, 123-129.
88. Delplanque, B.; Jacotot, B., Influence of environmental medium on fatty acid composition of human cells, leukocytes and fibroblasts. *Lipids*, **1987**, 22, 241-249.
89. Smith, F. B.; Kikkawa, Y.; Diglio, C. A.; Dalen, R. C.; Increased saturated phospholipid in cultured cells grown with linoleic acid. *In Vitro* **1982**, 18, 331-338.
90. Spector, A. A.; Kiser, R. E.; Denning, G. M.; Koh, S. W.; DeBault, L. E., Modification of the fatty acid composition of cultured human fibroblasts. *J. Lipid Res.* **1979**, 20, 536-547.
91. Stoll, L. L.; Spector, A. A., Changes in serum influence the fatty acid composition of established cell lines. *In Vitro* **1984**, 20, 732-738.
92. van den Elsen, L. W.; Nusse, Y.; Balvers, M.; Redegeld, F. A.; Knol, E. F.; Garssen, J.; Willemsen, L. E., n-3 Long-chain PUFA reduce allergy-related mediator release by human mast cells *in vitro* via inhibition of reactive oxygen species. *Br. J. Nutr.* **2013**, 109, 1821-1831.
93. Kroner, E. E.; Peskar, B. A.; Fischer, H.; Ferber, E., Control of arachidonic acid accumulation in bone marrow-derived macrophages by acyltransferases. *J. Biol. Chem.* **1981**, 256, 3690-3697.



94. Dalli, J.; Serhan, C. N., Specific lipid mediator signatures of human phagocytes, microparticles stimulate macrophage efferocytosis and pro-resolving mediators. *Blood* **2012**, 120, e60-72.
95. Rubio, J. M.; Rodriguez, J. P.; Gil-de-Gomez, L.; Guijas, C.; Balboa, M. A.; Balsinde, J., Group V secreted phospholipase A2 is upregulated by IL-4 in human macrophages and mediates phagocytosis via hydrolysis of ethanolamine phospholipids. *J. Immunol.* **2015**, 194, 3327-3339.
96. Balsinde, J.; Balboa, M. A.; Dennis, E. A., Functional coupling between secretory phospholipase A2 and cyclooxygenase-2 and its regulation by cytosolic group IV phospholipase A2. *Proc. Natl. Acad. Sci. U. S. A.* **1998**, 95, 7951-7956.
97. Kim, Y. J.; Kim, K. P.; Han, S. K.; Munoz, N. M.; Zhu, X.; Sano, H.; Leff, A. R.; Cho, W., Group V phospholipase A2 induces leukotriene biosynthesis in human neutrophils through the activation of group IVA phospholipase A2. *J. Biol. Chem.* **2002**, 277, 36479-36488.
98. Casas, J.; Meana, C.; Esquinas, E.; Valdearcos, M.; Pindado, J.; Balsinde, J.; Balboa, M. A.; 2009. Requirement of JNK-mediated phosphorylation for translocation of group IVA phospholipase A2 to phagosomes in human macrophages. *J. Immunol.* **2009**, 183, 2767-2774.
99. Takahashi, M.; Okazaki, H.; Ogata, Y.; Takeuchi, K.; Ikeda, U.; Shimada, K., Lysophosphatidylcholine induces apoptosis in human endothelial cells through a p38-mitogen-activated protein kinase-dependent mechanism. *Atherosclerosis* **2002**, 161, 387-394.
100. Munoz, N. M.; Kim, Y. J.; Meliton, A. Y.; Kim, K. P.; Han, S. K.; Boetticher, E.; O'Leary, E.; Myou, S.; Zhu, X.; Bonventre, J. V.; Leff, A. R.; Cho, W., Human group V phospholipase A2 induces group IVA phospholipase A2-independent cysteinyl leukotriene synthesis in human eosinophils. *J. Biol. Chem.* **2003**, 278, 38813-38820.
101. Ghosh, M.; Tucker, D. E.; Burchett, S. A.; Leslie, C. C., Properties of the Group IV phospholipase A2 family. *Prog. Lipid Res.* **2006**, 45, 487-510.
102. Fleetwood, A. J.; Dinh, H.; Cook, A. D.; Hertzog, P. J.; Hamilton, J. A., GM-CSF- and M-CSF-dependent macrophage phenotypes display differential dependence on Type I interferon signaling. *J. Leukocyte Biol.* **2009**, 86, 411-421.
103. Lacey, D. C.; Achuthan, A.; Fleetwood, A. J.; Dinh, H.; Roiniotis, J.; Scholz, G. M.; Chang, M. W.; Beckman, S. K.; Cook, A. D.; Hamilton, J. A., Defining GM-CSF- and macrophage-CSF-dependent macrophage responses by *in vitro* models. *J. Immunol.* **2012**, 188, 5752-5765.

104. Sierra-Filardi, E.; Nieto, C.; Dominguez-Soto, A.; Barroso, R.; Sanchez-Mateos, P.; Puig-Kroger, A.; Lopez-Bravo, M.; Joven, J.; Ardavin, C.; Rodriguez-Fernandez, J. L.; Sanchez-Torres, C.; Mellado, M.; Corbi, A. L., CCL2 shapes macrophage polarization by GM-CSF and M-CSF, identification of CCL2/CCR2-dependent gene expression profile. *J. Immunol.* **2014**, 192, 3858-3867.
105. Gomez Perdiguero, E.; Klapproth, K.; Schulz, C.; Busch, K.; Azzoni, E.; Crozet, L.; Garner, H.; Trouillet, C.; de Bruijn, M. F.; Geissmann, F.; Rodewald, H.-R., Tissue-resident macrophages originate from yolk-sac-derived erythro-myeloid progenitors. *Nature* **2015**, 518, 547-551.
106. Davies, L. C.; Jenkins, S. J.; Allen, J. E.; Taylor, P. R.; Tissue-resident macrophages. *Nature Immunol.* **2013**.14, 986-995.
107. Murray, P. J.; Allen, J. E.; Biswas, S. K.; Fisher, E. A.; Gilroy, D. W.; *et.al.*, Macrophage activation and polarization, nomenclature and experimental guidelines. *Immunity* **2014**, 41, 14-20.

## CHAPTER III

### METHODS FOR METABOLOME COVERAGE EXPANSION FOR UNTARGETED BIOMOLECULAR INTERROGATION

#### **3.1. Introduction**

With a declining trend in new drug approvals and a marked increase in the cost of drug development in recent years,<sup>1</sup> a paradigm shift in the current drug discovery pipeline is imminent. The estimated cost to bring a drug to market exceeds US \$1 billion dollars per drug (~\$0.8-1.8 billion), which is concurrent with a swell of alternative innovation for drug development testing using miniaturized 3D cell culture environments to mimic organ physiology.<sup>2</sup> When interconnected, these 3D cell-culture models provide a means to perform on-chip drug testing through monitoring mock-human organ functionality. The forthcoming integration of a system of organs into a human “circuit” will provide a potential realization of emulated human drug response.

However, a significant consideration for the determination of organ stability and homeostasis is how to best monitor organ health and the analytical implications that arise from determining organ response to stimuli. With certain organs, such as the heart, metrics such as contractility, morphology, or a small set of metabolic indicators are used to establish organ viability and status. However, many organs, such as the brain, gut, and liver, would benefit from the analytical means of monitoring organ fitness as a spectrum of descriptors, instead of a Boolean state. Additionally, mechanism-specific indicators would allow enhanced insight into off-target interactions and affected pathways, as opposed to monitoring generic indicators of organ failure, such as alanine transaminase

(ALT) or aspartate transaminase (AST) production. Certain bioreactor constructs preclude monitoring through optical microscopy, requiring alternative, non-invasive methods of interrogation. Congruently, morphology is often an all-or-none phenomenon, and organ stress and the dynamic nature of metabolic response are often not reflected.

Metabolic information can be obtained through monitoring of the fluctuations in small molecule production and consumption reflected in the medium of these mock-organ constructs through mass spectrometry-based methodologies.<sup>3</sup> This method, known as exometabolomic profiling, affords phenotypic insight of a system in a non-destructive manner.<sup>4</sup> As a result of the considerable interconnected nature of the metabolome, a small perturbation in the omic cascade can lead to propagated changes in the concentrations of many metabolites.<sup>5</sup>

Herein we present the analysis of temporal metabolic response of a perfused 3D four-compartment hollow-fiber membrane bioreactor grown with primary human liver cells to acetaminophen (para-acetylamino-phenol or APAP) and N-acetyl cysteine (NAC) exposure at different concentrations using ultraperformance liquid chromatography-ion mobility-mass spectrometry (UPLC-IM-MS) and self-organizing map (SOM) approaches to dynamic data analysis.<sup>6</sup> Using a metabolomics-based approach to liver bioreactor (LBR) interrogation, we demonstrate a method of interrogating organoid health, investigation of response to stimulus, and subsequent correlation to metabolic pathways. Liver response to, and metabolism of, APAP has been well-documented not only due to its wide use but also due to the high frequency of poisoning cases.<sup>7</sup> On the other hand, NAC is commonly used as antidote in APAP poisoning and prevents hepatic injury by restoring glutathione levels in the liver.<sup>8,9</sup> Thus, the combination of these two compounds

represents an appropriate system for study. Observed are small molecules, which are indicative of xenobiotic biotransformation, stimulus-specific and temporally-differential metabolic responses and dysregulation resulting from liver stress/damage. Significantly, many of these metabolic responses are observed in both dose-influenced and donor-dependent manner.

### **3.2. *Experimental***

#### *Bioreactor Fabrication and Seeding*

The 3D bioreactors used in this study (Stem Cell Systems, Germany) are made of four layers of hollow-fiber capillaries integrated into a polyurethane housing. Each hollow-fiber layer is composed of alternately arranged capillaries for gas perfusion (Mitsubishi, Japan) and medium perfusion (Micro PES®, Membrana, Germany). Cells are inoculated into the extra-capillary space serving as cell compartment (Figure 3.1). The capillary layers are arranged at an angle of 45° allowing for counter-current medium perfusion and decentralized gas exchange. The bioreactors are integrated into a tubing circuit with a total volume of 7 ml that allows for medium recirculation through the bioreactor, as well as fresh medium substitution and removal of used medium. Bioreactor cultures are maintained in a perfusion system (Stem Cell Systems, Germany) equipped with pumps for medium recirculation and medium feed, an electronically controlled heating unit and electronically operated gas valves (Vögtlin Instruments, Aesch, Switzerland) for regulation of the gas mixture (air, CO<sub>2</sub>) and gas supply rates..

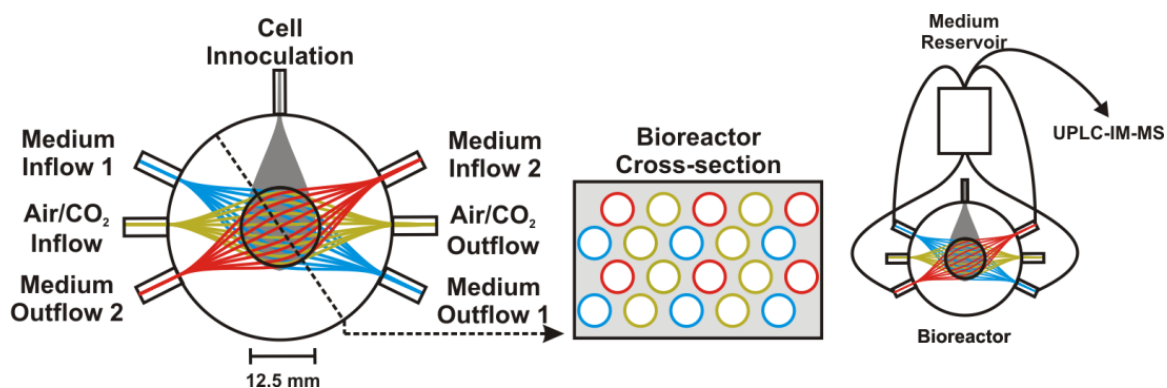


**Figure 3.1.** Configuration of artificial capillaries inside the bioreactor. The capillary bed consists of four capillary layers arranged on top of each other. Each layer is composed of medium perfusion capillaries belonging to two independent capillary systems (red and blue), which are counter-currently perfused to enhance mass exchange. Medium perfusion fibers alternate with capillaries for gas perfusion (yellow). Transparent lids at the bottom and the top of the cell compartment allow for observation of the cells seeded in the extra-capillary space (gray region). Media is recirculated through a pump module, and aliquots are extracted from the reservoir for UPLC-IM-MS analysis.

Each bioreactor was filled each with 10 million primary human hepatocytes from a unique donor. A total of 9 bioreactors with cells from 3 different donors were used for this study. Cells were isolated from tissue remaining from partial liver resection with agreement of the donors and with approval of the local ethical committee. Cell isolation was performed by collagenase digestion according to Damm et al.<sup>10</sup> The gained cell suspension was not further purified to avoid a loss of non-parenchymal cell fractions. The cell viability after isolation was 76-85% as determined by their capacity to exclude trypan blue.

#### *Bioreactor culture operation*

Bioreactors were perfused with Heparmed culture medium (Vito 143, Biochrom, Germany), a modification of Williams' Medium E specifically developed for serum-free perfusion culture of high-density 3D liver cell cultures. The medium was supplemented prior to use with 20 IU/L insulin, 5 mg/L transferrin, 3 mg/L glucagon, 100,000 U/L penicillin and 100 mg/L streptomycin (all purchased from Biochrom). Culture medium was recirculated at a rate of 1 ml /min, fresh medium was continuously fed into the perfusion circuit at a rate of 0.6 ml/h for the first 24 hours followed by 0.2 ml/h until the end of culture. Used medium was removed accordingly. The pH value in the recirculating medium was kept between 7.35 and 7.45 by adjusting the CO<sub>2</sub> concentration in the supplied gas mixture.

### *Chemical stimulus comparisons*

Cells from three different donors (Table 3.1) were loaded into 9 bioreactors (3 bioreactors for each donor) and treated with different drug cocktails (composition and concentration). Three different time courses were performed for each donor set of liver bioreactors. A control (no stimuli) and two different chemical stimuli were performed, ensuring biological replicates for the different conditions. The different conditions are summarized in Table 3.1. The exact time course can be seen in Figure C.1.

Drug application was started on culture day 3. APAP (Sigma-Aldrich, USA) and NAC (Sigma-Aldrich, USA) were dissolved in methanol. Subsequently the methanol was evaporated and the substance was resolved in culture medium. Drug incubation was initiated by adding 1 ml of a 7x concentrated solution (bolus application) to reach the desired final solution of each drug. Subsequently drug cocktails added to the fresh medium were continuously infused into the perfusion circuit.

### *Sample Collection and Processing*

In order to monitor the cell viability and functionality in the bioreactors, the release of intracellular enzymes alanine transaminase (ALT), aspartate transaminase (AST) and lactate dehydrogenase (LDH) were measured daily throughout the entire culture period in samples from the culture perfusate using an automated clinical chemistry analyzer (Cobas® 800, Roche Diagnostics, Germany).

For UPLC-IM-MS analysis additional samples from recirculating culture media were collected at set intervals during drug exposure. 100 µL aliquots were collected immediately prior to exposure for all experiments and then at 15 and 30 minutes, 1, 2, 6,



**Table 3.1.** Drug exposures to different liver bioreactors

LBR #	Patient gender (age)	APAP [mM]	NAC [mM]
1	male (64)	10	-
2	male (64)	5	-
3	male (64)	-	-
4	male (77)	10	-
5	male (77)	10	10
6	male (77)	-	-
7	female (47)	-	-
8	female (47)	5	10
9	female (47)	5	-

24 and 72 hours after drug exposure. 50  $\mu\text{L}$  from each aliquot were treated with 3:1 volume of cold ( $-20\text{ }^{\circ}\text{C}$ ) MeOH, vortexed for 15 seconds, and spun for 10 minutes at 14,500 rpm at  $4\text{ }^{\circ}\text{C}$ . 100  $\mu\text{L}$  aliquots were then extracted, avoiding the precipitated pellet, and samples were dried down in a SpeedVac. Samples were stored at  $-80^{\circ}\text{C}$  and reconstituted in 80:20 ACN:H<sub>2</sub>O shortly prior to analysis. The single exposure samples were reconstituted in 10  $\mu\text{L}$  aliquots were taken from each sample and pooled into a quality control sample, which is used as platform stability diagnostic.

#### *Data Acquisition and Processing*

UPLC-IM-MS<sup>E</sup> data acquisition was performed with a nanoAcquity LC-system coupled to a Synapt G2 HDMS mass spectrometer both from Waters Co. (Milford, MA). Samples were analyzed with hydrophilic interaction liquid chromatography (HILIC) and a 1x100 mm 1.7  $\mu\text{m}$  particle BEH Amide column (Waters Co.) was used. The mobile phase was composed of A = 10mM ammonium acetate + 0.1% formic acid in 90% ACN and B = 10mM ammonium acetate + 0.1% formic acid in 10% ACN. The initial solvent composition at 100  $\mu\text{L}/\text{min}$  was 87.5% A, which was held for 1 min and decreased to 62.5% over the next 3 minutes and held for 6 minutes. Then the composition of A was decreased to 50% and held for 2 minutes and returned to 87.5% and held for 10 minutes for equilibration. An autosampler was used for sample injection and held at  $4\text{ }^{\circ}\text{C}$ , with a loop size of 5  $\mu\text{L}$ .

IM-MS<sup>E</sup> spectra were acquired at a rate of 2Hz from 50-1400 Da in positive mode for the duration of the injection. The instrument was calibrated to greater than 1 ppm mass accuracy using sodium formate clusters prior to analysis. A two-point internal

standard of leucine enkephalin was infused in parallel at a flow rate of 7 $\mu$ L/min and acquired every 10 seconds. IM-MS conditions were as follows: source temperature, 80 °C; capillary, +3.5 kV; desolvation gas flow, 400 L/hr; and desolvation gas temperature, 150 °C, respectively. The sampling cone was held at a setting of 35.0, with the extraction cone at a setting of 4.0. In the MS<sup>E</sup> configuration, low and high energy spectra are acquired for each scan. High energy data performed a collision energy profile from 10-30 eV in the transfer region, providing post-mobility fragmentation. Ion mobility separations were performed with a wave velocity of 550 m/s, a wave height of 40.0 V, and a nitrogen gas flow of 90 mL/min, with the helium cell flow rate at 180mL/min. Internal calibrant correction was performed post acquisition.

Data were converted to mzXML format using the msconvert tool from the ProteoWizard package.<sup>11</sup> Peak picking and alignment were performed using XCMS in R.<sup>12</sup> The resulting data matrix contained 2691 detected features. Prior to SOM, analytical triplicates were averaged. Subsequently, the data was formatted for analysis using SOM with a grid of 30x31, 100 first phase training iterations and 180 in the second phase. An initial training radius of 8.0 was defined with a learning factor of 0.5, a neighborhood block size of 4, and a conscience of 3.0. For the second phase, a neighborhood radius of 2.0, learning factor of 0.05, neighborhood block size of 2, and conscience of 3.0 was defined. A random seed of 1 with a Pearson's correlation distance metric and random selection initialization was used.

### *Peak Identification*

Peak identifications were performed using accurate masses to search MELTIN,<sup>13</sup> LIPID MAPS,<sup>14</sup> and HMDB databases.<sup>15, 16</sup> Additionally, other literature sources were used for fragmentation spectra.<sup>17, 18</sup> When appropriate, adduct identities were inferred from spectral data. Fragmentation spectra were extracted using ion mobility separation to extract product ions specific to the analyte of interest, and these spectra were used to aid and confirm identifications, both through manual interpretation and comparison with database and literature fragmentation spectra, when available. For spectral interpretations of putative identified metabolites and fold changes, further information can be found in Appendix C.

### **3.3. Results and Discussion**

#### *Bioreactor Description*

The described 3D four-compartment hollow-fiber membrane bioreactor technology supports the high-density culture of primary human hepatocytes in a perfused environment. The creation of an artificial capillary bed made of four layers of capillaries, which each dispose of alternating medium and gas perfusion fibers allows for decentralized nutrient supply and metabolite removal, mimicking a highly-vascularized construct. Previously the sustained functionality of primary liver cells grown within the bioreactor has been reported, in addition to the formation of physiologically relevant liver constructs, including bile ducts, vascular structures and Kupffer cell distribution similar to native liver tissue *in vivo*.<sup>19</sup> Primary human hepatocytes cultivated in the bioreactor showed a better preservation of metabolic activities as compared to conventional 2D

cultures.<sup>20</sup> Moreover, the technology permits serum-free culture of primary liver cells without functional impairment,<sup>21</sup> which is advantageous for complex medium analyses. Due to the possibility of varying the perfusion flow and mode, different ways of drug application can be realized, including continuous infusion, closed-circuit incubation and single-pass application.

In this study, the effect on bioreactor cultures of primary human liver cells of APAP and NAC exposure were investigated on the basis of metabolites measured in the recirculating media. APAP was applied in two different concentrations, 5 and 10 mM, in order to detect possible effects of varying the drug concentrations. On the other hand NAC was applied at a constant concentration (10 mM) with both APAP concentrations. A commensurate concentration of the drugs applied was spiked into the media reservoir to achieve immediately either 5 or 10 mM APAP and 10 mM NAC. In addition the fresh medium used for supplementation was changed to drug containing medium, whereas the control bioreactor medium was changed, but no drug administered.

To investigate a possible influence of APAP on the cell integrity as well as the preventive function of NAC in APAP induced hepatic injury the liver enzymes AST, ALT and LDH were measured on a daily basis. Enzyme kinetics showed no significant changes upon drug application indicating no disturbance of membrane integrity.

### ***3.3.1. Metabolic Perturbations***

The exometabolomic effects of APAP exposure upon the liver bioreactor metabolome were investigated through analysis of media perfusate. We selected APAP and NAC based upon the comprehensive toxicological understanding already in place.

This provides a foundation to evaluate both i) bioreactor efficacy in emulating *in vivo* liver functionality and stability, and ii) the utility of the application of the proposed analytical methodologies to interrogate temporal perturbations in apparent metabolic phenotype. However, the data analysis for this system was approached in an untargeted manner, similar to the method for studying an unknown chemical.

### **3.3.2. *Self-organized Maps***

This SOM-based methodology is a data-driven organization of metabolic features based upon underlying patterns in the data, which uses unsupervised learning to create a low-dimensional projection of the data. This is a type of artificial neural network, which does not sacrifice the conditional and temporal connectivity of metabolic features in data depiction. For a comprehensive understanding of SOM analytics, we direct the reader to references 6 and 22. Conceptually, metabolites are grouped based upon similarities in production/consumption in response to both sampling time and chemical exposure. Metabolite locations in the grid are then used to depict samples based upon the intensities of these metabolites. As a result, heat maps of correlated metabolic features are generated for each sample condition. These heat maps can then be averaged across technical replicates and differential analyses are performed with time-matched controls, yielding regions of interest (ROI) with metabolites, which are dysregulated. These prioritized metabolites are then putatively identified through database searching, using accurate mass information and fragmentation data when standard reference material is not readily available. A primary advantage of utilizing a SOM-based approach for data analysis is

the ability to represent and cluster features, which have similar conditional and temporal intensities.

Figure 3.2 demonstrates the temporal metabolomic differences of biological replicates resulting from different APAP concentration exposure (Figure 3.2 (A, B) and Figure 3.2 (C, D) correspond to 10 and 5 mM APAP treatment respectively). The upper heat map time course represents metabolites that are found in increased abundances (red regions) when compared to the average control profile (days 3-5). The lower heat map time course displays the opposite, with red regions corresponding to metabolites that are found in decreased abundance as a result of APAP exposure. The corresponding intensity scale is shown on the right, and the number of peaks corresponding to each grid location is described in the metabolite density plot. These time courses demonstrate the temporal extracellular metabolic changes. Prior to APAP administration, the metabolic profiles of the experimental and control bioreactors loaded with cells from the same donor show strong similarities, but also, some small differences across time points can be apparent. This illustrates the metabolic signatures of cell adaptation to the new environment (Figure C.2). Immediately after APAP exposure, large differences appear, and persist throughout the time course, with the emergence and accumulation of other metabolite clusters prioritized through differential analysis. Furthermore, the effects of NAC as antidote during APAP can be observed in Figure 3.3. Similarly to the heat maps in Figure 3.2, the upper and lower heat maps represent increased and decreased metabolites also when compared to the average control profiles. In this treatment other regions are highlighted in addition to the regions highlighted during APAP treatment (Figure. 3.2).

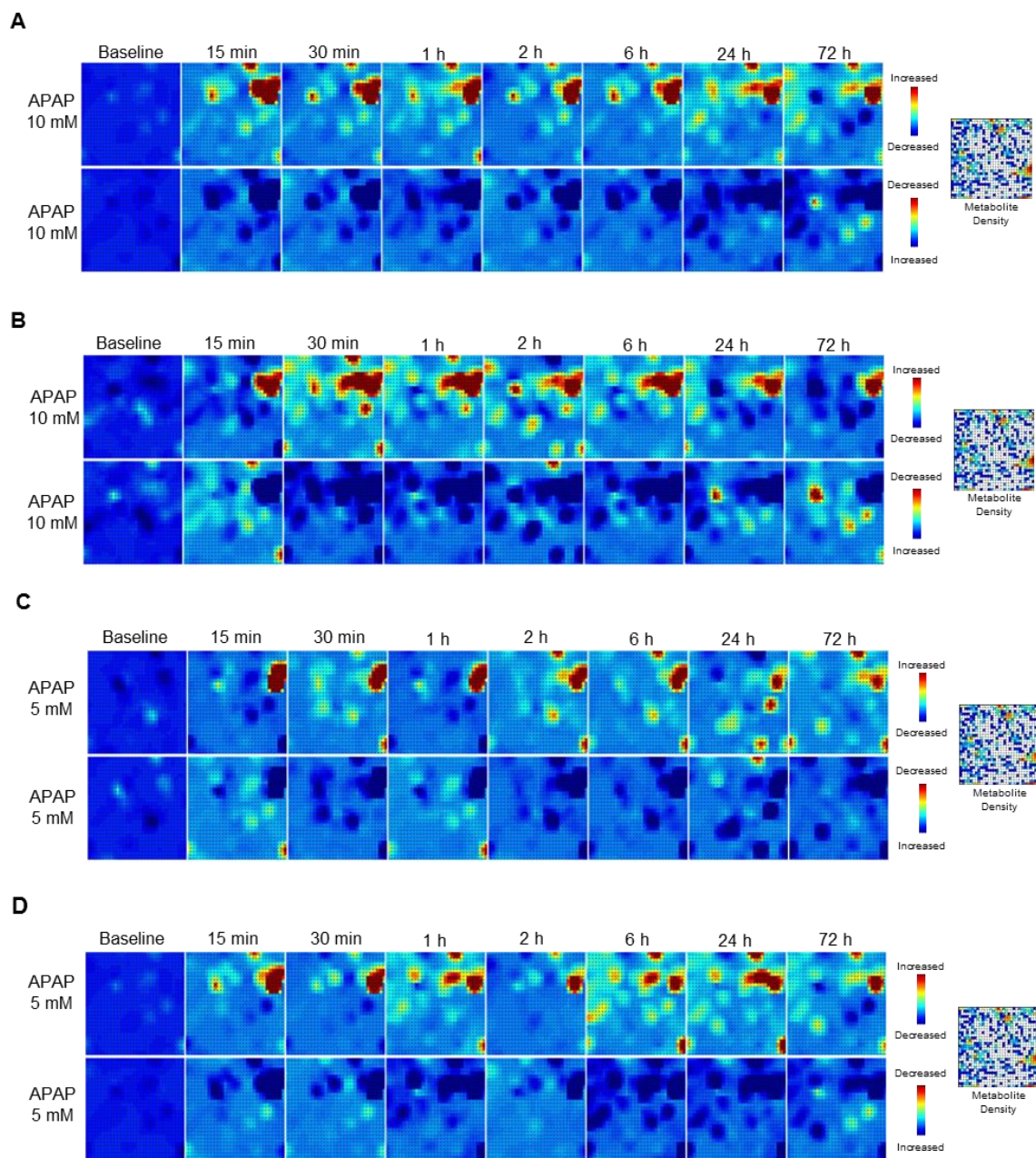


**Figure 3.2.** A) and B) SOM of 10 mM APAP exposure to cells from 2 different donors (64 and 77 years respectively). C) and D) SOM of 5 mM APAP exposure to cells from 2 different donors (47 and 64 years respectively). Features whose intensity increased and decreased relative to the corresponding control following APAP exposure are depicted in top and bottom rows respectively. The metabolite density plot depicts the number of peaks associated with a grid location.



A representation of the 10 mM APAP and 5 mM APAP + 10 mM NAC treated metabolic temporal profiles are depicted in Figure 3.3 (A) and (B) respectively. These result in other regions of metabolites with increased abundances (red and yellow). The relative number of metabolites per grid location is depicted in the metabolite density map in Figure 3.4 (C). These heat maps are the 72 hour and 30 minutes exposure time-points, baseline subtracted with the average control profiles of their respective bioreactors (control LBR with inoculated with cells from same donor). The immediately apparent region of interest 1 (ROI 1) of high intensity corresponds directly to APAP and 3,3'-Biacetaminophen (Bi-APAP) (Figure 3.4 (A)). The formation of Bi-APAP occurs rapidly, giving rise to a time profile similar to the parent drug. Additionally, other regions (ROI 2 and 3) can be observed on the edges of the map corresponding to phenylalanine and arginine respectively. The gradual appearance of region 4 corresponds to other APAP metabolites such as APAP-sulfate and APAP-glucuronide, which are metabolized for APAP secretion.<sup>17</sup> The different location on the heat map is due to the different time profile of these metabolites during the time courses. As previously mentioned, the effect of NAC in the metabolome is highlighted in other ROI's (Figure. 3.4 (B)). Regions 7 and 8 are only present when the cells are exposed to NAC and the metabolites identified in these regions are closely related to NAC metabolism. In region 7, the oxidized form of NAC (Ox-NAC) is found, while the product of both drugs (APAP and NAC) is highlighted in region 8. Interestingly other compounds in the media are highlighted in regions 5-8. These compounds correspond to different antibiotics such as penicillin G and streptomycin, which are used to prevent bacterial infection in the LBR during experiments. Region 5 corresponds to penicillin G and streptomycin-cysteine can be

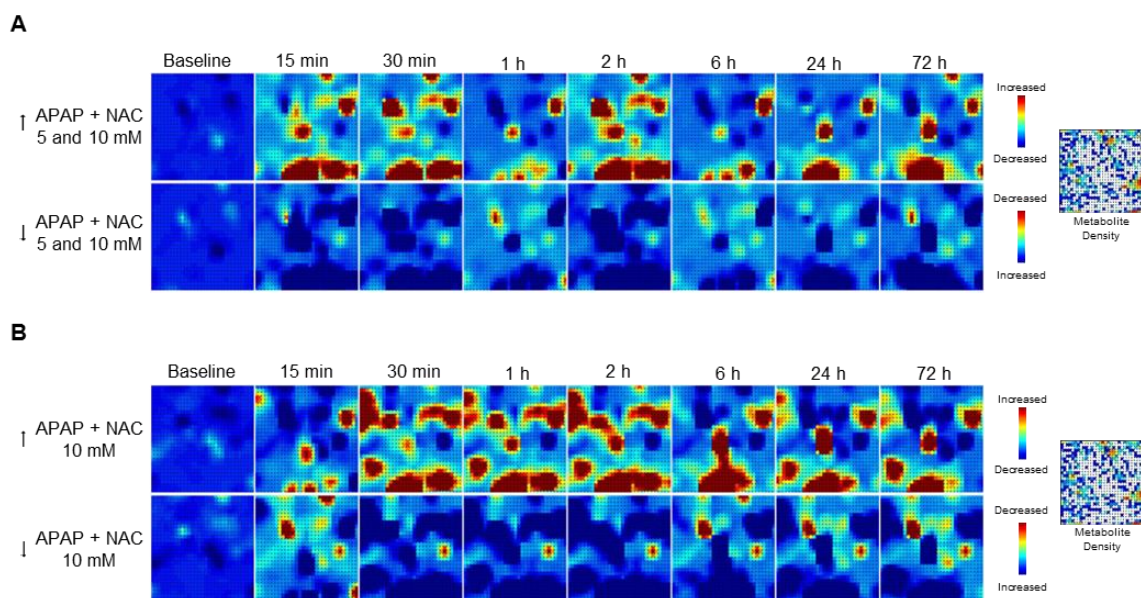


**Figure 3.3.** A) SOM of 5 mM APAP + 10 mM NAC exposure to cells (47 years). B) SOM of 10 mM APAP + 10 mM NAC exposure to cells (77 years). Features whose intensity increased and decreased relative to the corresponding control following APAP exposure are depicted in top and bottom rows respectively. The metabolite density plot depicts the number of peaks associated with a grid location.

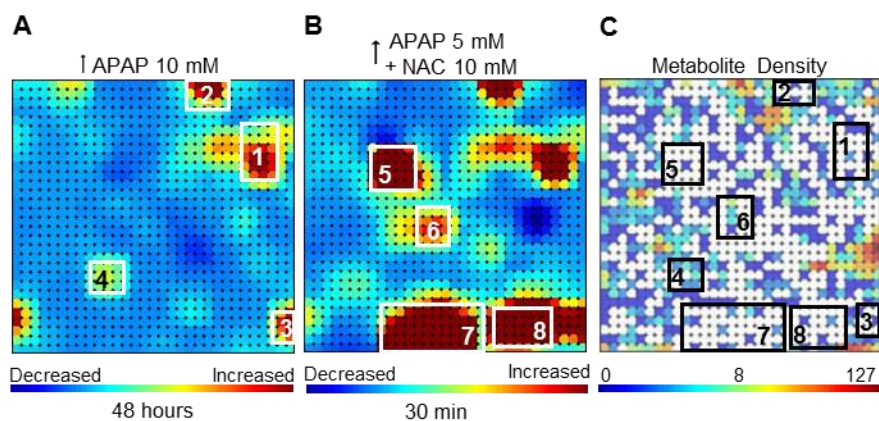


**Figure 3.4.** A) and B) Differential metabolic profiles depicting metabolites with elevated abundances in different ROI for 10 mM APAP exposed bioreactor, and metabolites with increased abundances for 5 mM APAP + 10 mM NAC exposed bioreactor respectively. The metabolite density plot indicates the numbers of peaks residing in the corresponding grid location (C).

observed in region 6. Interactions of antibiotics with thiol containing compounds have been previously reported.<sup>23-27</sup> We observe different dynamics of these reactions in regions 6, 7 and 8, where cysteine and NAC reacted with streptomycin and penicillin G. The different metabolites and their corresponding ROI are summarized in Table 3.2.

### **3.3.3 *Temporal metabolic signatures in APAP toxicity***

The extremely complex and highly dynamic changes of the hepatic metabolome during chemical stimuli represent a difficult challenge in the data analysis process. However, a general sense of the metabolomic profile during time course experiments can be visualized by SOM (Figures. 3.2 and 3.3). The increase and decrease of metabolites seeded in a particular ROI can be easily visualized by monitoring the color changes throughout the different time points. In Figure 3.5, these changes can be observed for a selected group of metabolites with different time profiles. Their time dependent differences are not only associated with both APAP and NAC exposure but also with the origin of the inoculated cells (donor). Variation in the production and consumption of some molecular species were observed in experiments conducted at equivalent conditions other than donor cells (biological replicates). In order to compensate for the differences in metabolism between the three donors, the highest relative intensity of a particular metabolite for all bioreactors from the same donor was set to 100% and all other intensities with their corresponding standard deviations (error bars) were normalized accordingly. It should be noted that this calculation was performed only for these plots (Figure. 3.5 and Figures. C.3-C.5) for visualization purposes and direct abundancy comparisons between different donors would be inaccurate. However, it allows us to

**Table 3.2.** Metabolites from ROIs in single chemical stimulus indicated in Figure 3.4.

Metabolite	ROI
APAP	1
3,3'-Biacetaminophen	1
Phenylalanine	2
Arginine	3
APAP-sulfate	4
APAP-glucuronide	4
Penicillin G	5
Streptomycin -cysteine	6
Ox-NAC	7
Penicillin G- cysteine	7
APAP-NAC	8
Penicillin G-NAC	8

examine time profiles of different donors at both equal and distinct conditions. Time points from different donors are represented by different marks (male 77-circles, male 64-triangles and female 47-squares), APAP exposure was color coded (10mM, 5 mM and controls are blue, red and black respectively) and the administration of NAC (10 mM) was differentiated with dashed lines. The rapid appearance of APAP and Bi-APAP (Figure 3.5 (A) and (B)) is similar for all biological replicates (same conditions but different donor). Additionally, a dose dependent decrease is observed for APAP, with 5mM being consumed at a faster rate than 10mM (red and blue triangles). Interesting but not surprising is the effect of NAC administration in the formation of Bi-APAP, which is formed through reactive oxygen species (ROS).<sup>28</sup> As mentioned above, the function of NAC in APAP toxicity is to replenish the glutathione levels, which one of its many functions is the protection of cells from toxic reactive oxygen compounds.<sup>29</sup> The levels of Bi-APAP are significantly lower when NAC is administered conjointly with APAP at two different compositions (blue circles and red squares). Changes in the concentration of NAC can be observed by monitoring the oxidized form of NAC (Ox-NAC), which occurs with the formation of a disulfide bond between two NAC molecules (Figure 3.5 (C)). This oxidation took place in standard reference material as well (data not shown). Here, distinctive profiles are observed for the liver bioreactors treated with same NAC but different APAP concentration, where more irregular changes in the lower APAP concentration (red squares). The conversion of APAP into the reactive electrophile, *N*-acetyl-*p*-benzoquinone imine (NAPQI), by P450-mediated reactions causes the depletion of glutathione and covalent binding (arylation) to macromolecules.<sup>30</sup> This leads to damage to mitochondria, cell membranes and nuclei, perturbation of vital cell signaling

and finally necrosis and apoptosis.<sup>31</sup> The formation of APAP-NAC (Figure 3.5 (D)) is a process of multiple reactions including P450-mediated bioactivation and has been previously detected in untreated human urine samples.<sup>17, 32</sup> Small profile differences between the NAC treated LBRs (blue circles and red squares with dashed lines) are observed at 30 and 60 minutes after drug exposure, which could be attributed to both varying concentrations and metabolic activity. On the other hand, the levels drop similarly over time after 2 hours. Other major urinary metabolites such as APAP-sulfate (Figure 3.5 (E)) and APAP-glucuronide (Figure C.3) were detected in all APAP exposed LBRs. It is believed that the purpose of these compounds is to facilitate the elimination of APAP due to their increased water solubility.<sup>8</sup> The slightly delayed formation of APAP-sulfate (6 hours) compared to other APAP metabolites lead to the grouping in ROI 4. Interestingly, several trends are observed during the time course measurements. i) higher concentrations are detected at lower APAP concentration (blue and red triangles), ii) the levels of APAP-sulfate at 10 mM APAP exposure drop between the last two time points (last 48 hours) with 2 different donors (blue circles and triangles) and with the exposure of NAC (blue circles with dashed line) and iii) the addition of NAC has a direct proportional effect on the production of APAP-sulfate (blue circles and red squares). These trends can be explained by the toxic effects of APAP at higher concentrations over time and the protective properties of NAC in the liver. Similar trends were observed for APAP-glucuronide except for earlier detection (2 hours) at 10 mM APAP and NAC (blue circles dashed line) and lower abundance at 5 mM APAP + 10 mM NAC when compared to 5 mM APAP (red squares). These differences suggest different activities and susceptibilities of sulfotransferase and uridine diphosphoglucuronosyltransferase.<sup>33</sup>

Additional metabolic perturbations during stimuli were caused by thiol containing compounds, antibiotics in particular. Streptomycin-cysteine (Strep.-Cys.) was detected only in NAC treated bioreactors and different dynamics can be observed in Figure 3.5 (F) between different concentrations. These interactions, which can result in antibacterial inactivation, have been observed both *in vitro* and *in vivo*.<sup>23, 24</sup> Further, penicillin G compounds also formed oxidized thiol compounds with cysteine and NAC causing the level of penicillin G to drop considerably, especially when NAC was used (Figure C.4). A comprehensive interpretation of these highly dynamic exometabolic interrogations is not possible at the moment and attributing all the trends and effects to a mechanism or pathway would be premature.

Both gradual and drastic changes in the exometabolome after drug exposure represent a challenge in the monitoring of bioreactor status. Molecular signatures with relative consistent signal or narrow fluctuations have the potential to be early indicators of liver bioreactor health in dynamic experiments, provided a high signal-to-noise ratio is present. Initially, the depletion of antibiotics would suggest microorganism invasion of the bioreactor or some type of biotransformation. However, non-biological processes can be the source of these changes as well. During our experiments we observed phenylalanine (ROI 2) to fluctuate within a narrow range and no apparent correlation to stimuli at all conditions (Figure C5). Similarly, arginine (ROI 3) showed no correlation to stimuli but wider fluctuations proved phenylalanine a better indicator of liver bioreactor health. On the other hand, this could potentially change in future experiments, especially if different chemical compounds are studied.



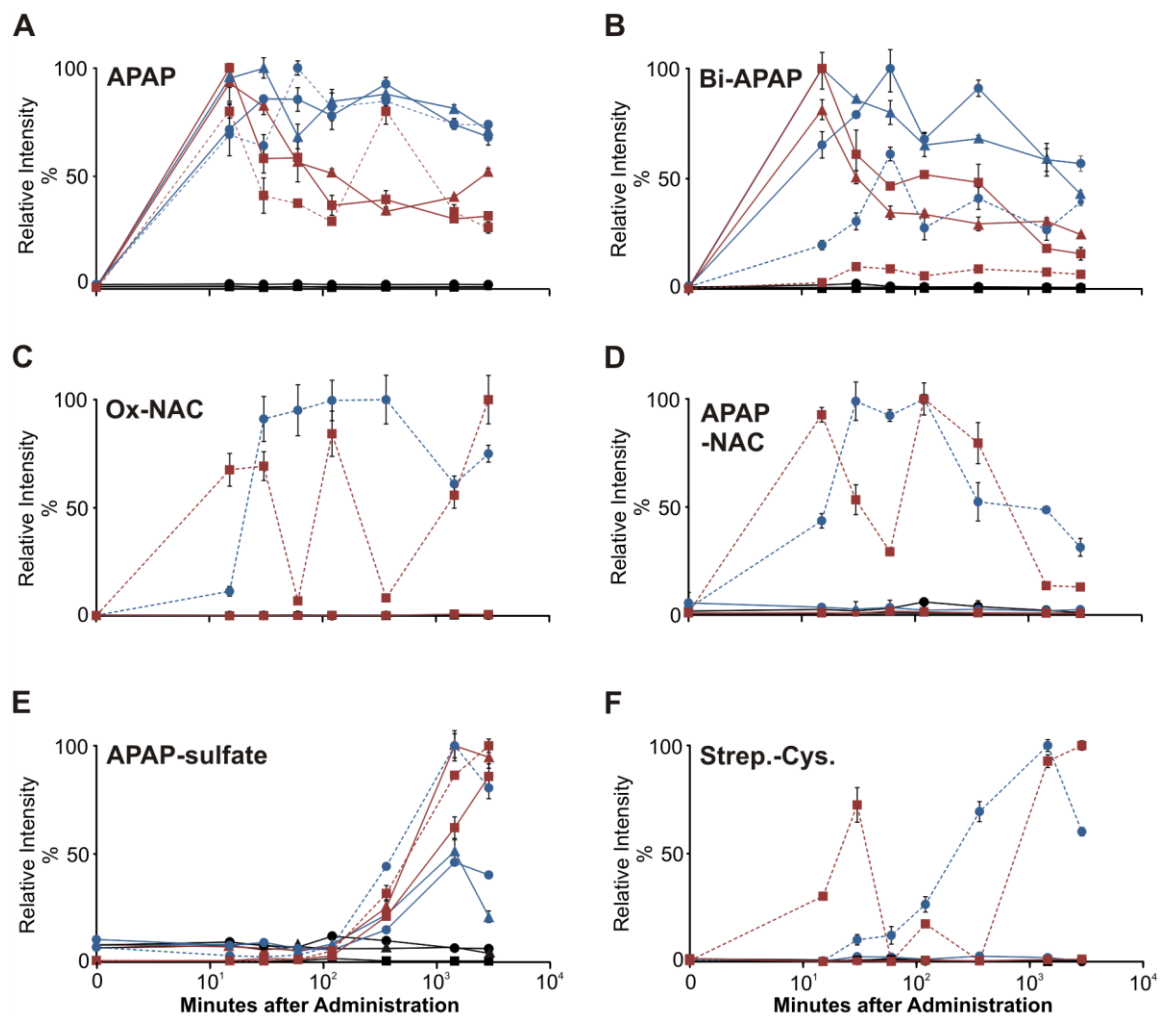


**Figure 3.5.** Selected metabolites time profiles after drug exposure with relative intensity calculated to maximum value measured in liver bioreactors inoculated with cells from the same donor. Donor age 77 (circles), 64 (triangles) and 47 (squares). Control (black), 10 mM APAP (blue), 5mM APAP (red). 10 mM NAC (dashed line). A) APAP and B) Bi-APAP were seeded in region 1 and show similar profiles. C) Ox-NAC and D) APAP-NAC are only present in LBRs treated with NAC (region 7 and 8 respectively). E) APAP-sulfate (ROI 4) is detected only after 6 hours of drug exposure. F) Streptomycin-Cysteine (Strep.-Cys.) detected in NAC treated LBRs was seeded in ROI 6.

### **3.4. Conclusions**

In this work we describe the implementation and analysis of the effects of APAP and NAC exposure on a surrogate liver bioreactor construct. This study provides a basis for the interrogation of bioreactor health and status by exometabolomic profiling. Through UPLC-IM-MS analysis of bioreactor effluent, we perform temporally resolved diagnostics of bioreactor health in a non-destructive manner. These preliminary data serve as a training set for the eventual extension as a diagnostic with high temporal resolution and extending beyond alive/dead assays. A set of metabolic signatures indicative of organ status for all organoids will be developed, allowing for on-line monitoring through targeted analyses. We apply a self-organizing map-based approach to clustering temporally covarying metabolites into regions of interest for further identification. This approach is used to distinguish the metabolomic response of liver organs mimic to varied doses of APAP and NAC inoculated with cells from different donors. Furthermore, similarities and differences between biological replicates not only further evidence the complexity of exometabolic responses but also support the organ-mimic capabilities of our 3D hepatocyte bioreactor. This method will next be applied to other liver toxins, and then extended to the heart, lungs, gut, and kidneys, leading to the eventual integration of all organs into a mock-human for pre-clinical drug testing.

#### ***4.5. Acknowledgements***

This chapter contains the research article: Montenegro-Burke, J.R.; Goodwin, C.R.; Knöspel, F.; Gerstmann, F.; Zeilinger, K.; Storch, L.; Damm, G.; Sherrod, S.; Iyer, S.; Iyer, R.; Wikswo, J.P. McLean, J.A.; Towards the Development of a  $\mu$ Human: Dynamic Exo-metabolomic Response Analysis of 3-Dimensional Hepatocyte Bioreactor to Acetaminophen and N-acetyl Cysteine Exposure, In preparation for *Analytical Chemistry*.

This work was supported in part by NIH grant RC2DA028981, the U.S. Defense Threat Reduction Agency grants HDTRA1-09-1-0013 and DTRA 100271 A-5196, the Vanderbilt Institute for Integrative Biosystems Research and Education, the Vanderbilt Institute of Chemical Biology, and the Systems Biology and Bioengineering Undergraduate Research Experience funded by Gideon Searle at Vanderbilt University. We thank Nolan Smith for his technical assistance.

#### 4.6. References

1. Kaitin, K. I. Deconstructing the Drug Development Process: The New Face of Innovation. *Clin. Pharmacol. Ther.* **2010**, 87, 356-361.
2. Huh, D.; Hamilton, G. A.; Ingber, D. E. From 3D cell culture to organs-on-chips. *Trends Cell Biol.* **2011**, 21, 745-754.
3. Patti, G. J., Yanes, O.; Siuzdak, G., Innovation, Metabolomics, the apogee of the omics trilogy. *Nat. Rev. Mol. Cell Biol.* **2012**, 13, 263-269.
4. Dunn, W. B.; Broadhurst, D. I.; Atherton, H. J.; Goodacre, R.; Griffin, J. L. Systems level studies of mammalian metabolomes: the roles of mass spectrometry and nuclear magnetic resonance spectroscopy. *Chem. Soc. Rev.* **2011**, 40, 387-426.
5. Nielsen, J.; Oliver, S. The next wave in metabolome analysis. *Trends Biotechnol.* **2005**, 23, 544-546.
6. Eichler, G. S.; Huang, S.; Ingber, D. E. Gene Expression Dynamics Inspector (GEDDI) for integrative analysis of expression profiles. *Bioinformatics*, **2003**, 19, 2321-2322.
7. Bajt, M. L.; Knight, T. R.; Lemasters, J. J. Jaeschke, H. Acetaminophen-induced oxidant stress and cell injury in cultured mouse hepatocytes: protection by N-acetyl cysteine. *Toxicol. Sci.* **2004**, 80, 343-349.
8. Bessems, J. G. M.; Vermeulen, N. P. E. Paracetamol (acetaminophen)-induced toxicity: molecular and biochemical mechanisms, analogues and protective approaches. *Crit. Rev. Toxicol.* **2001**, 31, 55-138.
9. Corcoran, G. B.; Wong, B. K. Role of glutathione in prevention of acetaminophen-induced hepatotoxicity by N-acetyl-L-cysteine *in vivo*: studies with N-acetyl-D-cysteine in mice. *J. Pharmacol. Ex. Ther.* **1986**, 238, 54-61.
10. Damm, G.; Pfeiffer, E.; Burkhardt, B.; Vermehren, J.; Nüssler, A. K.; Weiss, T. S. Human parenchymal and non-parenchymal liver cell isolation, culture and characterization. *Hepatology Int.* **2013**, 7, 951-958.
11. Kessner, D.; Chambers, M.; Burke, R.; Agus, D.; Mallick, P. Proteowizard: open source software for rapid proteomics tools development. *Bioinformatics*, **2008**, 24, 2534-2536.
12. Smith, C. A.; Want, E. J.; O'Maille, G.; Abagyan, R.; Siuzdak, G., XCMS, processing mass spectrometry data for metabolite profiling using nonlinear peak alignment, matching, and identification. *Anal. Chem.* **2006**, 78, 779-787.

13. Smith, C. A.; Maille, G. O.; Want, E. J.; Qin, C.; Trauger, S. A.; Brandon, T. R.; Custodio, D. E.; Abagyan, R.; Siuzdak, G., 2005. METLIN, A Metabolite Mass Spectral Database. *Ther. Drug Monit.* **2005**, *27*, 747-751.
14. Sud, M.; Fahy, E.; Cotter, D.; Brown, A.; Dennis, E. A.; Glass, C. K.; Merrill Jr, A. H.; Murphy, R.C.; H. Raetz, C. R.; Russell, D. W., LMSD, LIPID MAPS structure database. *Nucleic. Acids. Res.* **2007**, *35*, D527-532.
15. Wishart, D. S.; Knox, C.; Guo, A. C.; Eisner, R.; Young, N.; Gautam, B.; Hau, D. D.; Psychogios, N.; Dong, E.; Bouatra, S. HMDB: a knowledgebase for the human metabolome. *Nucleic. Acids. Res.* **2009**, *37*, D603-D610.
16. Wishart, D. S.; Tzur, D.; Knox, C.; Eisner, R.; Guo, A. C.; Young, N.; Cheng, D.; Jewell, K.; Arndt, D.; Sawhney, S. HMDB: the human metabolome database. *Nucleic. Acids. Res.* **2007**, *35*, D521-D526.
17. Chen, C.; Krausz, K. W.; Idle, J. R.; Gonzalez, F. J. Identification of novel toxicity-associated metabolites by metabolomics and mass isotopomer analysis of acetaminophen metabolism in wild-type and Cyp2e1-null mice. *J. Biol. Chem.* **2008**, *283*, 4543-4559.
18. Straub, R. F.; Voyksner, R. D. Determination of penicillin G, ampicillin, amoxicillin, cloxacilin and cephapirin by high-performance liquid chromatography-electrospray mass spectrometry. *J. Chromatogr. A*, **1993**, *647*, 167-181.
19. Zeilinger, K.; Schreiter, T.; Darnell, M.; Soderdahl, T.; Lübberstedt, M.; Dillner, B.; Knobloch, D.; Nüssler, A. K.; Gerlach, J. C.; Andersson, T. B. Scaling down of a clinical three-dimensional perfusion multicompartement hollow fiber liver bioreactor developed for extracorporeal liver support to an analytical scale device useful for hepatic pharmacological *in vitro* studies. *Tissue Eng., Part C*, **2011**, *17*, 549-556.
20. Hoffmann, S. A.; Müller-Vieira, U.; Biemel, K.; Knobloch, D.; Heydel, S.; Lübberstedt, M.; Nüssler, A. K.; Andersson, T. B.; Gerlach, J. C.; Zeilinger, K. Analysis of drug metabolism activities in a miniaturized liver cell bioreactor for use in pharmacological studies. *Biotechnol. Bioeng.* **2012**, *109*, 3172-3181.
21. Lübberstedt, M.; Müller-Vieira, U.; Biemel, K. M.; Darnell, M.; Hoffmann, S. A.; Knöspel, F.; Wönne, E. C.; Knobloch, D.; Nüssler, A. K.; Gerlach, J. C.; Andersson, T. B.; Zeilinger, K. Serum free culture of primary human hepatocytes in a miniaturized hollow-fibre membrane bioreactor for pharmacological *in vitro* studies. *J. Tissue Eng. Regener. Med.* **2015**, *9*, 1017-1026.
22. Kohonen, T.; Niklasson, L.; Bodén, M.; Ziemke, T. Self-organization of very large documents collections: State of the art. In Proceedings of ICANN98, the 8th

- International Conference on Artificial Neural Networks; Springer, 1998; Vol. 1, pp 65-74.
23. Cavallito, C. J. Relationship of thiol structures to reaction with antibiotics. *J. Biol. Chem.* **1946**, 164, 29-34.
  24. Suckle, H. M.; Liebenow, R. R.; Orth, O. S. The convulsive effects of Streptomycin topically applied to the cerebral cortex. *J. Neurosurg.* **1947**, 4, 370-79.
  25. Herrel, W. E.; Heilman, M. D. Streptomycin: General considerations, tests for bacterial sensitivity and methods of measurement of streptomycin in body fluids. *Am. J. Med.* **1947**, 2, 421-428.
  26. Simon, R. D. Antagonization of the antibacterial action of nearsphenamine, penicillin and streptomycin by -SH compounds. *Br. J. Exp. Pathol.* **1948**, 29, 202-215.
  27. Williamson, G. M. The mode of action of streptomycin. *J. Pharm. Pharmacol.* **1957**, 9, 433-445.
  28. Potter, D. W.; Miller, D. W.; Hinson, J. A. Identification of acetaminophen polymerization products catalyzed by horseradish peroxidase. *J. Biol. Chem.* **1985**, 260, 12174-12180.
  29. Mesiter, A. Glutathione metabolism and its selective modification. *J. Biol. Chem.*, **1988**, 263, 17205-172080.
  30. Dahlin, D. C.; Miwa, G. T.; Lu, A. Y.; Nelson, S. D. N-acetyl-p-benzoquinone imine: a cytochrome P450 mediated oxidation product of acetaminophen. *Proc Natl. Acad. Sci. U. S. A.* **1984**, 81, 1327-1331.
  31. Cohen, S. D.; Hoivik, D. J.; Khairallah, E. A. Acetaminophen-Induced Toxicity. In *Toxicology of the Liver*; Plaa, G.L.; Hewitt, W.R., Eds.; Taylor & Francis, Washington DC, 1998.
  32. Bales, J. R.; Sadler, P. J.; Nicholson, J. K.; Timbrell, J. A. Urinary excretion of acetaminophen and its metabolites as studied by proton NMR spectroscopy. *Clin. Chem.* 1984, 30, 1631-163.
  33. Bessems, J.G.; Vermeulen, N.P.E., Paracetamol (Acetaminophen)-Induced Toxicity: Molecular and Biochemical Mechanisms, Analogues and Protective Approaches. *Crit. Rev. Toxicol.* **2001**, 31, 55-138.

## CHAPTER IV

### ANALYSIS ADVANCES FOR CHARACTERIZATION OF WIDE MASS RANGE MOLECULAR COMPOSITION

#### **4.1. Introduction**

In previous chapters, we explored different pre-ionization separation techniques coupled to IM-MS for the expansion of metabolite coverage in bioanalytical applications as possible strategies to circumvent ionization suppression effects for small and chemically diverse molecules. However, the analysis of molecules spreading over a wide mass range has represented a challenge particularly to synthetic polymer chemists characterizing different types of materials. Polymers exhibit a wide array of structures such as, linear, cyclic, branched chains, copolymers, dendrimers and star shapes.<sup>1</sup> Variations in their molecular mass, chemical composition, end group functionality and topology determine their physical properties and their use as materials for applications ranging from industrial construction products to drug delivery systems in the life sciences. Although significant advances have occurred in polymer synthesis, the focal point of characterization has been mostly on molecular weight distribution (MWD).<sup>2, 3</sup> Typically, the MWD of synthetic polymers is determined by size exclusion chromatography (SEC) and/or matrix assisted laser desorption/ionization time-of-flight mass spectrometry (MALDI-TOF-MS).<sup>3</sup> The two techniques are essentially complementary. MALDI-TOF-MS can detect differences in chemical composition and end-group functionality and SEC separations are based on polymer size (hydrodynamic volume). MALDI-TOF suffers from mass dependent response for polymers having

relatively wide polydispersities ( $M_w/M_n > 1.2$ ), because of diminished signal contribution by chains with higher degrees of polymerization.<sup>4</sup> Additionally, the effectiveness of gel permeation chromatography (GPC) depends on the use of proper standards for calibration,<sup>5</sup> which oftentimes are not available. Differences in hydrodynamic volumes make a standard calibration for some polymers unfeasible. Even though these limitations were addressed by coupling GPC with MALDI two decades ago,<sup>6</sup> complete characterization of complex polymer mixtures still represents a challenging task for polymers with small chemical differences (*e.g.* cyclic and linear chains).<sup>7</sup>

Traditional spectroscopic methods such as infrared (IR) and nuclear magnetic resonance (NMR) have been used to characterize telechelic (functionalized) polymers.<sup>8,9</sup> However, low sensitivity and the inability to deal with functional complexity represent limitations. In contrast, liquid chromatography under critical conditions (LCCC) allows for the separation of complex mixtures solely on the chemical unit or moiety of interest. Entelis pioneered LCCC several decades ago and formulated a theory for operation under critical conditions, where both entropy and enthalpy values (which govern SEC and adsorption separations, respectively) are equal, eliminating interactions with the stationary phase (Gibbs free energy = 0).<sup>10,11</sup> Under critical conditions, polymers with the same chemical composition will elute at the same time independent of their molecular weight, whereas polymer chains with the same degree of polymerization but with different chemical compositions (*e.g.* end-group chemistry) will be separated, making one part of the analyte “chromatographically invisible”.<sup>2</sup> The downside is that this technique is not as straightforward as other chromatographic techniques. The empirical process of identifying the critical conditions for a specific polymer and maintaining these



conditions for chromatography is challenging. For example, composition changes as little as 0.1% in the mobile phase can alter the LCCC delicate balance and compromise the analysis.<sup>10, 11</sup>

In an ongoing study, investigating SEC coupled directly to MS for an improved comprehensive characterization of polyesters and polyurethanes, we observed two novel and interesting chromatographic effects. To the best of our knowledge, these effects have not been reported previously. We observed complete separation of cyclic and linear polyesters and polyurethanes with a pure solvent (acetonitrile - ACN) as the mobile phase (unlike LCCC, which requires at least two). Additionally, we observed an inverse elution order for cyclic chains under the same conditions, where shorter chains elute before longer ones, counter to normal SEC behavior. Currently, we are investigating these effects and a complete study for a wider range of polymers is under way to determine if the effect is general. These findings should be of great interest for the polymer community to develop alternative methods for the characterization of complex polymer samples.

## ***4.2. Experimental***

### *Materials*

All solvents were CHROMOSOLV-grade (Sigma-Aldrich, St. Louis, MO). The polyester (PE 225) was synthesized by melt polymerization using adipic acid (hexanedioic acid) and 1,4-butanediol (Bayer, Leverkusen, Germany) with  $M_n=2250$  (end-group analysis). A polyurethane (PUR 262) was synthesized using equimolar amounts of polybutylene adipate ( $M_n=1000$ ) and 4,4'-methylene diphenyl diisocyanate

(MDI), (Bayer, New Martinsville, WV). The crown-ethers (12-crown-4, 15-crown-5 and 18-crown-6) were purchased from Sigma-Aldrich, the methyl- and dimethyl-polyethylene glycol were purchased from Polymersource (Montreal, Canada) and the PEG was purchased from Polymersciences, Inc. (Warrington, PA). The structures of the oligomers observed are shown in Table 4.1 Mass spectra and ion mobility-mass spectra for the different polymers can be found in Appendix D (D.1-D.6)

#### *Size Exclusion Chromatography-Mass Spectrometry (SEC-MS)*

The SEC-MS experiments were carried out using a Waters (Milford, MA) 515 HPLC pump coupled directly to a Synapt G2-S (Waters, Milford, MA) mass spectrometer via an electrospray ionization (ESI) source. The positive-mode (+) ESI conditions were as follows: capillary, +3.0 kV; sampling cone, 40 V; source temperature, 100 °C; desolvation temperature, 120 °C; desolvation gas flow, 600 L/h; and cone gas flow, 18 L/h, respectively. The instrument was calibrated with sodium-formate in the mass range of 200-2500 amu. Separations were performed at a flow rate of 0.3 mL/min and a temperature of 35 °C unless specified otherwise. The temperature was monitored with an independent digital thermometer (Radnor, PA). Two types of SEC stationary phases were used: traditional polymer particle substrate (GPC) and ethylene bridged hybrid silica particles (APC) both from Waters (Milford, MA). In both cases two columns with different molecular weight ranges were coupled in series. For GPC experiments, 2 columns in the order of Styragel® HR 3 THF (4.6 x 300mm) and Styragel® HR 0.5 (4.6 x 300mm) were connected. In parallel, the columns ACQUITY APC XT 125 (2.5 µm, 4.6 x 150mm) and ACQUITY APC XT 45 (1.7 µm 4.6 x 150mm)

**Table 4.1.** Structural assignments for PE 225, PUR 262 oligomers and PEG compounds.

Species	Structure	Mass Na adduct
Linear PE 225		313.3 (n=1) 513.4 (n=2) 713.5 (n=3)
Cyclic PE 225		423.2 (n=2) 623.3 (n=3) 823.4 (n=4)
Linear PUR 262		453.2 (n=0) 653.3 (n=1) 853.4 (n=2)
Cyclic PUR 262		563.2 (n=1) 763.3 (n=2) 963.4 (n=3)
PEG		217.1 (n=4) 261.1 (n=5) 305.2 (n=6)
PEG-methyl ether		231.1 (n=4) 275.1 (n=5) 319.2 (n=6)
PEG-dimethyl ether		245.1 (n=4) 289.2 (n=5) 333.2 (n=6)
Cyclic PEG (crown-ether)		199.1 (n=4) 243.1 (n=5) 287.2 (n=6)

were used for APC. Tetrahydrofuran (THF) and ACN were the mobile phases for APC separations, while only THF was used for GPC. In order to obtain a stable electrospray with THF, ACN was infused at 0.3 mL/min via a T shortly before the ESI source. PE 225 and PUR 262 were dissolved and diluted in their respective solvents, 100 ng were injected. PEG compounds were injected at different concentrations and equimolar solutions were created to investigate the ionization efficiencies of the individual species.

### **4.3. Results and Discussion**

#### **4.3.1. Exploration of SEC stationary phases with polyesters and polyurethanes**

The hydrodynamic volume of polymers, and therefore their separation efficiency, strongly depends on the solvent used for the separation. GPC columns typically are certified for a particular MW range for a particular solvent and the use of a different solvent can compromise not only the separation but also the column integrity. Therefore, a stationary phase with a broad solvent compatibility would be of great benefit for polymer characterization. As part of a larger project we evaluated a silica based stationary phase (APC) for the separation of polyesters and polyurethanes and subsequently compared APC to traditional GPC columns. Figure 4.1 (A) illustrates the elution plots for polyester PE 225 using GPC in THF compared to APC in both THF and ACN. The GPC separation in THF shows a normal profile with both linear (green squares) and cyclic (green circles) chains co-eluting. The elution times of the larger cyclic chains overlap with linear chains of the same size, whereas the shorter cyclic chains tend to elute somewhat after their linear counterparts. On the other hand, the elution profiles for cyclic and linear chains using APC as the stationary phase and THF as

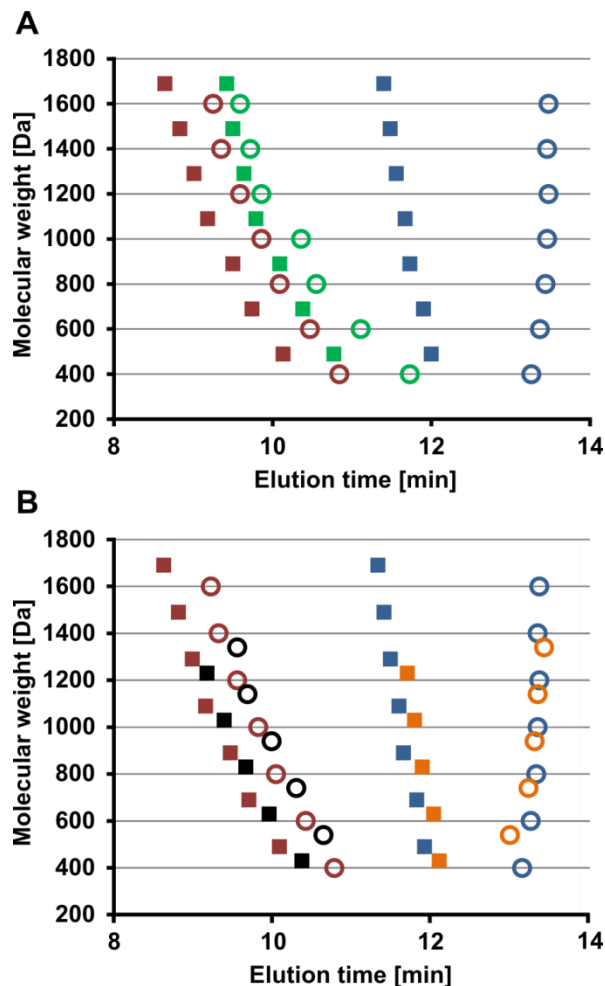


**Figure 4.1.** Elution plots of the molecular weights of cyclic (circles) and linear (squares) chains versus their elution times in SEC. A) Elution profiles for PE 225 and B) elution profiles for PE 225 and PUR 262 are color coded by polymer and separation conditions. PE 225 (green- GPC in THF, red- APC in THF and blue- APC in ACN), PUR 262 (black- APC in THF and orange- APC in ACN). From Montenegro-Burke, J.R.; Bennet, J.M.; McLean, J.A.; Hercules, D.M., *Analytical and Bioanalytical Chemistry* **2016**, 408, 677-681. Figure 1, with permission from Springer and RightsLink.

the solvent show a small, constant time interval (~45 sec.) between cyclic (red circles) and linear (red squares) chains having the same degree of polymerization.

A significant difference is quite evident when ACN is used as the mobile phase, significant separation of linear (blue squares) and cyclic (blue circles) oligomers is noted. There is a 2-3 minute longer elution time for linear chains and 3-4 minute for cyclic chains compared to THF for both stationary phases. More importantly, linear and cyclic chains were completely separated regardless of their close MW and chemical composition. It should be noted that the elution profiles with ACN are steeper compared to THF, which might suggest a smaller number of theoretical plates in the former. Also, the separation of linear and cyclic chains seems to widen as the degree of polymerization increases. The reproducibility of these separations was determined by calculating the difference of elution times of equal polymerization degree for linear and cyclic chains. This was analyzed for 3 separate runs in all conditions and it was determined that even though small elution time changes, commonly observed in chromatography experiments, were detected, the times between the elution of same length linear and cyclic chains showed low variability under all conditions (1-6 seconds in 0.3 to 2.1 minute separation of linear and cyclic oligomers). Furthermore, different temperatures were investigated, showing effects on the retention time of all chains in the same direction (earlier elution times for higher temperatures). However, the separation of linear and cyclic chains as well as the order of elution did not change (Figure 4.2).

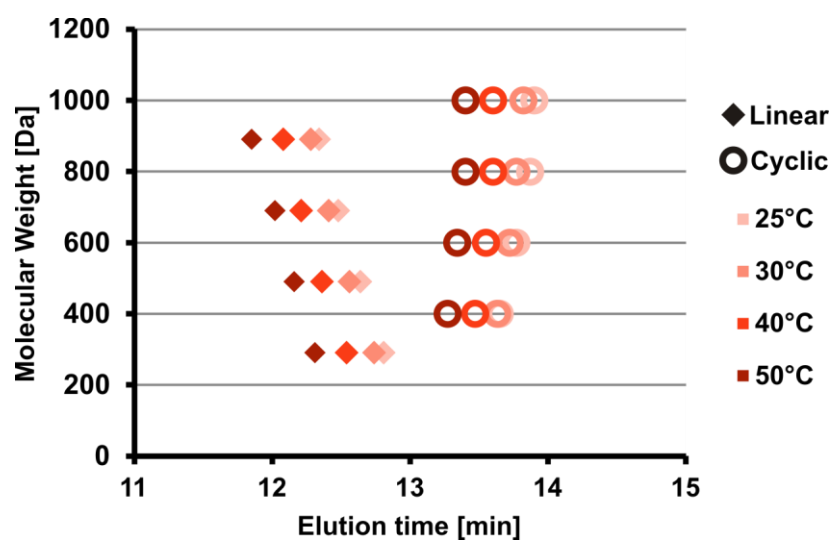


**Figure 4.2.** Temperature dependence of elution profiles for PE 225. Linear and cyclic chains are represented by diamonds and circles respectively. The temperature gradient is analog to the temperature gradient.

Given that different polymers will have different hydrodynamic volumes, and that these will be affected by the solvent (polarity), we selected a simple polyurethane (PUR 262) for study, to see if increased chain rigidity caused by the addition of MDI to the chains would have an effect for solvents with different polarities (THF and ACN relative polarities are 0.207 and 0.460 respectively).<sup>12</sup> Changes in flexibility can have an effect on the folding capability of the polymers, altering their hydrodynamic volumes. Figure 4.1 (B) illustrates comparisons between the separations of PE 225 and PUR 262 on an APC column in both THF and ACN. The difference between both polymer elution profiles with THF is minimal; the plots for PE 225 (red) and PUR 262 (black) overlap completely. Of greater interest is the behavior observed for both the polyester and polyurethane in ACN, where the linear and cyclic chains are separated and the PE 225 (blue) and PUR 262 (orange) data points completely overlap, showing the same separation of linear and cyclic oligomers. These results suggest that an increase in mobile phase polarity reduces the hydrodynamic volumes of these polymers, with the effect being greater for cyclic chains even in more rigid structures. Changes in elution times by altering the mobile phase composition are not unusual. Moreover, it is one of the main factors to be considered in any chromatographic experiment. However, the increase in separation between linear and cyclic chains under APC conditions with ACN as mobile phase provides an effective means to separate these architectures.

These separations were performed rapidly (less than 15 minutes) and minimal optimization was needed due to the use of a single solvent system, which increases the reproducibility and ease of analysis. In critical chromatography (LCCC), the selection of the solvents is determined by their interactions with the polymer and stationary phase.



Typically, a good polymer solvent with a column showing good SEC behavior is selected. Subsequently, a non-solvent for the polymer is added to the mobile phase to induce enthalpic interactions until a delicate solvent balance is reached.<sup>10, 11</sup> Previously, critical conditions for a single solvent system have been reported for polyisoprene (PI).<sup>13</sup> In that study PI chains eluted at the same time regardless of their MW with 1,4-Dioxane at exactly 47.7°C and small temperature changes (0.1°C) altered the balance. However, these conditions were not appropriate for the separation of block-copolymers (polystyrene-polyisoprene). This demonstrated that polymers with different chemical compositions need a two solvent system in order to successfully separate complex polymer samples using LCCC for the separation.

The coupling of LCCC's unique sorting capability with MALDI offers great potential for the characterization of complex polymer samples. The first separation allows for fractionation based on chemical composition followed by measurement of the MW distribution. For example, for the characterization of PE 225 and PU 262, linear and cyclic chains would first be separated in LCCC, and fractions would be collected for MW distribution measurements with MALDI. Interestingly, in the present work we observe not only the separation of linear and cyclic chains but also an SEC behavior for linear chains, where chain length is inversely proportional to elution time. To the contrary, an inverse SEC behavior for cyclic chains was observed. Figure 4.3 (A) displays a magnified region of the PE 225 (blue) and PUR 262 (orange) elution profiles of cyclic chains shown in Figure 4.1 (B). With APC and ACN as the stationary-mobile phase system, cyclic chains with lower degrees of polymerization elute before chains with higher degrees of polymerization. In the case of the polyester (blue), a linear elution

profile ( $R^2 = 0.98$ ) is observed for the first 3 species ( $n=2$  to  $n=4$ ). Nonetheless, this profile changes for longer chains ( $n=5$  to  $n=8$ ), where elution times are observed in a narrower time range, reminiscent of LCCC separations. This is not the case for polyurethane chains (orange), which show a more nearly linear elution profile ( $R^2 = 0.88$ ) for all observed species.

The two novel effects reported in this work can be visualized in the extracted ion chromatograms (EICs) shown in Figure 4.3 (B). The first eluting peaks correspond to linear polyester species, with longer chains eluting before shorter chains ( $n=6$  to  $n=1$ ). The later peaks correspond to the cyclic species with the opposite elution order ( $n=2$  to  $n=6$ ). The separation between both species is evident and given the well resolved characteristics of the separation, the possibilities of co-elution are minimal.

The reason(s) for these interesting differences under APC and ACN conditions are not entirely clear. It is understood from LCCC theory that entropy governs SEC separations while enthalpy governs adsorption separations. In SEC, as described above, longer chains have shorter elution times than shorter chains. On the other hand, in adsorption separations longer chains have longer elution times, due to the higher interactions between long chains and the stationary phase. One possible explanation for the effects we observe is that, at the specific conditions for ACN on APC columns, entropy governs the separation of linear chains while enthalpy governs the separation of cyclic chains. This would suggest that ACN is what would be considered a good solvent in LCCC theory only for linear chains but a non-solvent for cyclic chains under the same conditions. These differences between linear and cyclic chains are supported by the fact that smaller hydrodynamic volumes, lower viscosities, higher thermostabilities, higher

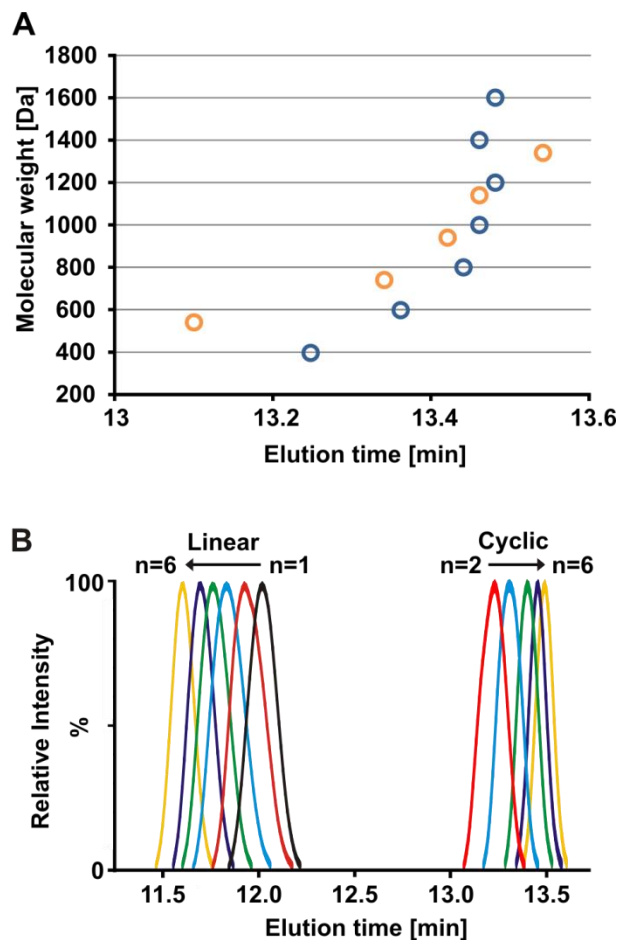


**Figure 4.3.** A) Expanded SEC elution plot of the molecular weights of cyclic chains of PE 225 (blue) and PUR 262 (orange) versus time. B) Extracted ion chromatograms (EIC) of linear and cyclic PE-225 B chains. Chains are color coded by their degree of polymerization (e.g. n=2 is red...n=6 is yellow). From Montenegro-Burke, J.R.; Bennet, J.M.; McLean, J.A.; Hercules, D.M., *Analytical and Bioanalytical Chemistry* **2016**, 408, 677-681. Figure 2, with permission from Springer and RightsLink.

self-diffusion coefficients, enhanced fluorescence as well as both lower and higher glass transition temperatures have been reported for cyclic chains compared to their linear counterparts.<sup>14, 15, 16</sup>

#### ***4.3.2. Application of novel chromatographic behavior for the separation and characterization of polyethylene glycol compounds***

This effect of ACN with APC columns was further explored for a type of polymer where linear and cyclic chains are currently used in different applications. Polyethylene glycol (PEG) is broadly used, especially in medicine and biotechnology applications for its water solubility and low toxicity.<sup>17, 18</sup> On the other hand, the cyclic counterparts, crown-ethers, are used as complexing agents due to their ability to bind alkali metal cations.<sup>19</sup> Figure 4.3 shows the EICs of different PEG compounds collected with ACN in APC column at a flow rate of 450 $\mu$ L/min. It is evident that the predominant chromatographic effect observed for the crown-ether species (cyclic PEG chains) is adsorption. The larger chain (18-crown-6, black) elutes after the shorter oligomers (12-crown-4 and 15-crown-5, green and purple, respectively) (Figure 4.4 (A)). Interestingly the shortest and longest crowns are separated from the linear PEG chain (red). This is not the case for 15-crown-5, which co-elutes with the linear PEG chains. Furthermore, the chromatographic separation of the crown-ethers is successful with baseline resolved peaks. It's worth mentioning that the 2 larger crown-ethers show similarities in their chromatographic behavior. Both species EICs seem to be composed of at least 2 peaks co-eluting. A possible explanation is that given their longer structures, different Na<sup>+</sup> bound conformations with different hydrodynamic volumes are possible.

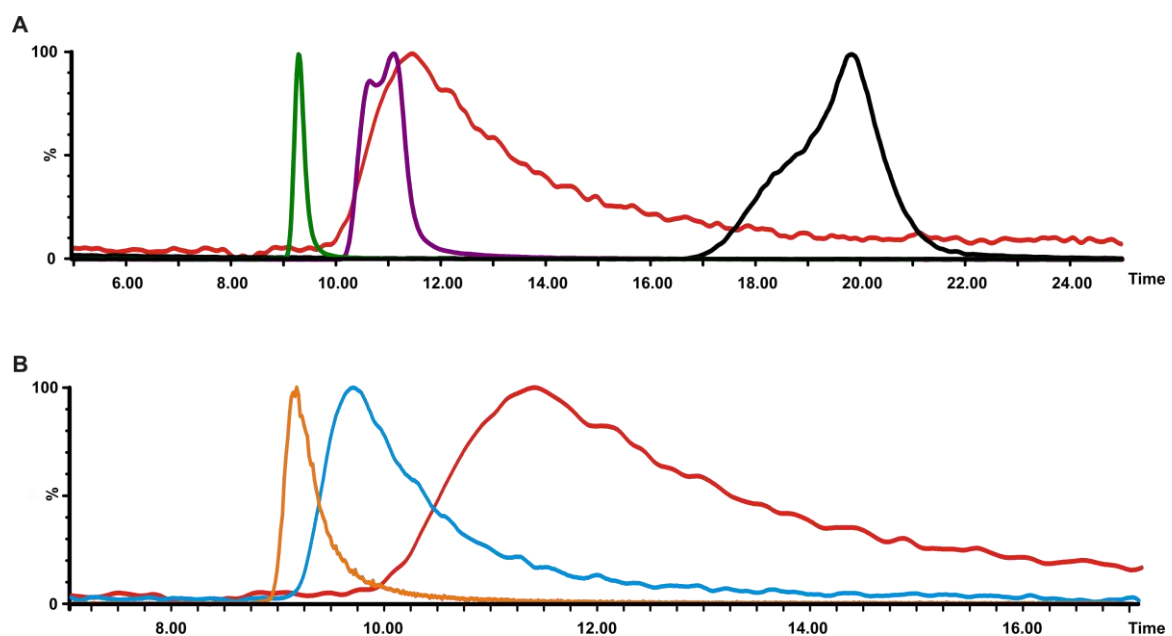


**Figure 4.4.** A) EIC of crown ethers and linear PEG. 12-crown-4 (green), 15-crown-5 (purple), 18-crown-6 (black) and linear PEG (n=6) (red). B) EIC of linear PEG chains (all n=6) with different end-groups. PEG-dimethyl ether (orange), PEG-methyl ether (blue) and PEG (red).

We further investigated the polarity effects of different end-groups in the linear species and plotted the EICs for  $n=6$  and  $\text{Na}^+$  adduct for chains containing two OH end-groups, one free OH and one methyl ether end-group and two methyl ether end-groups (Figure 4.4 (B)). As expected, given the polar properties of the Silica APC stationary phase, PEG chains with free hydroxyl groups have stronger interactions, resulting in longer elution times and peak broadening. These interactions are reduced in chains with only one methylated end-group, due to the lower number of free OH groups available for interaction. Lastly, species with both methylated end-groups eluted first and had the narrowest peak, confirming that adsorption is playing a dominant role in the separation of PEG compounds under ACN and APC conditions.

Interestingly, in spite of the large adsorption effects inherent for the polar stationary phase with polar solutes, a slight size exclusion behavior is observed for the three classes of linear PEG (Figure 4.5). PEG-dimethyl ether species have a steeper slope compared to the species with free OH end-groups suggesting very small changes in their hydrodynamic volume compared to the species with free OH end-groups. Taking into consideration the low mass of the repeating unit (44 Da), more gradual slopes, like the case of PE and PUR, are less likely. Furthermore the linearity of their elution profiles decreases with number of free OH end-groups ( $R^2 = 0.99, 0.91$  and  $0.84$ , respectively). This could be explained by the peak broadening effects observed for the different species in Figure 4.4 (B), where determining the apex can be more complicated.

The readily separation of the cyclic PEG species and in the commercial availability as pure compounds allowed us to calculate their respective ionization efficiencies and compare them to their linear PEF-dimethyl ether counterparts. For that,

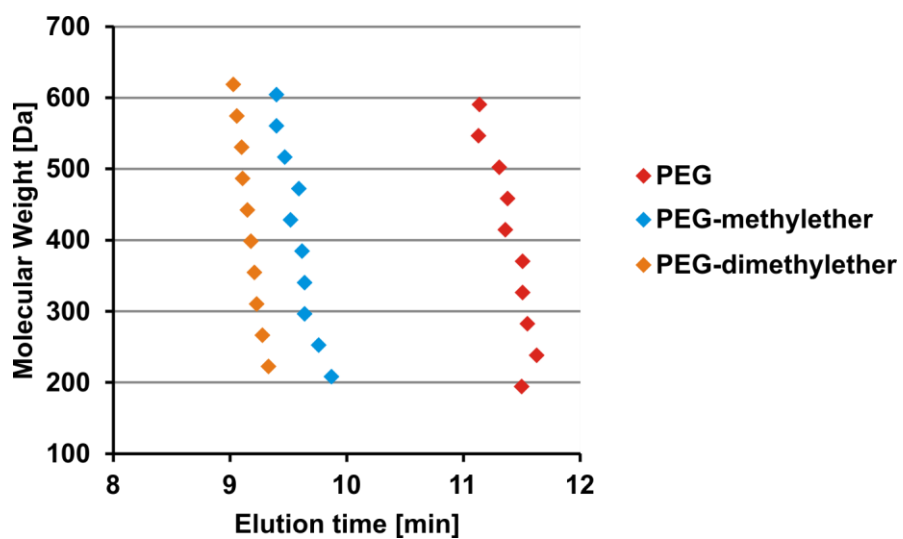


**Figure 4.5.** Elution plots of the molecular weights of linear PEG species versus their elution times in SEC.

equimolar solutions of the three crown-ethers (n=4, 5 and 6) were analyzed and the molecular weight distribution for the linear species was calculated, including n=4, 5 and 6. We appreciate that this calculation allows only for an estimate of ionization efficiencies, given the different peak width for the cyclic chains and the co-elution of all the linear chains. However, after integrating the detector response for the different species (*e.g.* cyclic, n = 4, area = 45195.2) and dividing by the moles injected of the same species (*e.g.* cyclic, n = 4, moles injected =  $2.7 \times 10^{-13}$ ), ionization efficiencies are calculated for each linear and cyclic species. For the cyclic species with a polymerization degree of 2, the ionization efficiency (area/ moles injected) was calculated to  $1.7 \times 10^{17}$ . By comparing ionization efficiencies between cyclic and linear chains, a factor of  $\sim 10^3$  higher efficiencies was determined for the cyclic chains compared to their respective linear chains (n = 4, 5 and 6) (Table 4.1). This is not entirely surprising given their high affinity to alkali metal cations (*e.g.*  $\text{Na}^+$ ).



**Table 4.2.** Calculation of ionization efficiencies for cyclic (crown-ethers) and dimethylated PEG oligomers.

n	Structure	Moles injected	Area	Area/moles injected
4	Cyclic	$2.7 \times 10^{-13}$	45195.2	$1.7 \times 10^{17}$
5	Cyclic	$2.2 \times 10^{-13}$	162669.5	$7.3 \times 10^{17}$
6	Cyclic	$2.2 \times 10^{-13}$	131260.8	$5.9 \times 10^{17}$
4	Linear	$6.9 \times 10^{-12}$	3998.5	$5.8 \times 10^{14}$
5	Linear	$2.2 \times 10^{-11}$	12228.7	$5.4 \times 10^{14}$
6	Linear	$5.3 \times 10^{-11}$	26918.7	$5.1 \times 10^{14}$

#### **4.4. Conclusions**

In this chapter, we have reported novel behavior observed for complex polymer samples using APC columns with ACN as a solvent, resulting in the separation of linear and cyclic oligomers for certain types of polymers. The methodology developed does not involve extensive optimization, utilizes an electrospray friendly solvent and has the potential for significantly improving polymer characterization. We identified that these conditions cannot be used for the general separation of all linear and cyclic polymers and a more comprehensive study using a broad library of polymer classes is necessary. Furthermore, the chromatographic behavior of polyesters and polyethers (PEGs), both with free hydroxyl and protected groups, show similarities and differences. The separation of linear and cyclic chains for PE and PUR was successful; on the other hand, this was not the case for cyclic PEGs and the methylated linear chains (both elute at 9 minutes). Additionally, in spite of the elution profiles of cyclic PE, PUR and PEG being governed solely by adsorption, the complete separation of the individual PE and PUR species (different length) seems unlikely with the current methodology, the complete separation of the individual crown-ethers is readily accessible. These observations suggest that end-group polarity and chemistry are not the only factor in the adsorption-size exclusion intricate balance. The opposite effects played by enthalpy and entropy seem to affect different chemistries to different extents under the investigated conditions, making a chromatographic prediction extremely challenging at the current state of understanding and data available.

#### 4.5. *Acknowledgements*

This chapter contains the research article: Montenegro-Burke, J.R.; Bennet, J.M.; McLean, J.A.; Hercules, D.M.; Novel behavior of the chromatographic separation of linear and cyclic polymers, *Analytical and Bioanalytical Chemistry*, **2016**, 408, 677-681. The authors thank Dr. Hartmut Nefzger and Dr. Stefan Wershofen of Bayer MaterialScience AG, Leverkusen, Germany for providing the polymer samples. Research reported in this publication was supported by the National Center For Advancing Translational Sciences of the National Institutes of Health under Award Numbers 5UH3TR000491-04 and 3UH3TR000491-04S1. The authors also acknowledge support for this work provided by the Vanderbilt University Center for Innovative Technologies, the Vanderbilt Institute for Chemical Biology, the Vanderbilt Institute for Integrative Biosystems Research and Education and Vanderbilt University College of Arts and Science.

#### 4.6. References

1. Montaudo, G.; Samperi, F.; Montaudo, M. S., Characterization of synthetic polymers by MALDI-MS. *Prog. Polym. Sci.* **2006**, 31, 277-357.
2. Crotty, S.; Weber, C.; Baumgaertel, A.; Fritz, N.; Altuntaş, E.; Kempe, K.; Schubert, U. S., Semi-automated multi-dimensional characterization of synthetic copolymers. *Eur. Polym. J.* **2014**, 60, 153-162.
3. Pretorius, N. O.; Willemse, C. M.; de Villiers, A.; Pasch, H., Combined size exclusion chromatography, supercritical fluid chromatography and electrospray ionization mass spectrometry for the analysis of complex aliphatic polyesters. *J. Chromatogr. A* **2014**, 1330, 74-81.
4. McEwen, C. N.; Jackson, C.; Larson, B. S., Instrumental effects in the analysis of polymers of wide polydispersity by MALDI mass spectrometry. *Int. J. Mass Spectrom. Ion Processes* **1997**, 160, 387-394.
5. Hanton, S. D.; Liu, X. M., GPC Separation of Polymer Samples for MALDI Analysis. *Anal. Chem.* **2000**, 72, 4550-4554.
6. Montaudo, G.; Montaudo, M. S.; Puglisi, C.; Samperi, F., Molecular weight distribution of poly(dimethylsiloxane) by combining matrix-assisted laser desorption/ionization time-of-flight mass spectrometry with gel-permeation chromatography fractionation. *Rapid Commun. Mass Spectrom.* **1995**, 9, 1158-1163.
7. Chen, H.; He, M., (2005) Quantitation of synthetic polymers using an internal standard by matrix-assisted laser desorption/ionization time-of-flight mass spectrometry. *J. Am. Soc. Mass Spectrom.* **2005**, 16, 100-106.
8. Iván, B.; Kennedy, J. P.; Chang, V. S. C., New telechelic polymers and sequential copolymers by polyfunctional *Initiator-transfer* agents (Inifers). VII. Synthesis and characterization of  $\alpha,\omega$ -di(hydroxy)polyisobutylene. *J. Polym. Sci. Polym. Chem. Ed.* **1980**, DOI: 10.1002/pol.1980.170181104 .
9. Hiltunen, K.; Härkönen, M.; Seppälä, J. V.; Väänänen, T., Synthesis and Characterization of Lactic Acid Based Telechelic Prepolymers. *Macromolecules* **1996**, 29, 8677-8682.
10. Entelis, S. G.; Evreinov, V. V.; Gorshkov, A. V., Functionality and molecular weight distribution of Telechelic polymers. *Adv. Polym. Sci.* **1986**, 76, 129-175.
11. Olesik, S. V., Liquid chromatography at the critical condition. *Anal. Bioanal. Chem.* **2004**, 378, 43-45.

12. Reichardt, C.; Welton, T., Solvents and Solvent effects in Organic Chemistry, Wiley-VCH, Weinheim, 2003.
13. Lee, W.; Park, S.; Chang, T., Liquid Chromatography at the Critical Condition for Polyisoprene Using a Single Solvent. *Anal. Chem.* **2001**, 73, 3884-3889.
14. Bielawski, C. W.; Benitez, D.; Grubbs, R. H., Synthesis of Cyclic Polybutadiene via Ring-Opening Metathesis Polymerization: The Importance of Removing Trace Linear Contaminants. *J. Am. Chem. Soc.* **2003**, 125, 8424-8425.
15. Laurent, B. A.; Grayson, S. M., Synthetic approaches for the preparation of cyclic polymers. *Chem. Soc. Rev.* **2009**, 38, 2202-2213.
16. Kricheldorf, H. R., Cyclic Polymers: Synthetic Strategies and Physical Properties. *J. Polym. Sci. Part A: Polym. Chem.* **2010**, 48, 251-284.
17. Chen, J.; Spear, S. K.; Huddleston, J. G.; Rogers, R.D. Polyethyleneglycol and solutions of polyethylene glycol as green reaction media. *Green Chem.* **2005**, 7, 64-82.
18. Rossi, J. J. RNAi therapeutics: SNALPing siRNAs *in vivo*. *Gene Ther.* **2006**, 13, 583-584.
19. Pedersen, C. J. Macrocyclic Polyethers: Dibenzo-18-crown-6 Polyether and Dicyclohexyl-18-crown-6 Polyether. *Org. Synth.* **1972**, 52, 66.

## CHAPTER V

### PERSPECTIVES AND PROPOSED IMPROVEMENTS ON THE APPLICATION OF SEPARATIONS WORKFLOWS FOR HIGH TEMPORAL RESOLUTION MEASUREMENTS

Systems biology is a comprehensive quantitative analysis, which focuses on studying the biochemical time-resolved networks interactions. In order to understand biology at a system level, the structure and dynamics of the cellular and organismal function must be analyzed as opposed to isolated parts of a cell or organism. While proteomics and genomics information continues to be important, systems-wide information encompasses more than genes and proteins alone. Diagrams depicting interactions cannot understand the system's properties. A good analogy would be to try to gain information about traffic patterns from a static roadmap. The roadmap cannot explain why these patterns occur or how they can be controlled for example.

A comprehensive understanding of the properties of whole systems would have an enormous influence in the future of medicine. The ability to predict the behavior of a system after any type of stimulus would make drug discovery more efficient and economical. Such information would also enable personalized medicine a routine treatment in healthcare. Redesigning gene regulatory networks with a specific stimulus could create new systems properties and would transform the field of preventive medicine. However, in order to acquire such data, sensitive tools for identifying the concentration, flux and interactions of various types of molecules at high resolution both in space and time need to be developed. Miniaturized and automated mock-organ

constructs and detection platforms capable of parallel multiparameter analysis are key elements for the reproducibility and multiplexing of this technology.

Mass spectrometry, as discussed in previous chapters, is a widely used high-throughput method for chemical analysis and can simultaneously detect multiple analytes even at low sample volumes. However, obtaining quantitative information across a broad dynamic range of concentrations is hindered by the need to remove the abundant low-volatile salts, which are present in all biological fluids and media used for cell cultures. Furthermore, other nonvolatile analytes, which exist in the sample, have long been known to have significant suppression effects on the electrospray process and ionization efficiencies. These effects limit quantitation and reproducibility for MS, and by proxy, any interfacing technologies such as IM.

To address these limitations, desalting techniques such as solid phase extraction, liquid chromatography and capillary electrophoresis have been implemented prior to MS analysis. To date, these approaches have necessitated offline sample preparation and, in some cases, low throughput fraction collection. Clearly this hinders the temporal resolution of the analysis since the biologically dynamic molecular signals, are averaged along the collection time. A problem with systems biology is that each level of biological interactions – gene expression, protein expression and metabolism – operates on a different timescale from one another, making it challenging to find casual linkages. Using the previous analogy of a static roadmap, the signal averaging would be similar to predicting the time of high vehicle traffic flows when the available data represents the average of vehicle traffic flows in a 48-hour window. This measurement would fail to recognize high vehicle traffic flows in the morning as well as the type of vehicles

involved for example. The Nyquist sampling theorem, which states that a function containing frequencies lower than  $x$  Hz can only be completely identified by collecting measurements at a series of points spaced  $1/(2x)$  seconds apart or less thus necessitates near real-time analysis. Therefore, developing a technique whereby the cell culture medium effluent is sampled and desalted online via microdialysis (MD), would increase the time resolution, while facilitating sample compatibility with MS instrumentation. Such a technology could potentially allow for real-time experiments, where cell cultures, mock-organ constructs or even animal models could be monitored directly to a mass spectrometer. For example, in Figure 5.1, a cell culture can be monitored with a microscope for morphological changes after any stimuli. The cellular secretome would then be processed by the microdialysis apparatus, displacing the nonvolatile salts (*e.g.*  $\text{Na}^+$ ) with volatile salts such as  $\text{NH}_4^+$ , and facilitating an efficient electrospray process. Finally, the biochemical signatures secreted by the cells following a specific stimulus can be measured with state-of-the-art mass spectrometers.

Preliminary experiments in our laboratory have been performed utilizing this technique by monitoring signal-to-noise ratio (S/N) of certain compounds dissolved in commonly used media, with  $\sim 130$  mM salt concentration. In Figure 5.2 (A), Ubiquitin (8.5 kDa) was injected at  $10 \mu\text{g/mL}$  in RPMI media with and without dialysis prior to the ionization source. It is evident that the microdialysis system has a significant improvement on the S/N of the measurement (Figure 5.2 (B)). We have previously applied this technology to metabolic studies by monitoring the activity of invertase in *Saccharomyces cerevisiae*. Invertase hydrolyzes sucrose into glucose and fructose on the cell surface and the monitoring of the increase of isobaric glucose and fructose signals



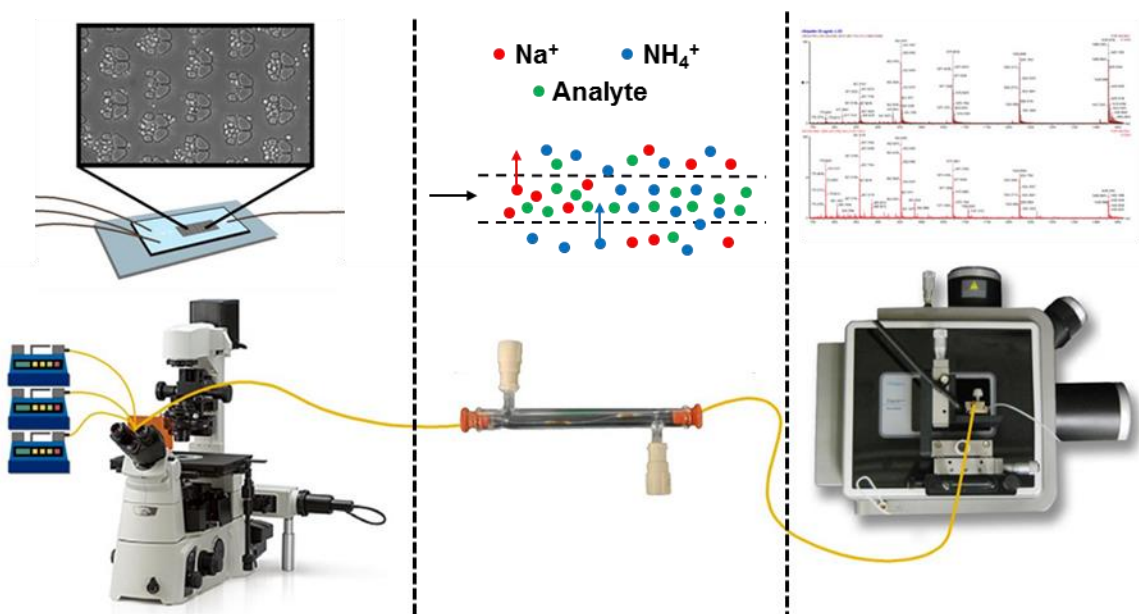


**Figure 5.1.** Cell culture-microdialysis-MS platform with (Left) Harvard Apparatus syringe pumps, Nikon Eclipse Ti-e inverted fluorescence microscope with stage incubator, (Center) microdialysis desalting device, (Right) nano-electrospray ionization source for continuous flow sample analysis in the Waters Synapt G2 mass spectrometer.

( $m/z = 203.05$ ,  $[M + Na^+]^+$ ) and the simultaneous decrease of sucrose ( $m/z = 365.11$ ,  $[M + Na^+]^+$ ), demonstrating in real time metabolomics data. It is worth mentioning that not only size but also polarity will have an effect on the recovery of the different analytes during the dialysis process. Larger molecules are less likely to travel across the membrane into the counter buffer flow. On the other hand, small metabolites such as monosaccharides diffuse faster through the pores of the hollow fiber membranes. Additionally, hydrophobic and hydrophilic characteristics of the different analytes will play an important role in the adsorption to the surface of the membrane or tubing. These issues can be mitigated to some degree by infusing mixtures of organic solvents and water between the cell culture and the microdialysis device, creating an environment capable of maintaining a wider range of molecules in the solvent, with the effect of a more comprehensive metabolite coverage of real time measurements.

With the improvement of temporal resolution towards the biomolecular characterization of the secretome, the characterization of the cellular composition could be approached in parallel by online sample preparation systems. Commonly, sample preparation of biological tissue and cell cultures involves cell lysis followed by protein precipitation for metabolomics studies. This is achieved by mixing the biological materials with organic solvents at low temperatures, which precipitates the proteins, and retains the metabolites in solution. Alternatively, hot water introduced for short periods of time can also be used to lyse cells and extract metabolites. The stationary phase used in the chromatographic separation of synthetic polymers discussed in Chapter IV represents the advantage of versatility in solvent selection over wide temperature ranges. This advantage could also potentially be utilized in the sample preparation steps by

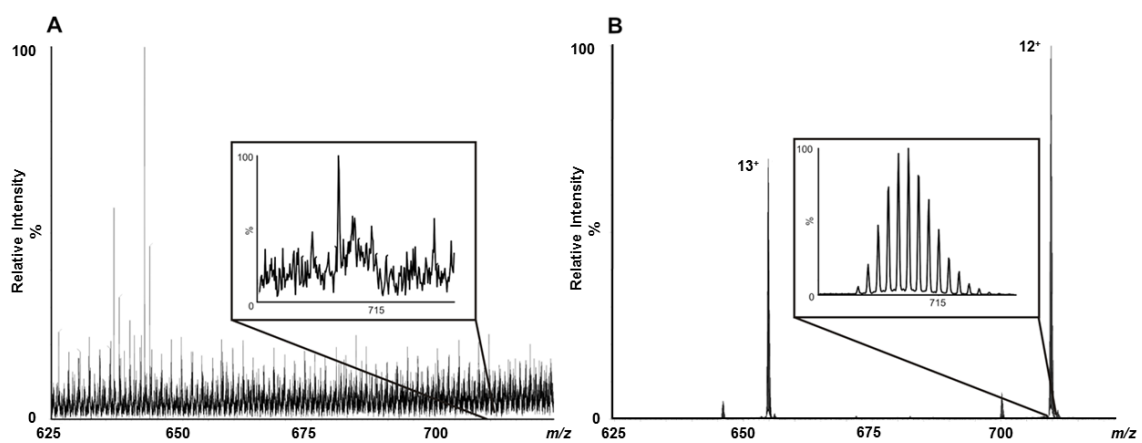


**Figure 5.2.** Comparison of 10  $\mu\text{g/mL}$  ubiquitin mass spectra in 1640 RPMI media ( $\sim 130$  mM NaCl) before microdialysis (A) and after microdialysis (B). Spectrum (B) is completely resolved (insert  $[\text{M}+12\text{H}]^{12+}$ ), while ubiquitin cannot be observed in the spectrum (A).

simultaneously lysing cells and separating molecules by their molecular weight using bioanalytical-friendly solvents. The size exclusion characteristics and the wide solvent and temperature range compatibility of the APC columns could potentially be utilized in the separation of macromolecules from smaller biomolecules in online systems. Large molecules elute much earlier than smaller molecules in SEC, allowing the separation of the high molecular fraction such as proteins to be separated from the small molecular fraction such as metabolites. The high molecular weight fraction could be further processed for proteomics studies, where denaturing protocols are commonly utilized. The lysing of the cells and the separation of the different molecular weight fractions in the distinct solvents could easily be coupled with downstream HPLC separations for further MS analysis. For example, the metabolite fraction collected by hot water sample preparation could be injected into a C18 column prior to MS analysis, without further manipulation. Furthermore, in the case of organic solvents being utilized for sample preparation, the small molecular fraction could be analyzed with HILIC stationary phases, where high organic solvent compositions are used in the early stages of the chromatogram. These techniques could easily be applied to SFC, where the inherent high flow rates make the polarity of the sample solvent negligible, allowing for a wide variety of stationary phases to be used for more comprehensive metabolomic studies such as previously discussed in the earlier chapters of this dissertation.

## APPENDIX A

### REFERENCES OF ADAPTATION FOR CHAPTERS

- Chapter I. **Montenegro-Burke, J.R.;** Goodwin, C.R.; Bachmann, B.O.; McLean, J.A. Supercritical Fluid Chromatography coupled with Ion Mobility-Mass Spectrometry for analysis of biological samples, In preparation for *Analytical Chemistry*.
- Chapter II. **Montenegro-Burke, J.R.;** Sutton, J.A.; Rogers, L.M.; McLean, J.A.; Aronoff, D.M. Lipid Profiling of 3-Dimensional Polarization Space of Human Monocyte-derived Macrophages, In preparation for *Prostaglandins & Other Lipid Mediators*.
- Montenegro-Burke, J.R.;** Xu, L.; Korade, Z.; Porter, N.A.; McLean, J.A. Expanding Lipidomic Separation Space by Integrating Supercritical Fluid Chromatography with Ion Mobility-Mass Spectrometry, In preparation for *Analytical and Bioanalytical Chemistry*.
- Chapter III. **Montenegro-Burke, J.R.;** Goodwin, C.R.; Knöspel, F.; Gerstmann, F.; Zeilinger, K.; Storch, L.; Damm, G.; Sherrod, S.; Iyer, S.; Iyer, R.; Wikswo, J.P. McLean, J.A.; Towards the Development of a  $\mu$ Human: Dynamic Exo-metabolomic Response Analysis of 3-Dimensional Hepatocyte Bioreactor to Acetaminophen and N-acetyl Cysteine Exposure, In preparation for *Analytical Chemistry*.
- Chapter IV. **Montenegro-Burke, J.R.;** Bennet, J.M.; McLean, J.A.; Hercules, D.M.; Novel behavior of the chromatographic separation of linear and cyclic polymers, *Analytical and Bioanalytical Chemistry*, 408, 677-681, (2016).

## APPENDIX B

### SUPPORTING INFORMATION FOR CHAPTER II

#### ***B.1. Data processing***

Data can be mass corrected with Lockspray during and after acquisition. The function “Automatic Peak Detection” from MassLynx software package (Waters, Milford, MA) is used to reduce the file sizes. The files are then converted to. mzXML format with ProteoWizard (<http://proteowizard.sourceforge.net/>) using the MSConvert and “sortByScanTime” function.

R studio is a user friendly version of the R package and it is compatible with XCMS. It can be downloaded from <http://www.r-project.org/>. For peak peaking, alignment and quantitation the XCMS package is used. It is downloaded directly from R studio by running the code below:

```
source("http://bioconductor.org/biocLite.R")
biocLite("xcms", dep=T)
```

#### ***B.1.1. XCMS Method***

```
NAME <-xcmsSet()
NAME <-group(NAME)
NAME2 <-retcor (NAME, method="obiwarp")
NAME2 <-group(NAME2, bw=10)
NAME3 <-fillPeaks(NAME2)
reporttab <-diffreport(NAME, "Group_1", "Group_2", "File_Name", Number of
EICs, Number of boxplots)
```

**Table B.1.** Fatty acid percentage composition of individual lipid classes for control MDMs obtained from MS<sup>E</sup> in negative ion mode.

Fatty Acid	Lipid classes					
	PG	PE	PI	PC	SM	PS
<b>14:0</b>	0.4 ± 0.1	0.2 ± 0.1	0.2 ± 0.1	2.2 ± 0.1	2.3 ± 0.3	1.4 ± 0.5
<b>16:0</b>	8.8 ± 0.1	6.2 ± 0.1	5.2 ± 0.05	32.6 ± 0.3	30.7 ± 0.9	17.7 ± 1
<b>16:1</b>	4.8 ± 0.2	8.6 ± 0.1	5.7 ± 0.1	15.5 ± 0.2	12.8 ± 0.2	6.2 ± 0.8
<b>16:2</b>	0.1 ± 0.1	0	0.1 ± 0.1	0.1 ± 0.1	0	0
<b>18:0</b>	8.0 ± 0.4	11.3 ± 0.2	4.5 ± 0.1	4.8 ± 0.1	9.9 ± 0.9	38.9 ± 1.5
<b>18:1</b>	54.2 ± 0.6	40.6 ± 0.6	24.2 ± 0.9	31.4 ± 0.5	27.0 ± 0.3	26.9 ± 1.2
<b>18:2</b>	5.6 ± 0.2	4.6 ± 0.1	4.1 ± 0.4	4.9 ± 0.5	5.1 ± 0.7	2.5 ± 0.3
<b>18:3</b>	0	0.3 ± 0.1	0.5 ± 0.1	0.2 ± 0.1	0	0
<b>20:0</b>	0.2 ± 0.1	0.1 ± 0.1	0.2 ± 0.1	0.1 ± 0.1	0.2 ± 0.1	0.3 ± 0.1
<b>20:1</b>	1.1 ± 0.1	0.7 ± 0.1	2.9 ± 0.1	0.6 ± 0.1	0.6 ± 0.1	0.7 ± 0.2
<b>20:2</b>	3.4 ± 0.1	0.8 ± 0.1	3.0 ± 0.9	0.6 ± 0.1	0.7 ± 0.2	0
<b>20:3</b>	4.1 ± 0.2	4.6 ± 0.1	9.4 ± 0.8	2.2 ± 0.1	2.8 ± 0.4	1.8 ± 0.5
<b>20:4</b>	2.3 ± 0.1	15.3 ± 0.2	22.2 ± 0.7	3.6 ± 0.3	6.0 ± 0.3	2.8 ± 0.4
<b>20:5</b>	0	0.8 ± 0.1	1.1 ± 0.1	0.3 ± 0.1	0	0
<b>22:0</b>	0.2 ± 0.1	0.1 ± 0.1	0.1 ± 0.1	0	0	0
<b>22:1</b>	0	0.1 ± 0.1	1.6 ± 0.1	0.1 ± 0.1	0	0
<b>22:3</b>	0	0.4 ± 0.1	2.9 ± 0.1	0.1 ± 0.1	0.2 ± 0.1	0
<b>22:4</b>	0.7 ± 0.1	1.5 ± 0.1	5.9 ± 0.5	0.3 ± 0.1	0.4 ± 0.1	0
<b>22:5</b>	2.2 ± 0.2	2.1 ± 0.2	5.0 ± 0.4	0	0	0
<b>22:6</b>	3.9 ± 0.3	1.7 ± 0.1	1.7 ± 0.1	0.4 ± 0.1	0.7 ± 0.4	0.8 ± 0.3
<b>24:6</b>	0	0	0.1 ± 0.1	0	0	0

**Table B.2.** Fatty acid percentage composition of individual lipid classes for M1 MDMs obtained from MS<sup>E</sup> in negative ion mode.

Fatty Acid	Lipid classes					
	PG	PE	PI	PC	SM	PS
<b>14:0</b>	0.7 ± 0.1	0.4 ± 0.1	0.1 ± 0.1	3.4 ± 0.2	3.1 ± 0.1	1.4 ± 0.4
<b>16:0</b>	10.6 ± 0.5	7.8 ± 0.3	7.1 ± 0.2	32.8 ± 0.6	31.9 ± 0.5	17.9 ± 2.4
<b>16:1</b>	5.0 ± 0.3	8.9 ± 0.1	5.7 ± 0.3	16.1 ± 0.1	13.8 ± 1	6.2 ± 0.6
<b>16:2</b>	0.2 ± 0.1	0	0	0.1 ± 0.1	0	0
<b>18:0</b>	7.4 ± 0.1	10.3 ± 0.3	4.8 ± 0.4	4.3 ± 0.1	9.2 ± 1.1	39.5 ± 3.4
<b>18:1</b>	56.6 ± 1.2	41.1 ± 0.3	24.8 ± 1.4	32.0 ± 0.6	27.6 ± 0.1	26.6 ± 0.5
<b>18:2</b>	5.0 ± 0.2	4.8 ± 0.1	4.0 ± 0.1	4.8 ± 0.1	5.0 ± 0.6	2.2 ± 0.3
<b>18:3</b>	0	0.3 ± 0.1	0.3 ± 0.1	0.2 ± 0.1	0	0
<b>20:0</b>	0.2 ± 0.1	0.1 ± 0.1	0.3 ± 0.1	0	0.2 ± 0.1	0.3 ± 0.1
<b>20:1</b>	1.4 ± 0.2	1.0 ± 0.1	3.4 ± 0.1	0.7 ± 0.1	0.8 ± 0.1	1.0 ± 0.2
<b>20:2</b>	3.6 ± 0.1	1.0 ± 0.1	2.4 ± 0.1	0.5 ± 0.1	0.6 ± 0.1	0
<b>20:3</b>	4.1 ± 0.2	4.1 ± 0.1	7.6 ± 0.1	1.5 ± 0	1.8 ± 0.2	1.6 ± 0.2
<b>20:4</b>	1.8 ± 0.2	12.7 ± 0.4	18.7 ± 0.1	2.4 ± 0.1	3.8 ± 0.4	2.1 ± 0.1
<b>20:5</b>	0	0.6 ± 0.1	0.9 ± 0.1	0.2 ± 0.1	0.3 ± 0.1	0
<b>22:0</b>	0.1 ± 0.1	0.1 ± 0.1	0.1 ± 0.1	0	0	0
<b>22:1</b>	0	0.2 ± 0.1	1.9 ± 0.1	0	0	0
<b>22:3</b>	0	0.6 ± 0.1	3.6 ± 0.2	0.1 ± 0.1	0	0
<b>22:4</b>	0.6 ± 0.1	1.8 ± 0.1	6.9 ± 0.5	0.3 ± 0.1	0.5 ± 0.1	0
<b>22:5</b>	1.0 ± 0.1	2.5 ± 0.1	5.4 ± 0.4	0	0	0
<b>22:6</b>	1.6 ± 0.1	1.6 ± 0.1	1.8 ± 0.1	0.4 ± 0.1	0.7 ± 0.2	0.6 ± 0.1
<b>24:6</b>	0	0	0.1 ± 0.1	0	0	0



**Table B.3.** Fatty acid percentage composition of individual lipid classes for M2a MDMs obtained from MS<sup>E</sup> in negative ion mode.

Fatty Acid	Lipid classes					
	PG	PE	PI	PC	SM	PS
<b>14:0</b>	0.5 ± 0.1	0.2 ± 0.1	0.2 ± 0.1	2.8 ± 0.1	2.6 ± 0.1	1.2 ± 0.1
<b>16:0</b>	9.2 ± 0.3	6.7 ± 0.3	5.5 ± 0.2	31.5 ± 0.4	30.1 ± 0.7	16.1 ± 1.1
<b>16:1</b>	6.3 ± 0.2	9.6 ± 0.1	6.1 ± 0.4	18.5 ± 0.6	16.6 ± 0.4	6.8 ± 0.7
<b>16:2</b>	0.1 ± 0.1	0	0	0.1 ± 0.1	0	0
<b>18:0</b>	6.7 ± 0.2	10.3 ± 0.1	4.9 ± 0.1	3.7 ± 0.1	7.2 ± 0.2	38.9 ± 2.7
<b>18:1</b>	56.8 ± 0.5	42.6 ± 0.2	25 ± 0.6	31.7 ± 0.9	28.3 ± 0.3	28.8 ± 0.6
<b>18:2</b>	5.7 ± 0.1	0.9 ± 0.1	4.2 ± 0.2	4.6 ± 0.1	4.9 ± 0.3	2.3 ± 0.4
<b>18:3</b>	0	0.3 ± 0.1	0.4 ± 0.1	0.3 ± 0.1	0	0
<b>20:0</b>	0.2 ± 0.1	0.1 ± 0.1	0.2 ± 0.1	0	0.2 ± 0.1	0.4 ± 0.1
<b>20:1</b>	1.2 ± 0.1	0.9 ± 0.1	3.0 ± 0.2	0.6 ± 0.1	0.6 ± 0.2	0.6 ± 0.1
<b>20:2</b>	3.2 ± 0.2	1.0 ± 0.1	2.6 ± 0.1	0.5 ± 0.1	0.7 ± 0.1	0
<b>20:3</b>	3.7 ± 0.1	4.7 ± 0.1	8.7 ± 0.2	1.6 ± 0.1	2.5 ± 0.2	1.7 ± 0.3
<b>20:4</b>	2.1 ± 0.2	14.9 ± 0.3	19.1 ± 0.6	3.1 ± 0.2	4.3 ± 0.6	2.3 ± 0.3
<b>20:5</b>	0	0.8 ± 0.1	1.0 ± 0.1	0.2 ± 0.1	0.4 ± 0.1	0
<b>22:0</b>	0.1 ± 0.1	0	0.1 ± 0.1	0	0	0
<b>22:1</b>	0	0.1 ± 0.1	1.6 ± 0.1	0	0	0
<b>22:3</b>	0	0.5 ± 0.1	3.2 ± 0.1	0	0.1 ± 0.1	0
<b>22:4</b>	0.5 ± 0.1	1.6 ± 0.1	6.2 ± 0.3	0.2 ± 0.1	0.5 ± 0.1	0
<b>22:5</b>	1.2 ± 0.1	2.5 ± 0.1	5.4 ± 0.2	0	0	0
<b>22:6</b>	2.1 ± 0.2	1.9 ± 0.1	1.8 ± 0.1	0.3 ± 0.1	0.7 ± 0.1	0.7 ± 0.1
<b>24:6</b>	0	0	0.1 ± 0.1	0	0	0

**Table B.4.** Fatty acid percentage composition of individual lipid classes for M2c MDMs obtained from MS<sup>E</sup> in negative ion mode.

Fatty Acid	Lipid classes					
	PG	PE	PI	PC	SM	PS
<b>14:0</b>	0.6 ± 0.1	0.6 ± 0.1	0.2 ± 0.1	2.6 ± 0.2	2.4 ± 0.2	1.1 ± 0.2
<b>16:0</b>	8.7 ± 0.1	6.6 ± 0.1	5.7 ± 0.1	31.5 ± 0.2	30.2 ± 1.5	17.5 ± 1.2
<b>16:1</b>	5.8 ± 0.5	8.7 ± 0.1	5.6 ± 0.1	16.9 ± 0.5	15.2 ± 0.1	5.4 ± 0.7
<b>16:2</b>	0.2 ± 0.1	0	0	0.1 ± 0.1	0	0
<b>18:0</b>	7.4 ± 0.4	9.6 ± 0.2	4.7 ± 0.1	4.2 ± 0.2	8.6 ± 0.3	39.0 ± 1.1
<b>18:1</b>	54.6 ± 1.9	39.7 ± 0.1	24.7 ± 0.8	32.2 ± 0.2	27.7 ± 0.3	28.1 ± 0.4
<b>18:2</b>	6.0 ± 0.1	4.6 ± 0.1	3.7 ± 0.2	5.0 ± 0.1	5.2 ± 0.2	2.4 ± 0.2
<b>18:3</b>	0	0.3 ± 0.1	0.4 ± 0.1	0.3 ± 0.1	0	0
<b>20:0</b>	0.2 ± 0.1	0.1 ± 0.1	0.2 ± 0.1	0	0.1 ± 0.1	0.3 ± 0.1
<b>20:1</b>	1.1 ± 0.1	0.8 ± 0.1	3.0 ± 0.1	0.5 ± 0.1	0.6 ± 0.2	0.7 ± 0.1
<b>20:2</b>	3.3 ± 0.1	0.9 ± 0.1	2.3 ± 0.1	0.5 ± 0.1	0.6 ± 0.1	0
<b>20:3</b>	4.1 ± 0.1	4.6 ± 0.1	8.7 ± 0.2	1.7 ± 0.1	2.5 ± 0.2	1.9 ± 0.3
<b>20:4</b>	2.7 ± 0.6	15.6 ± 0.1	20.6 ± 0.2	3.3 ± 0.2	4.7 ± 0.2	2.5 ± 0.1
<b>20:5</b>	0	0.8 ± 0.1	1.0 ± 0.1	0.3 ± 0.1	0.6 ± 0.2	0
<b>22:0</b>	0.1 ± 0.1	0	0.1 ± 0.1	0	0	0
<b>22:1</b>	0	0.1 ± 0.1	1.6 ± 0.1	0	0	0
<b>22:3</b>	0	0.5 ± 0.1	3.1 ± 0.1	0.1 ± 0.1	0.1 ± 0.1	0
<b>22:4</b>	0.7 ± 0.1	1.7 ± 0.1	6.1 ± 0.1	0.2 ± 0.1	0.4 ± 0.1	0
<b>22:5</b>	1.6 ± 0.1	2.5 ± 0.1	5.6 ± 0.2	0	0	0
<b>22:6</b>	2.5 ± 0.2	1.8 ± 0.1	1.8 ± 0.1	0.4 ± 0.1	0.8 ± 0.1	0.8 ± 0.2
<b>24:6</b>	0	0	0.1 ± 0.1	0	0	0

**Table B.5.** Monocyte-derived macrophages phosphatidylglycerols percent composition distribution.

Species	Control	M1	M2a	M2c
PG(34:1)	9.0 ± 0.1	11.7 ± 0.3	11.9 ± 0.1	8.9 ± 0.1
PG(34:2)	7.1 ± 0.1	7.9 ± 0.1	9.2 ± 0.3	8.9 ± 0.2
PG(36:1)	8.7 ± 0.1	9.5 ± 0.2	8.3 ± 0.2	8.5 ± 0.3
PG(36:2)	43.9 ± 0.1	45.5 ± 0.3	44.4 ± 0.6	45.4 ± 0.5
PG(36:3)	8.0 ± 0.1	7.9 ± 0.3	9.0 ± 0.1	9.3 ± 0.2
PG(38:3)	6.4 ± 0.3	6.2 ± 0.3	5.8 ± 0.2	6.1 ± 0.1
PG(38:4)	6.8 ± 0.1	6.6 ± 0.1	5.8 ± 0.1	6.6 ± 0.1
PG(40:7)	9.8 ± 0.5	4.2 ± 0.4	5.2 ± 0.3	6.0 ± 0.4

**Table B.6.** Monocyte-derived macrophages phosphatidylethanolamines percent composition distribution.

Species	Control	M1	M2a	M2c
PE(32:0)	0.4 ± 0.1	0.6 ± 0.1	0.5 ± 0.1	0.5 ± 0.1
PE(32:1)	1.9 ± 0.1	2.2 ± 0.1	2.1 ± 0.1	1.9 ± 0.1
PE(33:0)	0.2 ± 0.1	0.4 ± 0.1	0.3 ± 0.1	0.3 ± 0.1
PE(33:1)	0.7 ± 0.1	1.1 ± 0.1	0.8 ± 0.1	0.9 ± 0.1
PE(33:2)	0.2 ± 0.1	0.3 ± 0.1	0.3 ± 0.1	0.4 ± 0.1
PE(34:0)	1.2 ± 0.1	1.3 ± 0.1	1.1 ± 0.1	1.1 ± 0.1
PE(34:1)	9.6 ± 0.2	10.6 ± 0.3	9.7 ± 0.2	9.1 ± 0.1
PE(34:2)	4.3 ± 0.2	4.3 ± 0.2	4.7 ± 0.1	4.4 ± 0.1
PE(34:3)	0.2 ± 0.1	0.2 ± 0.1	0.2 ± 0.1	0.2 ± 0.1
PE(35:0)	0.7 ± 0.1	1.1 ± 0.1	0.9 ± 0.1	1.1 ± 0.1
PE(35:1)	1.4 ± 0.1	1.7 ± 0.1	1.5 ± 0.1	1.4 ± 0.1
PE(35:2)	0.8 ± 0.1	1.1 ± 0.1	0.9 ± 0.1	0.9 ± 0.1
PE(35:4)	0.6 ± 0.1	0.5 ± 0.1	0.6 ± 0.1	0.6 ± 0.1
PE(35:5)	0.3 ± 0.1	0.3 ± 0.1	0.5 ± 0.1	0.6 ± 0.1
PE(36:0)	1.4 ± 0.1	1.5 ± 0.1	1.4 ± 0.1	1.3 ± 0.1
PE(36:1)	13.3 ± 0.4	13.4 ± 0.2	12.8 ± 0.1	12.1 ± 0.2
PE(36:2)	15.2 ± 0.2	15.3 ± 0.1	16 ± 0.3	15.6 ± 0.1
PE(36:3)	2.6 ± 0.1	2.6 ± 0.1	2.8 ± 0.1	2.7 ± 0.1
PE(36:4)	2.6 ± 0.1	2.3 ± 0.1	2.6 ± 0.1	2.4 ± 0.1
PE(36:5)	1.1 ± 0.1	1.3 ± 0.1	1.3 ± 0.1	1.4 ± 0.1
PE(36:6)	1.4 ± 0.2	1.5 ± 0.1	1.5 ± 0.1	1.7 ± 0.1
PE(37:1)	0.5 ± 0.1	0.7 ± 0.1	0.6 ± 0.1	0.7 ± 0.1
PE(37:4)	0.9 ± 0.1	1.1 ± 0.1	1.1 ± 0.1	1.1 ± 0.1
PE(37:5)	1.7 ± 0.3	1.9 ± 0.1	1.9 ± 0.1	2.3 ± 0.2
PE(37:6)	1.1 ± 0.1	0.9 ± 0.1	0.9 ± 0.1	1.1 ± 0.1
PE(38:2)	1.4 ± 0.1	1.5 ± 0.1	1.4 ± 0.1	1.4 ± 0.1
PE(O-38:6 or P-38-5)	5.2 ± 0.1	4.6 ± 0.1	4.9 ± 0.1	5.2 ± 0.1
PE(38:4)	13.1 ± 0.2	10.6 ± 0.1	11.4 ± 0.3	11.5 ± 0.4
PE(38:5)	5.1 ± 0.1	4.3 ± 0.1	4.9 ± 0.1	5.0 ± 0.2
PE(38:6)	1.1 ± 0.1	1.1 ± 0.1	1.2 ± 0.1	1.1 ± 0.1
PE(38:7)	0.3 ± 0.1	0.3 ± 0.1	0.2 ± 0.1	0.4 ± 0.1
PE(39:5)	0.7 ± 0.1	0.8 ± 0.1	0.8 ± 0.1	0.9 ± 0.1
PE(40:4)	0.8 ± 0.1	0.9 ± 0.1	0.8 ± 0.1	0.8 ± 0.1
PE(40:5)	1.6 ± 0.1	1.7 ± 0.1	1.5 ± 0.1	1.5 ± 0.1
PE(40:6)	2.1 ± 0.1	2.0 ± 0.1	1.9 ± 0.1	1.9 ± 0.1
PE(40:7)	1.6 ± 0.1	1.4 ± 0.1	1.5 ± 0.1	1.6 ± 0.1
PE(40:8)	0.3 ± 0.1	0.2 ± 0.1	0.3 ± 0.1	0.3 ± 0.1

**Table B.7.** Monocyte-derived macrophages phosphatidylinositols percent composition distribution.

Species	Control	M1	M2a	M2c
PI(34:1)	5.0 ± 0.6	6.2 ± 0.7	4.6 ± 0.4	5.4 ± 0.7
PI(34:2)	5.8 ± 0.4	5.8 ± 0.1	6.7 ± 0.4	7.7 ± 0.5
PI(36:2)	13.6 ± 0.4	17.6 ± 0.4	14.5 ± 0.3	15.7 ± 0.4
PI(36:3)	4.9 ± 0.2	4.8 ± 0.2	5.9 ± 0.3	5.5 ± 0.3
PI(36:4)	3.7 ± 0.1	3.5 ± 0.1	4.2 ± 0.1	3.3 ± 0.1
PI(38:2)	4.6 ± 0.1	4.1 ± 0.1	4.4 ± 0.2	4.3 ± 0.1
PI(38:3)	21.5 ± 0.7	16.9 ± 0.3	19.5 ± 0.1	19.1 ± 0.1
PI(38:4)	32.3 ± 0.4	29.9 ± 0.2	29.1 ± 0.7	28.5 ± 1.2
PI(38:5)	8.2 ± 0.3	10.8 ± 0.1	10.6 ± 0.1	10.0 ± 0.3

**Table B.8.** Monocyte-derived macrophages phosphatidylcholines percent composition distribution.

Species	Control	M1	M2a	M2c
PC(30:0)	0.6 ± 0.1	0.6 ± 0.1	0.5 ± 0.1	0.5 ± 0.1
PC(30:1)	2.1 ± 0.1	2.3 ± 0.1	1.6 ± 0.1	1.7 ± 0.1
PC(32:0)	23.0 ± 0.2	23.9 ± 0.2	23.1 ± 0.1	21.9 ± 0.1
PC(32:1)	3.7 ± 0.1	3.4 ± 0.1	2.7 ± 0.1	3.1 ± 0.1
PC(O-32:1 or P-32:0)	9.4 ± 0.1	8.9 ± 0.1	7.2 ± 0.1	8.1 ± 0.1
PC(32:2)	0.7 ± 0.1	0.6 ± 0.1	0.6 ± 0.1	0.6 ± 0.1
PC(32:4)	1.3 ± 0.1	1.5 ± 0.1	1.4 ± 0.1	1.3 ± 0.1
PC(33:0)	0.7 ± 0.1	0.7 ± 0.1	0.7 ± 0.1	0.7 ± 0.1
PC(33:1)	14.8 ± 0.2	14.8 ± 0.2	14.6 ± 0.2	15.6 ± 0.1
PC(34:0)	1.5 ± 0.1	2.5 ± 0.1	1.8 ± 0.1	1.6 ± 0.1
PC(34:1)	0.6 ± 0.1	0.6 ± 0.1	0.7 ± 0.1	0.6 ± 0.1
PC(34:2)	0.7 ± 0.1	0.6 ± 0.1	0.6 ± 0.1	0.6 ± 0.1
PC(34:3)	10.7 ± 0.1	11.8 ± 0.1	12.9 ± 0.3	11.5 ± 0.1
PC(34:4)	0.3 ± 0.1	0.3 ± 0.1	0.2 ± 0.1	0.2 ± 0.1
PC(35:0)	2.1 ± 0.1	1.8 ± 0.1	1.8 ± 0.1	2.1 ± 0.1
PC(35:1)	0.4 ± 0.1	0.5 ± 0.1	0.4 ± 0.1	0.4 ± 0.1
PC(36:0)	11.6 ± 0.1	11.1 ± 0.1	12.8 ± 0.1	12.6 ± 0.1
PC(36:1)	5.2 ± 0.1	4.9 ± 0.1	5.6 ± 0.1	5.5 ± 0.1
PC(36:2)	0.5 ± 0.1	0.4 ± 0.1	0.5 ± 0.1	0.5 ± 0.1
PC(36:3)	4.6 ± 0.1	4.1 ± 0.1	4.2 ± 0.1	4.7 ± 0.1
PC(36:4)	0.6 ± 0.1	0.5 ± 0.1	0.8 ± 0.1	0.8 ± 0.1
PC(38:2)	0.4 ± 0.1	0.3 ± 0.1	0.3 ± 0.1	0.4 ± 0.1
PC(38:3)	0.5 ± 0.1	0.4 ± 0.1	0.5 ± 0.1	0.5 ± 0.1
PC(38:4)	1.5 ± 0.1	1.2 ± 0.1	2.1 ± 0.1	1.8 ± 0.1
PC(38:5)	0.5 ± 0.1	0.4 ± 0.1	0.4 ± 0.1	0.4 ± 0.1
PC(40:5)	1.1 ± 0.1	0.8 ± 0.1	0.9 ± 0.1	0.9 ± 0.1

**Table B.9.** Monocyte-derived macrophages sphingomyelins percent composition distribution.

Species	Control	M1	M2a	M2c
SM(d32:0)	12.4 ± 0.5	13.1 ± 0.1	12.2 ± 0.4	12.1 ± 0.1
SM(d32:1)	40.6 ± 0.1	40.9 ± 0.2	40.2 ± 0.1	40.6 ± 0.7
SM(d33:1)	19.6 ± 0.7	20.2 ± 0.3	19.9 ± 0.4	19.5 ± 0.7
SM(d41:1)	3.7 ± 0.1	3.4 ± 0.1	3.8 ± 0.1	3.8 ± 0.1
SM(d41:2)	5.6 ± 0.4	5.1 ± 0.1	5.9 ± 0.3	5.8 ± 0.3
SM(d42:1)	4.5 ± 0.1	4.1 ± 0.1	4.5 ± 0.1	4.4 ± 0.2
SM(d42:2)	7.5 ± 0.3	6.8 ± 0.3	7.6 ± 0.7	7.7 ± 0.3

**Table B.10.** Monocyte-derived macrophages phosphatidylserines percent composition distribution.

Species	Control	M1	M2a	M2c
PS(34:1)	10.9 ± 0.4	12.2 ± 0.3	12.2 ± 0.9	11.8 ± 0.4
PS(36:1)	55.9 ± 0.8	53.4 ± 0.1	53.5 ± 0.4	52.9 ± 0.5
PS(36:2)	10.6 ± 0.1	11.7 ± 0.1	11.6 ± 0.2	12.3 ± 0.2
PS(38:3)	6.1 ± 0.1	6.1 ± 0.2	6.3 ± 0.1	6.4 ± 0.4
PS(38:4)	13.0 ± 0.3	12.5 ± 0.2	12.5 ± 0.1	12.7 ± 0.5
PS(40:5)	3.2 ± 0.1	3.9 ± 0.1	3.6 ± 0.1	3.6 ± 0.2



APPENDIX C

SUPPORTING INFORMATION FOR CHAPTER III

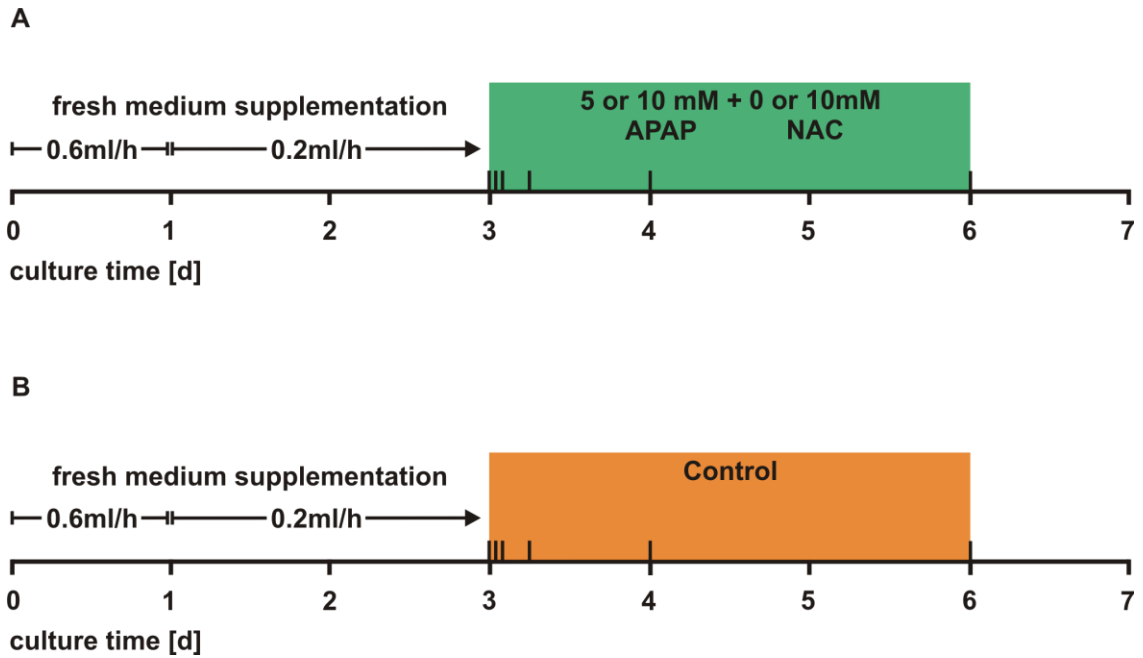


**Figure C.1.** A) Time course of A) APAP and NAC stimulus and B) control bioreactor experiments in primary human hepatocyte cultures maintained in 3D bioreactors.

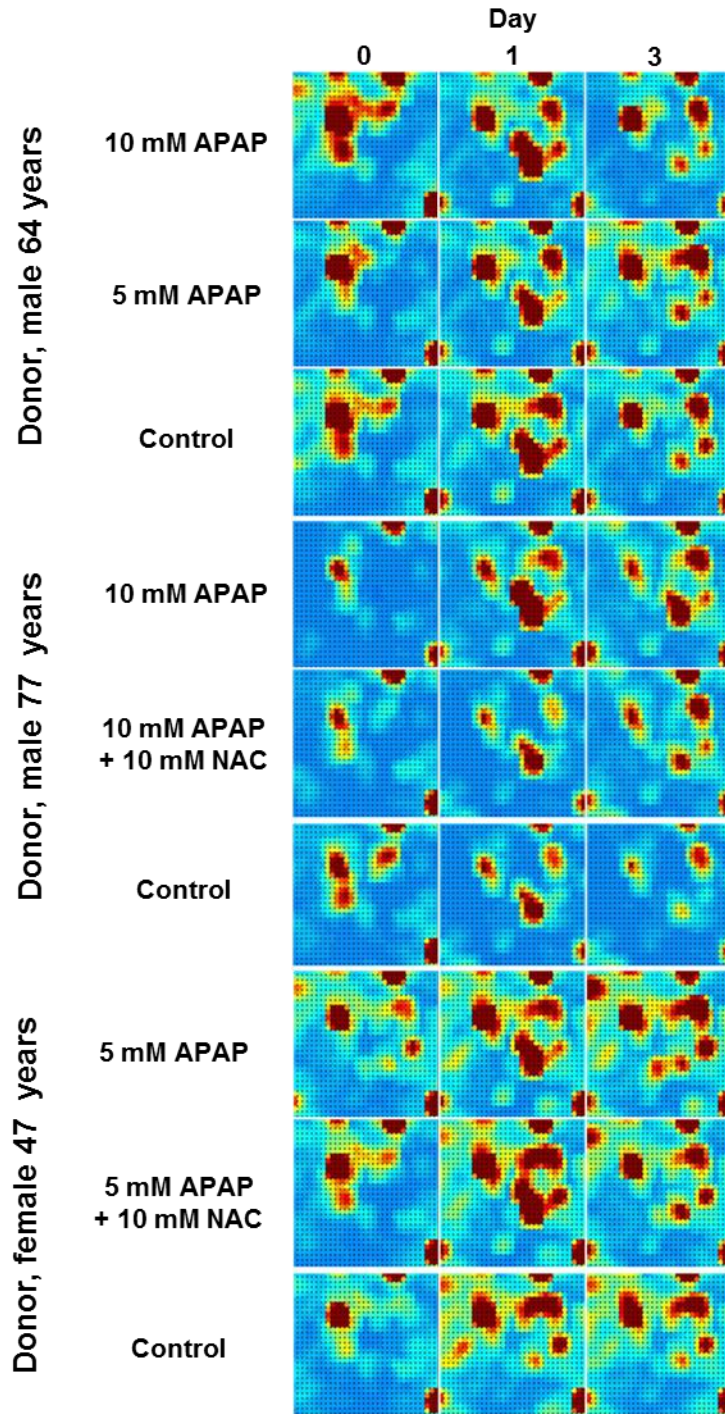


**Figure C.2.** SOM of first three days after LBR cell inoculation without baseline subtraction. At this point no LBR has been treated. Different LBR with cells from same donor show similar evolution through the 3 time points (horizontal comparison). Some similarities are also observed for all 9 LBRs at the same time point (vertical comparison).

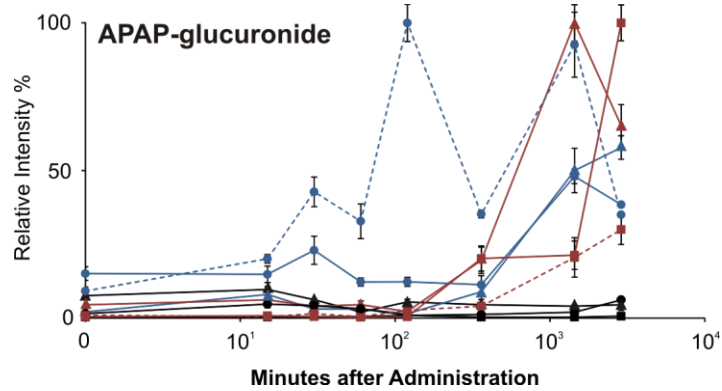


**Figure C.3.** APAP-glucuronide (ROI 4) time profiles after drug exposure with relative intensity calculated to maximum value measured in liver bioreactors inoculated with cells from the same donor. Donor age 77 (circles), 64 (triangles) and 47 (squares). Control (black), 10 mM APAP (blue), 5mM APAP (red). 10 mM NAC (dashed line).

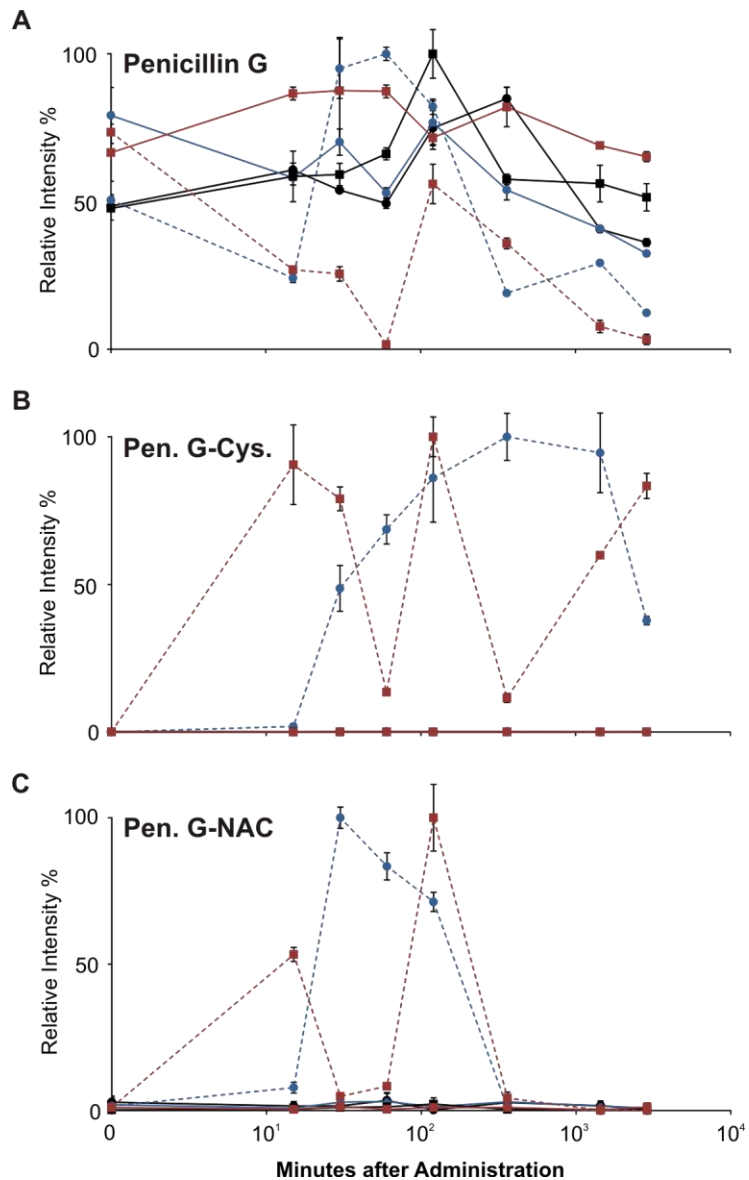


**Figure C.4.** Penicillin G compounds time profiles after drug exposure with relative intensity calculated to maximum value measured in liver bioreactors inoculated with cells from the same donor. Donor age 77 (circles) and 47 (squares). Control (black), 10 mM APAP (blue), 5 mM APAP (red). 10 mM NAC (dashed line). A) Penicillin G seeded in region 6. LBRs treated with NAC profile drops after 24 and 72 hours. B) Penicillin G-cysteine (Pen. G-Cys.) was grouped in region 7 with Ox-NAC. C) Penicillin G-NAC (Pen. G-NAC) has a profile closer related to APAP-NAC (grouped in ROI 8).

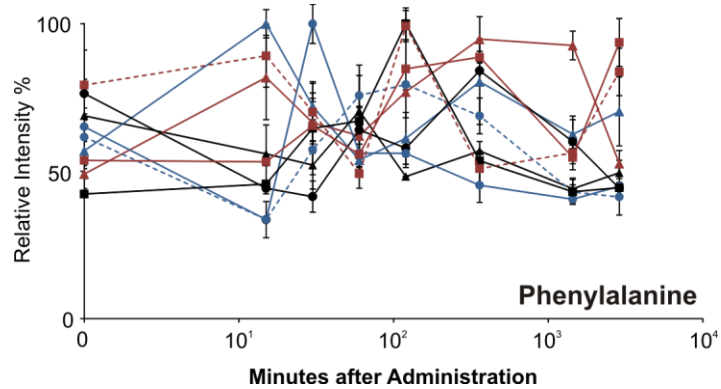


**Figure C.5.** Phenylalanine time profiles after drug exposure with relative intensity calculated to maximum value measured in liver bioreactors inoculated with cells from the same donor (ROI 2). Donor age 77 (circles), 64 (triangles) and 47 (squares). Control (black), 10 mM APAP (blue), 5 mM APAP (red), 10 mM NAC (dashed line).

**Table C.1.** Metabolites from ROIs in single chemical stimulus indicated in Figure 3.4.

Metabolite	ROI	Mass Accuracy (ppm)	Database/Reference
APAP	1	3.9	METLIN and Standard material
3,3'-Biacetaminophen	1	3.3	Ref. <sup>17</sup>
Phenylalanine	2	5.8	METLIN and Standard material
Arginine	3	1.1	METLIN and Standard material
APAP-sulfate	4	3.8	Ref. <sup>17</sup>
APAP-glucuronide	4	6.6	Ref. <sup>17</sup>
Penicillin G	5	0.6	Ref. <sup>18</sup>
Streptomycin -cysteine	6	1.6	METLN (separated)
Ox-NAC	7	4.3	Standard material
Penicillin G- cysteine	7	2.2	Ref. <sup>18</sup> and METLIN
APAP-NAC	8	8.7	METLIN and Standard Material
Penicillin G-NAC	8	1.4	Ref. <sup>18</sup> and Standard Material

**Table C.2.** Intensities, standard deviation and fold-changes for APAP from Patient 77

Patient age (years)	Treatment	Time point	Intensity	Standard Dev.	Fold change (compared to control)
77	Control	0	14217	3843	-
		15 min	16497	881	-
		30 min	15003	1000	-
		1 h	16247	1696	-
		2 h	14627	714	-
		6 h	14467	400	-
		24 h	15037	2183	-
		72 h	14359	233	-
77	10 mM APAP	0	12394	455	1
		15 min	471208	76511	29
		30 min	559935	10699	37
		1 h	558597	34342	34
		2 h	510845	39708	35
		6 h	603762	9507	42
		24 h	484631	864	32
		72 h	448827	22588	31
77	10 mM APAP + NAC	0	15564	783	1
		15 min	457098	5419	28
		30 min	423933	32793	28
		1 h	650636	20788	40
		2 h	537507	40371	37
		6 h	555148	15015	38
		24 h	487569	15854	32
		72 h	485677	3775	34

**Table C.3.** Intensities, standard deviation and fold-changes for APAP from Patient 64

Patient age (years)	Treatment	Time point	Intensity	Standard Dev.	Fold change (compared to control)
64	Control	0	10933	588	-
		15 min	13422	85	-
		30 min	9013	128	-
		1 h	9892	619	-
		2 h	11320	9	-
		6 h	7724	913	-
		24 h	9987	1375	-
		72 h	9922	948	-
64	5 mM APAP	0	11158	2523	1
		15 min	818114	73863	61
		30 min	726587	34451	81
		1 h	506924	78395	51
		2 h	464200	15789	41
		6 h	314662	16084	41
		24 h	370727	7130	37
		72 h	469217	12978	47
64	10 mM APAP	0	9816	1913	1
		15 min	835869	36553	62
		30 min	874999	39830	97
		1 h	606717	48615	61
		2 h	744140	46649	66
		6 h	772915	65134	100
		24 h	716844	14373	72
		72 h	629029	22004	63



**Table C.4.** Intensities, standard deviation and fold-changes for APAP from Patient 47

Patient age (years)	Treatment	Time point	Intensity	Standard Dev.	Fold change (compared to control)
47	Control	0	11444	743	-
		15 min	11765	726	-
		30 min	8708	1200	-
		1 h	12606	2543	-
		2 h	8621	191	-
		6 h	10281	3743	-
		24 h	9933	1978	-
		72 h	10114	1451	-
47	5 mM APAP	0	10834	617	1
		15 min	935562	10984	80
		30 min	556676	61198	64
		1 h	560266	2537	44
		2 h	360168	41657	42
		6 h	384825	36705	37
		24 h	303907	13658	31
		72 h	315689	16211	31
47	5 mM APAP + 10 mM NAC	0	9090	829	1
		15 min	753416	27997	64
		30 min	401047	73919	46
		1 h	368480	12224	29
		2 h	292710	12557	34
		6 h	753567	53519	73
		24 h	333144	29714	34
		72 h	266967	23552	26

**Table C.5.** Intensities, standard deviation and fold-changes for 3,3'-Biacetaminophen from Patient 77

Patient age (years)	Treatment	Time point	Intensity	Standard Dev.	Fold change (compared to control)
77	Control	0	1698	437	-
		15 min	3658	1779	-
		30 min	4965	1310	-
		1 h	2377	826	-
		2 h	1904	124	-
		6 h	1912	124	-
		24 h	1557	358	-
		72 h	1438	181	-
77	10 mM APAP	0	2288	375	1
		15 min	132312	12123	36
		30 min	160086	2507	32
		1 h	202462	19474	85
		2 h	137358	6489	72
		6 h	184326	7551	96
		24 h	118693	15038	76
		72 h	115202	7045	80
77	10 mM APAP + NAC	0	2018	279	1
		15 min	40310	4245	11
		30 min	62049	7753	12
		1 h	123915	6312	52
		2 h	56087	10941	29
		6 h	83209	10180	44
		24 h	54329	9639	35
		72 h	79832	3335	56

**Table C.6.** Intensities, standard deviation and fold-changes for 3,3'-Biacetaminophen from Patient 64

Patient age (years)	Treatment	Time point	Intensity	Standard Dev.	Fold change (compared to control)
64	Control	0	1837	141	-
		15 min	1578	274	-
		30 min	1774	139	-
		1 h	1765	38	-
		2 h	1556	115	-
		6 h	1625	155	-
		24 h	1429	68	-
		72 h	1469	62	-
64	5 mM APAP	0	1382	432	1
		15 min	190746	10679	121
		30 min	118959	6959	67
		1 h	81222	7031	46
		2 h	79352	3500	51
		6 h	69306	7285	43
		24 h	71951	3887	50
		72 h	57910	1574	39
64	10 mM APAP	0	2008	67	1
		15 min	234507	19520	149
		30 min	201145	3417	113
		1 h	187728	12749	106
		2 h	153054	12293	98
		6 h	159912	3331	98
		24 h	137293	12017	96
		72 h	100683	4388	69

**Table C.7.** Intensities, standard deviation and fold-changes for 3,3'-Biacetaminophen from Patient 47

Patient age (years)	Treatment	Time point	Intensity	Standard Dev.	Fold change (compared to control)
47	Control	0	1052	37	-
		15 min	1046	88	-
		30 min	1201	223	-
		1 h	766	221	-
		2 h	1505	199	-
		6 h	1115	89	-
		24 h	1060	108	-
		72 h	846	4	-
47	5 mM APAP	0	1920	429	2
		15 min	420156	2322	402
		30 min	256456	46395	214
		1 h	196048	227	256
		2 h	217945	4272	145
		6 h	202957	34837	182
		24 h	77139	5617	73
		72 h	66999	12092	79
47	5 mM APAP + 10 mM NAC	0	873	31	1
		15 min	12086	2271	12
		30 min	42519	4093	35
		1 h	38245	5574	50
		2 h	24824	3262	16
		6 h	38013	1660	34
		24 h	32190	517	30
		72 h	27900	4388	33

**Table C.8.** Intensities, standard deviation and fold-changes for Phenylalanine from Patient 77

Patient age (years)	Treatment	Time point	Intensity	Standard Dev.	Fold change (compared to control)
77	Control	0	977040	62580	-
		15 min	566092	23963	-
		30 min	529862	67837	-
		1 h	819285	17942	-
		2 h	740438	36990	-
		6 h	1076366	66579	-
		24 h	768309	95664	-
		72 h	566296	13166	-
77	10 mM APAP	0	833196	167876	1
		15 min	430033	78756	1
		30 min	1280034	85211	2
		1 h	718906	73486	1
		2 h	717487	61318	1
		6 h	579223	74222	1
		24 h	518486	14772	1
		72 h	574965	16562	1
77	10 mM APAP + NAC	0	788530	180833	1
		15 min	431250	5110	1
		30 min	733276	77653	1
		1 h	968616	131906	1
		2 h	1016462	11484	1
		6 h	880157	77540	1
		24 h	549990	53879	1
		72 h	528508	6331	1

**Table C.9.** Intensities, standard deviation and fold-changes for Phenylalanine from Patient 64

Patient age (years)	Treatment	Time point	Intensity	Standard Dev.	Fold change (compared to control)
64	Control	0	696726	6426	-
		15 min	565871	99094	-
		30 min	527079	81823	-
		1 h	713396	15683	-
		2 h	488158	494	-
		6 h	576057	32464	-
		24 h	446229	36697	-
		72 h	501032	20278	-
64	5 mM APAP	0	496905	50195	1
		15 min	828280	144791	1
		30 min	672615	72437	1
		1 h	628294	96478	1
		2 h	778622	7186	2
		6 h	959869	77206	2
		24 h	938160	49344	2
		72 h	532950	44572	1
64	10 mM APAP	0	576505	31675	1
		15 min	1012546	48573	2
		30 min	729072	46229	1
		1 h	544780	25743	1
		2 h	619168	88631	1
		6 h	813559	146781	1
		24 h	633260	62580	1
		72 h	711704	118510	1

**Table C.10.** Intensities, standard deviation and fold-changes for Phenylalanine from Patient 47

Patient age (years)	Treatment	Time point	Intensity	Standard Dev.	Fold change (compared to control)
47	Control	0	435564	7907	-
		15 min	470414	471	-
		30 min	665260	162623	-
		1 h	690277	158950	-
		2 h	1029969	55480	-
		6 h	551439	2091	-
		24 h	443436	24092	-
		72 h	457624	95731	-
47	5 mM APAP	0	552947	29138	1
		15 min	548104	13639	1
		30 min	674082	95526	1
		1 h	573892	35537	1
		2 h	872372	170690	1
		6 h	913432	20589	2
		24 h	563054	43164	1
		72 h	964871	83469	2
47	5 mM APAP + 10 mM NAC	0	815904	122333	2
		15 min	918113	109707	2
		30 min	721574	100309	1
		1 h	506147	50672	1
		2 h	1021825	54640	1
		6 h	524104	62157	1
		24 h	578714	15653	1
		72 h	862052	82884	2

**Table C.11.** Intensities, standard deviation and fold-changes for Arginine from Patient 77

Patient age (years)	Treatment	Time point	Intensity	Standard Dev.	Fold change (compared to control)
77	Control	0	1345457	204649	-
		15 min	410556	53621	-
		30 min	385843	79624	-
		1 h	1128906	165392	-
		2 h	836071	159868	-
		6 h	1575771	155031	-
		24 h	659176	160444	-
		72 h	477120	39	-
77	10 mM APAP	0	679689	188946	1
		15 min	391769	66499	1
		30 min	1374971	205989	4
		1 h	643168	217953	1
		2 h	1331008	159689	2
		6 h	498126	176045	0
		24 h	421690	16066	1
		72 h	382892	9507	1
77	10 mM APAP + NAC	0	939920	222194	1
		15 min	460387	56465	1
		30 min	737364	115520	2
		1 h	689806	60491	1
		2 h	1318750	213927	2
		6 h	1157185	72724	1
		24 h	657610	193914	1
		72 h	419117	3905	1



**Table C.12.** Intensities, standard deviation and fold-changes for Arginine from Patient 64

Patient age (years)	Treatment	Time point	Intensity	Standard Dev.	Fold change (compared to control)
64	Control	0	611381	33558	-
		15 min	440632	81226	-
		30 min	427186	67058	-
		1 h	1058685	74537	-
		2 h	414480	20956	-
		6 h	444487	4525	-
		24 h	411625	60369	-
		72 h	453469	5042	-
64	5 mM APAP	0	295212	47909	0
		15 min	489477	190521	1
		30 min	408092	128711	1
		1 h	436776	161277	0
		2 h	781667	33644	2
		6 h	1411024	116897	3
		24 h	947004	77754	2
		72 h	348591	1958	1
64	10 mM APAP	0	347771	45955	1
		15 min	697392	38308	2
		30 min	640884	26098	2
		1 h	396671	59735	0
		2 h	535752	117984	1
		6 h	850847	7810	2
		24 h	384354	18217	1
		72 h	321247	52916	1

**Table C.13.** Intensities, standard deviation and fold-changes for Arginine from Patient 47

Patient age (years)	Treatment	Time point	Intensity	Standard Dev.	Fold change (compared to control)
47	Control	0	310698	9919	-
		15 min	305709	12472	-
		30 min	923126	67562	-
		1 h	877311	63296	-
		2 h	872248	76009	-
		6 h	322164	1670	-
		24 h	349778	22754	-
		72 h	362761	20298	-
47	5 mM APAP	0	472213	77725	2
		15 min	335504	11411	1
		30 min	863497	50269	1
		1 h	285254	24020	0
		2 h	950137	129293	1
		6 h	1175813	84731	4
		24 h	368292	24562	1
		72 h	831213	60487	2
47	5 mM APAP + 10 mM NAC	0	694795	100882	2
		15 min	1010159	125652	3
		30 min	906995	21706	1
		1 h	379956	2474	0
		2 h	1309121	80285	2
		6 h	416396	50596	1
		24 h	683310	148653	2
		72 h	965813	176239	3

**Table C.14.** Intensities, standard deviation and fold-changes for APAP-sulfate from Patient 77

Patient age (years)	Treatment	Time point	Intensity	Standard Dev.	Fold change (compared to control)
77	Control	0	6326	260	-
		15 min	7496	523	-
		30 min	6157	246	-
		1 h	5617	59	-
		2 h	9676	564	-
		6 h	7979	297	-
		24 h	5224	400	-
		72 h	5021	588	-
77	10 mM APAP	0	8422	266	1
		15 min	6260	94	1
		30 min	7326	465	1
		1 h	5091	21	1
		2 h	4587	745	0
		6 h	12049	784	2
		24 h	37185	528	7
		72 h	32478	810	6
77	10 mM APAP + NAC	0	5538	217	1
		15 min	2404	24	0
		30 min	1986	102	0
		1 h	2653	73	0
		2 h	5969	163	1
		6 h	35670	1152	4
		24 h	80598	5650	15
		72 h	64900	4020	13

**Table C.15.** Intensities, standard deviation and fold-changes for APAP-sulfate from Patient 64

Patient age (years)	Treatment	Time point	Intensity	Standard Dev.	Fold change (compared to control)
64	Control	0	6762	146	-
		15 min	7849	399	-
		30 min	5881	425	-
		1 h	7363	499	-
		2 h	6367	581	-
		6 h	6481	145	-
		24 h	7057	1095	-
		72 h	4230	88	-
64	5 mM APAP	0	8258	335	1
		15 min	7295	413	1
		30 min	6613	539	1
		1 h	5517	260	1
		2 h	7377	932	1
		6 h	25912	3688	4
		24 h	102704	5746	15
		72 h	97275	5245	23
64	10 mM APAP	0	8166	640	1
		15 min	8473	1081	1
		30 min	8343	171	1
		1 h	4918	436	1
		2 h	8656	269	1
		6 h	22501	1858	3
		24 h	52542	5506	7
		72 h	21600	2708	5

**Table C.16.** Intensities, standard deviation and fold-changes for APAP-sulfate from Patient 47

Patient age (years)	Treatment	Time point	Intensity	Standard Dev.	Fold change (compared to control)
47	Control	0	682	17	-
		15 min	773	49	-
		30 min	688	128	-
		1 h	919	14	-
		2 h	2537	363	-
		6 h	810	27	-
		24 h	763	161	-
		72 h	765	117	-
47	5 mM APAP	0	766	2	1
		15 min	938	110	1
		30 min	2489	311	4
		1 h	1873	244	2
		2 h	4261	787	2
		6 h	31458	1835	39
		24 h	92311	7375	121
		72 h	127447	8647	167
47	5 mM APAP + 10 mM NAC	0	1120	306	2
		15 min	934	589	1
		30 min	835	174	1
		1 h	1816	387	2
		2 h	7767	826	3
		6 h	47144	5420	58
		24 h	128306	1189	168
		72 h	148508	4534	194

**Table C.17.** Intensities, standard deviation and fold-changes for APAP-glucuronide from Patient 77

Patient age (years)	Treatment	Time point	Intensity	Standard Dev.	Fold change (compared to control)
77	Control	0	1964	243	-
		15 min	5957	1494	-
		30 min	5302	89	-
		1 h	3977	1574	-
		2 h	1199	27	-
		6 h	1562	568	-
		24 h	2528	500	-
		72 h	7773	524	-
77	10 mM APAP	0	18969	2868	10
		15 min	18628	3468	3
		30 min	28883	6006	5
		1 h	15369	1680	4
		2 h	15434	1875	13
		6 h	14211	3856	9
		24 h	60275	3076	24
		72 h	48302	1075	6
77	10 mM APAP + NAC	0	11537	1663	6
		15 min	25233	1842	4
		30 min	53730	6286	10
		1 h	41225	7374	10
		2 h	125608	7941	105
		6 h	44289	1590	28
		24 h	116332	13817	46
		72 h	44023	513	6

**Table C.18.** Intensities, standard deviation and fold-changes for APAP-glucuronide from Patient 64

Patient age (years)	Treatment	Time point	Intensity	Standard Dev.	Fold change (compared to control)
64	Control	0	7899	1438	-
		15 min	10073	1013	-
		30 min	6495	251	-
		1 h	2131	181	-
		2 h	5703	934	-
		6 h	4725	373	-
		24 h	4219	397	-
		72 h	4707	2069	-
64	5 mM APAP	0	4678	441	1
		15 min	6401	1899	1
		30 min	4175	1996	1
		1 h	4732	1301	2
		2 h	2339	61	0
		6 h	20334	4620	4
		24 h	103776	6387	25
		72 h	67610	7445	14
64	10 mM APAP	0	2195	215	0
		15 min	8328	844	1
		30 min	3206	201	0
		1 h	3196	1380	1
		2 h	1553	199	0
		6 h	9283	2683	2
		24 h	51897	7817	12
		72 h	59968	4122	13

**Table C.19.** Intensities, standard deviation and fold-changes for APAP-glucuronide from Patient 47

Patient age (years)	Treatment	Time point	Intensity	Standard Dev.	Fold change (compared to control)
47	Control	0	909	108	-
		15 min	836	203	-
		30 min	1521	641	-
		1 h	1307	295	-
		2 h	2361	429	-
		6 h	871	29	-
		24 h	879	74	-
		72 h	1664	944	-
47	5 mM APAP	0	1163	375	1
		15 min	2047	199	2
		30 min	1270	152	1
		1 h	735	14	1
		2 h	1199	271	1
		6 h	51097	10794	59
		24 h	53933	12205	61
		72 h	253105	15368	152
47	5 mM APAP + 10 mM NAC	0	2441	2292	3
		15 min	1314	40	2
		30 min	3824	3361	3
		1 h	1303	289	1
		2 h	6662	1550	3
		6 h	10292	1200	12
		24 h	52033	16945	59
		72 h	75966	12833	46



**Table C.20.** Intensities, standard deviation and fold-changes for Penicillin G from Patient 77

Patient age (years)	Treatment	Time point	Intensity	Standard Dev.	Fold change (compared to control)
77	Control	0	226047	6780	-
		15 min	283327	10888	-
		30 min	251338	1228	-
		1 h	230408	7943	-
		2 h	349440	27626	-
		6 h	395965	17882	-
		24 h	189849	5081	-
		72 h	168579	6084	-
77	10 mM APAP	0	369482	44299	2
		15 min	270959	11528	1
		30 min	327306	20768	1
		1 h	247271	7916	1
		2 h	358094	34446	1
		6 h	251624	15654	1
		24 h	190686	2198	1
		72 h	151205	4103	1
77	10 mM APAP + NAC	0	235584	8585	1
		15 min	112568	7065	0
		30 min	443343	47030	2
		1 h	466668	10507	2
		2 h	383254	12077	1
		6 h	88729	361	0
		24 h	136216	392	1
		72 h	57494	270	0

**Table C.21.** Intensities, standard deviation and fold-changes for Penicillin G from Patient 64

Patient age (years)	Treatment	Time point	Intensity	Standard Dev.	Fold change (compared to control)
64	Control	0	274427	13290	-
		15 min	316398	14713	-
		30 min	243393	27461	-
		1 h	289313	21204	-
		2 h	229946	12623	-
		6 h	249083	12056	-
		24 h	295003	35491	-
		72 h	173425	11077	-
64	5 mM APAP	0	304603	20025	1
		15 min	307710	19191	1
		30 min	281029	8990	1
		1 h	247968	18770	1
		2 h	269255	120	1
		6 h	264745	14517	1
		24 h	254722	13700	1
		72 h	235465	3268	1
64	10 mM APAP	0	324034	26016	1
		15 min	309327	7538	1
		30 min	316134	1567	1
		1 h	302298	11182	1
		2 h	310863	13403	1
		6 h	322924	2664	1
		24 h	287316	9845	1
		72 h	214447	14771	1

**Table C.22.** Intensities, standard deviation and fold-changes for Penicillin G from Patient 47

Patient age (years)	Treatment	Time point	Intensity	Standard Dev.	Fold change (compared to control)
47	Control	0	55974	4656	-
		15 min	68675	10056	-
		30 min	69429	4430	-
		1 h	77630	2394	-
		2 h	117348	9669	-
		6 h	67499	2056	-
		24 h	65816	7296	-
		72 h	60355	5420	-
47	5 mM APAP	0	78124	11359	1
		15 min	101574	2537	1
		30 min	102735	21141	1
		1 h	102441	2542	1
		2 h	84030	4607	1
		6 h	96240	7856	1
		24 h	80938	427	1
		72 h	76488	1975	1
47	5 mM APAP + 10 mM NAC	0	86201	8018	2
		15 min	31615	1035	0
		30 min	29953	2878	0
		1 h	1928	118	0
		2 h	65663	7809	1
		6 h	42069	2140	1
		24 h	9076	2453	0
		72 h	3894	2036	0

**Table C.23.** Intensities, standard deviation and fold-changes for Streptomycin -cysteine from Patient 77

Patient age (years)	Treatment	Time point	Intensity	Standard Dev.	Fold change (compared to control)
77	Control	0	9515	1864	-
		15 min	6564	154	-
		30 min	2588	80	-
		1 h	12130	523	-
		2 h	2545	1472	-
		6 h	1682	119	-
		24 h	6583	1465	-
		72 h	467	269	-
77	10 mM APAP	0	9369	1967	1
		15 min	2070	331	0
		30 min	18197	6064	7
		1 h	16725	3734	1
		2 h	8965	6094	4
		6 h	20253	1208	12
		24 h	14813	147	2
		72 h	1963	75	4
77	10 mM APAP + NAC	0	6402	4361	1
		15 min	3034	1327	0
		30 min	79392	18617	31
		1 h	95281	31711	8
		2 h	207691	27640	82
		6 h	543754	36371	323
		24 h	783305	21390	119
		72 h	471220	14968	1008

**Table C.24.** Intensities, standard deviation and fold-changes for Streptomycin -cysteine from Patient 64

Patient age (years)	Treatment	Time point	Intensity	Standard Dev.	Fold change (compared to control)
64	Control	0	1224	762	-
		15 min	1457	1701	-
		30 min	3224	5079	-
		1 h	3239	2564	-
		2 h	1474	1886	-
		6 h	419	126	-
		24 h	389	88	-
		72 h	4015	6098	-
64	5 mM APAP	0	8422	5	7
		15 min	943	205	1
		30 min	607	192	0
		1 h	8497	110	3
		2 h	931	438	1
		6 h	8320	2003	20
		24 h	6135	358	16
		72 h	3718	19	1
64	10 mM APAP	0	609	146	0
		15 min	744	42	1
		30 min	692	125	0
		1 h	2797	79	1
		2 h	899	75	1
		6 h	1202	100	3
		24 h	8154	74	21
		72 h	3831	41	1

**Table C.25.** Intensities, standard deviation and fold-changes for Streptomycin -cysteine from Patient 47

Patient age (years)	Treatment	Time point	Intensity	Standard Dev.	Fold change (compared to control)
47	Control	0	386	25	-
		15 min	450	187	-
		30 min	3479	191	-
		1 h	3885	197	-
		2 h	3137	278	-
		6 h	519	129	-
		24 h	393	140	-
		72 h	2112	4	-
47	5 mM APAP	0	5612	80	15
		15 min	410	109	1
		30 min	1502	84	0
		1 h	344	121	0
		2 h	2649	70	1
		6 h	1616	330	3
		24 h	3966	72	10
		72 h	4730	312	2
47	5 mM APAP + 10 mM NAC	0	2051	28	5
		15 min	123487	1751	275
		30 min	295702	32525	85
		1 h	511	69	0
		2 h	71312	3800	23
		6 h	1550	149	3
		24 h	378139	12006	962
		72 h	407757	8710	193

**Table C.26.** Intensities, standard deviation and fold-changes for Ox-NAC from Patient 77

Patient age (years)	Treatment	Time point	Intensity	Standard Dev.	Fold change (compared to control)
77	Control	0	3133	888	-
		15 min	2377	499	-
		30 min	1934	383	-
		1 h	4601	1004	-
		2 h	494	102	-
		6 h	2521	346	-
		24 h	3201	920	-
		72 h	1250	327	-
77	10 mM APAP	0	3776	479	1
		15 min	1700	727	1
		30 min	3228	581	2
		1 h	1887	66	0
		2 h	4922	201	10
		6 h	2761	888	1
		24 h	2360	45	1
		72 h	1124	72	1
77	10 mM APAP + NAC	0	2868	849	1
		15 min	126551	24682	53
		30 min	1013909	116030	524
		1 h	1058428	131450	230
		2 h	1109359	104106	2246
		6 h	1113304	125592	442
		24 h	679229	40134	212
		72 h	834836	43395	668

**Table C.27.** Intensities, standard deviation and fold-changes for Ox-NAC from Patient 64

Patient age (years)	Treatment	Time point	Intensity	Standard Dev.	Fold change (compared to control)
64	Control	0	850	44	-
		15 min	2322	724	-
		30 min	1863	101	-
		1 h	1234	28	-
		2 h	4389	349	-
		6 h	703	297	-
		24 h	1217	476	-
		72 h	3560	4113	-
64	5 mM APAP	0	2024	233	2
		15 min	1179	300	1
		30 min	1310	261	1
		1 h	1605	141	1
		2 h	564	96	0
		6 h	2366	773	3
		24 h	2815	1133	2
		72 h	2888	705	1
64	10 mM APAP	0	975	375	1
		15 min	1330	442	1
		30 min	622	15	0
		1 h	822	296	1
		2 h	536	240	0
		6 h	1230	171	2
		24 h	1534	126	1
		72 h	2191	144	1



**Table C.28.** Intensities, standard deviation and fold-changes for Ox-NAC from Patient 47

Patient age (years)	Treatment	Time point	Intensity	Standard Dev.	Fold change (compared to control)
47	Control	0	789	74	-
		15 min	849	142	-
		30 min	2063	1803	-
		1 h	2078	2232	-
		2 h	2397	2304	-
		6 h	398	344	-
		24 h	871	234	-
		72 h	3098	2193	-
47	5 mM APAP	0	4004	3842	5
		15 min	634	56	1
		30 min	699	50	0
		1 h	589	177	0
		2 h	2112	1805	1
		6 h	2172	1596	5
		24 h	9710	15290	11
		72 h	7059	8097	2
47	5 mM APAP + 10 mM NAC	0	1959	81	2
		15 min	840655	94263	990
		30 min	861683	83236	418
		1 h	86020	571	41
		2 h	1048192	130420	437
		6 h	103043	2936	259
		24 h	694240	74720	797
		72 h	1244319	139659	402

**Table C.29.** Intensities, standard deviation and fold-changes for Penicillin G- cysteine from Patient 77

Patient age (years)	Treatment	Time point	Intensity	Standard Dev.	Fold change (compared to control)
77	Control	0	774	792	-
		15 min	360	366	-
		30 min	452	147	-
		1 h	580	393	-
		2 h	338	156	-
		6 h	553	396	-
		24 h	418	455	-
		72 h	153	115	-
77	10 mM APAP	0	588	573	1
		15 min	150	110	0
		30 min	728	604	2
		1 h	917	957	2
		2 h	424	525	1
		6 h	736	762	1
		24 h	478	535	1
		72 h	426	499	3
77	10 mM APAP + NAC	0	294	70	0
		15 min	13303	6144	37
		30 min	343097	54671	759
		1 h	483981	34810	834
		2 h	606764	105376	1794
		6 h	705125	56187	1276
		24 h	667079	95112	1596
		72 h	266176	10189	1735

**Table C.30.** Intensities, standard deviation and fold-changes for Penicillin G- cysteine from Patient 64

Patient age (years)	Treatment	Time point	Intensity	Standard Dev.	Fold change (compared to control)
64	Control	0	241	142	-
		15 min	278	87	-
		30 min	307	252	-
		1 h	334	135	-
		2 h	206	28	-
		6 h	202	65	-
		24 h	298	108	-
		72 h	260	136	-
64	5 mM APAP	0	560	686	2
		15 min	278	229	1
		30 min	343	173	1
		1 h	550	747	2
		2 h	272	54	1
		6 h	718	397	4
		24 h	706	306	2
		72 h	330	267	1
64	10 mM APAP	0	226	15	1
		15 min	360	28	1
		30 min	295	44	1
		1 h	492	32	1
		2 h	340	74	2
		6 h	320	29	2
		24 h	584	7	2
		72 h	479	117	2

**Table C.31.** Intensities, standard deviation and fold-changes for Penicillin G- cysteine from Patient 47

Patient age (years)	Treatment	Time point	Intensity	Standard Dev.	Fold change (compared to control)
47	Control	0	131	12	-
		15 min	135	7	-
		30 min	244	47	-
		1 h	238	95	-
		2 h	326	359	-
		6 h	155	116	-
		24 h	156	1	-
		72 h	245	128	-
47	5 mM APAP	0	295	311	2
		15 min	88	27	1
		30 min	243	59	1
		1 h	139	26	1
		2 h	200	144	1
		6 h	277	155	2
		24 h	119	60	1
		72 h	402	307	2
47	5 mM APAP + 10 mM NAC	0	321	143	2
		15 min	491536	73217	3633
		30 min	428933	21981	1761
		1 h	73199	5369	308
		2 h	542940	36588	1666
		6 h	62524	8257	403
		24 h	325300	2896	2088
		72 h	452593	23134	1851

**Table C.32.** Intensities, standard deviation and fold-changes for APAP-NAC from Patient 77

Patient age (years)	Treatment	Time point	Intensity	Standard Dev.	Fold change (compared to control)
77	Control	0	3782	153	-
		15 min	5308	1926	-
		30 min	3975	394	-
		1 h	6451	962	-
		2 h	12567	2027	-
		6 h	8157	5733	-
		24 h	4531	3829	-
		72 h	2343	1030	-
77	10 mM APAP	0	11647	10182	3
		15 min	7432	3198	1
		30 min	5748	7186	1
		1 h	7153	6989	1
		2 h	4601	2767	0
		6 h	5404	2348	1
		24 h	4006	1047	1
		72 h	5197	2159	2
77	10 mM APAP + NAC	0	6568	970	2
		15 min	90873	6965	17
		30 min	206155	18498	52
		1 h	192332	5560	30
		2 h	208412	2976	17
		6 h	109149	18469	13
		24 h	101356	2576	22
		72 h	65279	8635	28

**Table C.33.** Intensities, standard deviation and fold-changes for APAP-NAC from Patient 64

Patient age (years)	Treatment	Time point	Intensity	Standard Dev.	Fold change (compared to control)
64	Control	0	3669	4318	-
		15 min	1698	371	-
		30 min	1542	557	-
		1 h	1873	841	-
		2 h	37674	61605	-
		6 h	1237	297	-
		24 h	2800	2862	-
		72 h	1368	353	-
64	5 mM APAP	0	1100	188	0
		15 min	1378	188	1
		30 min	1984	338	1
		1 h	2484	2500	1
		2 h	1297	109	0
		6 h	2545	2322	2
		24 h	1836	1157	1
		72 h	1196	473	1
64	10 mM APAP	0	1411	244	0
		15 min	1500	369	1
		30 min	1575	87	1
		1 h	1453	4	1
		2 h	1348	109	0
		6 h	1669	190	1
		24 h	1191	12	0
		72 h	1793	143	1

**Table C.34.** Intensities, standard deviation and fold-changes for APAP-NAC from Patient 47

Patient age (years)	Treatment	Time point	Intensity	Standard Dev.	Fold change (compared to control)
47	Control	0	1559	52	-
		15 min	1397	289	-
		30 min	1943	569	-
		1 h	2170	1239	-
		2 h	1846	369	-
		6 h	1581	666	-
		24 h	1806	487	-
		72 h	1486	177	-
47	5 mM APAP	0	1826	857	1
		15 min	2016	275	1
		30 min	1405	1256	1
		1 h	3668	1118	2
		2 h	2824	470	2
		6 h	2066	753	1
		24 h	1711	44	1
		72 h	1398	1052	1
47	5 mM APAP + 10 mM NAC	0	1977	438	1
		15 min	190261	6921	136
		30 min	109519	14183	56
		1 h	60069	3607	28
		2 h	205375	15247	111
		6 h	163324	19564	103
		24 h	27859	2214	15
		72 h	26610	2158	18

**Table C.35.** Intensities, standard deviation and fold-changes for Penicillin G-NAC from Patient 77

Patient age (years)	Treatment	Time point	Intensity	Standard Dev.	Fold change (compared to control)
77	Control	0	18365	13559	-
		15 min	10060	9840	-
		30 min	10258	9366	-
		1 h	22205	15848	-
		2 h	1540	1302	-
		6 h	17525	11964	-
		24 h	10672	8006	-
		72 h	3130	2672	-
77	10 mM APAP	0	12722	15270	1
		15 min	5352	5881	1
		30 min	18721	14397	2
		1 h	20033	19746	1
		2 h	8366	11521	5
		6 h	19225	21498	1
		24 h	9803	11553	1
		72 h	5888	4813	2
77	10 mM APAP + NAC	0	10167	5294	1
		15 min	50632	11933	5
		30 min	644919	23487	63
		1 h	537961	29968	24
		2 h	459607	21109	298
		6 h	5038	1140	0
		24 h	229	81	0
		72 h	400	77	0



**Table C.36.** Intensities, standard deviation and fold-changes for Penicillin G-NAC from Patient 64

Patient age (years)	Treatment	Time point	Intensity	Standard Dev.	Fold change (compared to control)
64	Control	0	4873	4296	-
		15 min	4961	2369	-
		30 min	8563	6455	-
		1 h	2841	1070	-
		2 h	2780	2352	-
		6 h	5265	422	-
		24 h	4488	974	-
		72 h	7779	3201	-
64	5 mM APAP	0	14110	15532	3
		15 min	9426	5630	2
		30 min	6165	2009	1
		1 h	19441	24085	7
		2 h	3211	988	1
		6 h	15546	12282	3
		24 h	16599	6375	4
		72 h	12066	11813	2
64	10 mM APAP	0	3501	788	1
		15 min	12061	1900	2
		30 min	5768	735	1
		1 h	10071	9877	4
		2 h	4414	1739	2
		6 h	10043	5216	2
		24 h	15070	20349	3
		72 h	7701	8088	1

**Table C.37.** Intensities, standard deviation and fold-changes for Penicillin G-NAC from Patient 47

Patient age (years)	Treatment	Time point	Intensity	Standard Dev.	Fold change (compared to control)
47	Control	0	2001	280	-
		15 min	3190	81	-
		30 min	8045	7517	-
		1 h	9455	8310	-
		2 h	16384	15739	-
		6 h	2836	228	-
		24 h	2702	1033	-
		72 h	4171	2627	-
47	5 mM APAP	0	7591	7592	4
		15 min	3030	155	1
		30 min	10393	9893	1
		1 h	3326	94	0
		2 h	7929	7842	0
		6 h	7721	4838	3
		24 h	1790	1369	1
		72 h	9108	10287	2
47	5 mM APAP + 10 mM NAC	0	8463	847	4
		15 min	396645	17771	124
		30 min	36112	3263	4
		1 h	62046	3706	7
		2 h	744044	84705	45
		6 h	31940	6143	11
		24 h	796	93	0
		72 h	687	451	0

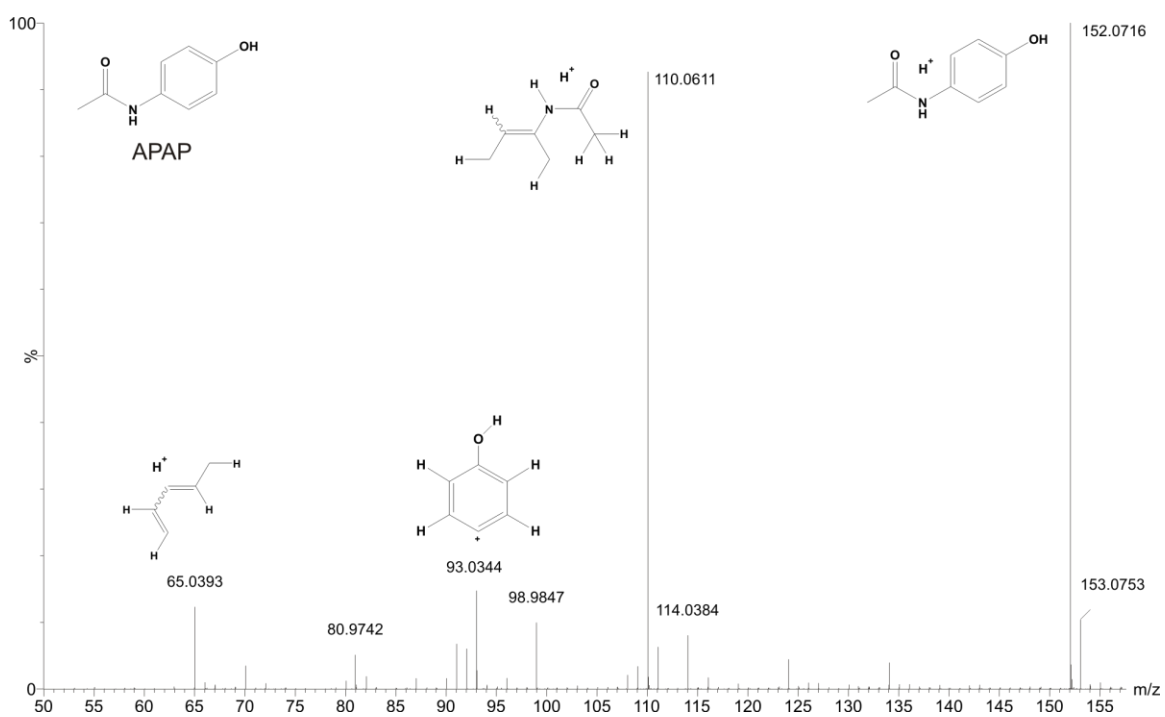


**Figure C.6.** Annotated retention time and drift selected fragmentation spectrum for Acetaminophen (APAP).

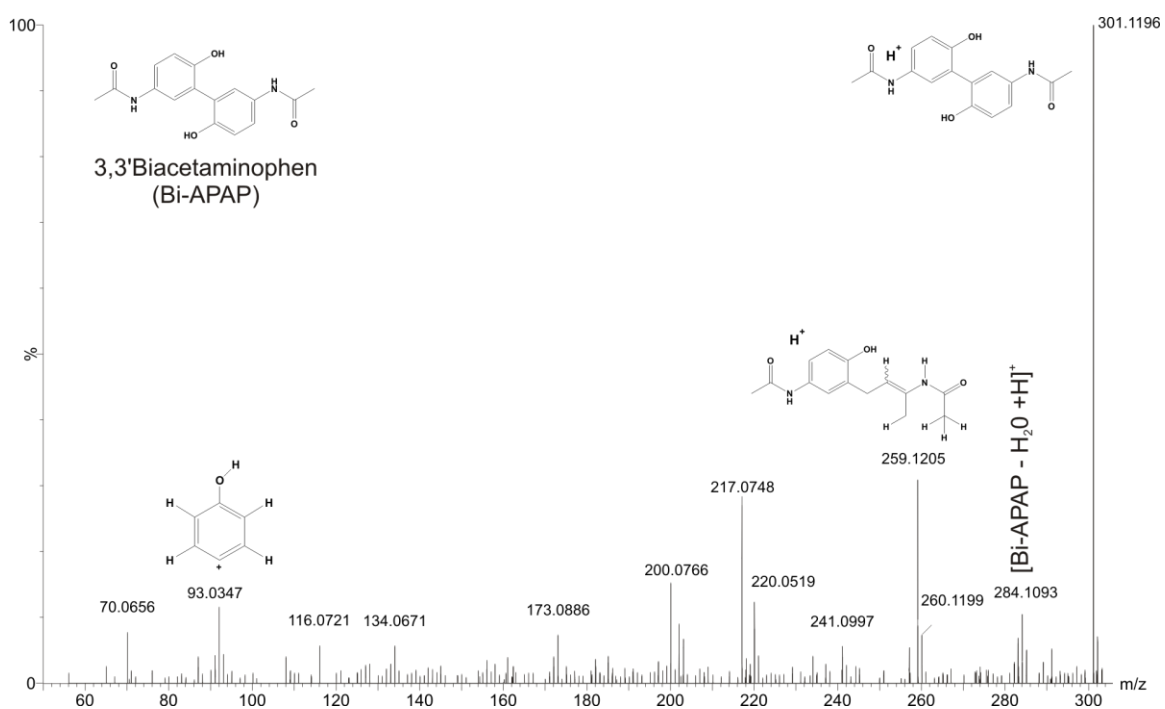


**Figure C.7.** Annotated retention time and drift selected fragmentation spectrum for 3,3'-Biacetaminophen (Bi-APAP).

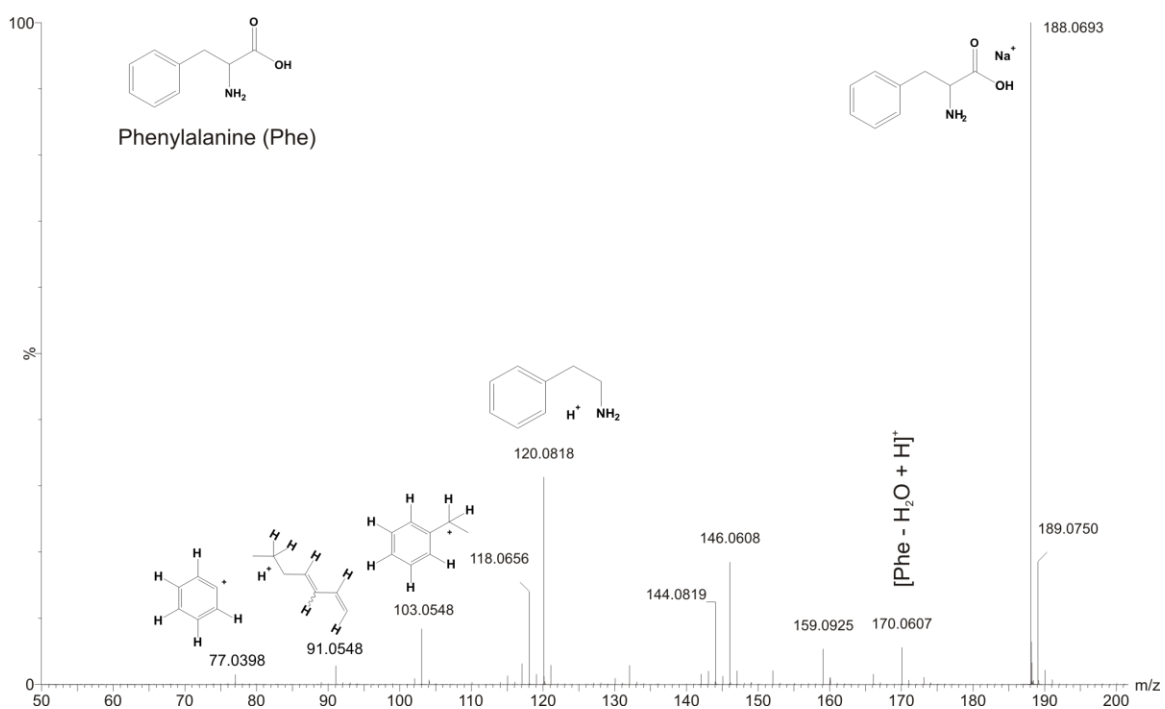


**Figure C.8.** Annotated retention time and drift selected fragmentation spectrum for Phenylalanine (Phe).

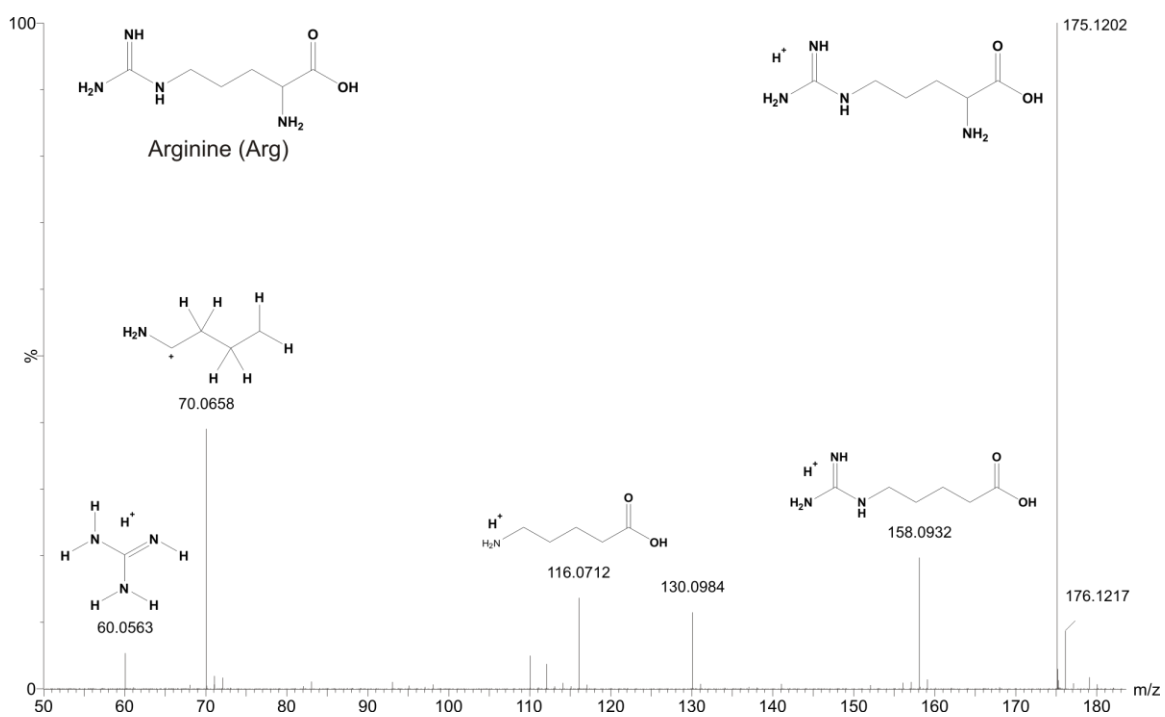


**Figure C.9.** Annotated retention time and drift selected fragmentation spectrum for Arginine (Arg).

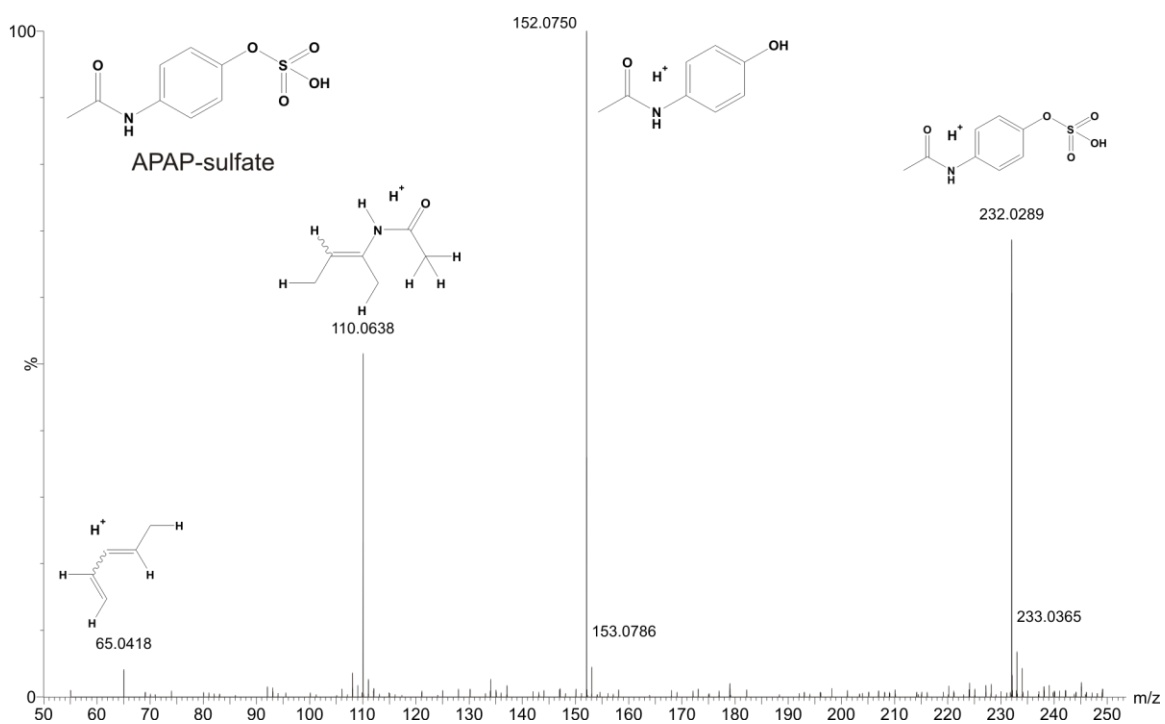


**Figure C.10.** Annotated retention time and drift selected fragmentation spectrum for Acetaminophen-sulfate (APAP-sulfate).

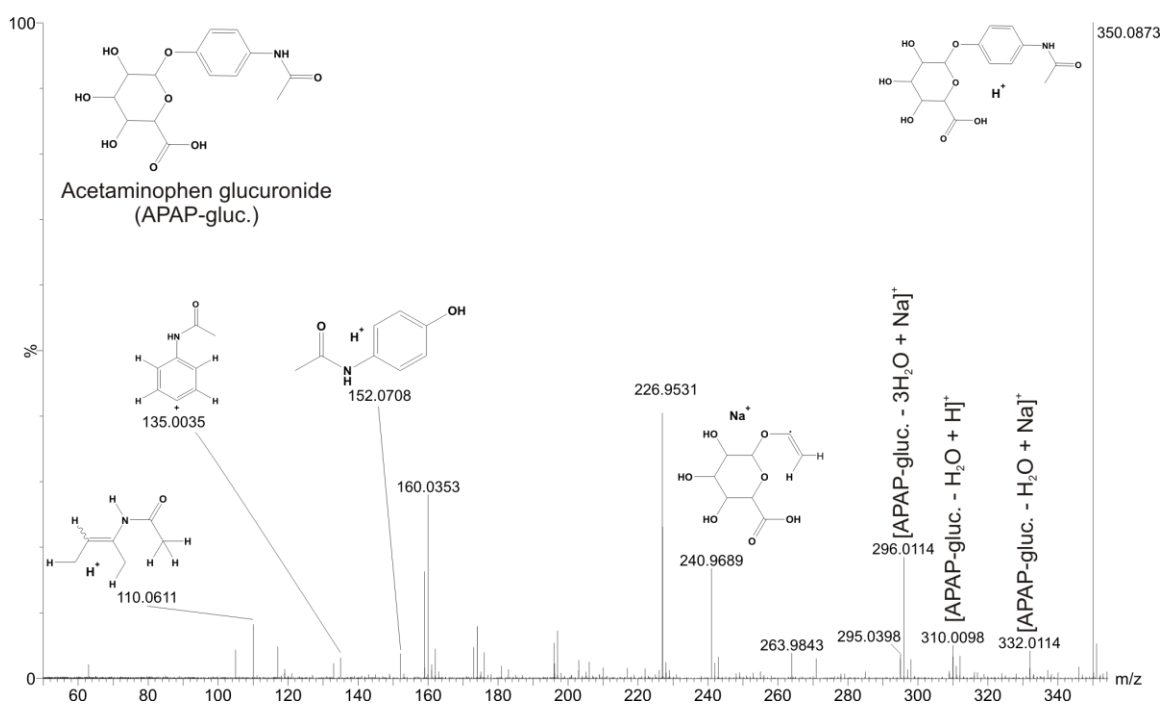


**Figure C.11.** Annotated retention time and drift selected fragmentation spectrum for Acetaminophen-glucuronide (APAP-gluc.)



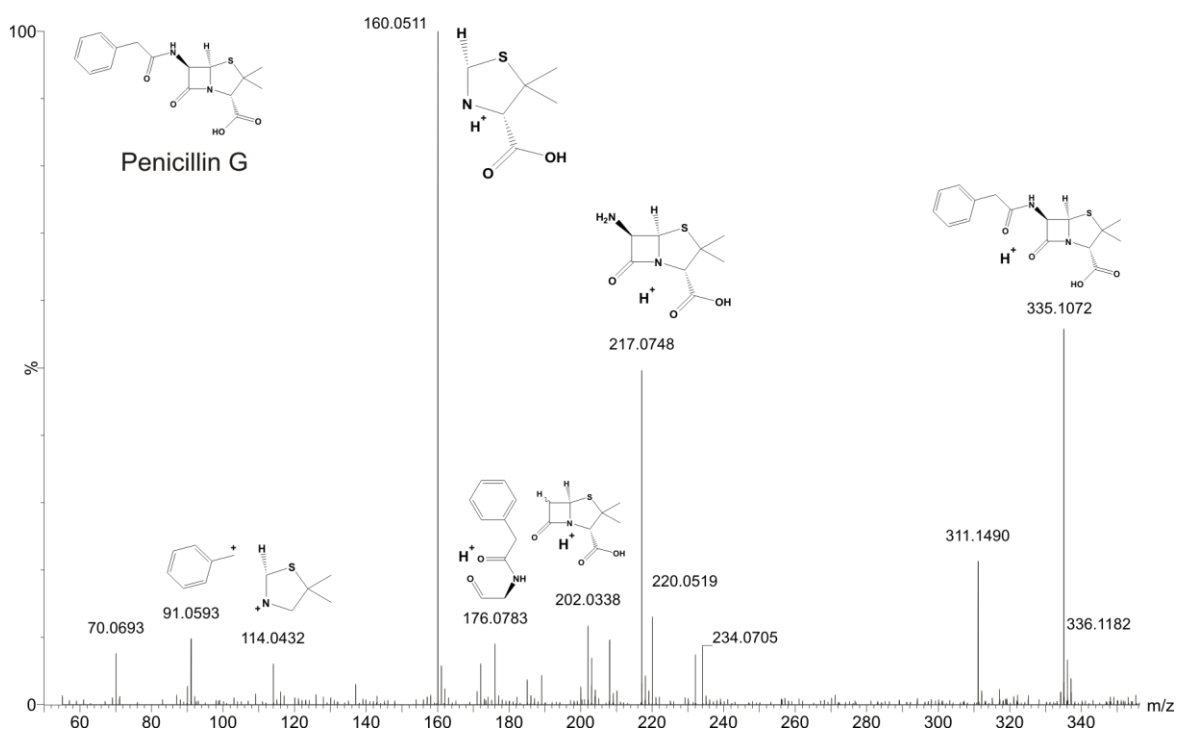


**Figure C.12.** Annotated retention time and drift selected fragmentation spectrum for penicillin G.

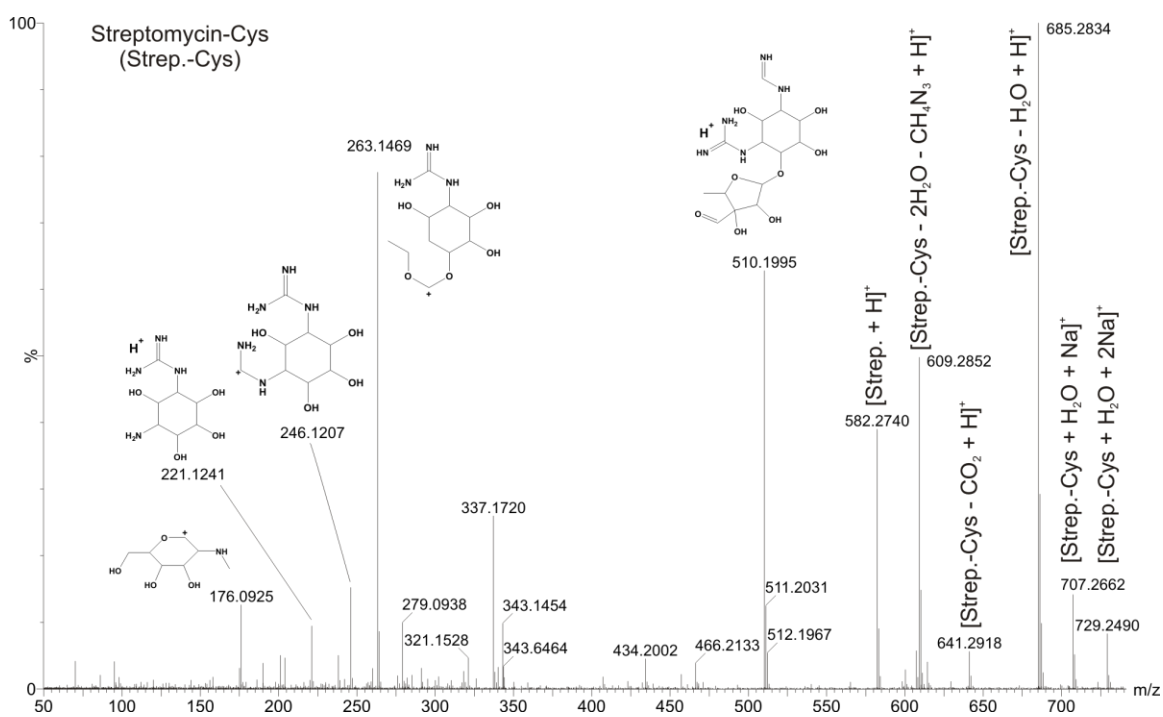


**Figure C.13.** Annotated retention time and drift selected fragmentation spectrum for streptomycin-cysteine (Strep.-Cys)

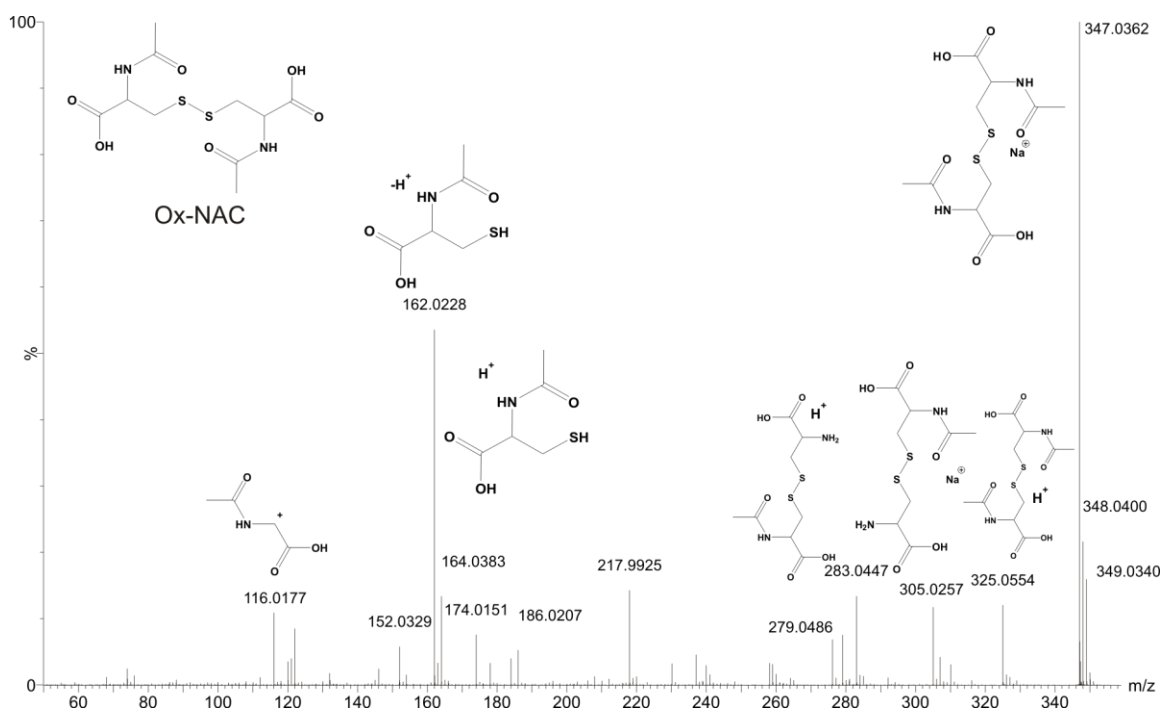


**Figure C.14.** Annotated retention time and drift selected fragmentation spectrum for oxidized N-acetyl cysteine (Ox-NAC).

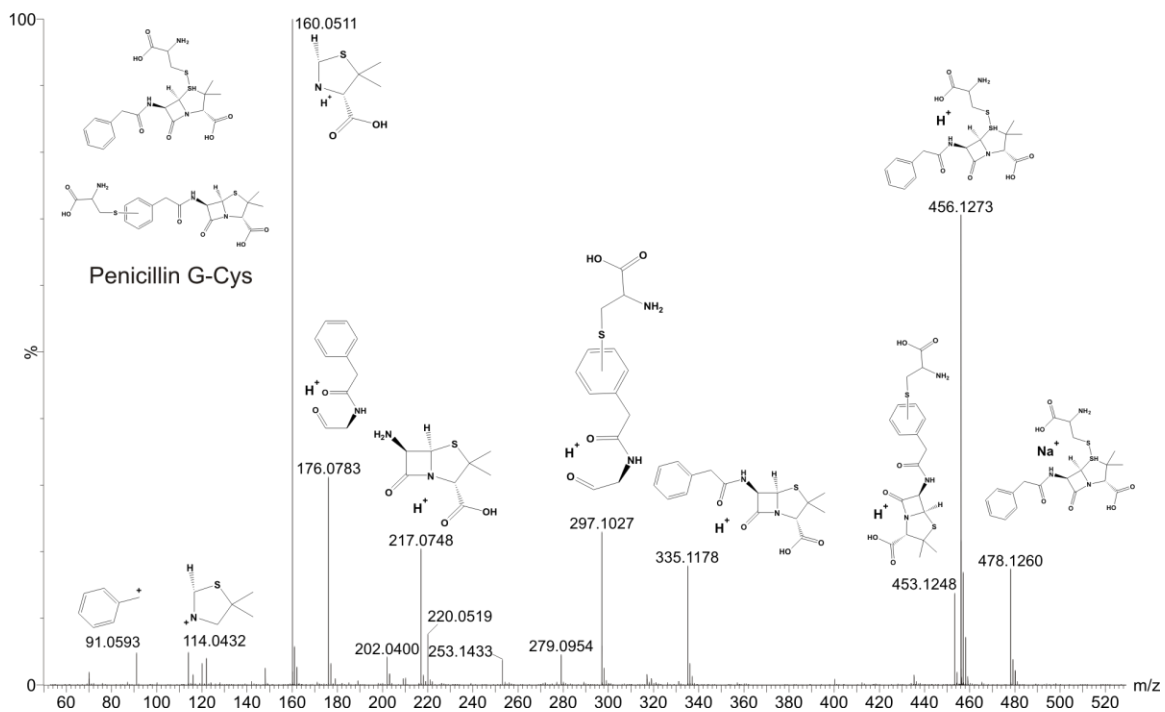


**Figure C.15.** Annotated retention time and drift selected fragmentation spectrum for penicillin G – cysteine (Pen. G-Cys).

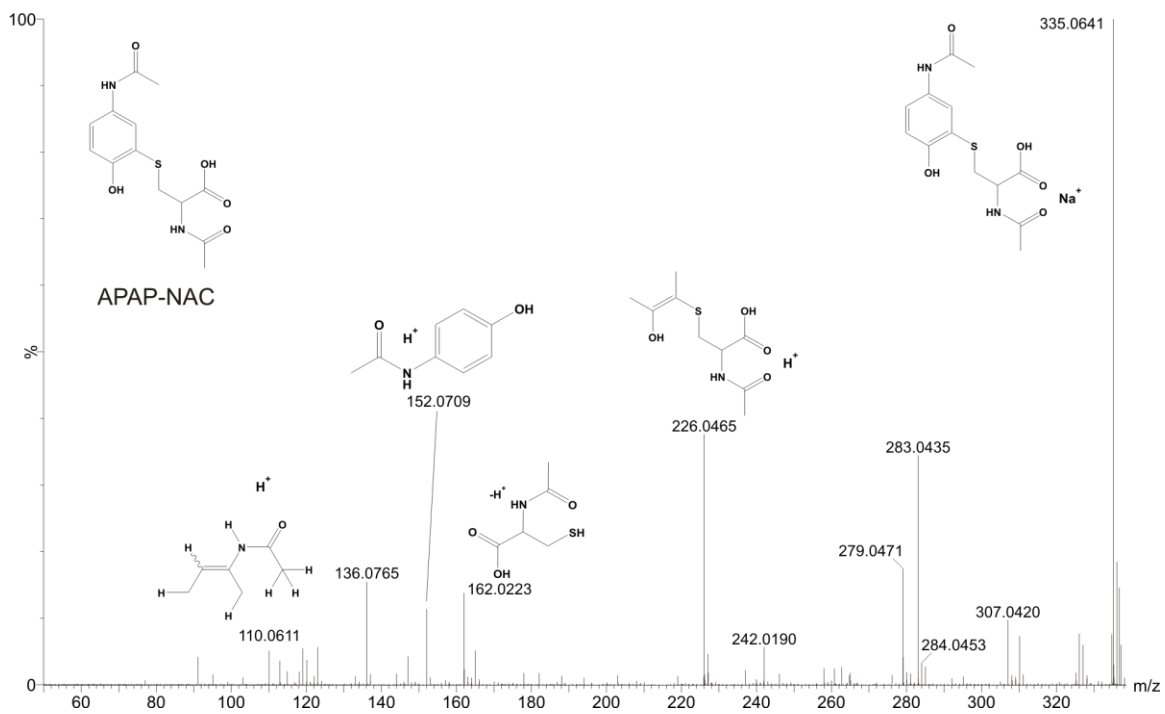


**Figure C.16.** Annotated retention time and drift selected fragmentation spectrum for Acetaminophen – N-acetyl cysteine (APAP-NAC).

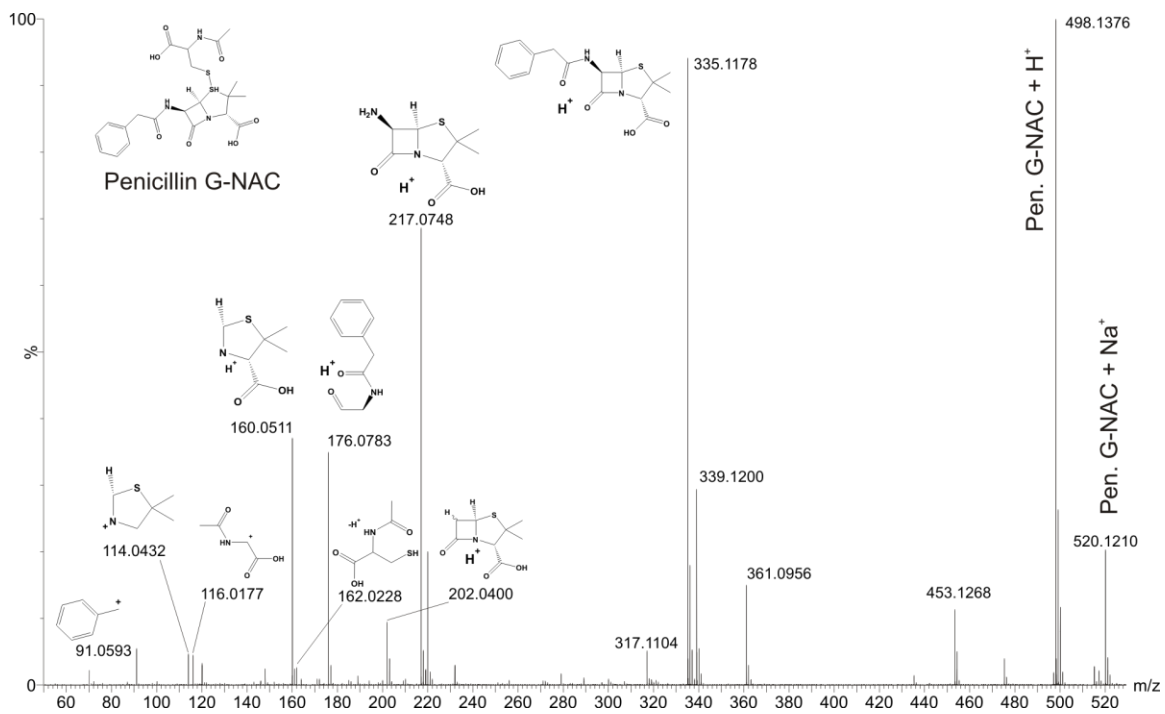


**Figure C.17.** Annotated retention time and drift selected fragmentation spectrum for penicillin G – N-acetylcysteine (Pen. G-NAC).

APPENDIX D

SUPPORTING INFORMATION FOR CHAPTER IV

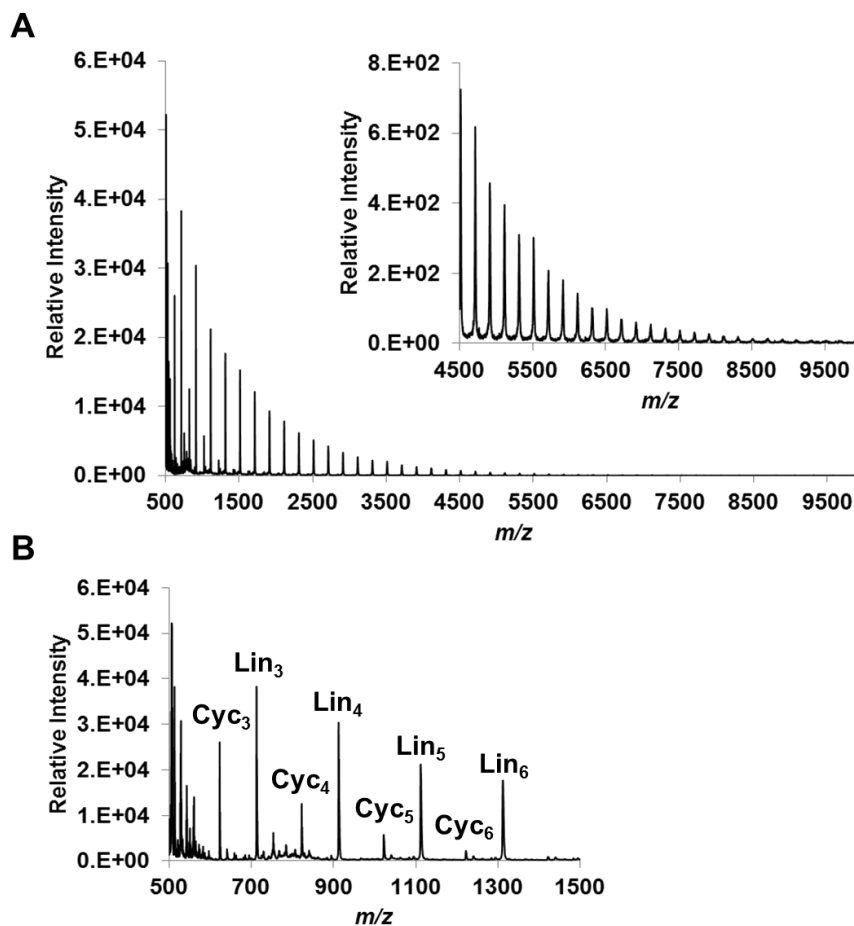


**Figure D.1.** MALDI spectrum of PE-225 in positive-ion mode. (A)  $m/z$  range of 500 to 10,000 and expanded range of 4500 to 10,000. (B) Expanded range of 500 to 1,500 shows linear (Lin) and cyclic (Cyc) species for  $n=3$  to  $n=6$ .

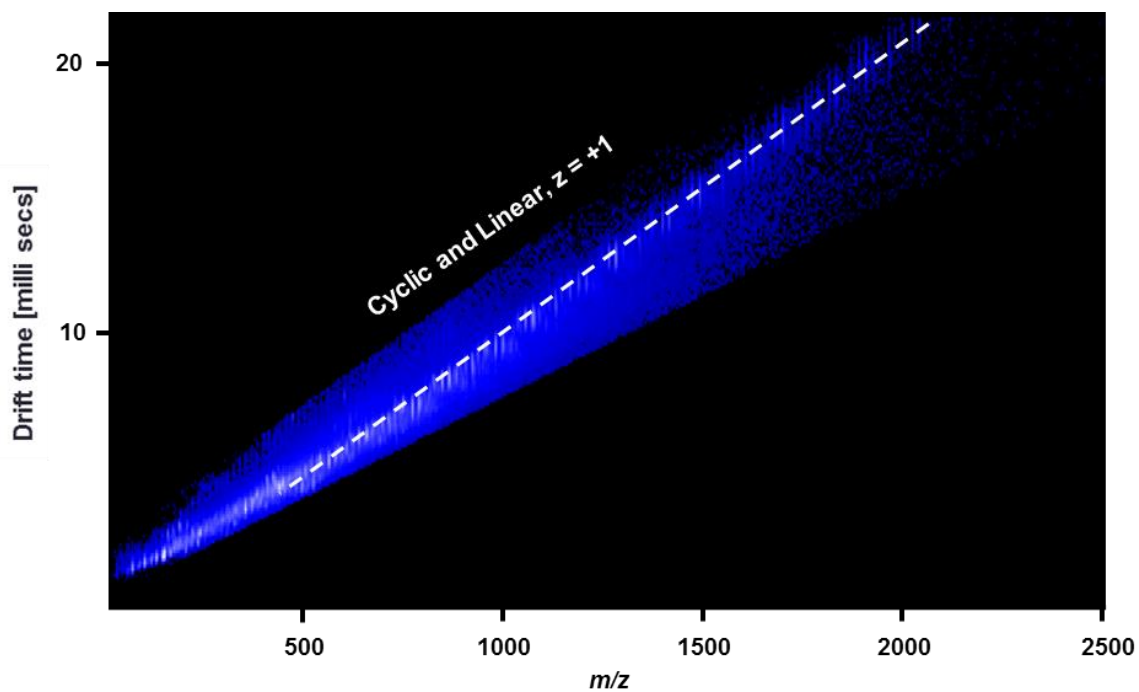


**Figure D.2.** MALDI IM-MS spectrum of PE-225 in positive-ion mode. Characteristic MALDI singly charged species are observed for both linear and cyclic chains as both  $\text{Na}^+$  and  $\text{H}^+$  species. Both linear and cyclic chains have linear gas-phase packing efficiency correlation proportional to their molecular weight.



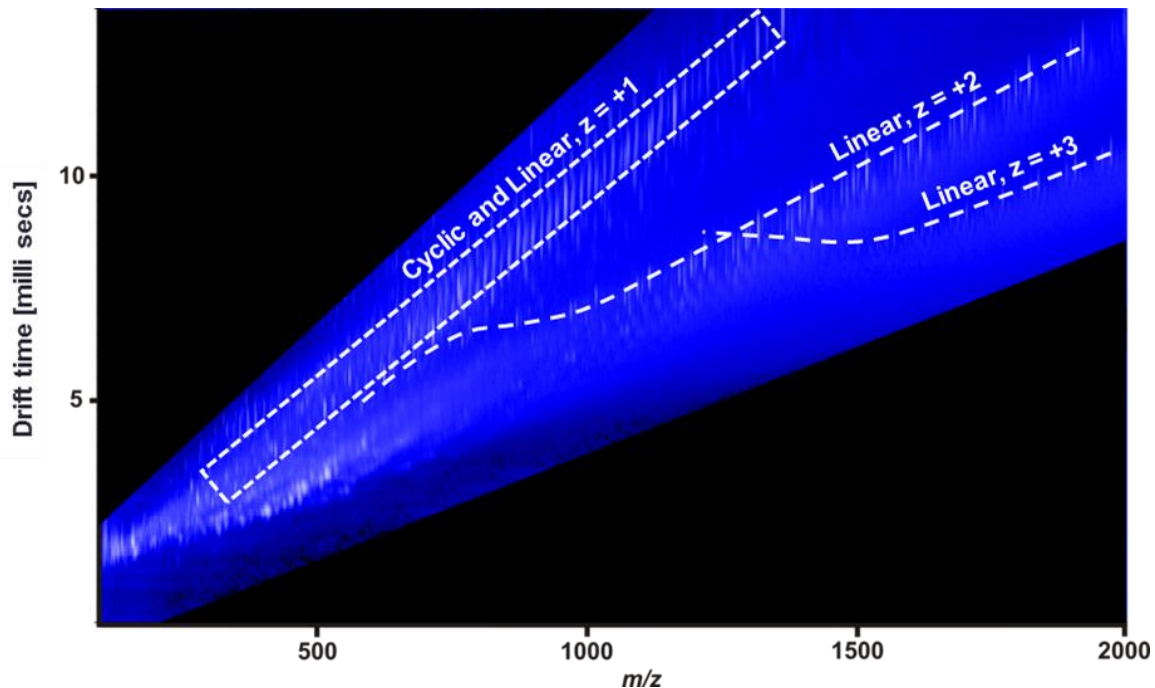


**Figure D.3.** ESI IM-MS spectrum of PE-225 in positive-ion mode. Characteristic ESI multiply charged species ( $z = +2$  and  $+3$ ) are observed for linear chains as both  $\text{Na}^+$  and  $\text{H}^+$  species. However, cyclic species are singly charged. The effects in their mobility behavior and gas-phase packing efficiency of multiply charged linear chains is observed in charged specific trend lines in the 2D IM-MS separation space.

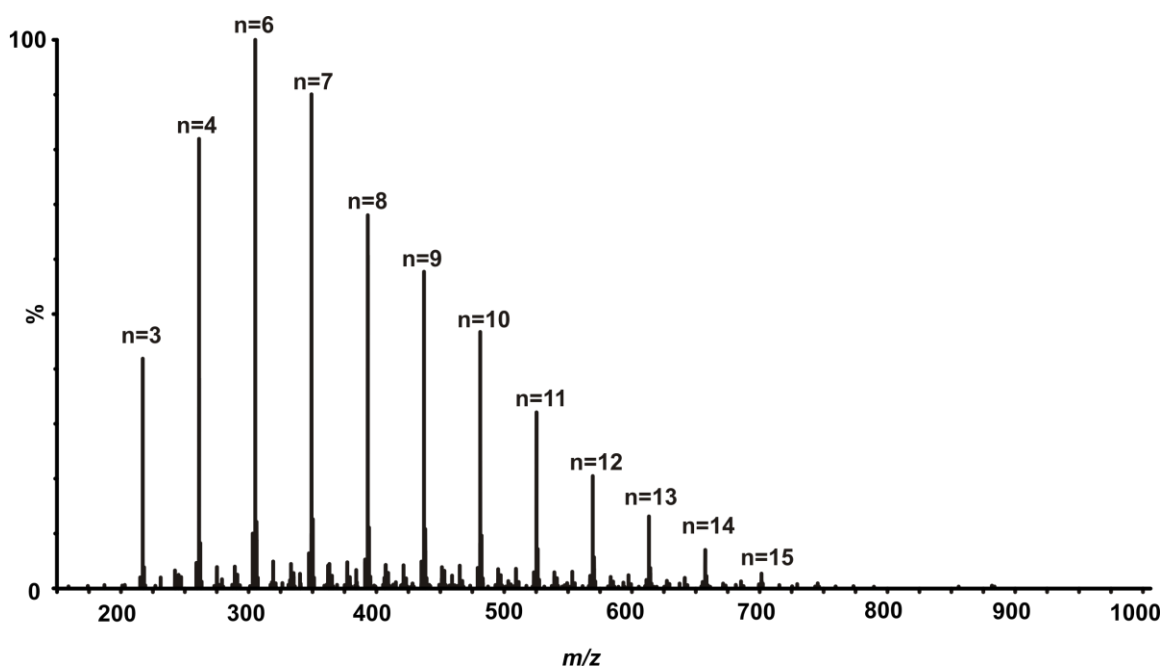


**Figure D.4.** MS of PEG with ESI in positive-ion mode. Species are  $[M+Na^+]^+$ .

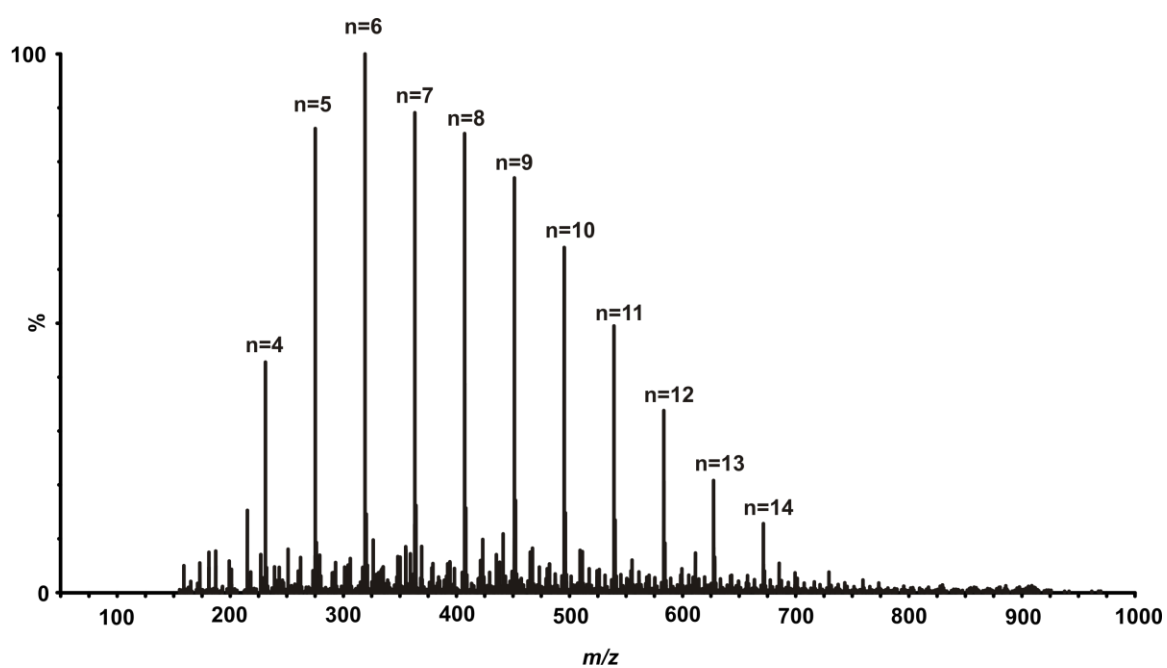


**Figure D.5.** MS of PEG methylether with ESI in positive-ion mode. Species are  $[M+Na^+]^+$ .

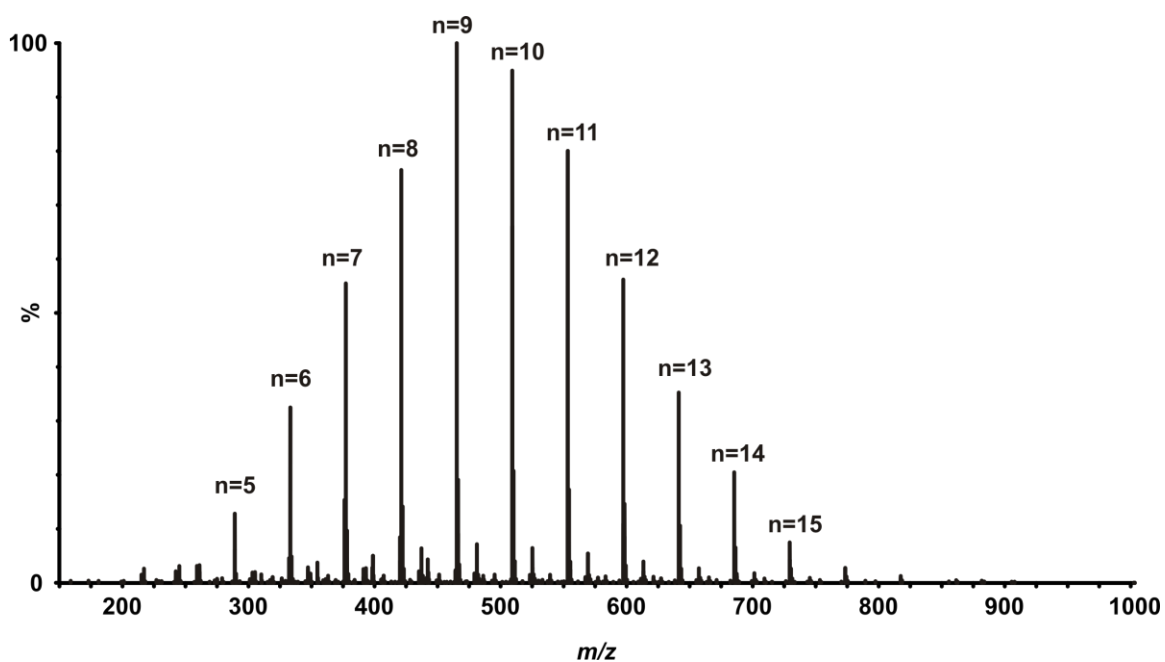


**Figure D.6.** MS of PEG dimethylether with ESI in positive-ion mode. Species are  $[M+Na^+]^+$ .

## APPENDIX E

### CURRICULUM VITAE

#### **J. Rafael Montenegro Burke**

Vanderbilt University Department of Chemistry  
7330 Stevenson Center, Station B 35-1822  
Nashville, TN 37235  
Cell: (615)-400-5809  
rafael.montenegro@vanderbilt.edu  
montenegroburke@gmail.com

#### **EDUCATION**

**Vanderbilt University** Nashville, TN  
Ph.D. Chemistry 04/15/2016

Dissertation: Enhanced Separation Strategies for Complex Sample Characterization  
Using Ion Mobility-Mass Spectrometry  
Advisor: Dr. John A. McLean

**Graz University of Technology** Graz, Austria  
Diplom Ingenieur 21/10/2009  
(Equal to Master of Science in Chemical Engineering)

Thesis: Trace analysis of palladium in plant material by Hg-coprecipitation and  
ICP-SFMS  
Advisors: Dr. Klaus Günther and Dr. J. Sabine Becker (Research Centre Jülich,  
Germany)

#### **RESEARCH EXPERIENCE**

##### **Graduate Research Assistant**

- Developed rapid separation methodologies for the analysis of a wide range lipids using supercritical fluid chromatography (SFC) coupled to ion mobility-mass spectrometry (IM-MS). This strategy was applied in the analysis of human monocyte derived macrophages during the polarization process, revealing highly

orchestrated and specific fatty acid mobilization for specific polarization phenotypes and stimuli.

- Defined the metabolic profiles of macaque and human amniotic fluid in an untargeted manner using ultra-performance liquid chromatography (UPLC) and SFC coupled to IM-MS. Performed multivariate statistical analyses as well as self-organizing maps (SOM) to reveal differentially expressed features. Characterized molecular features with accurate mass, MS/MS, drift time, and standard compounds to validate tentative identifications. Distinguished dysregulated small molecules based on time of delivery and/or length of bacterial infection.
- Developed separation techniques for the characterization of synthetic polymers capable of separating linear and cyclic species independently of their molecular weight. These separations show size exclusion chromatography as well as adsorption chromatography characteristics in a one-solvent system. The separation and characterization of different types of polymers such as polyesters, polyurethanes and polyethers have been achieved.

#### **Master's Thesis (Research Centre Juelich, Germany)**

- Determined the absorption of palladium (Pd) by plants by developing a mercury (Hg) co-precipitation protocol for sample preparation. Sector Field mass Spectrometry (ICP-SFMS) was used to quantify the total amount of Pd absorbed by the different plants and parts, where distinct differences were observed for different plants at different conditions.

#### **HONORS AND AWARDS**

- 2015 **MSACL Young Investigator Award**, Mass Spectrometry Applications to the Clinical Lab
- 2015 **College Teaching Certificate**, Vanderbilt University Center for Teaching
- 2014 **Vanderbilt Institute of Chemical Biology Poster Award**
- 2014 **ASMS Student Travel Award**, American Society of Mass Spectrometry

#### **PUBLICATIONS**

9. **Montenegro-Burke, J.R.**; Goodwin, C.R.; Bachmann, B.O.; McLean, J.A. Supercritical Fluid Chromatography coupled with Ion Mobility-Mass Spectrometry for analysis of biological samples, In preparation for *Analytical Chemistry*.

8. **Montenegro-Burke, J.R.;** Goodwin, C.R.; Knöspel, F.; Gerstmann, F.; Zeilinger, K.; Storch, L.; Damm, G.; Sherrod, S.; Iyer, S.; Iyer, R.; Wikswo, J.P. McLean, J.A.; Towards the Development of a  $\mu$ Human: Dynamic Exo-metabolomic Response Analysis of 3-Dimensional Hepatocyte Bioreactor to Acetaminophen and N-acetyl Cysteine Exposure, In preparation for *Analytical Chemistry*.
7. **Montenegro-Burke, J.R.;** Xu, L.; Korade, Z.; Porter, N.A.; McLean, J.A. Expanding Lipidomic Separation Space by Integrating Supercritical Fluid Chromatography with Ion Mobility-Mass Spectrometry, In preparation for *Analytical and Bioanalytical Chemistry*.
6. **Montenegro-Burke, J.R.;** Sutton, J.A.; Rogers, L.M.; McLean, J.A.; Aronoff, D.M. Lipid Profiling of 3-Dimensional Polarization Space of Human Monocyte-derived Macrophages, In preparation for *Prostaglandins & Other Lipid Mediators*.
5. Kitko, K.E.; Hong, T.; Lazarenko, R.M.; **Montenegro-Burke, J.R.;** Shah, A.T.; Ying, D.; Raghunathan, K.; Kenworthy, A.K.; Skala, M.C.; McLean, J.A.; Xu, Y.; Zhang, Q. Graphene reshapes cell communication via its interaction with membrane cholesterol, Submitted to *Nature Nanotechnology*, November 2015.
4. Marin, M.; Spears, B.R.; **Montenegro-Burke, J.R.;** McLean, J.A.; Harth, E.M. Aqueous Epoxide Ring Opening Polymerization (AEROP): Green Synthesis of Poly(glycidol) with Ultra-low Branching, *Macromolecules*, 49, 2022-2027, (2016).
3. **Montenegro-Burke, J.R.;** Bennet, J.M.; McLean, J.A.; Hercules, D.M.; Novel behavior of the chromatographic separation of linear and cyclic polymers, *Analytical and Bioanalytical Chemistry*, 408, 677-681, (2016).
2. Lamberson, C.R.; Xu, L.; Muchalski, H.; **Montenegro-Burke, J.R.;** Shmanai, V.V.; Bekish, A.V.; McLean, J.A.; Clarke, C.F.; Shchepinov, M.S.; Porter, N.A., Unusual Kinetic Isotope Effects of Deuterium Reinforced Polyunsaturated Fatty Acids in Tocopherol-Mediated Free Radical Chain Oxidations, *Journal of the American Chemical Society*, 136, 838-841, (2014).
1. Pototschnig, G.; Morales De Csáky C.; **Montenegro-Burke, J.R.;** Schitter G.; Stütz, A.E.; Tarling, C.A.; Withers, S.G.; Wrodnigg, T.M., Synthesis and biological evaluation of novel biotin-iminoalditol conjugates, *Bioorganic & Medicinal Chemistry Letters*, 20, 4077-4079, (2010).

## PRESENTATIONS

11. **Montenegro-Burke, J.R.,** *High dimensional separation strategies in analysis of complex biological samples using ion mobility-mass spectrometry*, 32<sup>nd</sup>

International Symposium on Microscale Separations and Bioanalysis, Niagara-on-the-Lake, Canada (April 2016). **(Oral)**

10. **Montenegro-Burke, J.R.;** Aronoff, D.M.; McLean, J.A.; Rajagopal, L.; Adams Waldorf, K. *Dynamic Changes in the Metabolic Signature of Amniotic Fluid during Infection-Associated Preterm Labor*, Society for Reproductive Investigation 63<sup>rd</sup> Annual Scientific Meeting, Montreal, Canada (March, 2016).
9. **Montenegro-Burke, J.R.;** Goodwin, C.R.; Knöspel, F.; Gerstmann, F.; Zeilinger, K.; Storch, L.; Damm, G.; Sherrod, S.; Iyer, S.; Iyer, R.; Wikswo, J.P. McLean, J.A., *Dynamic Exo-metabolomic Response Analysis of 3-Dimensional Liver Bioreactor to Acetaminophen and N-acetylcysteine Exposure*, Vanderbilt Institute of Chemical Biology Student Symposium, Nashville, TN (August, 2015).
8. **Montenegro-Burke, J. R.;** Hallingstrom, M.; Rogers, L.M.; Jacobsson, B.; Kacerovsky, M.; Aronoff, D.M.; Mclean, J.A., *Untargeted Ion Mobility-Mass Spectrometry (IM-MS) Based Metabolomics Study of Amniotic Fluid for Preterm Birth with Liquid and Supercritical Fluid Chromatography*, 63<sup>rd</sup> American Society for Mass Spectrometry Conference on Mass Spectrometry and Allied Topics, St. Louis, MO (June, 2015).
7. **Montenegro-Burke, J.R.;** Rogers, L.M.; Hallingstrom, M.; Jacobsson, B.; Kacerovsky, M.; Aronoff, D.M. and McLean, J.A., *Metabolomics Study of Premature Labor: Combined Supercritical Fluid Chromatography and Liquid Chromatography Coupled with Ion Mobility-Mass Spectrometry*, Mass Spectrometry: Applications to the Clinical Lab, San Diego, CA (March, 2015). **(Oral)**
6. **Montenegro-Burke, J.R.;** Rogers, L.M.; Hallingstrom, M.; Kacerovsky, M.; Jacobsson, B.; Aronoff, D.M. and McLean, J.A., *High-Dimensional Untargeted Metabolomics Strategy for Assessing Markers of Preterm Birth From Amniotic Fluid*, Society for Reproductive Investigation 62<sup>nd</sup> Annual Scientific Meeting, San Francisco, CA (March, 2015).
5. **Montenegro-Burke, J.R.;** Enders, J.R.; Seale, K.T.; Wikswo, J.P. and McLean, J.A., *Real Time Metabolomic Analysis of Saccharomyces cerevisiae*, Vanderbilt Institute of Chemical Biology Student Symposium, Nashville, TN (August, 2014).
4. **Montenegro-Burke, J.R.;** Goodwin, CR.; Xu, L.; Korade, Z.; Bachmann, B.; Porter, N.A. and McLean, J.A., *Integration of Supercritical Fluid Chromatography with Ion Mobility-Mass Spectrometry (SFC-IM-MS) for Metabolomics and Lipidomics*, 62<sup>nd</sup> American Society for Mass Spectrometry Conference on Mass Spectrometry and Allied Topics, Baltimore, MD (June, 2014). **(Oral)**



3. **Montenegro-Burke, J.R.;** Goodwin, CR.; Bachmann, B. and McLean, J.A. *Combined Utility of Ultra Performance Liquid Chromatography (UPLC) and Supercritical Fluid Chromatography (SFC) for Biological Samples*, Vanderbilt Institute of Chemical Biology Student Symposium, Nashville, TN (August, 2013).
2. **Montenegro-Burke, J.R.;** Goodwin, CR.; Bachmann, B. and McLean, J.A. *Integration of Supercritical Fluid Chromatography with Ion Mobility-Mass Spectrometry (SFC-IM-MS) for Natural Product Discovery*, Annual SFC Meeting, Boston, MA (July, 2013).
1. **Montenegro-Burke, J.R.;** Enders, J.R.; Seale, K.T.; Wikswo, J.P. and McLean, J.A. *Progress towards real-time cell secretome analysis by mass spectrometry*, 61<sup>st</sup> American Society for Mass Spectrometry Conference on Mass Spectrometry and Allied Topics, Minneapolis, MN (June, 2013).

### TEACHING AND LEADERSHIP EXPERIENCE

- **Teaching Assistant**, General Chemistry Laboratory, 08/2011 – 12/2011, 01/2012 – 05/2012, and 01/2014 – 05/2014.
- **Teaching Assistant**, Organic Chemistry Laboratory, 07/2012 – 08/2012, 01/2013 – 05/2013.
- **Teaching Assistant**, Advanced Analytical Chemistry Laboratory, 08/2012 – 12/2012.
- **Co-founder and V. President**, Latin American and Caribbean Vanderbilt Student Association, 12/2014 – 03/2016.
- **Undergraduate Research Mentor**, Honor's thesis 01/2015 – 05/2015.

### PROFESSIONAL MEMBERSHIPS

The American Society for Mass Spectrometry  
 American Society for biochemistry and Molecular Biology